

Growth and Properties of Vapor Diffused Nb<sub>3</sub>Sn Coating for Superconducting  
Radiofrequency Accelerator Cavity Applications

Uttar Pudasaini

Kathmandu, Nepal

M.S. Physics, Old Dominion University, 2014

A Dissertation presented to the Graduate Faculty of The College of William & Mary  
in Candidacy for the Degree of  
Doctor of Philosophy

Applied Science Department

College of William & Mary  
January 2020



## APPROVAL PAGE

This Dissertation is submitted in partial fulfillment of  
the requirements for the degree of

Doctor of Philosophy



---

Uttar Pudasaini

Approved by the Committee November 2019



---

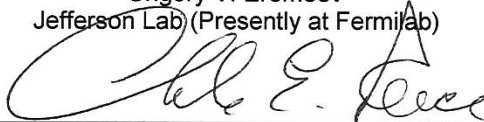
Committee Chair

Michael J. Kelley, Professor, Applied Science  
College of William & Mary



---

Grigory V. Ereemeev  
Jefferson Lab (Presently at Fermilab)



---

Charles E. Reece  
Jefferson Lab



---

Gunter Luepke, Professor, Applied Science  
College of William & Mary

## ABSTRACT

The desire to reduce construction and operating costs of future SRF accelerators motivates the search for higher-performing alternative materials. Nb<sub>3</sub>Sn ( $T_c \sim 18.3$  K and  $H_{sh} \sim 425$  mT) is the front runner. The tin vapor diffusion process is currently the technique of choice to produce promising Nb<sub>3</sub>Sn-coated cavities. Understanding Nb<sub>3</sub>Sn nucleation and growth in this process is essential to progress. Samples representing different stages of Nb<sub>3</sub>Sn formation have been produced and studied to elucidate the effects of nucleation, growth, process conditions, and impurities. Nb<sub>3</sub>Sn films with thickness from a few hundred nm up to  $\sim 15$   $\mu\text{m}$  were grown and characterized. The microscopic examination of samples suggests the mechanisms of thin film nucleation and growth. Broadly, nucleation deposits tin as a thin surface phase and, under some conditions, a few hundred nanometer sized particles as well. Conditions that impair nucleation promote the formation of defects, such as "patches", in subsequent coating growth. Analysis of coated samples is consistent with the model of Nb<sub>3</sub>Sn grown in which tin diffuses via grain boundaries to Nb<sub>3</sub>Sn-Nb interface, where the growth Nb<sub>3</sub>Sn into the niobium bulk takes place. Similar scaling laws are found for grain growth and layer thickness. Non-parabolic layer growth is consistent with significant grain growth, which reduces the number of Sn-transport channels. Examination of patchy region in Nb<sub>3</sub>Sn coating revealed it to be large single crystalline grains, pointing to impeded Nb<sub>3</sub>Sn layer growth due to low grain boundary density, resulting in a significantly thin coating in those areas. Examination of RF loss regions from a coated cavity, identified with a thermometry mapping system showed patchy regions and carbonus defects were associated with strong local field-dependent surface resistance. RF measurements of coated cavities were combined with material characterization of witness samples and coated-cavity cutouts to improve the coating process. Understanding obtained and applied to cavity coatings, resulted in single-cell Nb<sub>3</sub>Sn cavities with a quality factor of  $\sim 2 \times 10^{10}$  up to 15 MV/m accelerating gradient at 4 K, without "Wuppertal" Q-slope. We have also produced Nb<sub>3</sub>Sn-coated CEBAF 5-cell cavities with accelerating gradients useful for accelerator cryomodules. This dissertation will discuss the genesis of the Nb<sub>3</sub>Sn coating in a typical tin vapor diffusion process, effects of different process parameters, and its consequences to the coating of single-cell and multi-cell SRF cavities.

# TABLE OF CONTENTS

ACKNOWLEDGEMENTS .....	v
DEDICATION.....	vii
LIST OF TABLES.....	viii
LIST OF FIGURES .....	x
CHAPTER 1 Introduction .....	1
1.1 Organization of the Dissertation .....	3
1.2 Nb <sub>3</sub> Sn Application for SRF Accelerator Cavities.....	4
1.2.1 Discovery and Properties of Nb <sub>3</sub> Sn .....	4
1.2.2 Potential for Future SRF Applications.....	8
1.2.3 Nb <sub>3</sub> Sn Application in SRF .....	9
1.2.4 Recent Developments of Nb <sub>3</sub> Sn-coated Cavities.....	11
1.2.5 Tin Vapor Diffusion Coating of Nb <sub>3</sub> Sn .....	13
1.2.6 Jefferson Lab Coating System .....	16
1.2.7 Nb <sub>3</sub> Sn Coating Process.....	19
1.2.8 Typical Characteristics of Diffusion Coating of Nb <sub>3</sub> Sn .....	20
CHAPTER 2 Nucleation .....	24
2.1.1 Experimental .....	26
2.1.2 Characterization.....	26
2.2 Results and Discussion.....	29
2.2.1 Temperature Dependence of nucleation .....	29

2.2.2 Time Dependence of nucleation at 500 °C .....	40
2.2.3 Low vs. High Amount of tin chloride .....	42
2.2.4 Nucleation on Anodized Surfaces .....	44
2.2.5 Variation of Tin Particle Density .....	45
2.2.6 Nb <sub>3</sub> Sn Coatings with Different Nucleation Profiles.....	48
2.2.7 Role of Nucleation in Coating Genesis .....	49
2.2.8 Mechanism of Tin Deposition via SnCl <sub>2</sub> .....	52
2.3 Conclusions .....	55
CHAPTER 3 Growth .....	56
3.1 Coatings prepared under different coating conditions.....	58
3.1.1 Variation of substrate preparation .....	58
3.1.2 Coating with a low amount of tin.....	59
3.1.3 Inspection of samples coated at different facilities.....	62
3.1.4 Variation of coating time and temperature .....	66
3.2 Growth of Nb <sub>3</sub> Sn in vapor diffusion Process .....	74
3.2.1 Overcoat experiments .....	74
3.2.2 Results.....	75
3.2.3 Growth kinetics .....	85
3.2.4 Grain growth .....	93
3.3 Conclusions .....	96
CHAPTER 4 Studies of Samples Coated with SRF Cavity .....	98

4.1 RF and material analysis of cutouts from a Nb <sub>3</sub> Sn-coated single-cell cavity	99
4.1.1 Cavity Coating.....	99
4.1.2 Optical Inspection.....	101
4.1.3 RF Test Results .....	101
4.1.4 Sample Extraction .....	104
4.1.5 Temperature Mapping Data Analysis .....	108
4.1.6 Surface Analysis .....	114
4.1.7 Discussion .....	125
4.2 Witness Sample analysis linked with coating process and cavity performances	
.....	131
4.2.1 Witness sample studies and single-cell cavity coatings.....	131
4.2.2 Witness sample studies and five cell cavity coatings.....	140
4.2.3 Discussion .....	146
4.3 Conclusions .....	148
CHAPTER 5 Post-coating Treatments of Nb <sub>3</sub> Sn-coated Nb .....	150
5.1 BCP .....	152
5.2 Electro-chemical Treatment .....	154
5.3 Oxypolishing .....	165
5.4 Acid Immersion .....	170
5.4.1 HF Immersion .....	170
5.4.2 HNO <sub>3</sub> Immersion .....	172

5.4.3 HCl Immersion .....	172
5.5 Annealing.....	174
5.6 Conclusions .....	177
CHAPTER 6 Summary and Outlook.....	179
6.1 Summary .....	179
6.2 Outlook and Future Work .....	182
Appendix A .....	185
A.1 Superconductivity .....	185
A.2 SRF cavity .....	193
A.3 Niobium for SRF cavities .....	196
A.4 Alternate SRF cavity materials to bulk niobium .....	197
References .....	200

## ACKNOWLEDGEMENTS

First and foremost, I am incredibly grateful to my advisor Prof. Michael Kelley for his continuous support of my doctoral study and related research, for his care, patience, motivation, and decades of research and academic experiences. I am deeply indebted to him for providing me such an excellent research opportunity at Jefferson Lab. His guidance helped me in all the time and writing this dissertation. I could not have asked for a more supportive advisor than him. Besides benefited from his immense knowledge in materials science, I am also thankful for his seasonal vegetables.

The completion of this dissertation would not have been possible without the support and mentoring of Dr. Grigory Ereemeev at Jefferson Lab. I want to express my deepest gratitude to him for trusting me and letting me explore new ideas and skills. He had always been there whenever I needed his guidance. He ever listened to complains and frustrations patiently and encouraged me with timely pep talks. All the SRF and hardware skills (cleanroom practice, cavity preparation, coating, furnace operations, assembly, RF testing, etc.) that I have gained during my Ph.D. studies are credited to him. He assured me to complete my experiments on time and provided support to attend many conferences to present my work. I should also thank him for providing RF measurement data from several cavity tests.

My sincere thanks to Dr. Charlie Reece for his insightful comments, advice, encouragement, and guidance throughout my Ph.D. research project. His suggestions on several occasions helped me to widen my research from various perspectives. He was always ready to have a discussion, provide feedback, and ask hard questions, which always helped me to progress the study in the right direction.

I am thankful to Prof. Kelley, Dr. Ereemeev, and Dr. Reece for help in improving my writing and presentation skills all these years. They have had a significant impact on my professional development. Without their detailed reviews, this dissertation would not have been in this state.

I am also grateful to Prof. Gunter Luepke for taking time out of his busy schedule to serve as my dissertation committee member. His constructive comments and suggestions were valuable for this dissertation.

Many thanks to Dr. Jay Tuggle and Johny Angle at Virginia Tech. for characterizing many samples with XPS, TEM, and EBSD; without those, many analyses would not have been complete. Thanks also to Nizam Sayeed for helping me with the XRD characterization of some samples.

I must thank Olga Trofimova at Applied Research Center Core Lab for teaching me to use several microscopy instruments, and being always there to help me with AFM data collection. Thanks should also go to Amy Wilkerson for granting me any time access to characterization labs.

I would like to thank Lydia Whitaker and Lianne Ashburne for providing me all the necessary administrative support at William and Mary. I also want to thank Carolyn Camp at Jefferson Lab for administrative support and travel arrangements to attend many conferences.

My sincere thanks to Dr. Gianluigi Ciovati for providing several single-cell cavities for Nb<sub>3</sub>Sn coating and RF test data from several coated cavities, including the best performing single-cell cavity we produced so far at JLab. Thanks also to Dr. Pashupati Dhakal for helping me with several cavity tests. I would like to acknowledge Dr. Anne-Marie Valente-Feliciano, Dr. Rongli Geng, Dr. Hue Tian, Josh Spradlin, Ashley Anderson, Teena Harris, Bill Clemens, Kurt Macha, Tom Goodman, Hui Tian, and SRF technical staffs at JLab for productive discussion or supports to experimental research activities.

Last, and most importantly, I would like to thank all my family members, who have been my wonderful supporters and cheerleaders all these years. Special thanks to my parents, Janardan and Radha Pudasaini, who valued our education above all else. I can't thank enough to my brother Uttam Pudasaini for being such a great guardian, friend, motivator, and also a role model to me. Also, I like to thank my sister-in-law Mina Marasini and nephew Nirajan Chaulagain.

This Ph.D. is dedicated to my father, mother, and brother for constantly supporting and believing in me all the way.

## LIST OF TABLES

Table 2.1: Nucleation Experiments.....	26
Table 2.2: XPS elemental analysis of nucleated samples at different temperatures. The nucleation time for each sample was one hour. ....	32
Table 2.3: Calculated Fractional Surface Coverages.....	32
Table 2.4: Model parameters. ....	34
Table 2.5: Ratio of Sn to (Nb + Sn) obtained from the model calculation of dependence of intensity on the emission angle .....	35
Table 2.6: ARXPS ratio of Sn to (Nb+Sn).....	35
Table 2.7: XPS elemental analysis of nucleated samples for different durations at 500°C.41	
Table 2.8: XPS elemental analysis of nucleated sample U66 treated for 5 hours at 500 °C with a reduced amount of SnCl <sub>2</sub> . ....	43
Table 3.1: Investigated temperatures and durations of Nb <sub>3</sub> Sn diffusion coating. ....	66
Table 3.2: Overcoat experiments. Note that each experiment included new uncoated Nb samples along with samples from the previous run. ....	75
Table 3.3: Average grain sizes for the various total coating times. Note that there are two data sets for 3 hours of the coating. The first data set was obtained from the sample sequentially overcoated in the first three experiments (1+1+1 hour). The second data set was obtained on a new sample coated for 3 hours in the fourth experiment. ....	77
Table 3.4: Estimated average thicknesses for the sequential overcoat samples using different characterization techniques. ....	82
Table 4.1: Summary of estimated materials and RF parameters for different cutouts..	117
Table 5.1: Roughness of samples before and after electrochemical treatment at 21 °C.160	
Table 5.2: Roughness of samples before and after electrochemical treatment < 6 °C. 162	

Table 5.3: Averaged root mean square roughness ( $R_q$ ) of samples after ~ 50nm, 200 nm, and 500 nm EP removal. Note that the  $R_q$  value of similar untreated sample was  $(251 \pm 39)$  nm and  $(328 \pm 10)$  nm for  $10 \mu\text{m} \times 10 \mu\text{m}$  and  $50 \mu\text{m} \times 50 \mu\text{m}$ , respectively..... 164

Table 5.4: Estimated roughness for sequentially oxypolished samples. .... 169

Table 5.5: SEM result from coated samples immersed in  $\text{HNO}_3$  solution at different conditions ..... 173

Table A.1: Potential alternate SRF cavity materials with superconducting parameters [163]. ..... 199

## LIST OF FIGURES

Figure 1.1: Schematic A15 crystal structure of Nb <sub>3</sub> Sn. Yellow and blue spheres represent Sn and Nb, respectively. Adopted from [11]. .....	6
Figure 1.2: Binary phase diagram of the Nb-Sn system by Charlesworth et al. [7]. Adapted from [12].....	6
Figure 1.3: Variation of the critical temperature of Nb <sub>3</sub> Sn with Nb-Sn composition. T <sub>c</sub> (β) from equation 1.1 fits the available data [11]. .....	7
Figure 1.4: RF measurements from 1.5 GHz Nb <sub>3</sub> Sn/Nb cavities coated at Wuppertal University and tested at Jefferson Lab [22]. .....	10
Figure 1.5: State-of-the-art performances of 1.3 GHz single-cell Nb <sub>3</sub> Sn cavity at different labs. Data from Cornell and Fermilab were extracted from [35], [36]. .....	12
Figure 1.6: Nb <sub>3</sub> Sn coating configuration Wuppertal [49]. .....	14
Figure 1.7: Schematic of Nb <sub>3</sub> Sn coating furnaces at different labs (adopted from [35]). Siemens AG had used two configurations A and B. ....	16
Figure 1.8: A sketch of the upgraded coating chamber is shown in the image to the left. A CEBAF 5-cell cavity is shown loaded inside the hot zone of the furnace. A sample chamber replaces the cavity during the sample coating experiments. The coating system is shown at right. ...	18
Figure 1.9: Sample chamber, samples, tin and tin chloride packages, and Nb foils before setting up for the coating. The coating chamber of the furnace is not shown. ....	21
Figure 1.10: Temperature profile used for coating Nb <sub>3</sub> Sn on Nb samples at Jlab. The temperature of the insert during the process is monitored with three thermocouples outside the reaction insert at different sections of the insert. Because of very similar temperature readings, the temperature curves overlap in the plot. ....	21

Figure 1.11: Scanning electron microscopy (SEM) image of Nb<sub>3</sub>Sn-coated surface [left]. Atomic force microscopy (AFM) image of the same surface [right]. The average roughness was 150 nm. .... 22

Figure 1.12: Cross-section EBSD image from Nb<sub>3</sub>Sn coated surface. Note the larger size of Nb grains compared to Nb<sub>3</sub>Sn grains at the surface. .... 23

Figure 2.1: Vapor pressure of tin and tin chloride. The plot is reproduced from [33], which cites [57], [58]. .... 25

Figure 2.2: SEM images obtained from samples nucleated at temperatures of (a) 300 °C, (b) 400 °C, (c) 450 °C, and (d) 500 °C for one hour. Circular bright features are tin particles, as revealed by EDS [30]. .... 30

Figure 2.3: XPS data obtained from a sample after one hour at 500 °C. .... 31

Figure 2.4: SAM elemental mapping of Sn coverage after sputtering for thirty seconds is shown in the image (lower left). The brighter areas are richer in Sn than darker areas, as shown in the intensity scale. Equivalent data for Nb appear at the lower right. Elemental composition comparison of particle and background is shown in spectra at the top right. .... 37

Figure 2.5: (a) TEM cross-section of a sample nucleated at 500 °C for 5 h with EDS spectra from a line scan that follows a solid red line is superimposed on top of the TEM image. Nb signal is left out to make scaling reasonable for other signals. (b) Only the Sn spectra along the scan line. Note the jump of the Sn and O signals near the surface. .... 38

Figure 2.6: AFM image obtained from a sample treated at 500 °C for an hour is shown in (a). Note that the scan size is only 1 μm × 1 μm. Sn particles appear to be three-dimensional clusters forming islands. Height profile along the line passing through the tin island is shown in (b). Triangles of the matching color are reference points for the height measurements. .... 39

Figure 2.7: SEM images from samples obtained from experiments with a nucleation temperature of 500°C for (a) 4 hours and (b) 5 minutes. .... 40

Figure 2.8: AFM image of the surface after 4 hours of nucleation at 500 °C is shown in (a). (b) shows height profile along a line passing through tin particles. The largest particle is ~ 300 nm in diameter with height of ~175 nm. The triangles of the matching color are for the height measurements. .... 42

Figure 2.9: (a) SEM image of a nucleated surface obtained by using low tin chloride. (b) SAM elemental mapping of tin. .... 43

Figure 2.10: Nucleation on anodized Nb. The appearance and distribution of particles on the surface are different from those obtained on non-anodized samples..... 45

Figure 2.11: Variation of tin particles in different Nb grains. The arrows at the top figure indicate the direction of some scratches next to them. Particle distributions in areas A1 and A2 are evidently different. .... 46

Figure 2.12: a) Particle density variation in an anodized sample treated for 1 hour at 600 °C. (b) A zoom view of an area showing areas with different density of particles. (c) A clear transition line between the two regions. (d) The triangular appearance of deposited particles. .... 47

Figure 2.13: Nb<sub>3</sub>Sn coatings obtained by applying different nucleation profiles. U146, U105, U149, and U153 involved nucleation step 400 °C for 1 h, 500 °C for 1 h and 500 °C for 4 h and 500 °C for 5 h respectively. U153 was coated with only ~ 10 µg<sup>-2</sup> cm-of SnCl<sub>2</sub> and involved an additional coating time of 6.5 h at 1100 °C. .... 49

Figure 2.14: Different stages of Nb<sub>3</sub>Sn coating evolution during the coating process, including tin chloride. The bigger tin particles are still visible after 5 min at 1200 °C. .... 51

Figure 2.15: Different stages of Nb<sub>3</sub>Sn coating evolution during the coating process, excluding tin chloride. Coatings obtained after 1 min, 1 h, and 3 h at 1200 °C are shown from left to right respectively. .... 51

Figure 2.16: Coating prepared with the only SnCl<sub>2</sub> [left]. Complete coverage of coating was obtained, including some irregular grain structures. A corresponding X-ray diffraction pattern showing Nb<sub>3</sub>Sn phase..... 52

Figure 3.1: Topography of Nb<sub>3</sub>Sn surfaces growth on substrates prepared with NP (top-right), EP (top-left), and BCP (bottom). ..... 59

Figure 3.2: Average PSDs from Nb<sub>3</sub>Sn coating grown on differently prepared Nb substrates. Note the evolution of roughness compared to pre-coating nanopolished Nb surface. The cavity sample was obtained from a coated cavity that received BCP prior to the coating..... 60

Figure 3.3: Coating obtained with Sn flux of about 80 atoms.nm<sup>-2</sup>.min<sup>-1</sup> [left] and Sn flux of about 60 atoms nm<sup>-2</sup> min<sup>-1</sup> [right] of supplied tin consumption during the coating process..... 61

Figure 3.4: Variation of the coating at the bottom side of the sample that was dropped during the installation of the sample chamber into the coating chamber. Images were taken from 1 mm, 2.5 mm, and 5 mm from the edge. .... 62

Figure 3.5: Coatings prepared at JLab [left] and Cornell [right]. All the samples were BCP treated before coating. .... 64

Figure 3.6: Topography of samples coated at Jlab [left] and Cornell [right]. The average roughness obtained 10 μm × 10 μm area scans were ..... 64

Figure 3.7: SIMS depth profile of Ti before the coating system upgrade. JLab sample has shown significantly higher levels of Ti than the Cornell sample. .... 65

Figure 3.8: SEM images from pre-anodized [right] and regular BCP sample coated at 900 °C for 12 hours [left]. ..... 67

Figure 3.9: Microstructure and topography of Nb<sub>3</sub>Sn prepared at 1000–1100 °C for different durations. All the samples received NP before coating. Scale for AFM images is 2 μm/div along x-direction and 1 μm/div for z-direction..... 69

Figure 3.10: SEM and AFM images from NP samples coated at 1200 °C for 5 min, 3 hours, and 12 hours..... 70

Figure 3.11: PSD comparison of samples coated with different deposition parameters. 71

Figure 3.12: XPS depth profile from samples prepared as indicated. .... 72

Figure 3.13: Observed relationship between grain size, coating thickness, and surface roughness. Average roughness values (50 μm×50 μm scan) here were averaged values from five different locations of the sample. Average grain sizes were estimated from 5–6 SEM images of 2000–3500 magnification. Thickness was estimated from XPS depth profiles shown in Figure 3.12.73

Figure 3.14: SEM images of the sequentially overcoated samples coated at 1200 °C for different durations. Note that all images were captured at the same magnification. .... 76

Figure 3.15: Grain size as a function of the coating time at 1200 °C. .... 78

Figure 3.16: XPS depth profiles from the sequentially overcoated samples. OC1 to OC5 represents overcoat samples sequentially coated for 1, 1, 3, 12, and 60 hours, respectively. .... 79

Figure 3.17: Cross-sectional EBSD images from sequential overcoat samples. Note that the different colors here are associated with different crystallographic orientations. Nb<sub>3</sub>Sn grains are significantly smaller than Nb grains, which are represented by a single color at the top of each image, e.g., (a). The total coating time at 1200 °C is shown at the bottom right corner of each image..... 81

Figure 3.18: Thickness variation with coating time. Note that the error bars are the measurement errors tabulated in Table 3.4. Those errors were used as the weighting factors to fit the data using nonlinear least square fitting. .... 83

Figure 3.19: Locations of EDS line scans are shown in EBSD images (a) and (b). The measured Sn concentration along the scan line is shown in (c). .... 84

Figure 3.20: The concentration contour produced by grain boundary diffusion in a columnar structure, adapted with permission from [30]. Note that for the vapor diffusion process, Nb<sub>3</sub>Sn formation is simultaneously in progress..... 86

Figure 3.21: Growth kinetics observed in single-coat and overcoat samples compared to the Wuppertal data [12]..... 87

Figure 3.22: The reported values of prefactors at different temperatures. The prefactor value measured in the present study is shown in red. Data from other studies are reproduced from [49].  
..... 87

Figure 3.23: Growth kinetics observed in single-coat and overcoat samples. Two straight lines here represent growth kinetics for coating times of 1-6 hours and 6-78 hours..... 89

Figure 3.24: SEM image of a patchy area observed in Nb<sub>3</sub>Sn coated sample..... 91

Figure 3.25: (a) SEM image and (b) the corresponding EBSD image of a patchy region. Black areas arise from a combination of grain topography and the low electron beam incident angle (20°). (c) SEM image of FIB cross-section and (d) the corresponding EBSD image of the patchy area. .... 92

Figure 3.26: SEM image from sample coated for 60 hours at 1200 °C. Note the grain boundaries indicated by yellow arrows. .... 95

Figure 3.27: Elimination of two triple junctions by a single rotation-coalescence event, adapted with permission from [49]. Topology before (a) and after (b) the coalescence of grains A and B.  
..... 95

Figure 4.1: Cavity C3C4 after the coating run. Note discoloration on the NbTi cavity flange (b) and 'tin' droplets on the niobium foil from the cavity top flange (d)..... 100

Figure 4.2: Optical inspection pictures of C3C4. (a) shows the coated surface of the cavity viewed via one of the beam tubes. (b) and (d) show characteristic equatorial weld regions of the coated

cavity. (c) shows an equatorial region with several observed unusual features marked with red ellipses.....	101
Figure 4.3: $Q_0$ vs. $E_{acc}$ for cavity C3C4.....	102
Figure 4.4: Temperature mapping system on a single-cell cavity [left]. The image to the right shows a board with temperature sensors.....	104
Figure 4.5: Temperature map of C3C4 at $E_{acc} = 6$ MV/m shows the temperature increase on the outer cavity surface due to RF fields.....	104
Figure 4.6: Setup used to mill out marked areas from the cavity C3C4 noted in Figure 4.5.....	105
Figure 4.7: Sample #14 (CVT14) following each cleaning step prior to the analysis....	106
Figure 4.8: Cutting artifacts in CVT8. Note that the cracks are aligned in the same direction. Some traces of contamination can be seen, which was found to be niobium.....	107
Figure 4.9: Cross-sectional view of a crack observed in CVT14. Note that the crack extends all the way down to the Nb-Nb <sub>3</sub> Sn interface.....	107
Figure 4.10: The intrinsic quality factor derived from both RF and temperature mapping data.....	111
Figure 4.11: The average surface resistance of the top and bottom half cells derived from temperature mapping data.....	111
Figure 4.12: The calculated surface resistance dependence with the field for all cutouts.....	112
Figure 4.13: The average surface resistance for cutouts that show a nearly field-independent loss.....	112
Figure 4.14: The average surface resistance for cutouts that have a resistance switch near $E_{acc} = 4.5$ MV/m.....	113
Figure 4.15: The average surface resistance for the cutouts that have a strongly consistent field-dependent loss.....	113

Figure 4.16: SEM images from cutouts representing different field dependence of average surface resistance. Images in the first, second, and third columns belong to sets of samples showing field-independent loss, strong field-dependent loss, and resistance switch near  $E_{acc} = 4.5$  MV/m, respectively..... 115

Figure 4.17: Several voids (enclosed by ovals) from sample CVT3 are shown in the SEM image to the left. The other two images show pits found in CVT11 (center) and CVT12 [right]. Bright outlines indicate sharp edges. Note that the diameter of the pit in CVT11 is about 600 nm. .... 115

Figure 4.18: SEM images obtained from CVT10 (a), bottom beam pipe (b), and top beam pipe (c). .... 116

Figure 4.19: SEM image of patchy areas obtained from CVT14 [left] and CVT2 [right].117

Figure 4.20: Patchy areas near grain boundaries. Yellow lines indicate the grain boundaries. Patchy regions are marked with ellipses. .... 118

Figure 4.21: AFM image of regular  $Nb_3Sn$  coatings on CVT2. Roughness is evident with curved convex facets..... 119

Figure 4.22: Comparison of average PSDs of cutouts calculated using AFM data. CVT4 and CVT10 were rougher in the high-frequency domain (lateral scale  $0.1 \mu m$  and smaller) than CVT2 and CVT3..... 119

Figure 4.23: Profile of a pit observed in CVT2. Pit appears to be  $\approx 750$  nm deep. .... 120

Figure 4.24: SEM image of a FIB cross-section obtained from CVT 10 on the left. Thickness varied from  $2.34$ - $2.96 \mu m$ . FIB cross-section of a patchy area similar to Figure 4.19 on the right. The coating is significantly thin ( $400$ - $600$  nm) compared to the neighboring area ( $> 1.3 \mu m$ ).121

Figure 4.25: EBSD image from sample CVT 10 at the top, which is cut from the cavity region. Image at the bottom is from beam pipe cutout. Beam pipe has a thinner coating with more

columnar grains than CVT10. Some instrumental artefacts (dark area in between Nb-Nb<sub>3</sub>Sn grains) are present..... 121

Figure 4.26: Bright spots observed in different cutouts..... 122

Figure 4.27: Bright spots observed in CVT10. Note EDS examination of dark boundaries of these features shows a clear presence of carbon. .... 123

Figure 4.28: An unusual appearance of coating in CVT10. .... 123

Figure 4.29: AFM image from CVT 10. Note the residue covering the surface. .... 124

Figure 4.30: Defect found in CVT14. .... 125

Figure 4.31: Detailed structure within the defect found in CVT8. (a) shows the unusual area marked with yellow lines. (b), (c) and (e) shows the transition from unusual area to regular area. (d) and (f) show close-up views of grains from unusual and regular areas, respectively. Note the patchy region found close to the transition. .... 125

Figure 4.32: Defect density as a function of distance from the equator. Note the negative correlation; defects are more likely to occur in the regions close to the equator. .... 126

Figure 4.33: Alumina hardware before [left] and after [right] the coating of a cavity with NbTi flanges. EDS examination shows a significant amount of Ti (Al : Ti = 2 : 3) following the coating. .... 132

Figure 4.34: Top left and bottom left images are SEM images captured from witness samples coated with RDT7 and RDT10, respectively. Images to the right show the interior appearance of the cavities after coating. .... 134

Figure 4.35: Sn residue on Nb<sub>3</sub>Sn coating..... 134

Figure 4.36: Two-cavity setup for RDT7 coating..... 136

Figure 4.37: Temperature profile used to coat cavities in a two-cavity setup. .... 136

Figure 4.38: Comparison of RF results from RDT7 with previous data with Q-slopes.. 137

Figure 4.39: RDT10-RDT2 coating. SEM image [left] shows patchy regions observed in the witness sample. Non-uniformity in the coating can be seen in the right picture. Note that the top half cell had less non-uniformity than the bottom..... 139

Figure 4.40: SEM images from RDT10-RDT2 coating. Note that there is no Sn residue on the surface [right]. ..... 139

Figure 4.41: Comparison of the latest RF test results from RDT10 and RDT7 with those after their first coating. RDT10 is expected to have higher  $Q_0$  at 4 K than presented here as we expect losses on the flanges because of shorter beam pipes. .... 140

Figure 4.42: Post-coating appearance of IA110. The view from the bottom (next to the Sn source) is on the left. The picture at the left is the view from the top. Up-down asymmetry is evident. .... 141

Figure 4.43: SEM images from the witness rod coated with a five-cell cavity. Note the absence of patchy regions in the first few cells..... 141

Figure 4.44: Optical and SEM images from a coupon sample. The non-uniform appearance was seen in the sitting edge of the sample. The optical appearance and SEM images are consistent with the non-uniformity seen in the five-cell cavity coatings..... 142

Figure 4.45: Results from the first few five-cell cavities coated at JLab. IA320 was coated uniformly, whereas IA110 and IA114 had up-down asymmetry. .... 143

Figure 4.46: Sn residue seen on the surface following the coating with two Sn sources.143

Figure 4.47: Pictures C75-RI-NbSn1 taken from the bottom [left] and the top [right]. The coating looks non-uniform from the top..... 145

Figure 4.48: Pictures from C75-RI-NbSn2 taken from the bottom [left] and the top [right]. The coating looks mostly uniform from each side..... 145

Figure 4.49: SEM images from the witness sample coated with C75-RI-NbSn2. Note the absence of patchy regions [left] and tin Sn-residues [right]..... 146

Figure 4.50: Test results from C75-RI-NbSn1 and C75-RI-NbSn2 at 4 K and 2 K. ....	147
Figure 5.1: Typical topography of a Nb <sub>3</sub> Sn coating.....	152
Figure 5.2: SEM images of Nb <sub>3</sub> Sn coated samples before and after flash BCP for 5 seconds. Note that darker areas represent the concave structures in sample U162, which were confirmed with AFM. Bright curves are sharp edges. ....	153
Figure 5.3: Evolution of Nb <sub>3</sub> Sn coated Nb following BCP. ....	154
Figure 5.4: Typical I-V characteristics for electropolishing [8]. ....	155
Figure 5.5: Experimental setup used for electro-chemical treatment. ....	156
Figure 5.6: I-V characteristics for Nb and Nb <sub>3</sub> Sn-coated Nb samples.....	157
Figure 5.7: Nb <sub>3</sub> Sn-coated samples before (U208-first row) and after 1 min of electrochemical treatment (U187-second row) at 21°C.....	158
Figure 5.8: Nb <sub>3</sub> Sn-coated samples after 2 min (U199 - first row) and 3 min of electrochemical treatment (U202 -second row) at 21°C. The first rows of images represent 50 μm × 50 μm scan areas whereas second rows images represent 10 μm × 10 μm scan areas. ....	159
Figure 5.9: Nb <sub>3</sub> Sn-coated samples before and after electrochemical treatment at < 6 °C. Images obtained from as-coated samples U107 and U208 are shown in the first row. Samples in the first and second columns respectively received NP and BCP before the coating. Samples U107, U152, U208, and U214 received 1, 1.5 and 2 and 2.5 minutes of treatments, respectively....	161
Figure 5.10: Comparison of PSDs from Nb <sub>3</sub> Sn coated samples before and after EP. Note that all the samples were coated in the same run. ....	163
Figure 5.11: Topography of surfaces after electropolishing. (a) and (e) are as coated reference Nb <sub>3</sub> Sn surfaces. (a), (b) and (c) were coated together, showed no tin residues. Others were from another coating run showing potential tin residues as seen in (e). (b), (c) and (d) respectively received ~50 nm, 200nm, and 500 nm EP removal in 1:49 volume ratio mixture of 96% HF and	

48% H<sub>2</sub>SO<sub>4</sub>. (f), (g) and (h) subjected to EP for similar removal of ~ 50nm, 200 nm, and 500nm in 4:46 volume ratio of 96% HF and 48% H<sub>2</sub>SO<sub>4</sub>..... 165

Figure 5.12: Thickness-voltage relation for the oxide layer grown in Nb<sub>3</sub>Sn. The image next to the x-axis, obtained by sequentially anodizing a Nb<sub>3</sub>Sn-coated Nb foil, shows the colors of the oxide layer for different voltages. .... 166

Figure 5.13: Surfaces obtained by HF rinsing of 30 V anodized samples for different intervals. Note that new features, indicated by bright grainy appearance in SEM image were developed on the surface after 5 minutes..... 167

Figure 5.14: AFM image from sample U111, which received 4 cycles of 50V anodization followed by 90 s HF rinse. Small features (like in the black rectangle) appear on the surface. .. 168

Figure 5.15: (a), (b) and (c) received 2, 8 and 12 cycle of 30 V oxypolishing for ~50 nm, 200nm and 550 nm removal successively..... 169

Figure 5.16: SEM image SEM image from sample after 22 successive oxypolishing (~550 nm removal). Note new features, as in inside yellow boxes. .... 170

Figure 5.17: AFM images of Nb<sub>3</sub>Sn coated sample U153 before [left] and after [right] 30 min HF immersion. Note the rough appearance of each grain that after the treatment. .... 171

Figure 5.18: SEM images from samples after 5 min and 1 h dipping in HF. Note small features developed in the grains following 1 h treatment..... 172

Figure 5.19: SEM images of witness sample coated with RDT10 before [left] and after [right] 22% HNO<sub>3</sub> soak at ~110 °C. Bright features are Sn-rich residues..... 173

Figure 5.20: SEM images of witness sample coated with RDT7 before [left] and after [right] 5 % HCl soak for one hour ..... 174

Figure 5.21: RF performance of the cavity before and after annealing. The test was limited by input RF power..... 175

Figure 5.22: SEM image from Nb sample after annealing at 1100 °C for 2 hours with a coated cavity. .... 176

Figure 5.23: SEM image at the top was from the sample that was coated for 1 h, and annealed for 12 hours at 1200 °C. Other images are from another sample coated for 12 h, before (bottom-left) and after (top-right) annealing at the same conditions. .... 177

Figure A.1.1: Historic plot of resistance ( $\Omega$ ) versus temperature (K) by Kamerlingh Onnes showing drop in resistivity of mercury at 4.2 K, signifying the superconducting transition [left] [154]. Graphic representation of the Meissner effect [right]. .... 186

Figure A.1.2: Variation of low-field surface resistance of bulk niobium (1.3 GHz 9-cell TESLA cavity) with the temperature, shows saturation to a temperature-independent value of  $R_s$ ,  $R_{res}$  at low temperatures [159]..... 192

# CHAPTER 1

## Introduction

Particle accelerators are machines that produce energetic beams of electrically charged particles. They are used in many applications, from advanced light sources that provide unique analysis tools to biologists, chemists, and material scientists, to high-energy colliders that probe subatomic particles revealing the fundamental laws of physics. Accelerators are also used in numerous medical, environmental, and industrial applications. Superconducting radio frequency (SRF) cavities are the leading technology to accelerate charged particle beams in modern particle accelerators that require continuous-wave (CW) operation at accelerating gradients on the order of ten megavolts per meter. These cavities are resonant metallic structures made of a superconductor, chiefly Nb. SRF cavities are designed to operate at a particular frequency (typically, 200 MHz — 3 GHz). Electromagnetic fields are excited inside the cavity by coupling in RF power from an external source using an antenna. When driven at the right RF frequency, the resonant fields build to high amplitudes. For properly adjusted timing between the arrival of the charged particles and the oscillating electromagnetic field, particles are accelerated by the electric fields and deflected by the magnetic fields. RF cavities made of superconducting materials enable more powerful accelerators and reduces initial and operating costs compared to a normal conducting material. Some examples of existing large SRF technology-based accelerator facilities include Large Hadron Collider (LHC) at CERN in Switzerland, Continuous Electron Beam Accelerator Facility (CEBAF) at

Jefferson Lab in U.S.A., European X-Ray Free-Electron Laser Facility (European XFEL) at DESY in Germany. Some notable SRF based accelerators that are under construction or commissioning stages are the Facility for Rare Isotope Beams (FRIB) at Michigan State University in U.S.A., Linac Coherent Light Source (LCLS) II at SLAC in U.S.A, and European Spallation Source ERIC (ESS) in Sweden. The proposed Electron-Ion Collider (JLEIC) at Jefferson Lab, the next upgrade for LCLS-II (LCLS-II-HE) at SLAC, and the Proton Improvement Plan-II (PIP-II) at Fermilab are a few of the future facilities in U.S.A. which plan to use SRF technology. Besides these large scale science facilities, small scale compact SRF accelerators are operating or under development aiming at industrial, medical, and security applications [1]. The basic concept of RF superconductivity followed by the RF cavity fundamentals are outlined in Appendix A.

Bulk Nb ( $T_c \sim 9.2$  K,  $H_{sh} \sim 200$  mT and  $\Delta \sim 1.45$  meV) is almost the only material used so far to fabricate SRF cavities. The main reason is that Nb has the best superconducting properties (Type II superconductor with the highest  $T_c$  and  $H_{c1}$ ) among all the pure elements. Also, mechanical properties of Nb make it more appealing for the fabrication of complicated shaped cavities. Even though SRF cavities made of Nb are significantly more efficient and cheaper compared to normal conducting copper cavities, optimum performance is often attained at about 2 K. Sophisticated cryogenic facilities based on superfluid liquid helium are required to achieve such low temperatures. They are costly to build, operate, and maintain. Over the past five decades, continuing research and development efforts have significantly advanced the Nb SRF cavity technology. Many extrinsic mechanisms limiting cavity performance were discovered, and adequate processes were developed to avoid them. Following these advances, the state-of-the-art Nb cavities are now approaching the performances set by the intrinsic material properties [2, 3]. Looking at the trend, the gap between the practical cavity performances and the

theoretical best performances is closing in the not so distant future. The desire for ever more energetic, economical, and efficient particle accelerators inspires the pursuit of alternatives based on other superconducting materials.

$\text{Nb}_3\text{Sn}$  is an intermetallic compound with superconducting properties superior to Nb. A few other properties of this material restrict its application into a thin film or coating form for successful fabrication and operation of SRF cavities. Tin vapor diffusion is so far the most promising technique to obtain  $\text{Nb}_3\text{Sn}$  coated SRF cavities. The present study investigated the growth of  $\text{Nb}_3\text{Sn}$  during a typical vapor diffusion process via sample studies. Besides witness sample studies, a coated cavity was dissected, followed by materials analysis of cutout samples to understand the fundamental and technical limitations in a real SRF accelerator cavity coating. The effects of several post-coating treatments were also extensively explored.

## **1.1 Organization of the Dissertation**

This dissertation first presents an introduction to  $\text{Nb}_3\text{Sn}$  focused on its properties and history related to the SRF field. Tin vapor diffusion coating of Nb cavity interiors via a nucleation-then-growth sequence is described next, including the  $\text{Nb}_3\text{Sn}$  coating facility and protocol used at Jefferson Lab. Results of systematic studies of coated samples undertaken to elucidate the growth mechanism during the coating process are presented in the next two chapters. Chapter 2 mainly focuses on the nucleation stage of the coating. An investigation of the coating growth mechanism as well as the study of the variation of different coating parameters are presented in Chapter 3. RF and thermometry measurement results from a  $\text{Nb}_3\text{Sn}$ -coated cavity are correlated with the surface science findings of the cutouts from the same cavity in Chapter 4. This chapter also include results from material studies of witness samples associated with cavity coating and RF performance. Chapter 5 presents sample studies of  $\text{Nb}_3\text{Sn}$  subjected to several different

post-processing techniques. Finally, the dissertation concludes with a summary and outlook for the future in Chapter 6.

## 1.2 Nb<sub>3</sub>Sn Application for SRF Accelerator Cavities

This section presents an introduction to Nb<sub>3</sub>Sn in reference to its application for SRF accelerator cavities. It begins with a brief discussion of its discovery and follows with the fundamental material properties of Nb<sub>3</sub>Sn. A brief history of the Nb<sub>3</sub>Sn application in the SRF field follows with emphasis on the widely-employed vapor diffusion technique. A typical protocol and a description of the facility used for Nb<sub>3</sub>Sn coating via tin vapor diffusion at Jefferson Lab are presented, together with the basic features of coated layers.

### 1.2.1 Discovery and Properties of Nb<sub>3</sub>Sn

Superconductivity in the intermetallic compound Nb<sub>3</sub>Sn was first discovered by Matthias *et al.* in 1954 [4]. The discovery came just after the discovery of V<sub>3</sub>Si [5], the first superconductor with A15 crystal structure by Hardy and Hulm, which Hulm recalls in his memoir as [6] :

*"In the spring of 1952, I was working with a graduate student, George Hardy. We decided that the carbides and nitrides were more or less exhausted, so we moved down to silicides and germanides in the second and third periods. We also began arc-melting our samples. These were two very fortunate moves. Not only was the general quality of the samples improved over our earlier sintered materials, but we soon discovered a new high T<sub>c</sub> superconductor, V<sub>3</sub>Si, at 17 K. It belonged to what was then known, erroneously, as the beta-tungsten structure; of course, this was subsequently changed to A15. I told this news to Bernd Matthias almost immediately. By then Bernd Matthias had teamed up with Ted Geballe, Ernie Corenzwit, and Seymour Geller at the Bell Laboratories. These*

*investigators proceeded to execute a tour-de-force in creative synthesis by discovering about 30 new A15's, including several new high T<sub>c</sub> materials, most prominently Nb<sub>3</sub>Sn at 18 K, in 1954."*

Intermetallic compounds with A15 crystal structure have the chemical formula A<sub>3</sub>B, where A represents a transition metal and B can be either transition or non-transition element. Several of the potential alternative materials (Mo<sub>3</sub>Re, Nb<sub>3</sub>Al, and Nb<sub>3</sub>Sn) have the A15 crystal structure. The stoichiometric A15 crystal structure of Nb<sub>3</sub>Sn is shown in Figure 1.1. The Sn atoms form a body center cubic (BCC) lattice. Each face of the cubic lattice is bisected by mutually orthogonal one-dimensional chains of Nb atoms. This gives a closer Nb-Nb spacing of ~0.265 nm in A15 crystal structure with a lattice parameter of ~0.529 nm compared to ~0.286 nm in BCC crystal structure of pure Nb. This proximity has an important influence on the physical properties, e.g., electronic density of state at the Fermi energy level, which is proposed to cause the higher critical temperature in Nb<sub>3</sub>Sn compared to Nb.

When Nb is combined with Sn in thermal equilibrium, several different Nb-Sn compounds can form. According to the generally accepted phase diagram Nb-Sn system by Charlesworth et al. [7], Figure 1.2, the phase of interest (Nb<sub>1-β</sub>Sn<sub>β</sub>, 0.18 < β < 0.25) can form exclusively above 930 °C in the presence of Nb (s) and Sn-melt. In other phase diagrams suggested by Tofflon et al. and by Okamoto, the threshold temperature is 911 °C instead of 930 °C [8–10]. It is believed that an excess of Nb atoms occupies Sn sites of A15 crystal structure in Nb<sub>3</sub>Sn phases with composition parameter β < 0.25. Other weakly superconducting phases, Nb<sub>6</sub>Sn<sub>5</sub> (T<sub>c</sub> < 2.68 K) or NbSn<sub>2</sub> (T<sub>c</sub> < 2.8 K) can occur below this temperature.

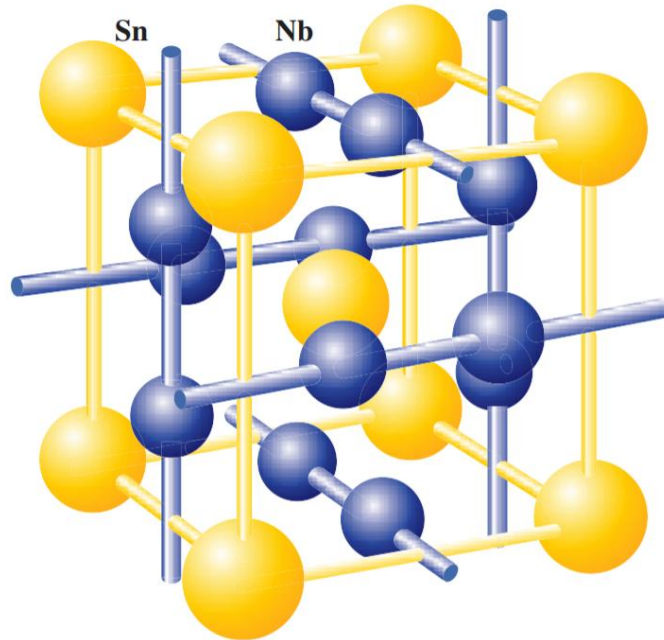


Figure 1.1: Schematic A15 crystal structure of  $\text{Nb}_3\text{Sn}$ . Yellow and blue spheres represent Sn and Nb, respectively. Adopted from [11].

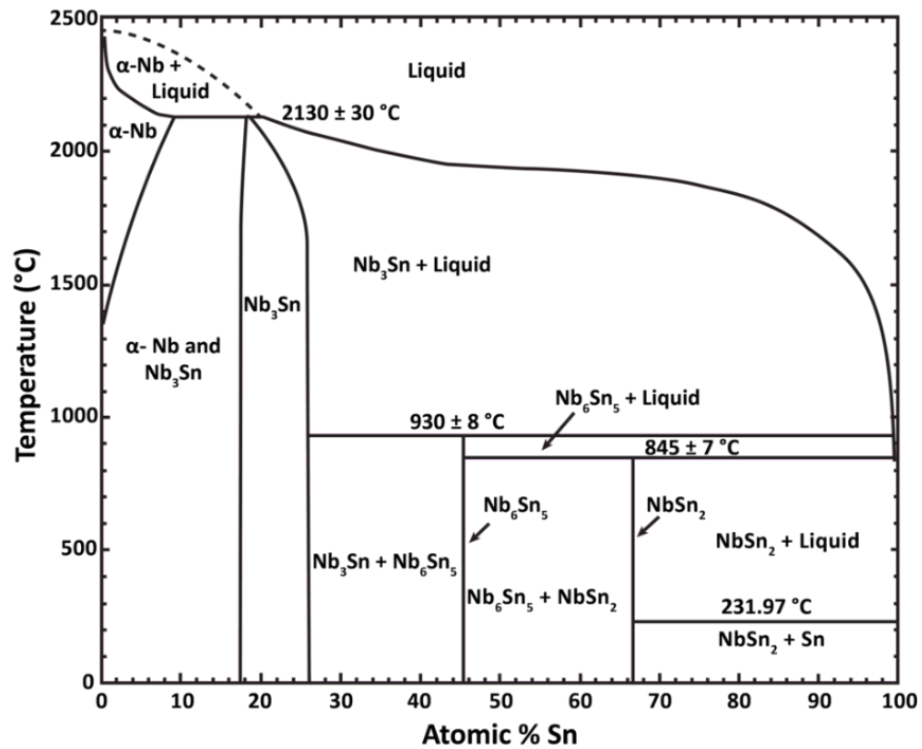


Figure 1.2: Binary phase diagram of the Nb-Sn system by Charlesworth et al. [7]. Adapted from [12].

Superconducting properties of the  $\text{Nb}_3\text{Sn}$  phase depends critically on the Sn content. As the atomic concentration of tin decreases from 25% to 18%,  $T_c$  drops from approximately 18 K to 6 K. Figure 1.3 summarizes the literature data for the critical temperature as a function of Nb-Sn composition. The variation can be well approximated by a Boltzmann function [11]:

$$T_c(\beta) = -\frac{12.3}{1 + \exp\left(\frac{\beta - 0.22}{0.009}\right)} + 18.3 \text{ (K)} \quad 1.1$$

From equation 1.1, deviation from stoichiometric  $\text{Nb}_3\text{Sn}$  results in a lower transition temperature and a lower energy gap. So, stoichiometric  $\text{Nb}_3\text{Sn}$  is needed to attain a high transition temperatures in an SRF cavity.

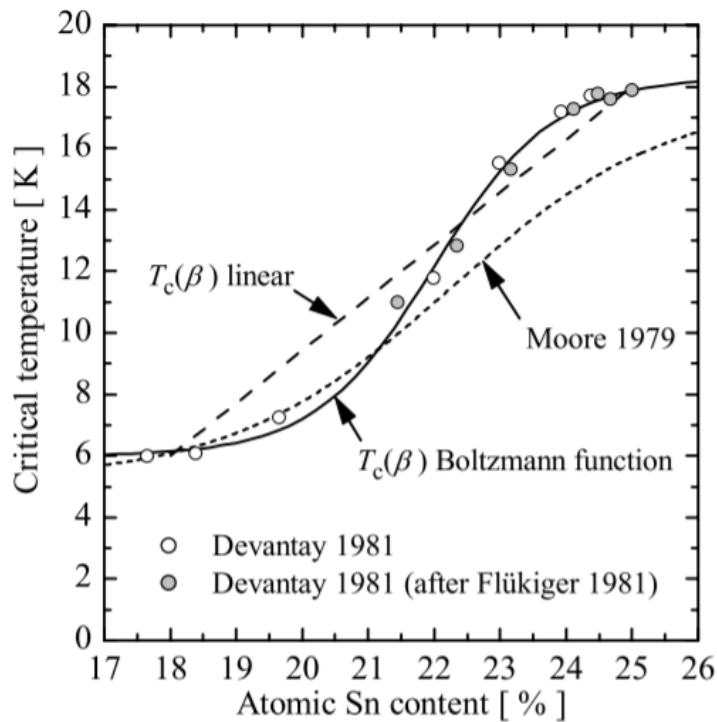


Figure 1.3: Variation of the critical temperature of  $\text{Nb}_3\text{Sn}$  with Nb-Sn composition.  $T_c(\beta)$  from equation 1.1 fits the available data [11].

Despite having superior superconducting properties,  $\text{Nb}_3\text{Sn}$  has a thermal conductivity about 1000 times lower than that of Nb at low temperatures [13, 14]. Further,

it is very brittle and prone to develop cracks easily under stress. An example of the formation of such crack will be discussed in chapter 5. In SRF applications, therefore, the compound is typically used as coating deposited on the interior of a cavity structure for SRF application. Thankfully, Nb<sub>3</sub>Sn and Nb have similar thermal expansion coefficients ( $9.8 \times 10^{-6} \text{ K}^{-1}$  for Nb<sub>3</sub>Sn,  $7.6 \times 10^{-6} \text{ K}^{-1}$  for Nb at 20 °C), which allows the use of Nb<sub>3</sub>Sn as a coating on Nb.

## 1.2.2 Potential for Future SRF Applications

In a broad sense, Nb<sub>3</sub>Sn has a potential to enable the development of a new generation of more powerful, economical, and cryogenically simplified SRF accelerators. Significant advantages of Nb<sub>3</sub>Sn are:

- Because of superior superconducting properties ( $T_c$  and  $H_{sh}$  both twice that of Nb), a maximum accelerating gradient of almost twice that of Nb and higher quality factors are predicted.
- Nb<sub>3</sub>Sn cavities may deliver at 4.2 K a comparable RF performance to that of Nb cavities at 2 K. These cavities can be operated with atmospheric liquid helium, simplifying and reducing the cost of the cryogenic facilities.
- Nb<sub>3</sub>Sn has attracted researchers since the early days of superconducting RF cavities. In terms of fabrication and performance, no other alternative material is as mature as Nb<sub>3</sub>Sn. The performance of R&D Nb<sub>3</sub>Sn cavities is already very promising, see section 1.2.4. Several laboratories are currently working to develop multi-cell Nb<sub>3</sub>Sn cavities for use in accelerators.
- Cryocoolers can be used to operate these cavities at low fields, which can enable efficient small-scale accelerators suitable for industrial and environmental applications. Some of the proposed small-scale accelerators already plan to exploit

this opportunity, and research has been started to use cryocoolers to operate Nb<sub>3</sub>Sn cavities [15, 16].

### 1.2.3 Nb<sub>3</sub>Sn Application in SRF

Attempts to apply Nb<sub>3</sub>Sn in SRF cavities date back to early 1970's at Siemens AG in Germany, where researchers used the tin vapor diffusion technique to coat TE<sub>011</sub> and TM<sub>010</sub> (8–10 GHz, X-band ) Nb cavities. The best values of peak magnetic field achieved in TE<sub>011</sub> (9.5 GHz) cavities were:  $B_c = 106$  mT with  $Q_0 = 2.3 \times 10^9$  at 1.5 K and  $Q_0 \sim 10^9$  at 4.2 K and  $B_c = 80$  mT [17]. Although the geometries of those cavities were not suitable for particle accelerators, attained peak surface magnetic field values correspond to the highest accelerating gradient reported so far. Around the same time, Kernforschungszentrum Karlsruhe (KfK) and Wuppertal University started exploring Nb<sub>3</sub>Sn for SRF cavities. They undertook sample studies to explore the effect of coating parameters and material properties, including transition temperature, penetration depth, pinning behavior, and surface morphology. There were also some studies on the frequency dependence of the surface resistance of the Nb<sub>3</sub>Sn layer using cylindrical cavities. A more systematic, decade-long study of Nb<sub>3</sub>Sn was carried out at Wuppertal University, including a collaboration with Jefferson Lab to coat 1.5 GHz (CEBAF) single-cell and multi-cell cavities. Their best RF performance are shown in Figure 1.4 [18]. The best cavity gave a low-field  $Q_0$  of  $\sim 10^{11}$  at 2 K and  $>10^{10}$  at 4.2 K, significantly higher than those of Nb cavities at the time. The cavity performances were consistently limited by a strong Q-slope with increasing gradient. The magnetic field at the onset of the Q-slope was very similar among them and nearly corresponded to the lower critical field of Nb<sub>3</sub>Sn [19]. Temperature maps showed that the effect is not local, and hence could be a fundamental property of Nb<sub>3</sub>Sn [20]. They also coated a five-cell 3 GHz cavity which

achieved  $Q_0 \sim 10^9$  and  $E_{acc} \sim 7$  MV/m [21]. Despite these encouraging results, research efforts diverted in the mid-90s to the newly discovered high-temperature superconductors. The continual improvement in fabrication-friendly Nb cavities further overshadowed the development of Nb<sub>3</sub>Sn for the next several years. A research group at INFN-LNL, Italy attempted to produce Nb<sub>3</sub>Sn coated 6 GHz SRF cavities using a so-called hybrid liquid diffusion process in 2006 but reported no RF measurements [22]. Research on Nb<sub>3</sub>Sn was revived with the Nb<sub>3</sub>Sn program at Cornell University in 2008 [23]. Development efforts are now also in progress at Jefferson Lab, starting in 2012, and Fermilab since 2015 [24], [25]. In summary, Nb<sub>3</sub>Sn is the front-running alternative material to replace Nb in SRF cavities and is being pursued by several research groups using different techniques [26]-[32]. Excellent reviews are available by Kneisel [33], Ereemeev [34], and more recently from Posen and Hall [35].

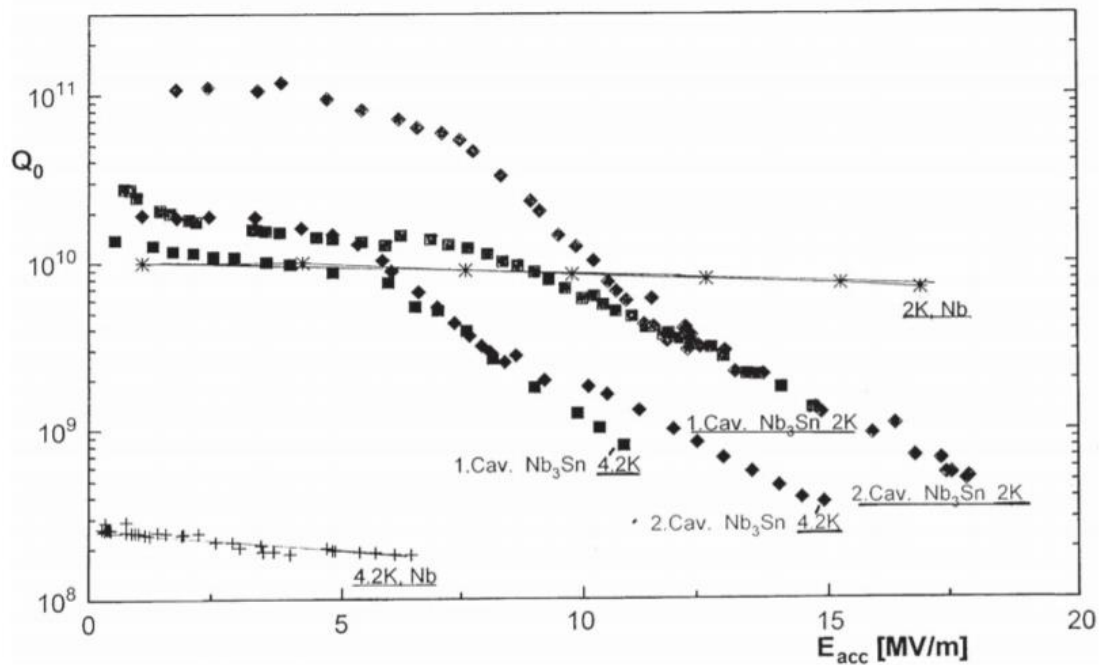


Figure 1.4: RF measurements from 1.5 GHz Nb<sub>3</sub>Sn/Nb cavities coated at Wuppertal University and tested at Jefferson Lab [22].

## 1.2.4 Recent Developments of Nb<sub>3</sub>Sn-coated Cavities

Following the revival of Nb<sub>3</sub>Sn research in 2009, several SRF cavities were coated and tested at Cornell University, Jefferson Lab, and Fermilab. The first cavities coated at each lab showed quality factors ( $Q_0$ ) as high as  $> 1 \times 10^{10}$  at 4 K but suffered a strong Q-slope, limiting the attainable maximum gradient. The Q-slope was very similar to that observed by researchers at Wuppertal, Figure 1.4. However, cavities coated at Cornell in 2013 were able to maintain  $Q_0 > 1 \times 10^{10}$  for accelerating gradient up to 14 MV/m without strong Q-slopes in several cavities. These results demonstrated that the characteristic Q-slope seen before was not fundamental. Researchers in latest studies speculated that the reduction in Q-slope was due to the reduction in the quantity of low tin content material in the RF layer [35]. Around the same time, several cavities coated at Jefferson lab consistently suffered from strong Q-slope. Our material analysis of samples coated at Cornell University and Jefferson Lab did not show any significant differences except for the level of Ti impurity, which was notably higher in Jefferson Lab samples. We considered Ti-contamination, which could transfer from (typical) Nb-Ti flanges of a cavity during the coating, as a potential candidate to cause strong Q-slope. During the Jefferson Lab coating system upgrade in 2017, Ti-free hygiene was adopted for Nb<sub>3</sub>Sn coating, which we correlated with our first Q-slope free cavity. Several cavities coated later resulted in Q-slope, but they were linked to the presence of Sn-residue, non-uniformity and to macroscopic defects in the starting Nb substrate. After recent modifications in the coating protocol to mitigate these issues, cavities with significantly improved performance were produced.

At the time of writing this dissertation, the best-coated cavity at Jefferson Lab had  $Q_0 \geq 2 \times 10^{10}$  at 4 K and  $> 3 \times 10^{10}$  at 2 K before quenching at  $\geq 15$  MV/m. Figure 1.5 summarizes the state-of-the-art performance of 1.3 GHz single-cell Nb<sub>3</sub>Sn cavities. It

should be noted that one of the cavities coated at Fermilab recently had been reported to reach a record-setting gradient of  $\sim 23$  MV/m with  $Q_0 > 1 \times 10^{10}$  up to  $\sim 20$  M/m [36]. Each lab is attempting to reproduce the performances of 1.3 GHz  $Nb_3Sn$  cavities in other cavities with different resonant frequencies: 952 MHz at Jefferson Lab, 650 MHz at Fermilab, and 2.6/3.9 GHz at Cornell [36, 37]. Besides single-cell cavities, researchers at Jefferson Lab and Fermilab are progressing with  $Nb_3Sn$  multi-cell cavities, as a step toward application in practical particle accelerators. Recent multi-cell cavities coated at both labs appear to reach practical accelerating gradients  $>10$  MV/m with  $Q_0 > 5 \times 10^9$  before quench.

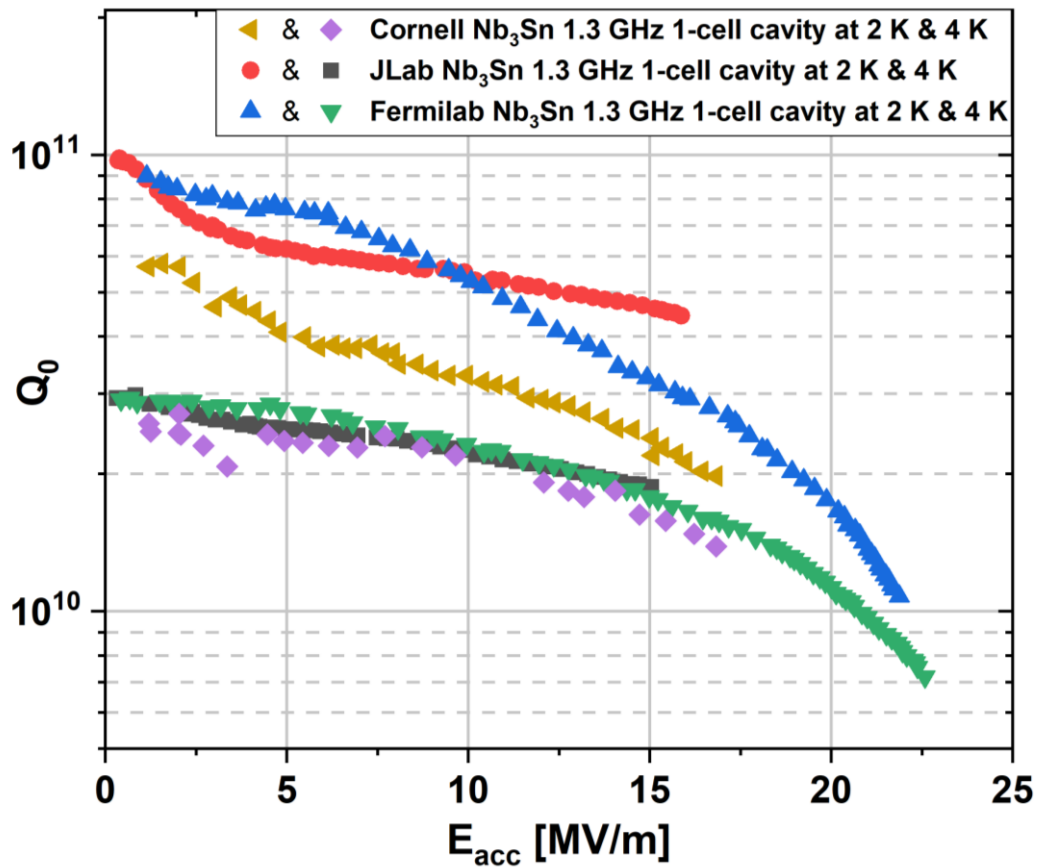


Figure 1.5: State-of-the-art performances of 1.3 GHz single-cell  $Nb_3Sn$  cavity at different labs. Data from Cornell and Fermilab were extracted from [35, 36].

### 1.2.5 Tin Vapor Diffusion Coating of Nb<sub>3</sub>Sn

Several techniques to deposit Nb<sub>3</sub>Sn layers have been attempted: chemical vapor deposition, co-evaporation, tin bath dipping and annealing, pulsed laser deposition, electro-deposition, and sputtering [28, 30, 38–43]. However, vapor diffusion coating of Nb<sub>3</sub>Sn on Nb, attributed to Saur and Wurm [44], is the most favorable technique so far. Development began in the 1970s, producing the first successful results with RF cavities [45–48]. It is preferred by the majority of research institutions currently working to develop Nb<sub>3</sub>Sn coated cavities [45, 46, 49–52]. At the time of writing this dissertation, it is the only technique that produces promising RF performance, attaining quality factor  $>10^{10}$  operating at 4.2 K with gradient more than 15 MV/m. The essence of the process is to generate and transport tin vapor to the substrate Nb at a temperature above 930 °C to form the Nb<sub>3</sub>Sn phase exclusively, as determined by the binary phase diagram, Figure 1.2. At Siemens AG, Nb resonators were initially heated with Sn inside sealed-off quartz tubes. After Si contamination, presumably originating from the quartz tube, was discovered in coated layers of Nb<sub>3</sub>Sn, reaction chambers made of Nb were used instead [53]. Initial efforts appeared to have two major challenges: Sn droplets on the coated surface and the absence of complete coating coverage [17, 48]. Post-coating treatments such as annealing and HNO<sub>3</sub>/HCl/Acetic/HF acid treatment were attempted to remove those Sn-spots. Since the success of those techniques was not clear, the best approach appeared to be avoidance of the Sn accumulation itself. This problem still appears in some of our recent coating, discussed in Chapter 4 and 5. The next issue was the non-complete coating coverage, which was linked to non-uniform nucleation at the beginning of the coating process. The problem was mitigated by anodizing the substrate before the coating or by application of tin halides [17, 48]. We will discuss this further in the next chapter.

The tin vapor diffusion technique was then adopted at Wuppertal University following Siemens AG. In the Siemens configuration, the coating system used only one heater; that is, the temperature of the substrate and the tin source remained the same during the coating process. Unlike the Siemens configuration, the coating system at Wuppertal was provided with a secondary heater, which independently controlled the temperature of the tin-containing crucible (made of tungsten) in a long tube underneath the cavity, Figure 12. The addition of a secondary heater presented an extra knob to adjust the vapor pressure of tin at the beginning and the end of the coating process, which helped to tackle both of the challenges discussed above.

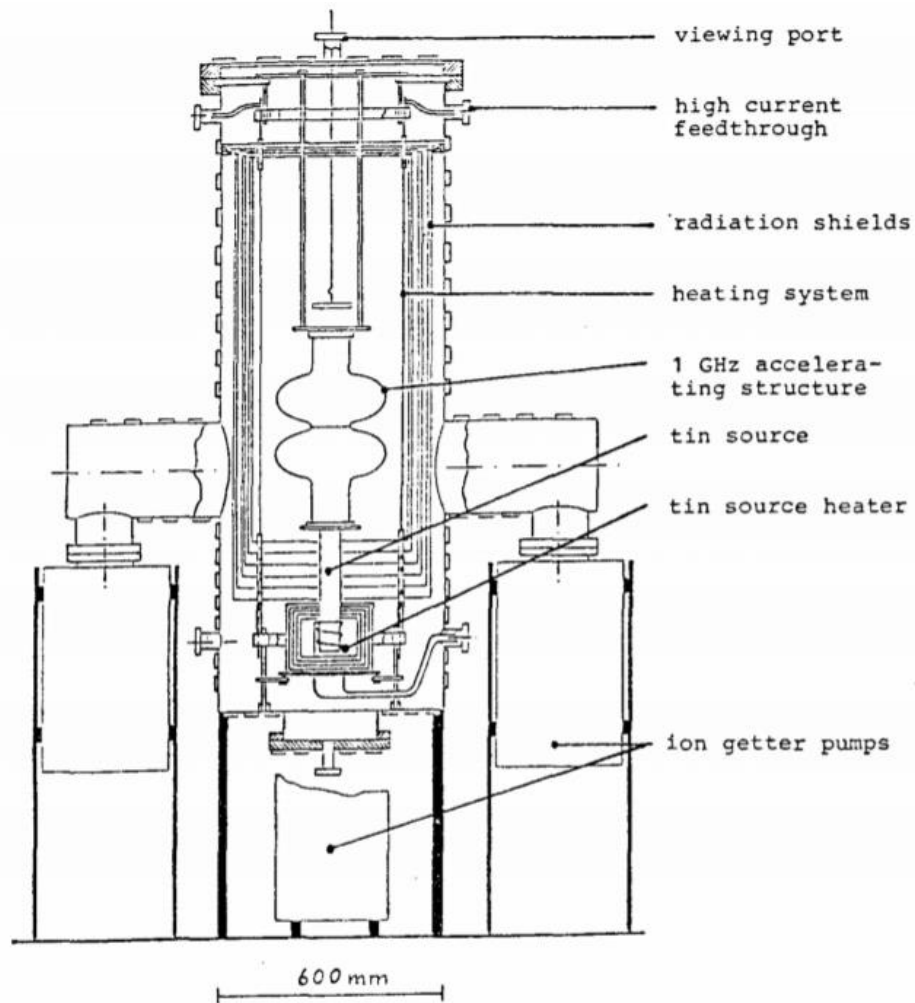


Figure 1.6: Nb<sub>3</sub>Sn coating configuration Wuppertal [49].

The fabrication of Nb<sub>3</sub>Sn cavities at Wuppertal experimental was divided into four steps:

1. The Nb cavity was manufactured, subjected to standard preparation treatments for surface optimization, and tested to ensure its RF performance in the superconducting state.
2. The second step was the formation of Nb-Sn nucleation centers on the Nb cavity surface. An oxide layer was grown on the Nb surface by electrolytic anodization of the cavity before mounting in the coating furnace. A small tray was suspended from the top of the cavity and filled with a small amount of SnCl<sub>2</sub> (~ 20 μm.cm<sup>2</sup>). The Sn chloride was assumed to evaporate at 500 °C to deposit Sn on the Nb surface. This temperature was typically held constant for 5 hours. Nb<sub>2</sub>O<sub>5</sub> was believed to decompose, bringing Nb into contact with the deposited Sn to yield a uniform layer of Nb-Sn nucleation centers.
3. The third step was to form a Nb<sub>3</sub>Sn layer of several microns. The temperature of the cavity and the tin source was typically raised to 1100 °C and 1200 °C, respectively, and held for 3 hours. The cavity heater was switched off half an hour later than the tin source to avoid surplus Sn on the final Nb<sub>3</sub>Sn layer.
4. The fourth step is the cavity cooling down, during which it was speculated that the spurious low T<sub>c</sub> Nb-Sn phases formed. To remove them, the Nb<sub>3</sub>Sn cavity surface was oxipolished. Here, the coated cavity was anodized, and the oxide layer was dissolved subsequently with 48% HF acid. This step was repeated several times until a thickness of (0.1–0.5) μm was removed. The cavity was rinsed with water and methanol.

Present vapor diffusion processes mostly follow the Wuppertal or Siemens protocol, with some modifications to the setup. The coating systems at the Cornell and

Fermilab are provided with a secondary heater for the tin source: the Wuppertal configuration. The horizontal coating system at Fermilab has two separate sources aiming to coat the 9-cell 1.3 GHz cavities uniformly. The furnace design at Jefferson Lab, discussed in the next section, does not have a separate heater for the tin source: the Siemens configuration. The comparison of coating configurations at different coating facilities, adopted from [35], is shown in Figure 1.7.

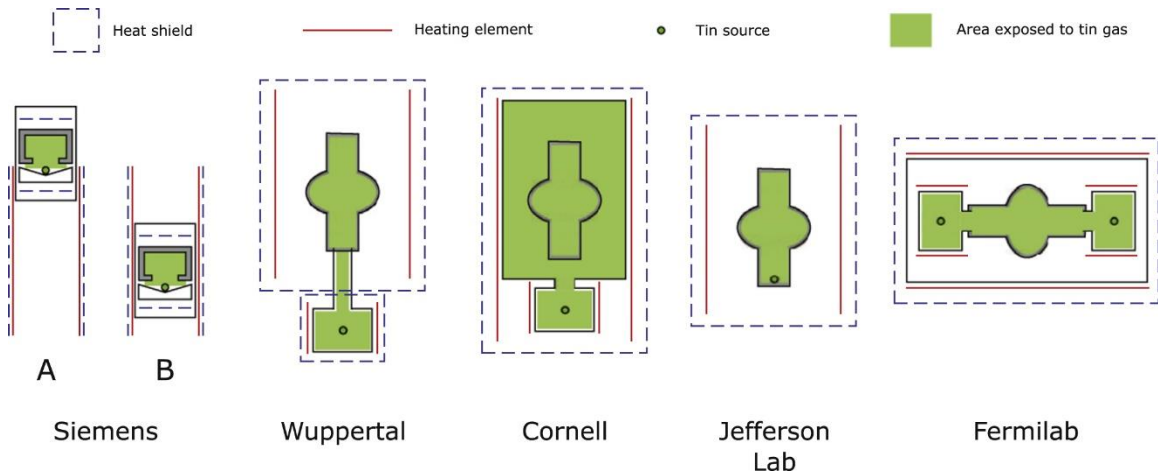


Figure 1.7: Schematic of Nb<sub>3</sub>Sn coating furnaces at different labs (adopted from [35]). Siemens AG had used two configurations A and B.

## 1.2.6 Jefferson Lab Coating System

The vapor diffusion process was adopted at Jefferson Lab in 2012. It was initially designed to coat 1.3–1.5 GHz single-cell cavities [25]. The system consists of two main parts: the furnace that provides a clean heating environment to the coating chamber and the coating chamber (“insert”) that hosts the process vapors to coat Nb parts. The high vacuum furnace was procured from T-M Vacuum Products Inc.; the coating chamber was built in-house at JLab. The coating chamber and the furnace are provided with separate pumping systems for evacuation. The coating system has gone through several upgrades since its commissioning. A major upgrade was in 2017 when both the furnace and the

coating chamber were modified to accommodate original five-cell CEBAF cavities, Figure 1.8 [26]. To replace the original coating chamber (32" long × 11.5" OD), a new coating chamber was fabricated out of a 4 mm Nb sheets into a 17" OD by 40" long cylinder via rolling half-cylinders and electron beam welding them. The bottom end of the hollow cylinder was closed by an electron beam welding a 4 mm Nb blank, which was deep-drawn into a dome shape for mechanical stability. Following unsuccessful attempts to braze the top end of the cylinder to a stainless steel flange, the cylinder was TIG welded to a 21" OD titanium (grade 5) flange, which had half-dovetail 0.25" o-ring grooves on one side.

It should be noted that the first choice was a stainless-steel flange to avoid having any titanium close to the chamber, as the titanium was speculated to cause Q-slope in the Nb<sub>3</sub>Sn-coated cavities [54]. Since the flange resides outside the heating zone, we were confident not to derive any Ti contaminations to the coating chamber, which was verified later by secondary ion mass spectroscopy (SIMS) analysis of coated samples in the new chamber. The bottom side of the Ti flange provided vacuum insulation via o-ring to the new furnace door, and the o-ring on the other side was sealed against a zero-length water-cooled reducer. This zero-length reducer allowed to re-use instrumentation and to evacuate using the existing multiport spool piece and top plate. To accommodate larger cavities, the furnace volume had to be increased, which was accomplished by replacing the original flat furnace door with a dome-shaped door and extending the heat shields at the top. The door that sits on top of the furnace was procured from Kurt J. Lesker Company per specifications provided by Jefferson Lab. It interfaces with the furnace vacuum vessel on the bottom via an O-ring seal and has another O-ring seal on the top, which mates to the reaction chamber titanium flange. The heat shields were built in-house out of 0.015" molybdenum and Nb sheets. Six heat shield layers were used, similar to the construction

in the existing furnace. The heat shields were supported by a stainless steel support cylinder around them. Three Nb rods were attached at the top to the multiport plate and extended downwards into the hot zone. Nb rods support a 4 mm Nb plate, to which the top flange of a cavity or the sample chamber is attached with molybdenum hardware. Figure 1.8[left] shows the latest sketch of the coating chamber. The coating facility is shown in Figure 1.8 [right].

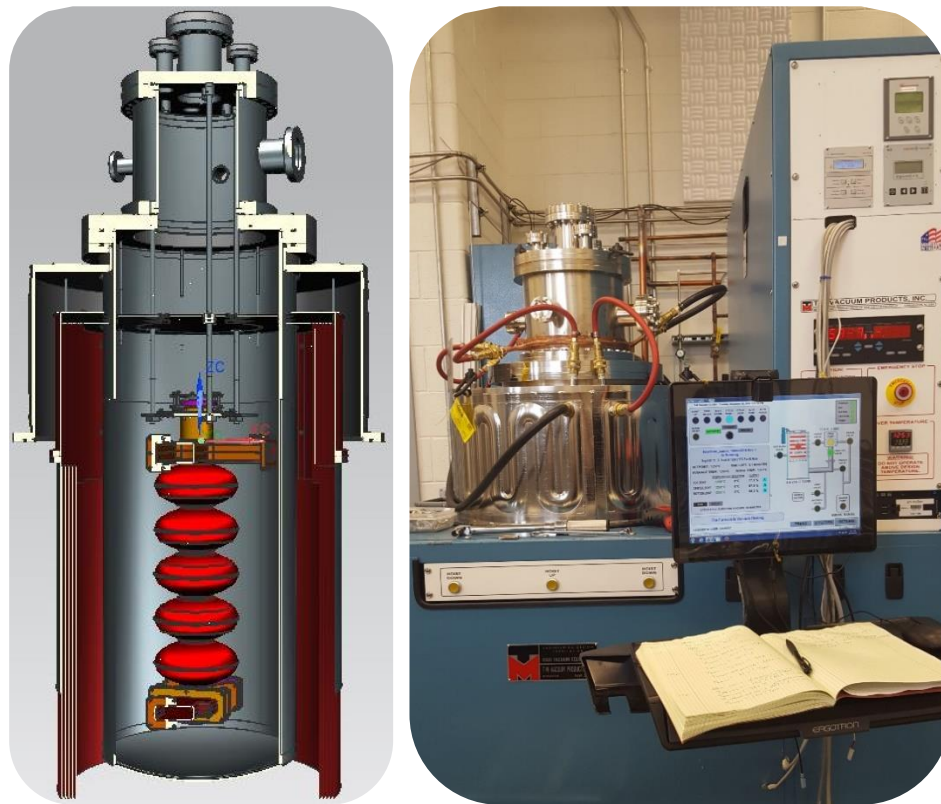


Figure 1.8: A sketch of the upgraded coating chamber is shown in the image to the left. A CEBAF 5-cell cavity is shown loaded inside the hot zone of the furnace. A sample chamber replaces the cavity during the sample coating experiments. The coating system is shown at right.

Several type C thermocouples extending into the hot zone were added to monitor the temperature of cavities during coating. The first run with the thermocouples showed

that a temperature gradient of about 70 °C exists from bottom to the top of the hot zone, while the three furnace thermocouples outside the coating chamber indicate uniform temperature within 0.3 °C. The furnace control relies on these temperatures measured by the thermocouples outside the chamber. The gradient was compensated to about 20 °C by adjusting the three independently controlled heating elements of the furnace. All the experiments presented in chapter 2 of this dissertation were conducted before the coating system upgrade and cited experimental temperatures were based on the temperatures of different heating zones. Elsewhere, we will explicitly refer to the upgraded coating system for experiments conducted following the coating system upgrade.

### **1.2.7 Nb<sub>3</sub>Sn Coating Process**

A “standard” procedure to coat samples and cavities is described here briefly.

The substrate samples were 10 mm × 10 mm Nb coupons, cut by electrical discharge machining (EDM) from 3 or 4 mm thick, high RRR (~300) sheet material of the type used to fabricate SRF cavities. Most of the samples were subjected to buffered chemical polishing etch (BCP) using a solution of 49% HF, 70% HNO<sub>3</sub>, and 85% H<sub>3</sub>PO<sub>4</sub> in the ratio of 1:1:1 or 1:1:2 by volume for minimum removal of 50 μm. This etching process removes the “damaged” layer exposing a clean Nb surface. A subset of those samples further received metallographic polishing, also known as nanopolishing (NP), to obtain smoother surfaces. Nanopolishing typically removes >100 μm and produces smoother surfaces that are favorable to most material characterization techniques. The average roughness of NP samples was below 5 nm, measured from 50 μm × 50 μm scan areas using atomic force microscopy (AFM). Another subset of samples was electrochemically anodized in 15% NH<sub>4</sub>OH solution by applying a fixed cell voltage of 30 V. The thickness of the oxide layer was estimated to be ~60 nm for those samples using the thickness-

voltage ratio from [55]. A few Nb samples received electropolishing (EP) using a 1:9 mixture of 49% HF and 96% H<sub>2</sub>SO<sub>4</sub> for one hour at room temperature with ~10 V DC voltage, removing about 30–40 μm.

The coating chamber (insert) houses a sample chamber made of Nb with a shelf inside to mount coupon samples, Figure 1.9. One gram (~3 mg.cm<sup>-2</sup>) of 99.999% or better purity tin shots and an equal amount of 99.99% tin chloride powder (from American Elements) were packaged loosely in Nb foil and placed on the Nb foil which covered the bottom end of the sample chamber. Nb foil was commercial grade unalloyed Nb from Eagle Alloys. Sn and SnCl<sub>2</sub> vapor are expected to exit from the package readily from the narrow openings. The top end was later covered by Nb foil after mounting the experimental coupon samples inside. The sample chamber, samples, chemicals, and the covering foils were assembled in the cleanroom to limit any contamination before installation into the coating deposition system. The setup described above best represents the experiments discussed in Chapter 2. Later experiments used Nb plates and molybdenum fasteners to cover both ends of the sample chamber. A Nb crucible was implemented to supply the required amount of Sn for the coating. The sample chamber is replaced with a cavity during cavity coating, with an adjusted amount of Sn and SnCl<sub>2</sub>, and will be discussed in Chapter 4.

### **1.2.8 Typical Characteristics of Diffusion Coating of Nb<sub>3</sub>Sn**

A shiny Nb surface develops a matte gray appearance following Nb<sub>3</sub>Sn coating. A representative microstructure of the Nb<sub>3</sub>Sn coating is shown in Figure 1.11 [left]. It typically features equiaxed grains of an average size of (2.2 ± 0.2) μm. Composition measurement with EDS shows (24 ± 1) at. %, Sn, close to a nominal Nb<sub>3</sub>Sn. An example of surface

topography of a coated surface can be seen in Figure 1.11 [right]. The surface develops a characteristic roughness at the surface following  $\text{Nb}_3\text{Sn}$  coating.



Figure 1.9: Sample chamber, samples, tin and tin chloride packages, and Nb foils before setting up for the coating. The coating chamber of the furnace is not shown.

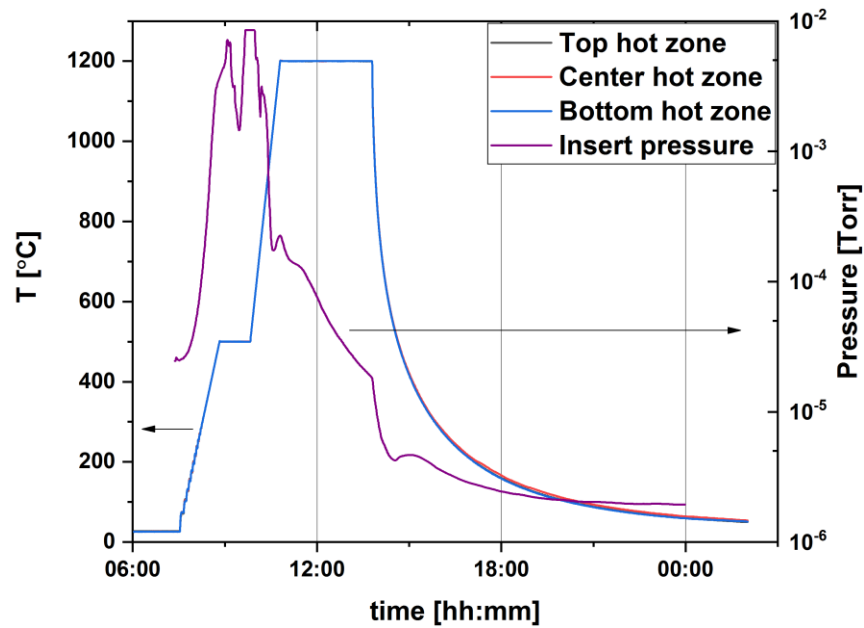


Figure 1.10: Temperature profile used for coating  $\text{Nb}_3\text{Sn}$  on Nb samples at Jlab. The temperature of the insert during the process is monitored with three thermocouples outside

the reaction insert at different sections of the insert. Because of very similar temperature readings, the temperature curves overlap in the plot.

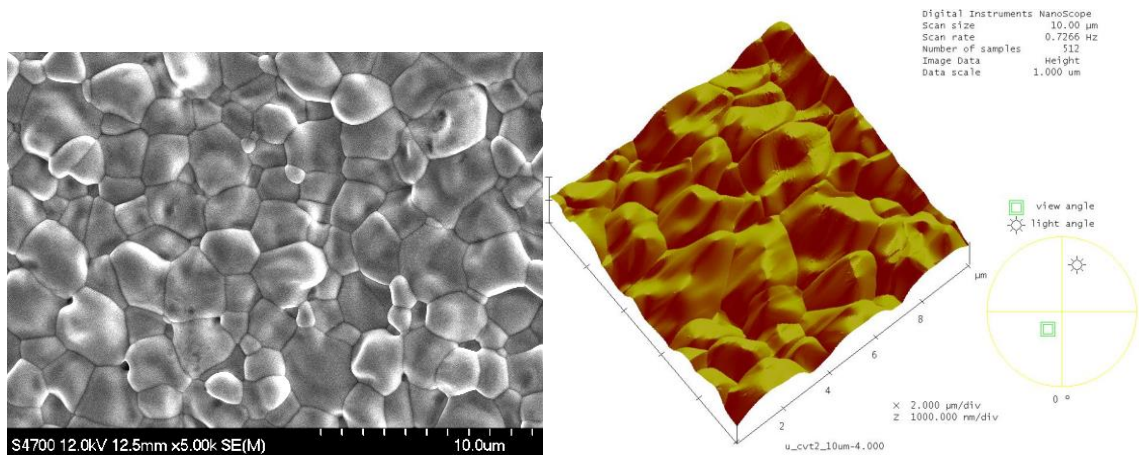


Figure 1.11: Scanning electron microscopy (SEM) image of  $\text{Nb}_3\text{Sn}$ -coated surface [left]. Atomic force microscopy (AFM) image of the same surface [right]. The average roughness was 150 nm.

It is expected to produce 2–3  $\mu\text{m}$  thick coatings following the coating process described above. Electron backscattered diffraction (EBSD) images from a cross-sectional examination of the  $\text{Nb}_3\text{Sn}$ -coated Nb sample are shown in Figure 1.12. Grains typically appeared to be columnar, extending from the surface to the  $\text{Nb}_3\text{Sn}$ -Nb interface. Some smaller grains are also seen occasionally close to the interface. The  $\text{Nb}_3\text{Sn}$ -Nb interface develops roughness even for a nanopolished starting substrate. Note that, different colors here represent the different orientation of  $\text{Nb}_3\text{Sn}$  grains showing polycrystalline  $\text{Nb}_3\text{Sn}$  with no apparent orientation dependency to the underlying Nb substrate.

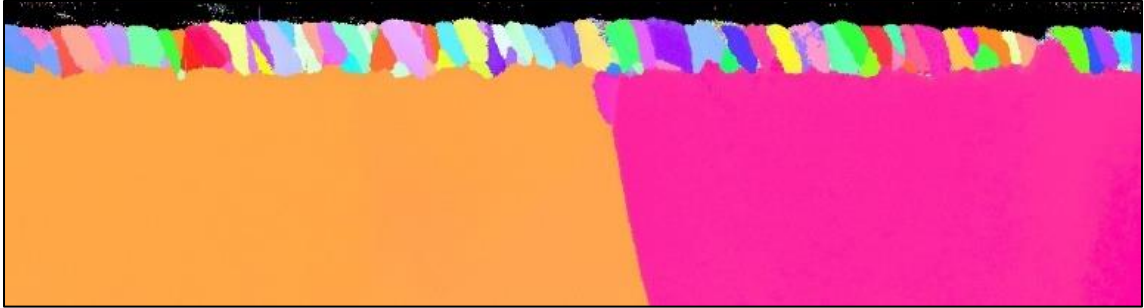


Figure 1.12: Cross-section EBSD image from Nb<sub>3</sub>Sn coated surface. Note the larger size of Nb grains compared to Nb<sub>3</sub>Sn grains at the surface.

The characteristics of the resultant Nb<sub>3</sub>Sn primarily depend on the coating protocol used. A proper understanding of how the coating evolves during the progression of the coating process is fundamental to tune the microstructure and properties of the final layer of Nb<sub>3</sub>Sn, which eventually determines the performance of Nb<sub>3</sub>Sn-coated SRF cavities. As suggested by Figure 1.10, two significant stages of the Nb<sub>3</sub>Sn coating “recipe” that require in-depth investigation are the end of the nucleation step and the progression of the Nb<sub>3</sub>Sn-layer during the deposition. The following chapter will now solely focus on the nucleation stage, presenting results from our experimental investigations

## CHAPTER 2

### **Nucleation**

Early attempts at vapor diffusion coating of Nb<sub>3</sub>Sn at Siemens AG resulted in regions which were not entirely covered [17]. The proposed cause was poor Sn coverage at the early stages of the coating process, i.e., an irregular nucleation. The first attempted solution was to anodize the Nb-substrate before coating and to set the temperature of the tin source about 200 °C higher than the substrate temperature. The devised solution help to improve the homogeneity of the coating, but the mechanism that caused improvement was never fully explained. Siemens researchers speculated that the nucleation was more uniform because of the higher amount of tin supply at a higher temperature [17]. They also reported the production of Nb<sub>3</sub>Sn coatings with good RF properties without introducing the measures discussed above, which they attributed to “uncontrolled small amounts of HF”. This attribution was also motivated by the observation of the isothermal chemical transport reaction in manufacturing of Nb<sub>3</sub>Sn multifilament wires, where 0.01–0.07 mbar HCl (*g*) was introduced into the chamber loaded with Cu-Nb wires coated with tin [56]. Motivated by wire manufacturing experience, Siemens researchers started adding a small amount of Sn-halide (SnF<sub>2</sub> or SnCl<sub>2</sub>) into the reaction chamber, which improved the uniformity of Nb<sub>3</sub>Sn layers. Sn-halide evaporates and reacts with the substrate surface at a lower temperature to yield an increased Sn supply. The idea was also driven by the expected benefit from a higher vapor pressure of tin halide than that of elemental tin. For example,

the comparison of Sn vapor pressure to SnCl<sub>2</sub> vapor pressure is shown in Figure 2.1. SnCl<sub>2</sub> evaporates at the temperature of about 500 °C to deposit tin sites on the Nb surface, which were assumed to act as Nb<sub>3</sub>Sn nucleation sites.

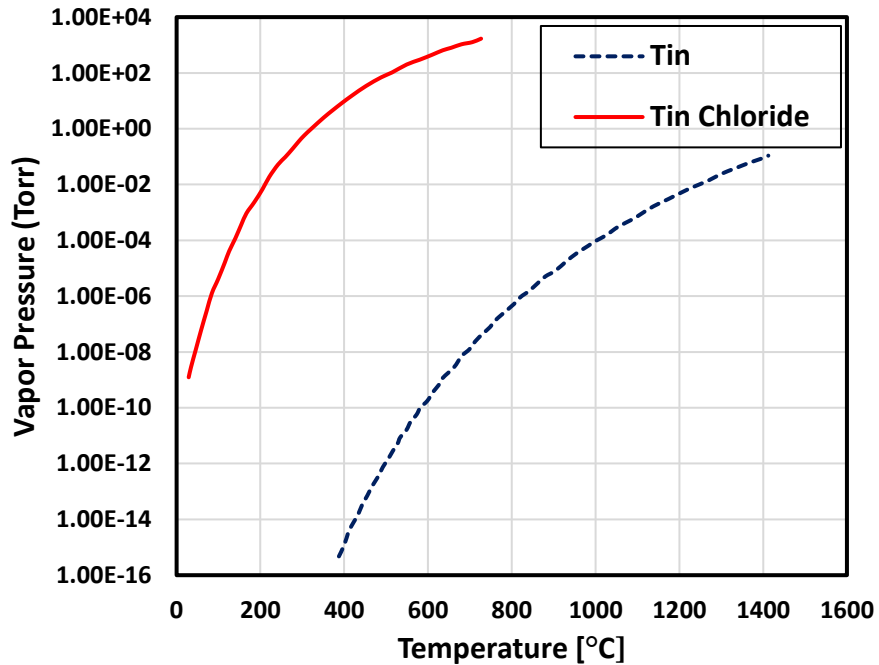


Figure 2.1: Vapor pressure of tin and tin chloride. The plot is reproduced from [33], which cites [57, 58].

Research institutions following a similar Nb<sub>3</sub>Sn coating process later preferred SnCl<sub>2</sub>, sometimes combined with substrate anodization or a temperature gradient between the tin source and the Nb substrate. Further studies suggested that substrate anodization is not mandatory, and it results in RRR degradation due to oxygen absorption from the anodic layer [49]. Application of Sn halide is especially helpful for coating systems that do not have a secondary heater to set up a temperature gradient between the Sn source and the substrate, as discussed above.

While the inclusion of a nucleation step has a long history in practice, only limited research has been done to understand the fundamentals. The following sections are based on [59] and discuss our experimental studies to gain more insight into the nucleation

step that features SnCl<sub>2</sub>. Due to the design of the coating system, a temperature gradient between the Sn source and the substrate was not tried, but anodized Nb samples were included in a few experiments.

### 2.1.1 Experimental

The samples here were mostly the nanopolished coupons. The experimental setup and the substrate preparation are already described in section 1.2.7. A selected few experiments also featured pre-anodized Nb samples along with regular Nb samples. In this process, the reaction chamber containing the sample chamber was evacuated to the 10<sup>-5</sup> Torr range, then the heating profile was initiated. The temperature was raised at the rate of 6 °C.min<sup>-1</sup> to the target nucleation temperature (Table 2.1). The temperature was maintained constant for different durations (nucleation time) before ceasing the heating process. After the nucleation at given condition, the chamber was allowed to cool in vacuum. After reaching room temperature, the insert was purged with nitrogen to regain atmospheric pressure. The sample chamber was then taken out to remove the samples.

Table 2.1: Nucleation Experiments

Nucleation Temperature	300 °C	400 °C	450 °C	500 °C
Nucleation Time	1 h, 4 h	1 h	1 h	5 min, 1h, 5 h
Amount of SnCl <sub>2</sub>	1 g	1 g	1 g	5 mg, 1 g
Amount of Sn	1 g	1 g	1 g	0 g, 1 g

### 2.1.2 Characterization

A basic premise of materials science is that structure (composition, microstructure, topography, etc.) determines properties. It is important to understand how nucleation

affects structure of Nb<sub>3</sub>Sn. SRF cavity materials had not attracted widespread attention in the materials characterization community, so a consensus approach to characterization has not yet developed. We sought to take steps in that direction by applying several well-established techniques, deferring novel and emerging techniques to the future. Probably the most familiar technique is scanning electron microscopy with elemental analysis. An Hitachi 4700 field emission scanning electron microscope (FE-SEM) equipped with an energy-dispersive X-ray spectroscopy (EDS) detector was used to examine the nucleated samples. SEM images were taken after each experiment, and elemental composition was analyzed with EDS. All SEM images were taken at 0° tilt angle, and used a 12/15 kV accelerating voltage. Under ideal conditions, SEM/EDS can measure element concentration down to approximately 0.1 atomic percent. As the primary beam enters the specimen, electrons lose energy so that they reach a limited depth while retaining enough energy to cause x-ray emission. They are also deflected outside the original beam path, so that lateral resolution decreases. The maximum penetration depth of 15 kV electron beam into Nb or Sn were estimated using an expression from Kanaya and Okayam[60]. The corresponding values of electron range were 1.0 μm and 1.3 μm for Nb and Sn, respectively. The X-ray generation depth is typically estimated by X-ray range equations from Castaing [61] or Andersen and Hasler [62]. The Castaing approximation permits estimation leading to X-ray generation depth of 0.8 μm for Nb and 1.0 μm for Sn with a 15 kV primary beam energy. For the same beam energy, Anderson and Hasler equation estimates X-ray ranges of 0.7 μm and 0.8 μm for Nb and Sn, respectively.

Topographic examination used a Digital Instruments IV AFM in tapping mode with aluminum reflex coated silicon tips with diameter less than 10 nm, resonant frequency 190 kHz and force constant 48 Nm<sup>-1</sup>. The selected samples were scanned for 5 μm × 5 μm and 1 μm × 1 μm sizes with 512 × 512 data points. The expected lateral resolution of AFM

is defined by the spacing of sampling points. For example, the expected lateral resolution for a 5  $\mu\text{m}$  scan is  $\sim 10$  nm ( $5 \mu\text{m} / 512$ ) under optimal conditions. AFM and SEM/EDS analysis was done at the Applied Research Center Core Labs, William and Mary.

Surface sensitive elemental analysis was done by X-ray photoelectron spectroscopy (XPS), probing the elemental composition of the first few nanometers down to the concentration of approximately 0.1 atomic percent. The XPS measurements were carried out in an ULVAC-PHI “Quantera SXM” instrument equipped with a monochromated Al  $K_{\alpha}$  X-ray source. Spectra were collected at 50 W/15 kV from a 200  $\mu\text{m}$  spot size, 45° take-off angle.

Transmission electron microscopy (TEM) imaging of the cross-section of a nucleated sample was carried out by a JEOL 2100 operating at 200 kV. The specimen was prepared by a focused ion beam (FIB–Helios Nano Lab 600) sectioning using the lift-out technique. To preserve the surface of a nucleated sample and create an intact cross-section, a protective layer of Pt was deposited on the sample surface over the area of interest prior to sectioning. Initial material removal steps were performed at the highest removal rate with a beam energy of 30 kV. The final polishing step was done with 2 kV Ga ions at an angle of 7°. More details are available in [63]. XPS and TEM analysis was performed by J. Tuggle at Nanoscale Characterization and Fabrication Laboratory (NCFL), Virginia Tech.

Scanning Auger microscopy (SAM) using a PHI 680 system was employed for several samples. The SAM consists of an FE-SEM with a Schottky emission cathode, a secondary electron detector, and an axial cylindrical mirror analyzer with a multi-channel detector to collect Auger electrons produced during electron imaging. Very small spot sizes can be realized with this instrument, down to 7 nm. The measurement was done at Swagelok Center for Materials at Case Western Reserve University.

## 2.2 Results and Discussion

### 2.2.1 Temperature Dependence of nucleation

Temperatures of 300 °C, 400 °C, 450 °C, and 500 °C were chosen to study the effect of nucleation temperature. Since the vapor pressure of SnCl<sub>2</sub> drops rapidly below 300 °C, see Figure 2.1, this was chosen as the lower bound. The treatment time was kept constant at one hour, and the amount of SnCl<sub>2</sub> was fixed at 1 g. Residual SnCl<sub>2</sub> was found inside the Nb foil containing supplied SnCl<sub>2</sub>, only after 300 °C and 400 °C.

Variation in the treatment parameters resulted in different surface features. After 300 °C nucleation, a significant portion of SnCl<sub>2</sub> was found inside each package. SEM images revealed nanometer-sized particles, assumed to be tin, on the Nb surface, Figure 2.2(a). However, only Nb was detected with EDS, possibly due to the shallow coverage of a very small amount of deposited tin. The nucleation temperature of 400 °C produced distinct features on the surface, Figure 2.2(b). Besides micron-sized spherical particles, extended interconnected 'mud-crack' like features were seen in SEM images. Several SEM images, not shown here, suggested that the big particles were formed by the accumulation of those features. Both Nb and tin signals were detected with EDS not only at the spherical particles, which we assume are tin but also between the particles, where the irregular structures can be seen in the SEM image.

Nucleation temperatures of 450 °C and 500 °C created similar looking surfaces with sub-micron sized spherical particles visible in the SEM, appearing as bright features in Figure 2.2(c) and Figure 2.2(d). The size and distribution of the particles were slightly varied between these two temperatures. Spherical particles were examined with EDS, showed 40–70 at. % Sn depending on size. Larger particles showed more tin, as would be expected since the spatial resolution limit of EDS is larger than the particle size for

small particles. Therefore, the data from individual particles included more or less Nb signal as well from the adjacent or underlying material. EDS was unable to detect any tin in between those particles.

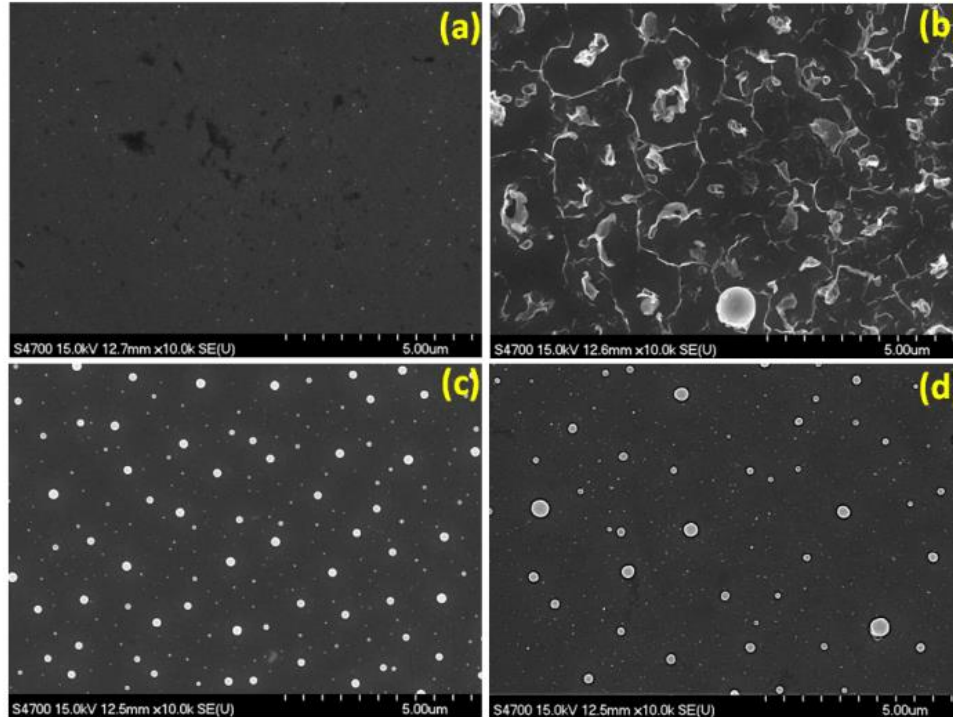


Figure 2.2: SEM images obtained from samples nucleated at temperatures of (a) 300 °C, (b) 400 °C, (c) 450 °C, and (d) 500 °C for one hour. Circular bright features are Sn particles, as revealed by EDS [30].

Samples from each experiment were examined using XPS (Table 2.2). Carbon and oxygen were found, which is expected from post-experiment exposure to the ambient atmosphere. The samples were then sputtered lightly (1 kV Ar, 30 s) to reduce the contaminants contribution and scanned again. Pre-sputtering resulted in an increased amount of oxygen and reduced carbon in each XPS analysis. Removing the carbon increased the ratio of Nb to Sn, raising the possibility that tin may be present as a very thin surface layer, which was slightly sputtered. Alternatively, tin may have been preferentially sputtered compared to niobium. Sn and Nb were present only as an oxide.

This is expected since both are highly reactive and the samples were handled in air. The data obtained from samples with nucleation temperature above 400 °C showed (20–30)% total tin. A typical XPS scan is shown in Figure 2.3. Note the absence of chlorine peaks: no chlorine was ever found in any of the nucleated samples. The amount of tin found with XPS on the surface is clearly more than what can be expected from the very low surface coverage by tin particles alone (Table 2.3). For example, tin coverage of the sample surface after 450 °C nucleation was estimated at about  $(3.9 \pm 0.6)\%$ , but XPS measurements indicated 22.3% of Sn surface coverage.

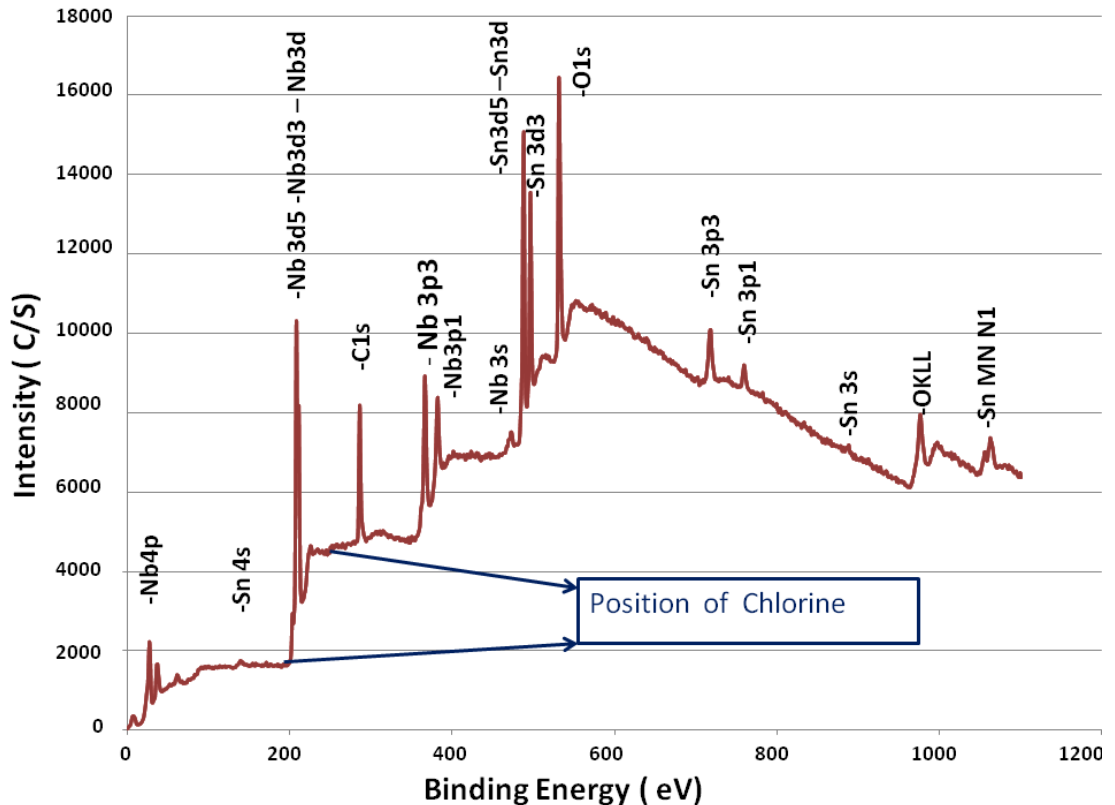


Figure 2.3: XPS data obtained from a sample after one hour at 500 °C.

This discrepancy of tin content between SEM and XPS analysis indicated the presence of more tin than the particles visible in SEM. To gain insight into the form of tin on the surface, we adopted a model for calculation, consisting of the visible particles and a thin surface layer. The particles are treated as pure tin hemispheres, consistent with the

SEM images and the AFM results presented later. The tin signal comes only from the surface of the particle. The surface layer is treated as a pure tin film, one atomic layer thick. The layer is too thin to be revealed by SEM/EDS but can be detected by XPS. A rough intensity ratio of Sn/Nb in XPS was then estimated considering a homogeneous Sn layer of monoatomic thickness in between tin particles on the Nb surface. For the case when there is a thin layer of Sn on top of bulk Nb, the layer and substrate intensities are given by [64],

Table 2.2: XPS elemental analysis of nucleated samples at different temperatures. The nucleation time for each sample was one hour.

Nucleation Temperature (°C)	Sample	C (at. %)	O (at. %)	Nb (at. %)	Sn (at. %)	$\frac{Sn}{Nb + Sn} \times 100$	
300	U55	48.5	32.5	13.7	5.3	27.9	
		6.1	61.5	28.5	3.9	12.0	With pre-sputtering
400	U73	35.0	41.5	9.4	14.1	60.0	
		4.9	57.8	25.1	12.2	32.7	With pre-sputtering
450	U59	62.5	25.5	5.7	6.3	52.5	
	U47	9.0	54.2	28.6	8.2	22.3	With pre-sputtering
500	U90	56.8	31.2	7.3	4.7	39.2	
		13.3	52.5	25.3	8.9	26.0	With pre-sputtering

Table 2.3: Calculated Fractional Surface Coverages

Nucleation Condition	1 h at 500 °C	1 h at 450 °C	4 h at 500 °C (section 2.2.2)	5 h at 500 °C (section 2.2.3)
Coverage by particles (%)	2.8 ± 0.6	3.9 ± 0.6	10.0 ± 0.8	1.9 ± 0.4

$$I_{Sn} = I_{Sn}^{\infty} \left[ 1 - \exp\left(-\frac{d}{\lambda_{Sn,Sn} \cos \theta}\right) \right] \quad (2.1)$$

$$I_{Nb} = I_{Nb}^{\infty} \exp\left(-\frac{d}{\lambda_{Nb,Sn} \cos \theta}\right) \quad (2.2)$$

where  $I_{Sn}^{\infty}$  and  $I_{Nb}^{\infty}$  are the intensities of the pure bulk tin and Nb.  $\lambda_{Sn,Sn}$  and  $\lambda_{Nb,Sn}$  are the attenuation length (inelastic mean free path) of the electrons in tin emitted by the first subscript element to the second subscript element. Emission angle,  $\theta$  is the angle between the surface normal and direction of measured electron emission.

Dividing equation (2.1) by (2.2),

$$\frac{I_{Sn}}{I_{Nb}} = \frac{I_{Sn}^{\infty} \left[ 1 - \exp\left(-\frac{d}{\lambda_{Sn,Sn} \cos \theta}\right) \right]}{I_{Nb}^{\infty} \exp\left(-\frac{d}{\lambda_{Nb,Sn} \cos \theta}\right)} \quad (2.3)$$

The intensity ratio of bulk tin and Nb is given by [65],

$$\frac{I_{Sn}^{\infty}}{I_{Nb}^{\infty}} = \frac{N_{Sn} \sigma_{Sn} \lambda_{Sn} T_{Sn}}{N_{Nb} \sigma_{Nb} \lambda_{Nb} T_{Nb}} \quad (2.4)$$

where  $N$  is atomic density,  $\sigma$  is photo-ionization cross-section for observed photoelectron line, and  $T$  is the transmission factor of the instrument. From (2.3) and (2.4),

$$\frac{\frac{I_{Sn}}{\sigma_{Sn} \lambda_{Sn} T_{Sn}}}{\frac{I_{Nb}}{N_{Nb} \sigma_{Nb} \lambda_{Nb} T_{Nb}}} = \frac{N_{Sn} \left[ 1 - \exp\left(-\frac{d}{\lambda_{Sn,Sn} \cos \theta}\right) \right]}{N_{Nb} \exp\left(-\frac{d}{\lambda_{Nb,Sn} \cos \theta}\right)} \quad (2.5)$$

The ratio on the left-hand side gives the corrected intensity ratio  $\eta$ , that is, the ratio of tin to Nb,

$$\frac{\eta_{Sn}}{\eta_{Nb}} = \frac{N_{Sn} \left[ 1 - \exp\left(-\frac{d}{\lambda_{Sn,Sn} \cos \theta}\right) \right]}{N_{Nb} \exp\left(-\frac{d}{\lambda_{Nb,Sn} \cos \theta}\right)} \quad (2.6)$$

Let us use the  $3d_{5/2}$  photoelectron line for calculation. For  $E(Al K_{\alpha}) = 1486.7 \text{ eV}$ ,

$$K.E. \left( 3d_{\frac{5}{2}} \right) Sn = E(Al K_{\alpha}) - E_b = 1486.7 - 484.9 = 1001.8 \text{ eV} \quad (2.7)$$

where  $K.E. \left( 3d_{\frac{5}{2}} \right)$  and  $E_b$ , respectively are the kinetic energy and binding energy of emitted  $3d_{5/2}$  photoelectrons.

For simplicity,  $\lambda_{Sn,Sn} = \lambda_{Nb,Sn} = \lambda_{Sn}$ , which can be extracted from NIST electron inelastic mean free path (IMFP) database, [66], using the kinetic energy of emitted photoelectrons. The required parameters to calculate the ratio of tin to Nb, in equation 2.6, are shown in Table 2.4.  $\theta = 45^\circ$ , as used in XPS measurements was chosen.

Table 2.4: Model parameters.

$N_{Sn}$ (atoms/cm <sup>3</sup> )	$N_{Nb}$ (atoms/cm <sup>3</sup> )	$\lambda_{Sn}$ for 3d <sub>5/2</sub> (nm)	Monolayer thickness d (nm)
$3.708 \times 10^{22}$	$5.555 \times 10^{22}$	2.316 nm	0.290 nm

Table 2.5 presents calculations for 0, 3%, 5%, and 10% coverage by tin particles thick enough to shield all the photoelectrons from underlying Nb. The representative Sn/(Sn+Nb) ratio for 10% surface coverage was found to be ~20%, obtained by taking the weighted average of contributions from Sn particles (10%) and a monolayer of Sn on bulk Nb (90%). This ratio is consistent with the Sn concentration range of XPS analysis above, which supports the notion of a thin Sn layer on nucleated surfaces.

To further corroborate the finding, angle-resolved XPS (ARXPS) was attempted on a few samples. XPS data were collected by varying the angle between the XPS detector and sample surfaces (Table 2.6). XPS intensity from a thin film is expected to vary depending on the emission angle, since the angle changes the effective information depth, see equation 1.1. The shallower angles increase signal contribution from the topmost layer. ARXPS results are summarized in Table 2.6. While all four samples were nucleated at 500 °C, M46 and U90 were subjected to standard protocol (1 h of nucleation time with 1 g of SnCl<sub>2</sub>). Two other samples, U101 and U66, were prepared with 5 mg (~10 μgcm<sup>-2</sup>) of SnCl<sub>2</sub> and 5 h of nucleation time. A detailed description of the preparation and analysis of similar samples will be presented later.

Table 2.5: Ratio of Sn to (Nb + Sn) obtained from the model calculation of dependence of intensity on the emission angle

Model	Angle between the surface normal and direction of electron emission (°)			
	30	45	60	75
Monolayer only	0.09	0.11	0.16	0.29
With 3% particles	0.12	0.14	0.18	0.31
With 5% particles	0.14	0.16	0.20	0.33
With 10% particles	0.18	0.20	0.24	0.36

The model calculations indicate that a continuous film is expected to give a tin ratio at 75° at least twice that at 30° for all particle coverages. Sample U66 is an example. A surface covered by separated nanoparticles (not the SEM visible particles) will show no such variation with angle since the information depth is not changing with rotation. U101 and M46 offer examples. U90 evidence some measure of the expected angle dependence, but not to the degree that would support any firm conclusion. Results from several other samples, not shown here indicates that the two-dimensional species on the surface after nucleation are rather variable.

Table 2.6: ARXPS ratio of Sn to (Nb+Sn).

Samples	Angle between the surface normal and direction of electron emission (°)			
	30	45	60	75
U101(5 mg SnCl <sub>2</sub> )	0.15	0.15	0.14	0.12
M46 (1 g SnCl <sub>2</sub> )	0.19	0.18	0.22	0.19
U66(~5 mg SnCl <sub>2</sub> )	0.31	0.35	0.42	0.50
U90 (1 g SnCl <sub>2</sub> )	0.16	0.18	0.20	0.22

To gain more insight, a few samples were examined with a scanning auger microscopy (SAM). In SAM, 10 kV primary electron beam bombards the sample surface producing Auger, secondary and backscattered electrons. Auger electrons are used to

identify the elements present; secondary and backscattered electrons are used for imaging at the same time, thus providing an opportunity for surface-sensitive elemental mapping in an SEM image. Results from a sample nucleated at 500 °C for one hour are shown in Figure 2.4. Large and small bright features are evident in the secondary electron image (top left). The large features (red box) are consistent with the tin particles seen in the SEM and show expectedly high tin content in the spectral scans (top right). The intervening area shows small bright features and the presence of tin, (blue scan) at a much lower level. Elemental mapping of Sn and Nb appears in the lower images. More investigation with a higher resolution instrument is needed to learn if these are an imaging artifact or tin nanoparticles.

An AFM image from a sample prepared under similar conditions (Figure 2.6 (a)) showed the presence of tin particles as islands. More features, see area enclosed by a rectangle in Figure 2.6(a), were seen in between tin islands. These features appeared following the nucleation; they are absent from a typical nano polished sample. A height profile of a section from Figure 2.6(a), passing through a big particle is shown in Figure 2.6(b). The diameter of the largest particle in this scan was ~200 nm with a height of ~ 60 nm. Note that the largest particles observed were ~300 nm in diameter.

The initial growth mode of thin films is commonly divided into three categories (Frank-Van Der Merve: two-dimensional (2D) layer growth; Stranski-Krastanov: layer plus three dimensional (3D) islands and Volmer-Weber: 3D island growth). Our data qualitatively resemble Stranski-Krastanov mode; the tin film is formed in addition to distributed tin particles. Similar growth has been reported before during the growth of tin on Al or Nb [67, 68]. The formation of a thin film, i.e., Frank-Van Der Merve growth, during nucleation was suggested from the early days of Nb<sub>3</sub>Sn diffusion coating [17, 69]. The growth of such a continuous layer has been suggested to be crucial to establish uniform

coating of Nb<sub>3</sub>Sn, and the role of SnCl<sub>2</sub> and the anodic oxide layer was to retard Nb-Sn reaction until a uniform tin film is formed. However, previous studies of the nucleated surface only indicated the formation of tin particles like in Volmer-Weber mode on the surface following nucleation [47]. The presence of a tin film was not previously established.

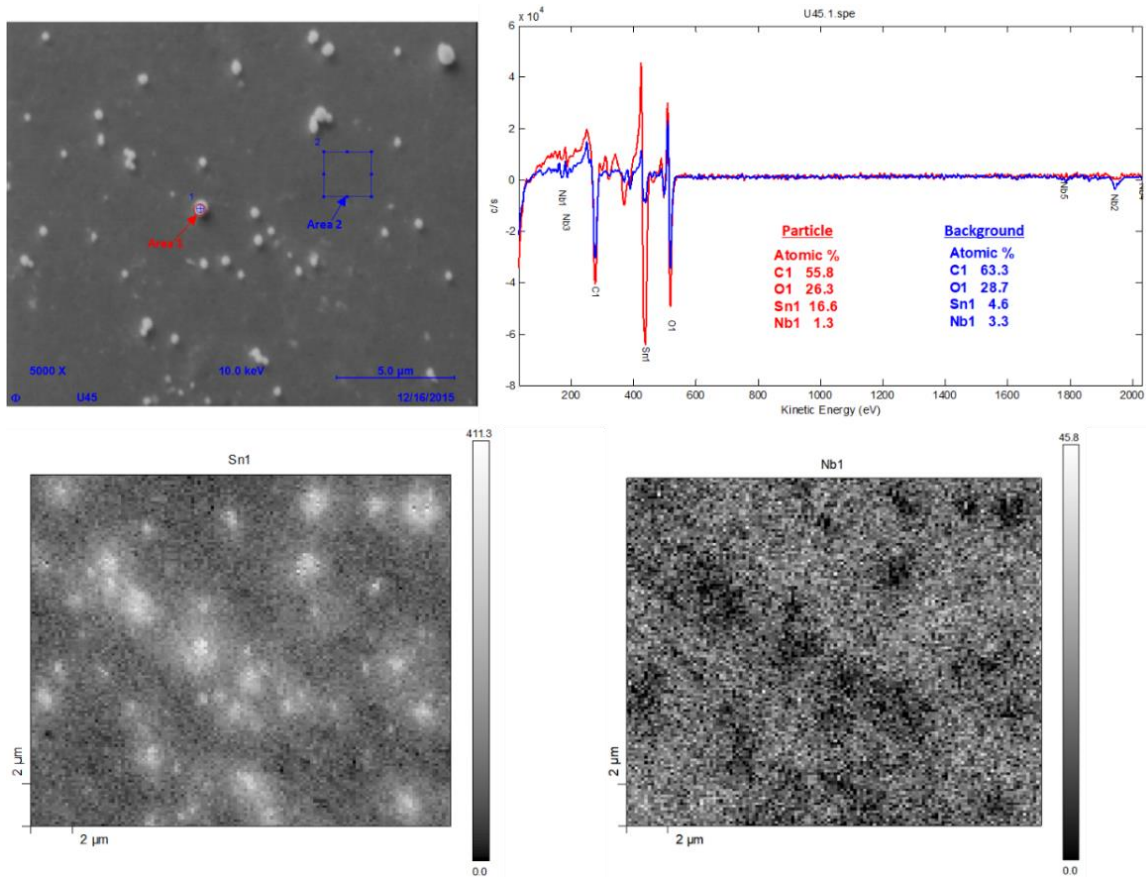


Figure 2.4: SAM elemental mapping of Sn coverage after sputtering for thirty seconds is shown in the image (lower left). The brighter areas are richer in Sn than darker areas, as shown in the intensity scale. Equivalent data for Nb appear at the lower right. Elemental composition comparison of particle and background is shown in spectra at the top right.

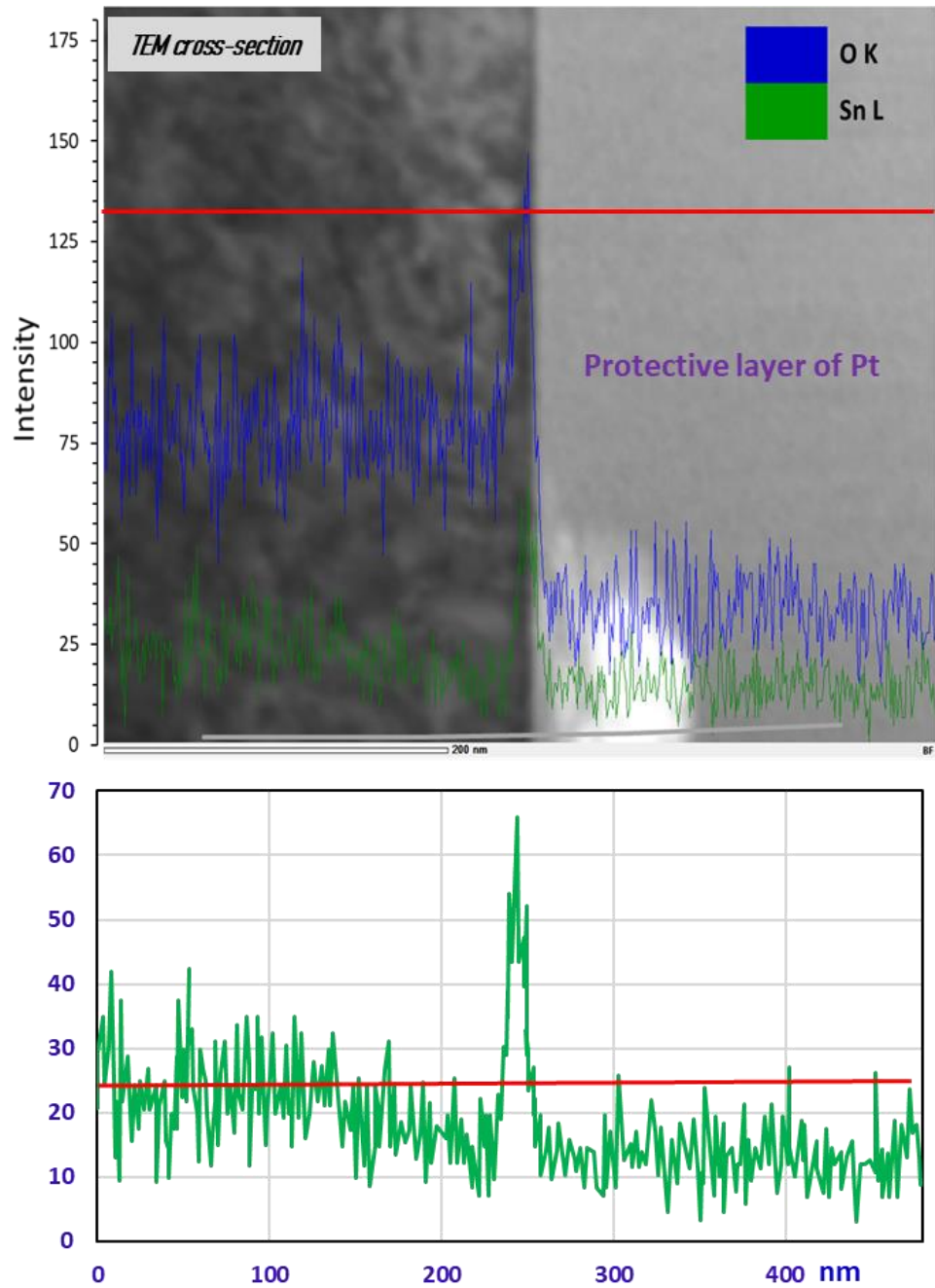


Figure 2.5: (a) TEM cross-section of a sample nucleated at 500 °C for 5 h with EDS spectra from a line scan that follows a solid red line is superimposed on top of the TEM image. Nb signal is left out to make scaling reasonable for other signals. (b) Only the Sn spectra along the scan line. Note the jump of the Sn and O signals near the surface.

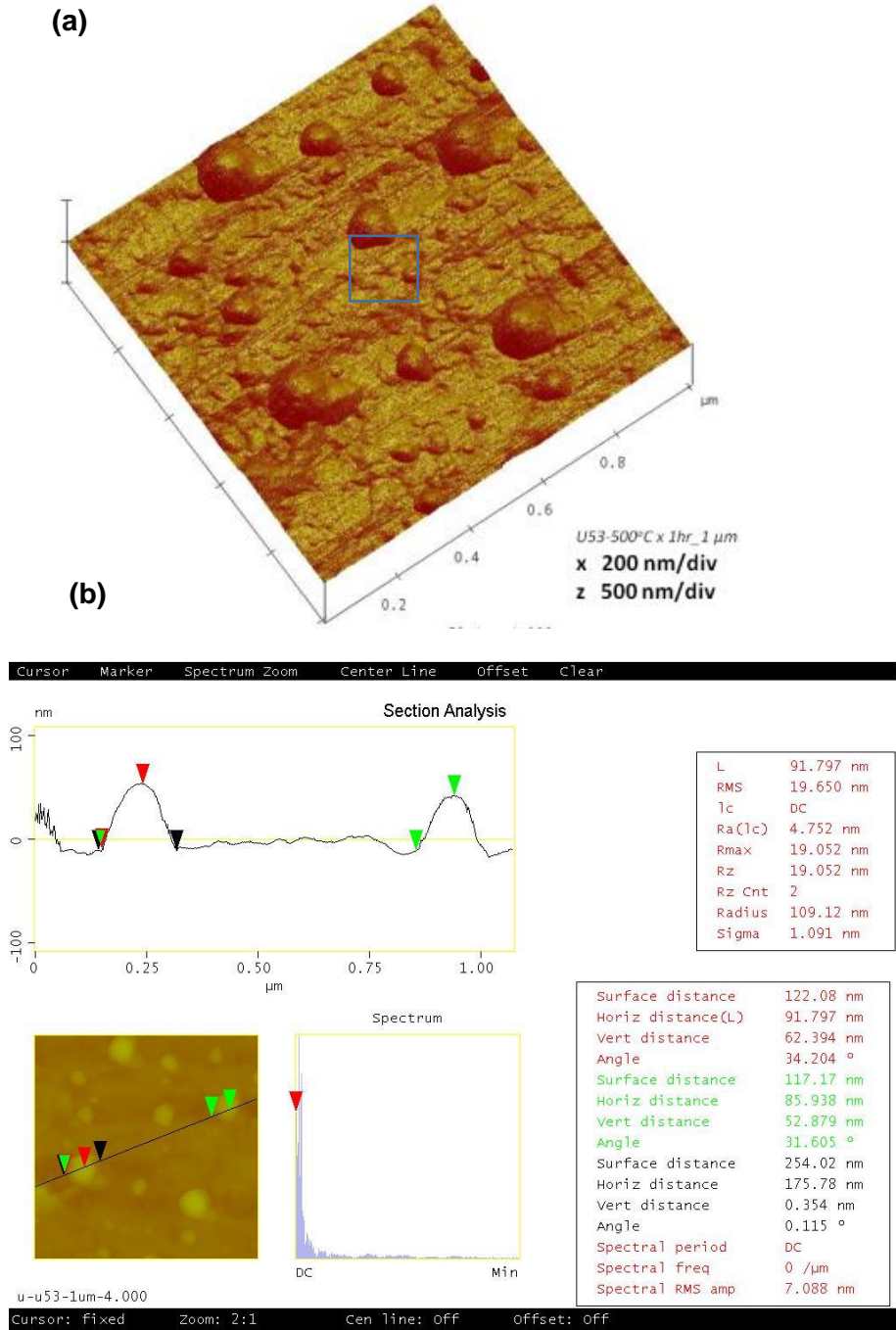


Figure 2.6: AFM image obtained from a sample treated at 500 °C for an hour is shown in (a). Note that the scan size is only 1 μm × 1 μm. Sn particles appear to be three-dimensional clusters forming islands. Height profile along the line passing through the tin island is shown in (b). Triangles of the matching color are reference distance points for the height measurements.

## 2.2.2 Time Dependence of nucleation at 500 °C

The nucleation period was varied while keeping the temperature constant at 500 °C. It was found that five minutes at 500 °C was not enough to evaporate all the Sn chloride (1 g), but it was sufficient to produce some Sn particles already. The surface was covered with 'curly' features, as shown in Figure 2.7(a). Results obtained after an hour at the same temperature were discussed already in the previous section. The surface produced after four hours at 500 °C is shown in Figure 2.7(b) Comparing with the result obtained after an hour at 500 °C, four hours at the same temperature appears to produce additional small Sn particles resulting in more coverage on the surface. EDS was only able to detect Sn from large Sn particles, but once again, XPS analysis showed more Sn than SEM/EDS analysis reported. A comparison of XPS analysis is presented in Table 2.7.

The AFM image captured from a sample prepared at the nucleation temperature of 500 °C for 4 hours is shown in Figure 2.8(a). Note that tin particles (see height profile of a section in Figure 2.8(b)) are thicker when compared to that obtained after an hour at 500 °C (Figure 2.6).

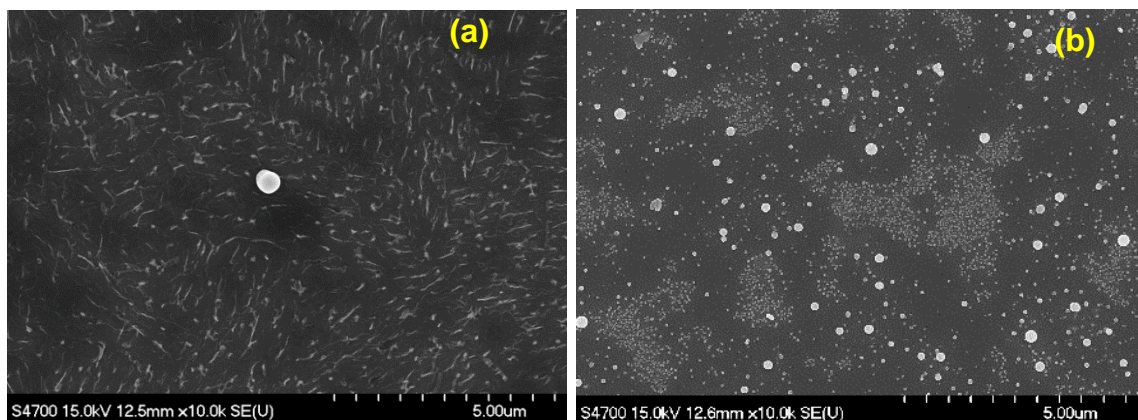
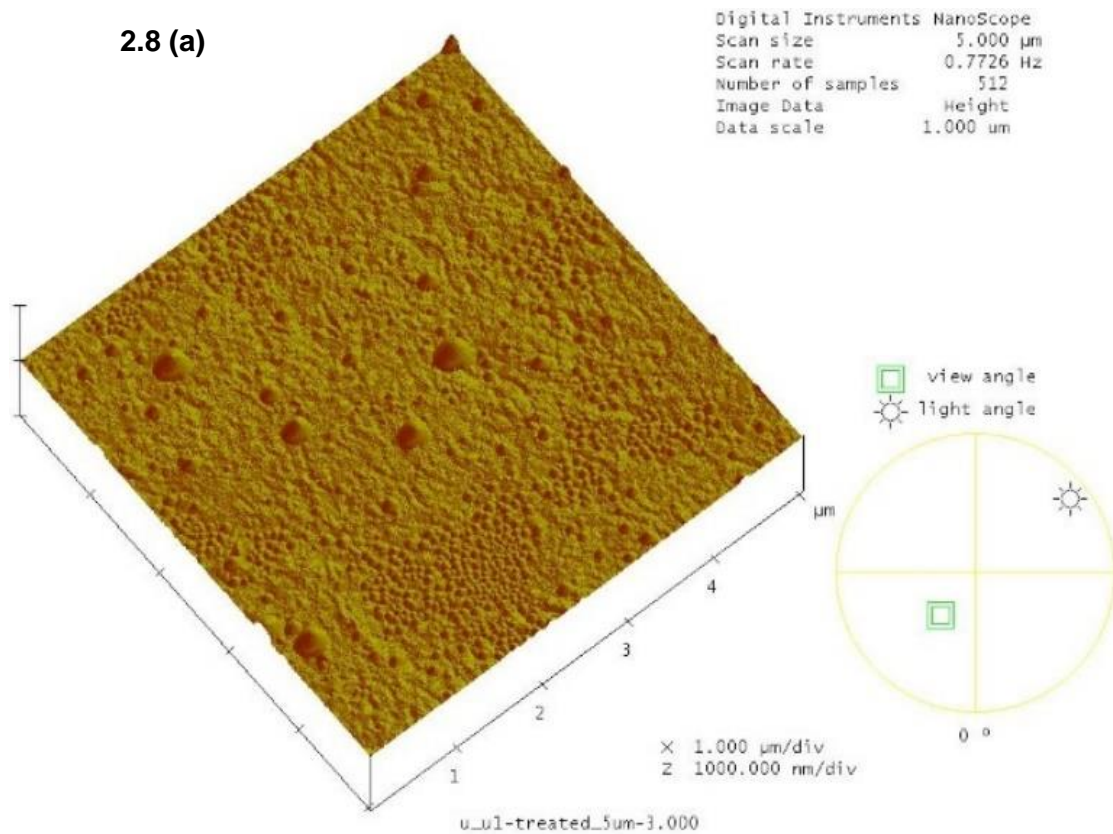


Figure 2.7: SEM images from samples obtained from experiments with a nucleation temperature of 500°C for (a) 4 hours and (b) 5 minutes.

Table 2.7: XPS elemental analysis of nucleated samples for different durations at 500°C.

Nucleation Temperature	Time	Sample	C (at. %)	O (at.%)	Nb (at. %)	Sn (at. %)	$\frac{Sn}{Nb + Sn} \times 100$	
500 °C	4 h	U1	7.2	56.8	23.9	12.0	33.43	With pre-sputtering
500 °C	1 h	U90	56.8	31.2	7.3	4.7	39.17	
			13.3	52.5	25.3	8.9	26.02	With pre-sputtering
500 °C	5 min	U9	39.9	42.0	11.9	6.2	34.25	
			2.4	42.7	51.3	3.6	6.55	With pre-sputtering



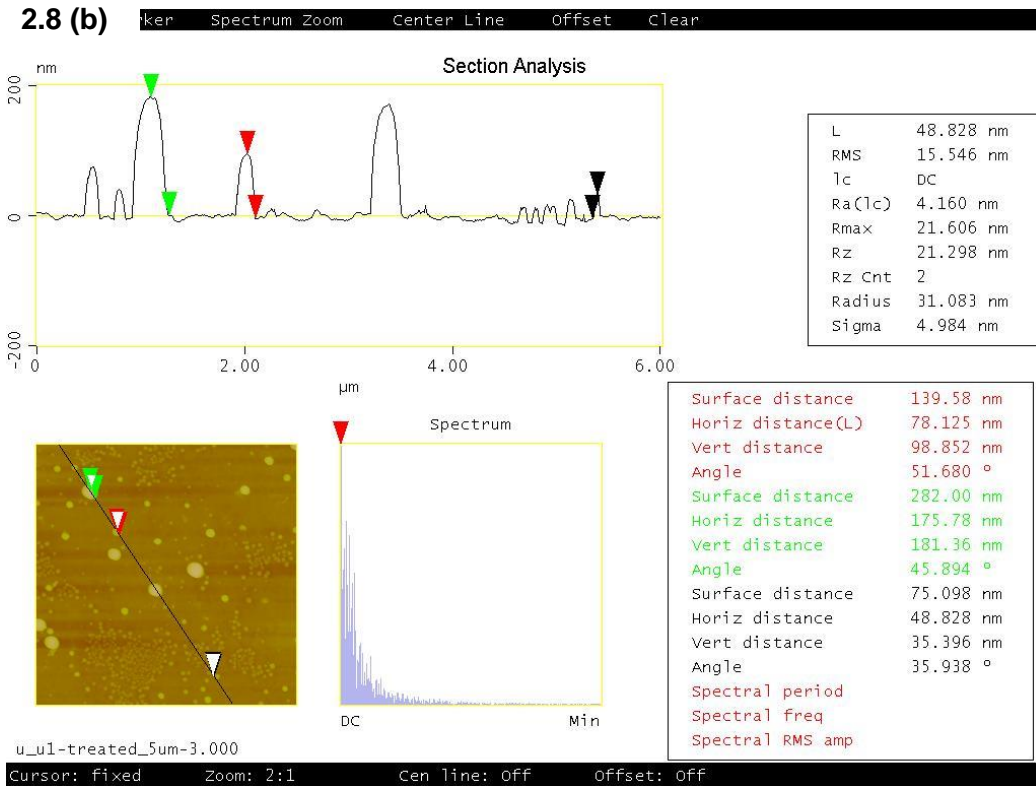


Figure 2.8: AFM image of the surface after 4 hours of nucleation at 500 °C is shown in (a). (b) shows height profile along a line passing through tin particles. The largest particle is ~ 300 nm in diameter with height of ~ 175 nm. The triangles of the matching color are for the height measurements.

### 2.2.3 Low vs. High Amount of tin chloride

The recipe for diffusion coating of Nb<sub>3</sub>Sn first developed at Siemens AG used a small amount of tin halide (20 μg.cm<sup>-2</sup>). Recent recipes in practice at different research facilities use different amounts of tin chloride. We compare the nucleated surfaces produced using the Jlab protocol (~3 mg.cm<sup>-2</sup>) of tin chloride, 500 °C for an hour, with the temperature ramp of 6 °C.min<sup>-1</sup>, to a protocol using much less tin chloride (~10 μg.cm<sup>-2</sup>), reported by Cornell University, 500 °C for five hours, with the temperature ramp of 3 °C.min<sup>-1</sup> [37]. SEM images, in Figure 2.9, show a uniform distribution of particles

produced with a low amount of tin chloride. They are tiny compared to the nucleation provided with a higher amount of tin chloride. EDS examination showed only Nb indicating that these particles are thin. XPS analysis (Table 2.8) shows comparable tin coverage in nucleated samples obtained from both experiments. Notice that removal of carbon by pre-sputtering revealed significant Nb, but reduced the tin, consistent with the notion of a very thin surface layer. More tin chloride produces bigger tin particles with similar tin coverage on a Nb surface. The longer nucleation time in the latter recipe may have an important role to produce such good coverage of tin with a small amount of tin chloride.

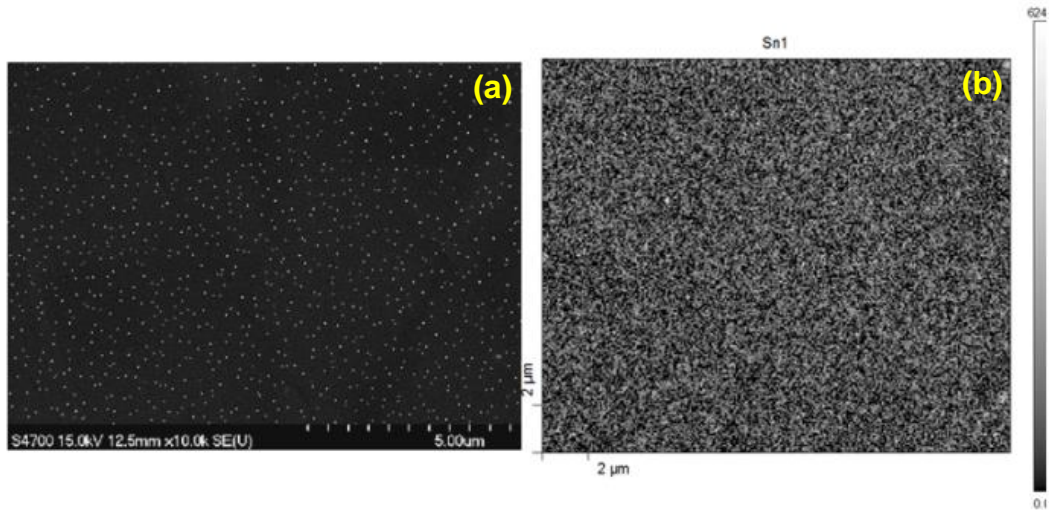


Figure 2.9: (a) SEM image of a nucleated surface obtained by using low tin chloride. (b) SAM elemental mapping of tin.

Table 2.8: XPS elemental analysis of nucleated sample U66 treated for 5 hours at 500 °C with a reduced amount of SnCl<sub>2</sub>.

Nucleation Temperature	Time	C (at. %)	O (at. %)	Nb (at. %)	Sn (at. %)	$\frac{Sn}{Nb + Sn} \times 100$	
500 °C	5 h	30.5	40.7	11.1	17.7	61.45	
		6.0	45.5	39.7	8.8	18.1	With pre-sputtering

## 2.2.4 Nucleation on Anodized Surfaces

Substrate anodization was introduced in the 1970s to overcome non-uniformity and was often combined with the setup that maintains a higher temperature of the tin source compared to the substrate [17]. Despite the expected RRR loss, recent coating experiments with anodized substrates using the “standard” nucleation protocol indicated a positive effect on coating uniformity [70, 71]. The effect of tin chloride on anodized and non-anodized Nb surfaces following the nucleation step was compared. To prepare samples, a fixed cell voltage of 30 V or 50 V was applied to grow anodic oxide layers on BCP treated Nb samples with a 15%  $\text{NH}_4\text{OH}$  solution as an electrolyte. The thickness of the oxide layers was estimated to be  $\sim 60$  nm and  $\sim 100$  nm for the samples using the reported thickness-voltage ratio [55]. These samples were subjected to 5 hours of nucleation at 500 °C with the usual  $\sim 3$   $\text{mg}\cdot\text{cm}^{-2}$  of  $\text{Sn}/\text{SnCl}_2$ . SEM images of the obtained surfaces are shown in Figure 12. Features were present on the surface following nucleation in each sample, but the appearance and distribution of these features (presumably tin) were different from those observed for non-anodized samples. The features were more prominent and more sparsely distributed in a 50 V anodized sample compared to those in a 30 V anodized sample. Our result appears to be different from recent results from similar studies [72], which report the formation of big tin particles on the surface after pre-anodization, unlike non-anodized Nb. Note that, a smaller amount of tin chloride and different anodization parameters were used in the latter studies compared to our experiments.

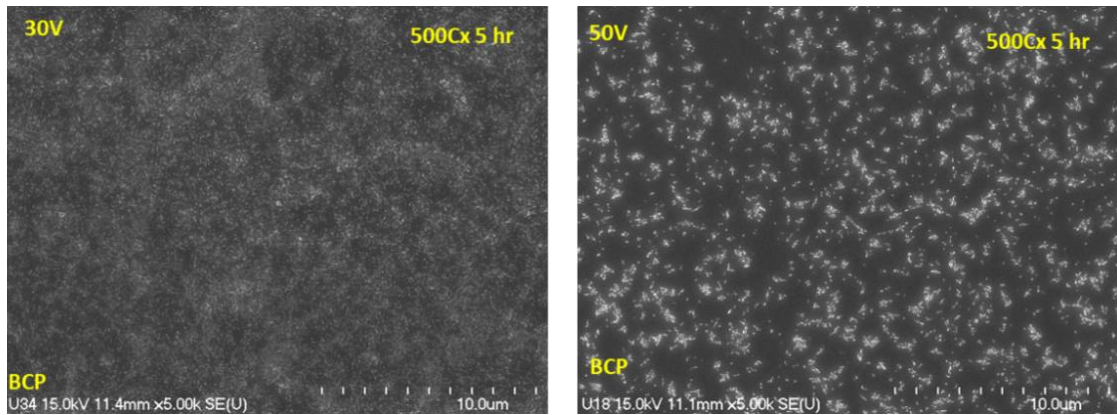


Figure 2.10: Nucleation on anodized Nb. The appearance and distribution of particles on the surface are different from those obtained on non-anodized samples.

### 2.2.5 Variation of Tin Particle Density

During the course of nucleation studies, the accumulation of visible tin particles was observed to vary for different grains of Nb in some cases. Here we particularly present two examples. The first one was from a sample treated at 500 °C for 1 h, shown in Figure 13. The size and shape of tin particles on different Nb grains visibly varied in this case. Area A1 appears to have fewer particles that appear to be near-circular under SEM whereas area A2 seems to have more particles with noncircular shape. Surface defects in substrate Nb appeared to be the favorite location for particle accumulation in many cases. One example of such defect is a surface scratch, as shown with arrows in Figure 13, developed during the polishing of the Nb sample. Each scratch line is decorated with a higher density of particles following the nucleation.

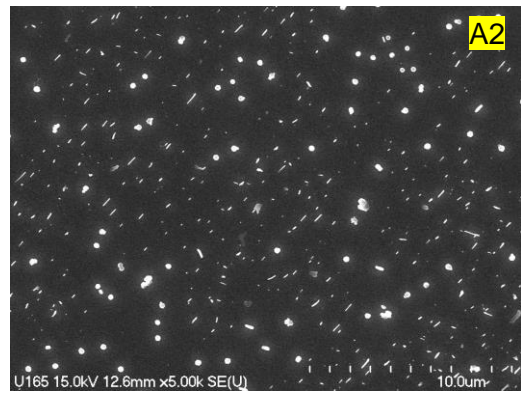
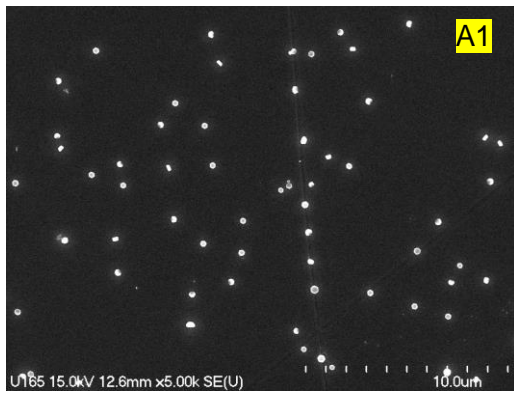
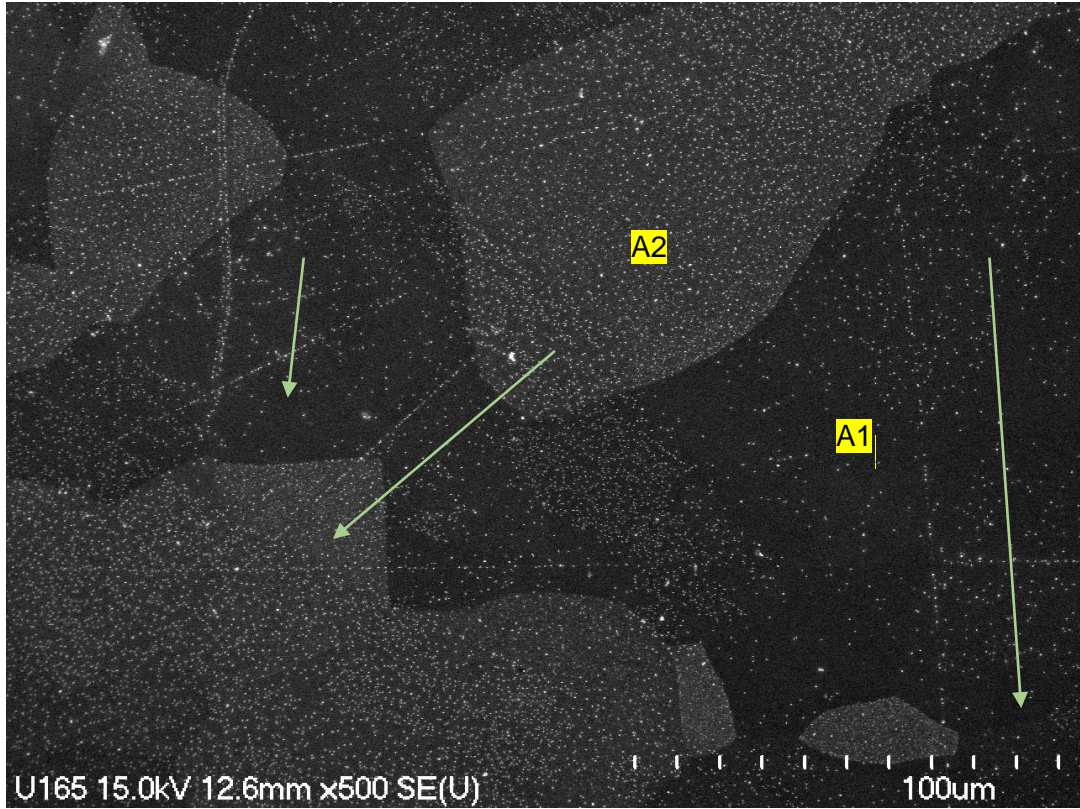


Figure 2.11: Variation of tin particles in different Nb grains. The arrows at the top figure indicate the direction of some scratches next to them. Particle distributions in areas A1 and A2 are evidently different.

The second example is shown in Figure 2.12. Here, the sample was pre-anodized (30 V, 15%  $\text{NH}_4\text{OH}$  solution) prior to the experiment, then nucleated at 600 °C for 1 h during an exploratory experiment. The image displays similar characteristic of decoration variation on the surface. Figure 2.12(c) shows a clear transition boundary between the two

areas having significantly different particle density. The appearance of Sn particles here was different from others discussed in previous sections. They appear mostly triangular, Figure 2.12(d), having a faceted shape similar to a pyramid. The appearance of these triangular islands looks similar to the appearance of Nb-Sn triangular crystals at 800 °C, reported by Hall *et al.* following 5 h of nucleation at 500 °C [72]. The appearance of Sn particles was very similar on regular sample when treated at 600 °C, suggesting that the hemispherical particle evolves to triangular pyramid following nucleation at higher temperature.

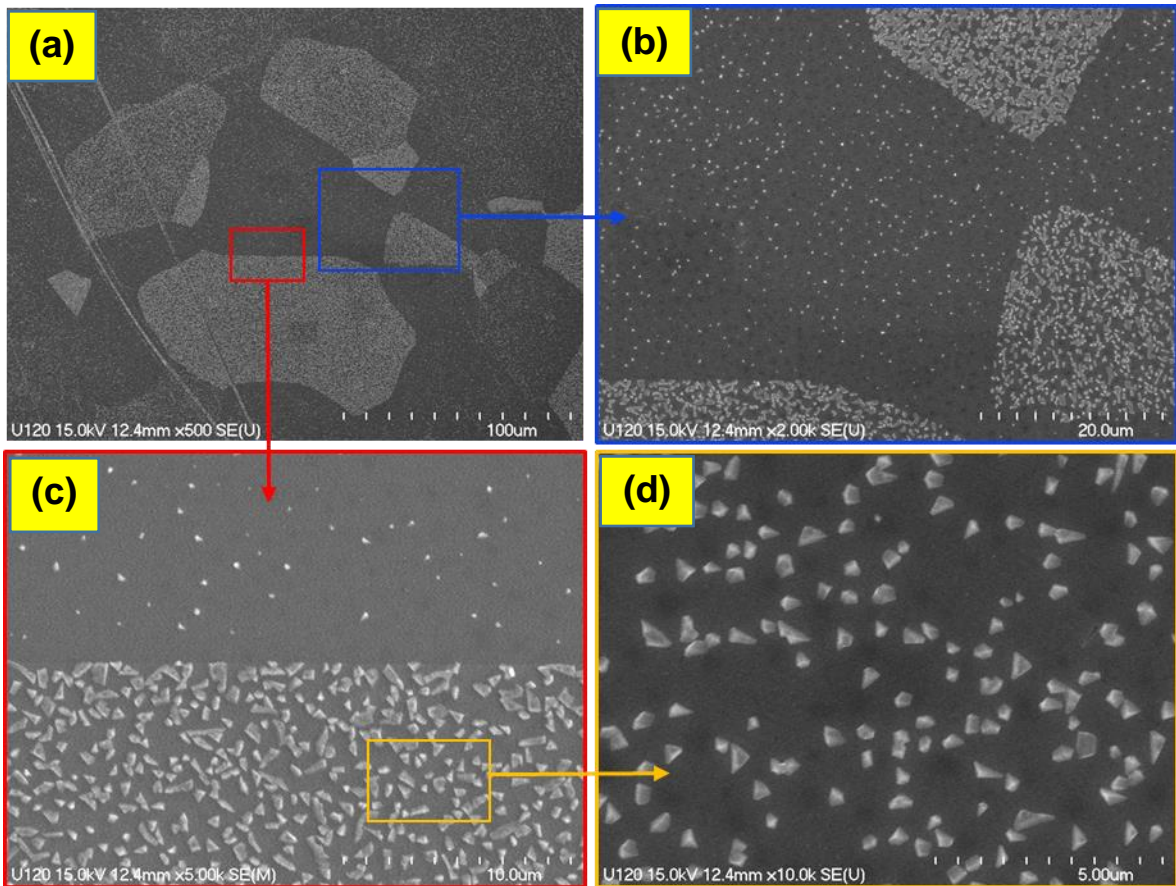


Figure 2.12: a) Particle density variation in an anodized sample treated for 1 hour at 600 °C. (b) A zoom view of an area showing areas with different density of particles. (c) A clear transition line between the two regions. (d) The triangular appearance of deposited particles.

Following the examination of nucleated samples, a set of different nucleation profiles were employed to grow the complete Nb<sub>3</sub>Sn coatings by a further coating step, as illustrated in Figure 1.10. Other experiments included interruption of the process at different stages with/without nucleation to understand its effect further in the subsequent coating. Results and discussions from these experiments are presented next.

### **2.2.6 Nb<sub>3</sub>Sn Coatings with Different Nucleation Profiles**

A selected few nucleation profiles were used for complete Nb<sub>3</sub>Sn coating. The temperature profile used during the coating was similar to Figure 1.10, except for the variation in nucleation parameters. There were no evident differences in terms of structure and composition in SEM/EDS between the coatings produced with different nucleation profiles: 400 °C for an hour, 500 °C for an hour and 500 °C for 4 hours for a similar amount (3 mg.cm<sup>-2</sup>) of tin and tin chloride. SEM images are shown in Figure 2.13, which also include the coating produced by applying a relatively small amount (~ 10 µg cm<sup>-2</sup>) of tin chloride for nucleation.

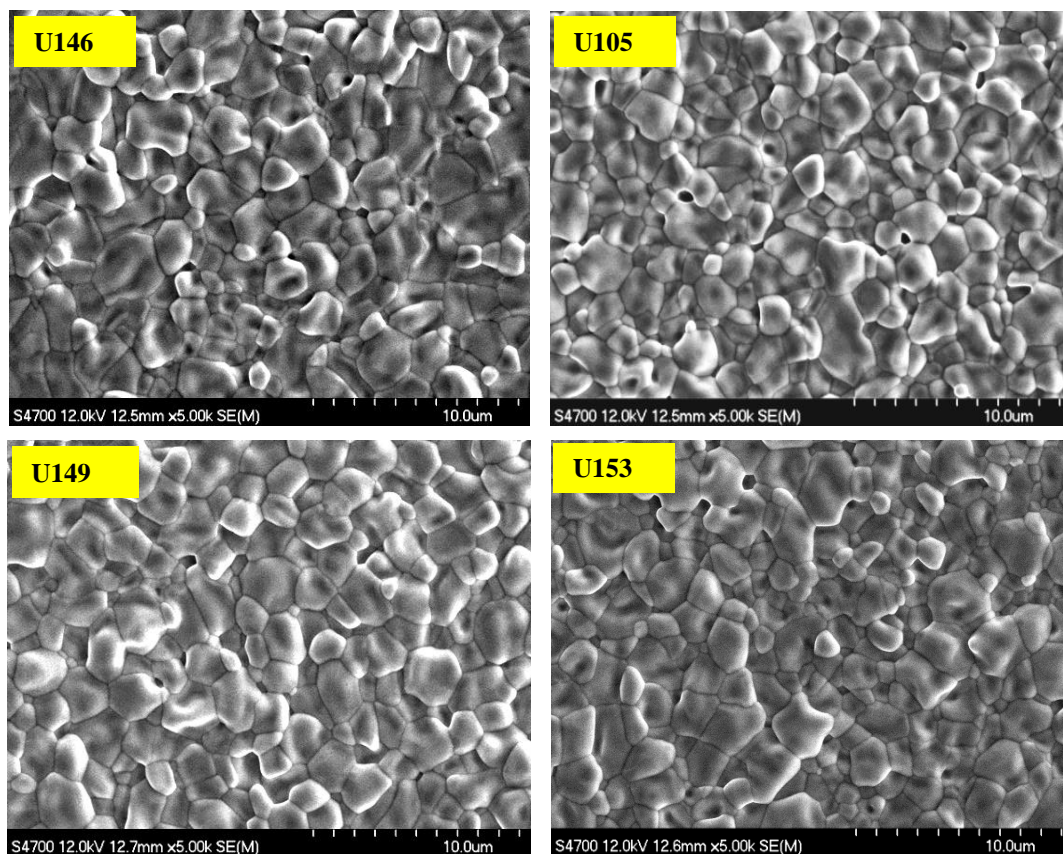


Figure 2.13: Nb<sub>3</sub>Sn coatings obtained by applying different nucleation profiles. U146, U105, U149, and U153 involved nucleation step 400 °C for 1 h, 500 °C for 1 h and 500 °C for 4 h and 500 °C for 5 h respectively. U153 was coated with only ~ 10 μg.cm<sup>-2</sup> of SnCl<sub>2</sub> and involved an additional coating time of 6.5 h at 1100 °C.

## 2.2.7 Role of Nucleation in Coating Genesis

The coating process with or without tin chloride was interrupted at different times while following the standard temperature profile, as shown in Figure 2. The heat was turned off after approximately 5 min, 1 h, or 3 h after reaching the coating temperature. SEM images obtained from each experiment are presented in Figure 2.14 and Figure 2.15. Five minutes after reaching 1200 °C, a uniform coating with grain sizes of few tens of nanometers was developed on the whole Nb surface, when tin chloride was included.

Some tin particles were visible. Similar experiments for one minute at 1200 °C without tin chloride resulted in a coating that included many patchy areas with irregular grain structures. These patchy areas appeared both after 1 h and the complete coating for 3 h at 1200 °C. On the other hand, coatings obtained from similar experiments with provided tin chloride demonstrated little to no patchy regions. Repeated complete coating experiments without tin chloride often produced patchy regions with irregular grain structure. This indicated that the inclusion of a nucleation step with tin chloride helps to assure a uniform Nb<sub>3</sub>Sn coating compared to that without tin chloride. Note that patch-free coatings were also obtained in an experiment without tin chloride. This may have been due to higher tin evaporation rate than normal, since the supplied tin was not packaged in Nb foil, thus providing relatively more surface area for evaporation. Taken together with previous observations, the notion emerges that patch-free coatings are promoted by increased tin supply obtained by tin chloride, more open tin source, and increased tin source temperature (secondary heater).

Finally, we attempted to grow the complete coating without any tin, i.e., only SnCl<sub>2</sub> was used. The coating process included nucleation (500 °C for 5 h) and growth (1200 °C for 3 h) profile with ~ 6 mg.cm<sup>-3</sup> of tin chloride. An SEM image of the coating is shown in Figure 2.16 [left]. Complete coverage of coating was observed with some patchy areas and elongated grains. However, this observation indicates that SnCl<sub>2</sub> plays an important role to establish a continuous tin layer before tin evaporation during the growth process. An EDS analysis showed only about 16 at. % of Sn, possibly because of a thin coating due to a small amount of tin deposited via SnCl<sub>2</sub>. Further examination with X-ray diffraction (XRD, Miniflex II, Rigaku) using CuK<sub>α</sub> radiation ( $\lambda = 1.504056 \text{ \AA}$ ) showed well-defined Nb<sub>3</sub>Sn phase, Figure 2.16 [right].

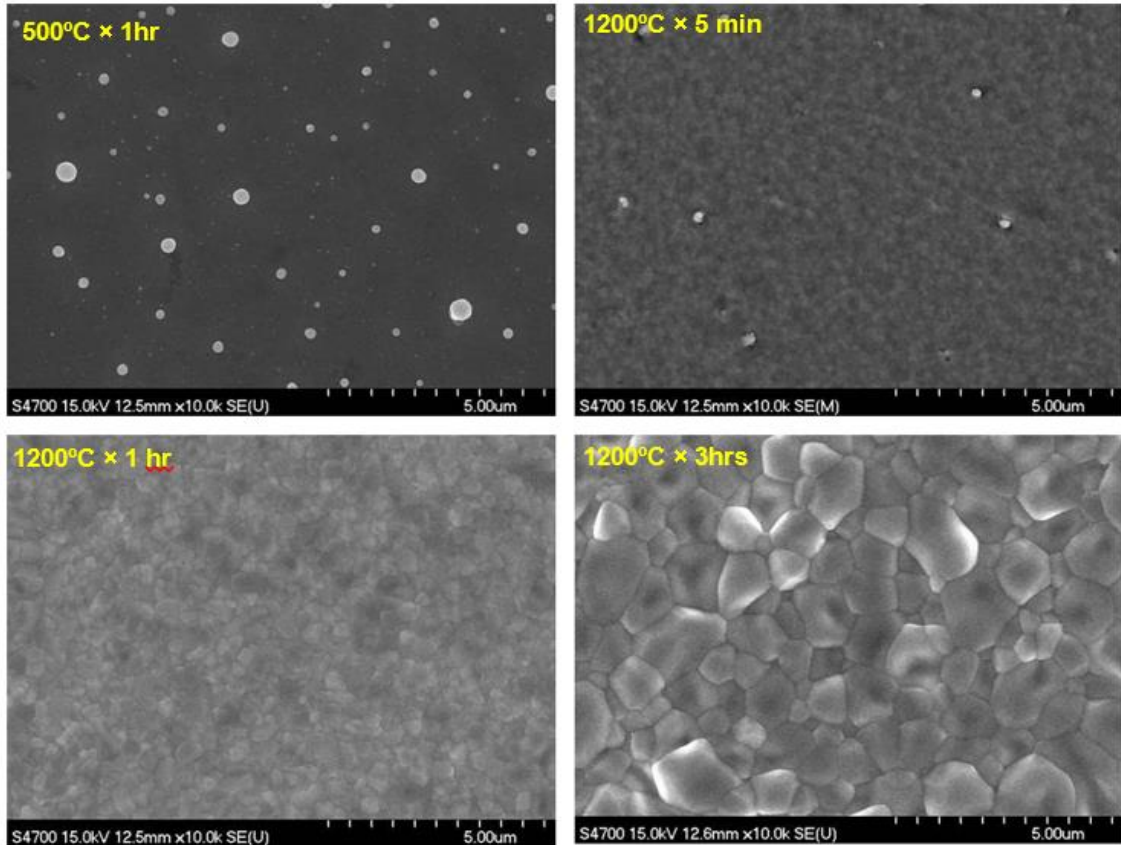


Figure 2.14: Different stages of Nb<sub>3</sub>Sn coating evolution during the coating process, including tin chloride. The bigger tin particles are still visible after 5 min at 1200 °C.

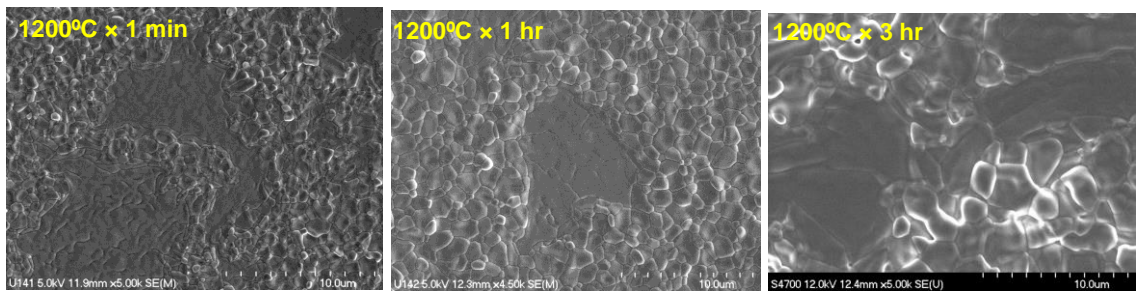


Figure 2.15: Different stages of Nb<sub>3</sub>Sn coating evolution during the coating process, excluding tin chloride. Coatings obtained after 1 min, 1 h, and 3 h at 1200 °C are shown from left to right respectively.

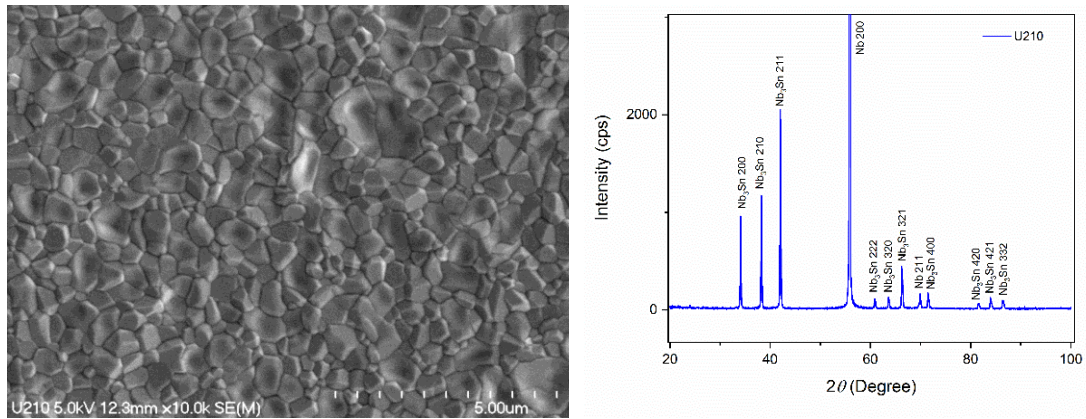


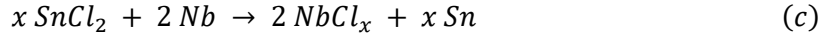
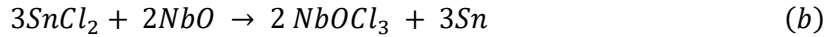
Figure 2.16: Coating prepared with the only  $\text{SnCl}_2$  [left]. Complete coverage of coating was obtained, including some irregular grain structures. A corresponding X-ray diffraction pattern showing  $\text{Nb}_3\text{Sn}$  phase.

## 2.2.8 Mechanism of Tin Deposition via $\text{SnCl}_2$

The as-prepared Nb surface is naturally covered with a (4–6) nm thick oxide layer because of its high chemical reactivity [73].  $\text{Nb}_2\text{O}_5$  is the dominant form of oxide because of its higher free energy of dissociation compared to other oxide forms. The presence of other suboxides ( $\text{NbO}_2$ ,  $\text{NbO}$ ,  $\text{Nb}_2\text{O}$ , and  $\text{Nb}_2\text{O}_3$ ) was inferred from Nb binding energy observed by XPS [74, 75]. The thermal stability of the native oxide layer has been studied for SRF cavities. These works generally agree that the typical  $\text{Nb}_2\text{O}_5$  layer reduces to  $\text{NbO}_2$ , and then to  $\text{NbO}$  following UHV baking at temperature  $>300$  °C [74]. The studied nucleation temperatures are in the range where the reduction of the native  $\text{Nb}_2\text{O}_5$  layer progresses.

The deposition of tin-rich features at the surface following each experiment involves some interchange or reduction reaction with  $\text{SnCl}_2$ , which may happen in three different ways here. First,  $\text{SnCl}_2$  can react with some small amount of hydroxyl present in the nucleation chamber. Second, the possible interaction with Nb oxide covering the

surface. Another possibility is a direct reaction between  $\text{SnCl}_2$  and the Nb surface. Representative possible reactions are



Gibbs free energy data [76] show that reaction (a) happens at  $\sim 1500$  °C under standard conditions, which indicates that it is less favored thermo-chemically for our nucleation temperatures.

On the other hand, reduction of  $\text{SnCl}_2$  with hydrogen had been reported before to deposit Sn on copper in a similar scenario, where they mention that it is necessary to keep HCl pressure at a low level by removing it for such reaction [77]. We can expect a level of HCl in our experiment to be low as it was constantly pumped during the experiment. As both hydrogen and HCl were observed with a residual gas analyzer (RGA) during some of our nucleation experiments, we believe that the tin deposition during the nucleation process arises by reduction of  $\text{SnCl}_2$  with already available hydrogen in the reaction chamber. Since possible chlorination of  $\text{Nb}_2\text{O}_5$  at low temperature through an intermediate step involving the formation of Nb oxychloride has been suggested before [78–80], we consider the possible interaction of  $\text{SnCl}_2$  with Nb oxide. X-Ray Reflectivity (XRR) studies on Nb(110) claim that  $\text{Nb}_2\text{O}_5$  and  $\text{NbO}_2$  both reduce to NbO following 30 minutes of vacuum annealing at 300 °C [81]. Therefore, we only illustrated equation (b) here, but the thermodynamic data are not all available to check its feasibility. In reaction (c),  $x$  can be 3, 4, or 5. It is found that  $\text{NbCl}_3$  is favored the most for any temperature  $< 500$  °C compared to  $\text{NbCl}_4$  under standard conditions.  $\text{NbCl}_5$  is not thermodynamically favored at our experimental temperatures [76]. Besides the possible reactions producing tin, concomitant reduction of Nb oxide layer upon the arrival of  $\text{SnCl}_2$  vapor, the mobility and surface

diffusion of tin, Nb surface properties (e.g., defects, orientation) are other factors to be considered to explain the produced nucleated surfaces from different experiments.

Evaporation of  $\text{SnCl}_2$  is expected to start at  $\sim 250$  °C and the known transformation of the native  $\text{Nb}_2\text{O}_5$  surface in this temperature range also occurs. We assume that as we heat the Nb surface, oxide dissolution results in randomly distributed defects. These sites are favorable to trap tin early. Because of a small amount of  $\text{SnCl}_2$  evaporation at a lower temperature ( $\sim 300$  °C), these particles are only of few nanometers in size. Further heating increases both the defect population and the  $\text{SnCl}_2$  partial pressure. Such locations enhance  $\text{SnCl}_2$  interaction with the Nb surface producing more tin, bringing in features shown in Figure 4(b) at  $\sim 400$  °C. Raising nucleation temperature further to (450–500) °C is expected to produce more defects in the oxide layer leading to more particles. The native Nb oxide layer would have reduced to mostly NbO at these temperatures. A reaction between  $\text{SnCl}_2$  and Nb may take place uniformly, as suggested by reaction (c) at this point; forming a tin film by the direct reaction between  $\text{SnCl}_2$  and Nb. Longer nucleation may add further tin to the thin film and particles. The equilibrium surface composition is influenced by tin arrival as well as tin-tin and tin-surface interaction.

Surface defects, like the scratch discussed here, have different surface diffusion rates from the flat surface [82]. Sn atoms bond well to these less coordinated sites, and they serve as sinks for Sn during Sn vapor deposition favoring the formation of tin particles. The different density of particles on different grains points to an orientation-dependent adatom-surface interaction. One can expect the anisotropy in tin adsorption because of anisotropic surface energy. For example, Nb (110) has the lowest surface energy because of the bcc structure [83].

## 2.3 Conclusions

Several materials characterization tools, notably XPS, TEM SAM, SEM, and AFM, were used to investigate the nucleation process commonly used in diffusion coating of Nb<sub>3</sub>Sn. Several samples were prepared under many different nucleation conditions. Despite the fact that the nucleation is primarily the action of SnCl<sub>2</sub>, no chlorine was detected in any of nucleated samples. Nucleation yields two tin forms. Three-dimensional tin particles are generally deposited on Nb at a nucleation temperature of 450 °C and higher. Especially at higher loadings, these particles are quite visible to scanning electron microscopy and atomic force microscopy. At all loadings; XPS analysis, SAM elemental mapping and TEM analysis of the cross-section reveal a clear presence of two-dimensional phase of extra tin between tin particles, which resembles the surfaces produced by the Stranski-Krastanov growth mode. A comparison of Nb<sub>3</sub>Sn surfaces grown with and without nucleation clearly shows that the exclusion of nucleation seemingly increases the chances of forming patchy regions with irregular grain structure. Despite some patchy areas and irregular grain structure present at the surface, SnCl<sub>2</sub> alone was able to produce continuous coating, which shows the importance of nucleation for coverage. A thin-film of tin deposited during the nucleation appears to be crucial for such coverage. Even though the variation of nucleation parameters was able to produce drastically different surfaces, no evidence of any significant impact on the microstructure and composition of the final coating was found with SEM/EDS, which indicates that the final structure of Nb<sub>3</sub>Sn coating is most likely determined by the tin deposition at elevated temperature rather than the nucleation. The following chapter will discuss how the parameters at elevated temperature affect the final structure of the coating and what the mechanism behind it.

## CHAPTER 3

### Growth

The performance of Nb<sub>3</sub>Sn-coated cavities depends mainly on the quality of the coating, which is defined by the material properties (composition, microstructure, topography, crystallography, etc.). The material properties could be contingent on several process parameters which may include substrate preparations, nucleation and coating conditions, and post-coating treatments, to which the surface is before the RF testing. A few material studies were conducted in the past to analyze the effects of those parameters on the resulting Nb<sub>3</sub>Sn coating. Wuppertal researchers studied the growth kinetics at 1160 °C. Focused on thickness measurements, they investigated the dependence of the thickness of the coated layers on the tin vapor pressure, determined by the temperature of the Sn-source [84]. They found only a weak dependence of vapor pressure on the thickness. Siemens researchers studied the thickness and surface morphology of Nb<sub>3</sub>Sn coatings prepared at coating temperatures of 1050 °C, 1500 °C and 1850 °C [85]. Researchers at Cornell performed studies on the substrate quality, initial chemistry, annealing time, and some post-processing treatments of Nb<sub>3</sub>Sn [86]. They revisited the substrate pre-anodization and investigated its effect on Nb<sub>3</sub>Sn growth [72].

The effect of nucleation parameters and their relevance to the final coating were discussed in the previous chapter. We now investigate the other coating parameters to optimize the process and to overcome the current limitations on the performance of

Nb<sub>3</sub>Sn-coated SRF cavities. The first portion of this chapter will present the study of coatings prepared under different conditions to determine the effect of these parameters. The second portion will address some fundamental deposition mechanisms, shedding light on the kinetics and growth of the coating. For simplicity, we first describe several material characterization techniques used throughout the studies of Nb<sub>3</sub>Sn-coated samples.

Local composition and microstructure were examined with Hitachi 4700 FESEM equipped with the EDS detector, described in section 2.1.2. Topographic characterization was carried out with a Digital Instruments IV AFM in tapping mode using silicon tips with a resonant frequency of 300 kHz, a force constant of 40 N/m, and a tip radius of < 10 nm. Several areas from each sample were scanned at 50  $\mu\text{m} \times 50 \mu\text{m}$ , 10  $\mu\text{m} \times 10 \mu\text{m}$  or 5  $\mu\text{m} \times 5 \mu\text{m}$  with point resolution of 512  $\times$  512. Four to five areas from several samples were scanned and analyzed in terms of surface height power spectral density (PSD) as described in [87, 88]. The PSD is calculated by the Fourier transform of the scan data to reveal the average contribution by features at different lateral scales. PSD was calculated for each of the 512 scans in each data set and averaged to obtain one-dimensional average PSD. PSD profiles measured at different locations under the same scan condition were then averaged to get a representative PSD profile of each sample. Another feature of these profiles is that the area under each PSD curve corresponds directly to root mean square (RMS) roughness.

XPS depth profile data was collected at 50 W/15 kV with a spot size of 200  $\mu\text{m}$ , 45° take-off angle and 280 eV pass energy with a PHI Quantera SXM. Sputtering was accomplished via an argon ion source at 5 kV over a 2  $\times$  2 mm<sup>2</sup> area.

Focused ion beam (FIB) cross-sections were first prepared with the FEI NanoLab 600 dual beam. The NanoLab is equipped with a Ga source capable of 1–30 kV beam

energy with a maximum of 21 nA of current. A surface protective layer of platinum (~ 2  $\mu\text{m}$ ) was deposited prior to material removal with the FIB. Initial material removal was performed at 30 kV to remove material quickly. Subsequent polishing steps were performed by decreasing the FIB to a final polishing voltage of 2 kV, which yields optimal EBSD indexing conditions. The EBSD data were collected using an integrated EDS/EBSD collection system, including an EDAX TSL EBSD camera and Octane Elite EDS with a 25 mm<sup>2</sup> detector. Typical EBSD conditions range from 10 to 30 kV and beam current of 1–50 nA at a 20° incidence angle. Details on FIB cross-section preparation and EBSD data collection are available in [63].

### **3.1 Coatings prepared under different coating conditions**

#### **3.1.1 Variation of substrate preparation**

The success of Nb cavities relies on surface preparation techniques that produce “smooth and clean” surfaces, typically with BCP or EP. These techniques were used to prepare Nb substrates before coating, as described in section 1.2.7. Several samples were coated according to a typical process described in the same section. SEM/EDS examination showed no notable differences in the composition and microstructure of coating grown on differently prepared Nb substrates. This appears to correspond with cavity measurements at Cornell showing similar performances of the cavities prepared using BCP or EP [35].

AFM images in Figure 3.1 show similar post-coating topography on samples that received BCP, EP, or NP before coating. A comparison of representative PSD profiles obtained from coated surfaces grown on differently prepared substrates is shown in Figure 3.2. The coating process generates a characteristic topography that is independent of pre-

coating topography (see Figure 3.2). The nature of the PSD obtained here qualitatively resembles a PSD profile from BCP-treated Nb surface [88], as characterized by a sharp slope in the high-frequency regime.

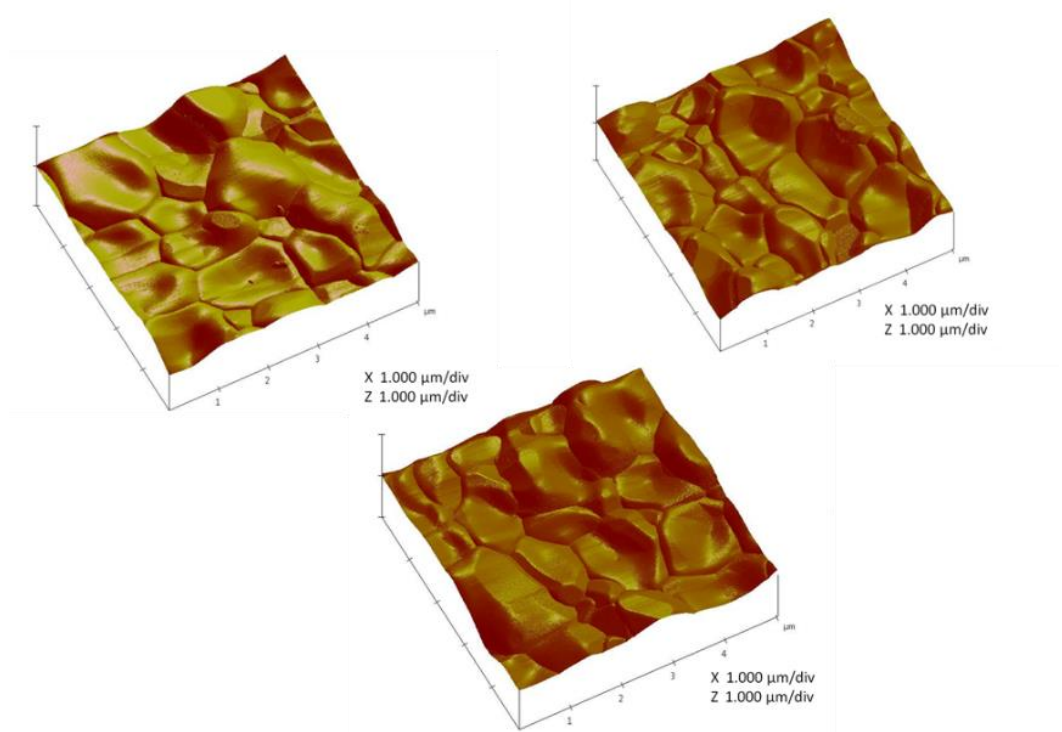


Figure 3.1: Topography of  $\text{Nb}_3\text{Sn}$  surfaces grown on substrates prepared with NP (top-right), EP (top-left), and BCP (bottom). Each sample was coated under the standard coating conditions described in section 1.2.7.

### 3.1.2 Coating with a low amount of tin

Existing  $\text{Nb}_3\text{Sn}$  coating protocols begin with loading tin into the furnace sample chamber along with the Nb samples or a cavity. The amount of tin provided usually is more than what would be consumed during the coating process. While coating facilities at Cornell University and Fermilab use an open crucible for tin loadings, at Jefferson Lab, the required amount of tin was supplied by packaging it inside Nb foil at the beginning, as shown in Figure 1.9. The amount of tin consumed during the coating process was

monitored by weighing the tin packages before and after the experiment. It was found that the amount of tin evaporated during the experiments was varying under similar coating conditions. The low consumption of tin was imputed to Sn packaging inside the Nb foil. Evaporative surface area varied between different packages, which was causing variation in tin evaporation. This variability was used to study surface properties of Nb<sub>3</sub>Sn coating associated with low tin evaporation.

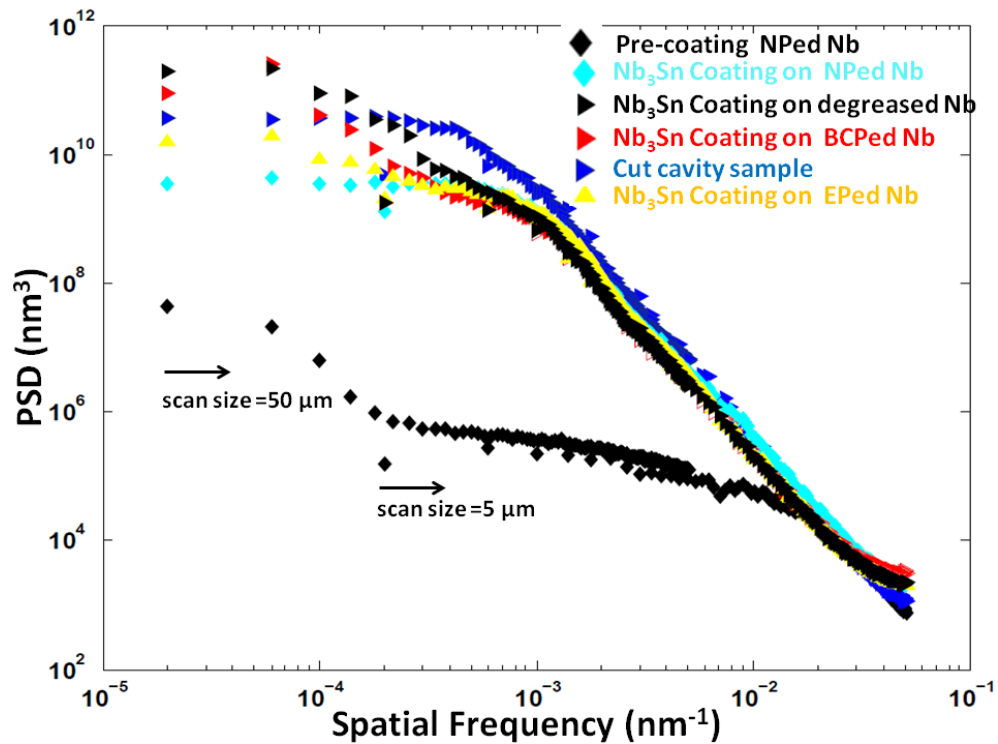


Figure 3.2: Average PSDs from Nb<sub>3</sub>Sn coating grown on differently prepared Nb substrates. Note the evolution of roughness compared to pre-coating nanopolished Nb surface. The cavity sample was obtained from a coated cavity that received BCP prior to the coating.

SEM images in Figure 3.3 compare the two Nb<sub>3</sub>Sn coatings prepared with identical coating parameters except the Sn consumptions were lower than usual. For the given coating condition, 1 hour nucleation step at 400 °C and a 3 hour deposition step at 1200 °C, ~ 40% (Sn-flux ~ 200 atoms.nm<sup>-2</sup>.min<sup>-1</sup>) consumption of the total Sn supply was

found to produce usual  $\text{Nb}_3\text{Sn}$ . For the case of 12% tin consumption (Sn flux  $\sim 60 \text{ atoms nm}^{-2} \text{ min}^{-1}$ ) (Figure 3.3), thread-like structures developed on the surface. However, 17% (Sn flux  $\sim 80 \text{ atoms.nm}^{-2}.\text{min}^{-1}$ ) of tin consumption resulted in a patchy region with relatively small grain sizes. In both cases, EDS analysis showed  $\sim 20 \text{ at. \%}$  of tin, indicating a thin layer of coating.

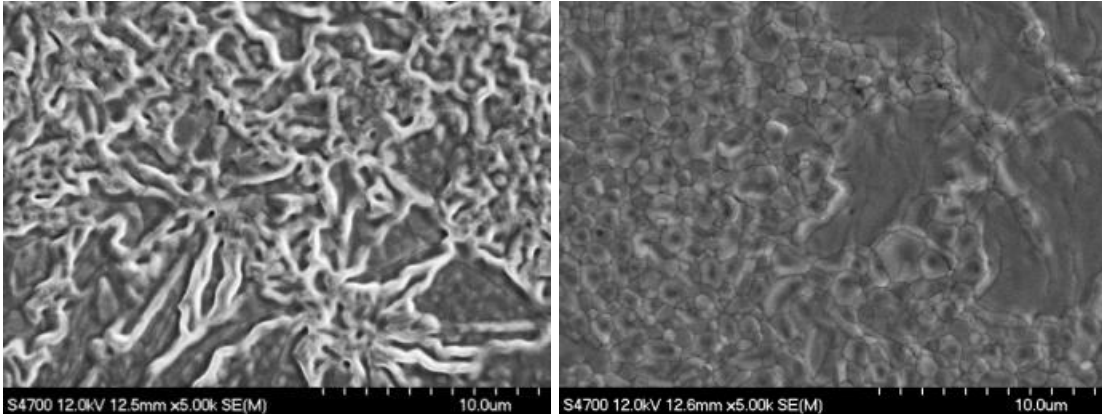


Figure 3.3: Coating obtained with Sn flux of about  $80 \text{ atoms.nm}^{-2}.\text{min}^{-1}$  [left] and Sn flux of about  $60 \text{ atoms nm}^{-2} \text{ min}^{-1}$  [right] of supplied tin consumption during the coating process.

Similar results were obtained during the examination of a sample that was accidentally dropped from the shelf of the sample chamber onto the Nb foil covering its bottom end. Various locations on the bottom side of the fallen sample were examined from the edge to the center. The coating near the edge shows small grains with occasional patches. At  $\sim 2.5 \text{ mm}$  away from the edge, the coating had thread-like structures, similar to one described above. EDS analysis revealed  $\sim 20 \text{ at. \%}$  tin. At  $5 \text{ mm}$  away from the sample edge, close to the center, no structures were present. Only Nb was detected with EDS. SEM images representing coating from edge to center are shown in Figure 3.4. Since the coating was normal at the top side of the sample that was exposed to Sn vapor, the different appearances of the coating at the bottom come from the gradient of available Sn vapor.

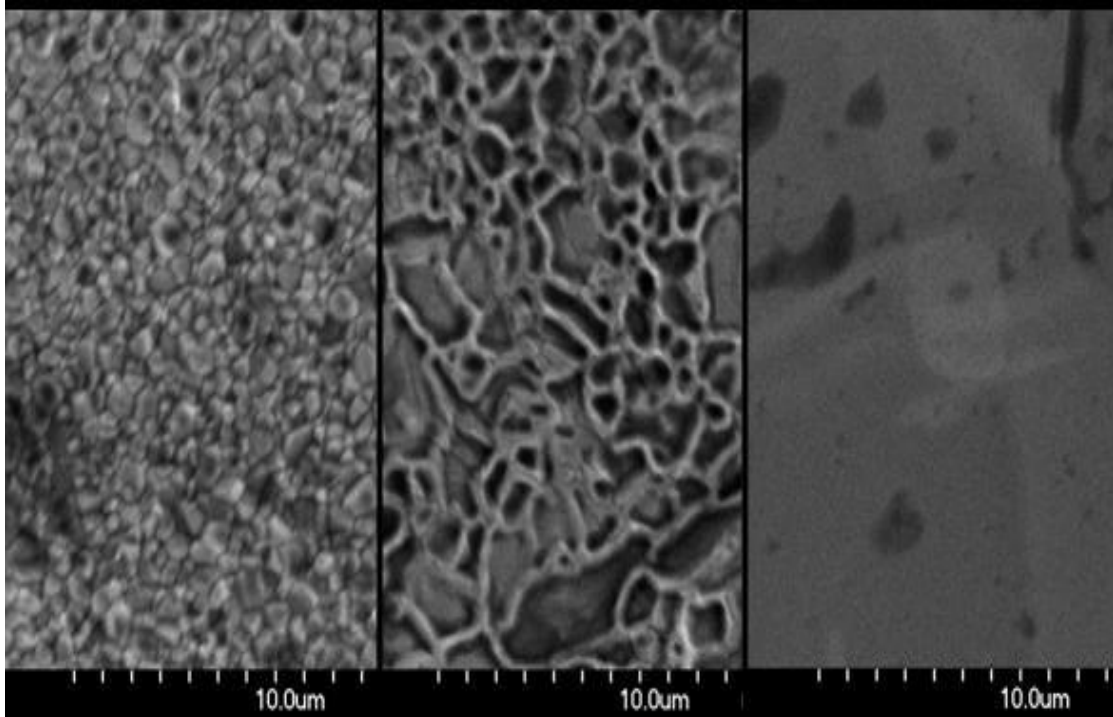


Figure 3.4: Variation of the coating at the bottom side of the sample that was dropped during the installation of the sample chamber into the coating chamber. Images were taken from 1 mm, 2.5 mm, and 5 mm from the edge.

### 3.1.3 Inspection of samples coated at different facilities

Even though the tin vapor diffusion technique is common, there are variation in coating protocols between different facilities. Whereas the Jefferson Lab furnace maintains both the tin source and the Nb substrate approximately at the same temperature, the Cornell heating system can hold the tin source at a higher temperature than the substrate [35]. The typical Cornell coating process includes an initial temperature ramp up at 3 °C/min to attain the nucleation temperature of 500 °C. The process has a 5-hour long nucleation step, which is followed by a temperature ramping of the substrate at 10 °C/min to reach the coating temperature of 1100 °C. The temperature of the tin source simultaneously undergoes a separate ramping such that the temperature of tin reaches

1250 °C at the same time the Nb reaches 1100 °C. After one hour, heating of the tin source terminates while the substrate temperature is maintained at the coating temperature for one additional hour. In contrast, the standard Jefferson Lab coating process consists of an hour nucleation step at 500 °C followed by a 3-hour deposition step at 1200 °C. With Siemens-type configuration of the furnace at JLab, it was not possible to reproduce the Cornell protocol to examine relative properties of the coating prepared by two different protocols. The study at the time was prompted by the fact that Nb<sub>3</sub>Sn cavities produced at Cornell were free from the Q-slope, whereas the cavities coated at Jlab were consistently showing strong Q-slopes. Prof. M. Liepe and Dr. D. Hall provided samples for this study, which were witness samples coated alongside a cavity during the coating at Cornell University's coating facility

Samples coated at both facilities were examined using SEM/EDS, AFM, and SIMS. Samples coated at JLab was produced by a typical coating procedure discussed in section 1.2.7. Several samples coated at JLab were compared with Cornell samples. SEM/EDS results from each sample exhibited mostly uniform coatings with the usual stoichiometry of Nb<sub>3</sub>Sn, ~ 24 at. % tin. As shown in Figure 3.5 and Figure 3.6, the grain structure and topography of the Cornell sample were found similar to that of JLab samples. Four areas from each sample, shown in Figure 3.6, were examined. For 10 μm × 10 μm scans, the average roughness of JLab sample and Cornell sample were (114 ± 17) nm and (105 ± 13) nm, respectively.

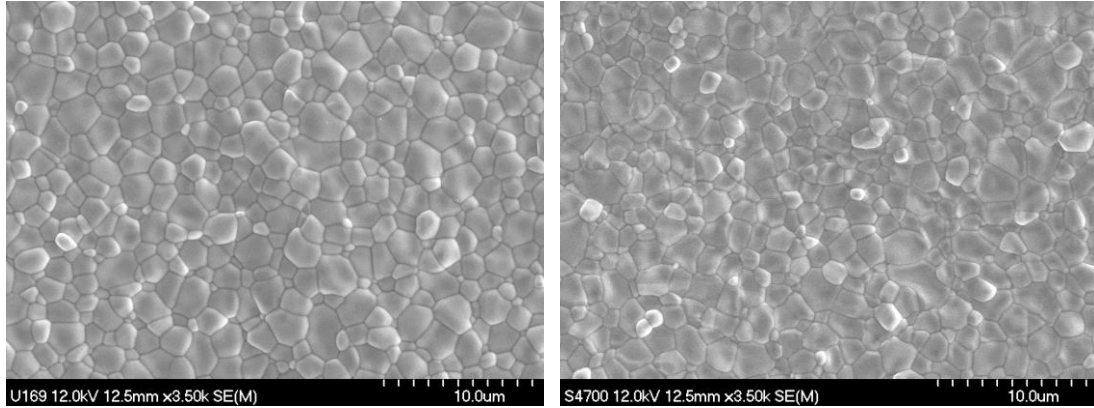


Figure 3.5: Coatings prepared at JLab [left] and Cornell [right]. All the samples were BCP treated before coating.

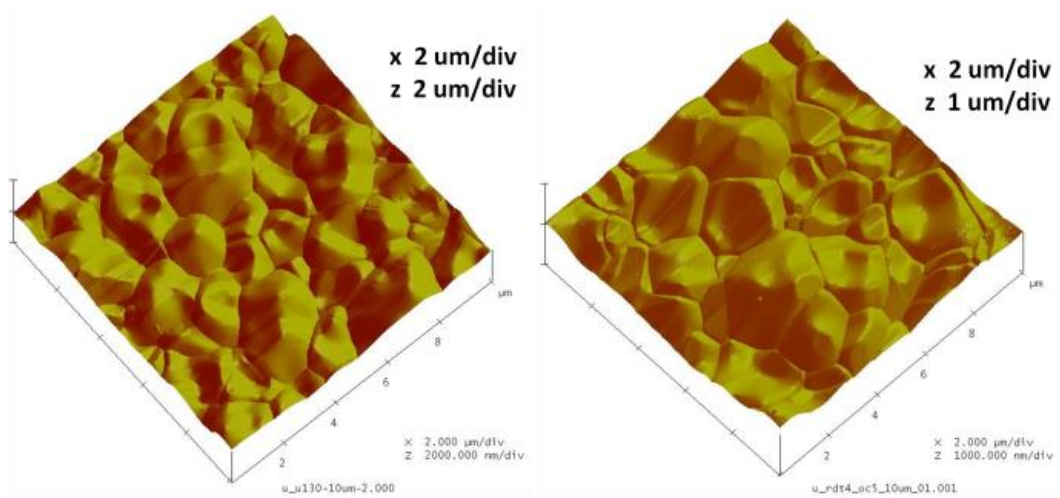


Figure 3.6: Topography of samples coated at Jlab [left] and Cornell [right].

$\text{Nb}_3\text{Sn}$ -coated samples from both facilities were analysed by SIMS with a CAMECA IMS7fGEO magnetic sector instrument for possible sources of trace contamination in the coatings. A detailed description of the data collection and analysis is available in [13]. A SIMS depth profile showed the presence of carbon and oxygen on the surface of the coatings, but these elements were not detected deeper within the  $\text{Nb}_3\text{Sn}$  layer. Even though significantly more tin chloride is used during the coating of  $\text{Nb}_3\text{Sn}$  at Jefferson Lab, no chlorine was detected. On the other hand, titanium was found in Jefferson Lab samples. Because the depth profile of titanium was similar to that of tin, it was speculated

that it might have been deposited during the coating process. From a comparison of the tin and titanium depth profiles in Figure 3.7, it is clear that the Jefferson Lab sample contained a significantly higher level of titanium.

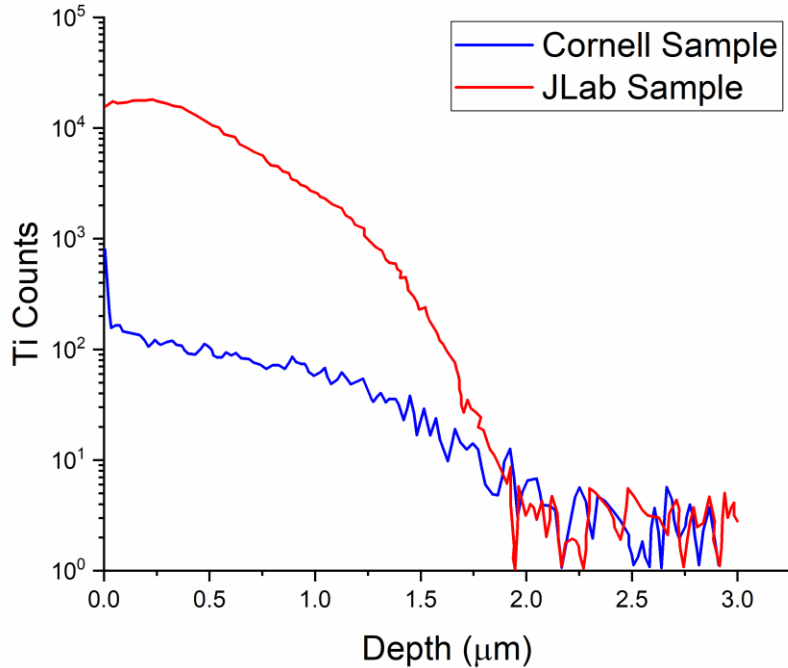


Figure 3.7: SIMS depth profile of Ti before the coating system upgrade. JLab sample has shown significantly higher levels of Ti than the Cornell sample.

The source of titanium contamination in JLab samples was residual tungsten inert gas (TIG) weld spots in the sample chamber flanges, which used titanium feed wire. Titanium contamination in SRF cavities can originate from Nb-Ti flanges [89]. These issues were addressed during a recent upgrade of the Jefferson Lab coating system by commissioning a new insert and sample chamber fabricated entirely from Nb, section 1.2.6. A SIMS analysis of samples coated after the coating system upgrade showed that titanium levels in JLab samples were then comparable to that of Cornell samples. Low

levels of titanium appearing in these samples could be traced from past treatments done in the same furnace, but a more thorough investigation is required.

### 3.1.4 Variation of coating time and temperature

The coating time and the coating temperature are the critical parameters that significantly affect the properties of the final coating. We investigated Nb<sub>3</sub>Sn coatings prepared at the temperature range of 900 °C to 1200 °C and durations of up to 12 h. Each coating included the standard nucleation step of 500 °C for 1 hour. The lower bound of temperature was chosen as 900 °C, which we believed may produce surfaces resembling the transition stage from nucleation to deposition in a usual coating. Nb samples used in this study had received BCP, BCP with anodization, or NP prior to the experiment. The coating temperature and durations used are summarized in Table 3.1. Unless specified, the nucleation step was fixed as usual, and identical experimental setups were used for each experiment. The present experiments were conducted after the coating system upgrade. The temperatures were measured with thermocouples attached to the sample chamber. The duration of deposition was accounted from when the sample chamber reaches the target deposition temperature. A fixed amount of SnCl<sub>2</sub> (~1 mg/cm<sup>2</sup>) and Sn (~ 3 mg/cm<sup>2</sup>) was supplied for each experiment. Tin was loaded in a Nb crucible, whereas SnCl<sub>2</sub> was packaged in Nb foil similar to past experiments.

Table 3.1: Investigated temperatures and durations of Nb<sub>3</sub>Sn diffusion coating.

Temperature (°C)	900	1000	1100	1200
Duration (hr)	3, 12	3, 12	3, 12	0.1, 3, 6

The consumption of tin was very low (<10 mg) at 900 °C, most remained in the crucible. Coatings obtained after 12 hours on NP and BCP samples appeared very similar,

which had thread-like structures and a very few pronounced grain boundaries (not visible in the image) on the surface. Pre-anodized samples, on the other hand, show well-connected usual  $\text{Nb}_3\text{Sn}$  grains (Figure 3.8). EDS analysis found  $16 \pm 1$  at. % tin in each sample. The lower Sn-content may be explained with a shallow coating produced with a small amount of tin consumption. A similar result was obtained for 3 hours of coating at  $1000^\circ\text{C}$ , except the BCP sample lacked a thread-like structure compared to the NP sample, and showed the usual grains. EDS shows  $21 \pm 1$  at % tin.

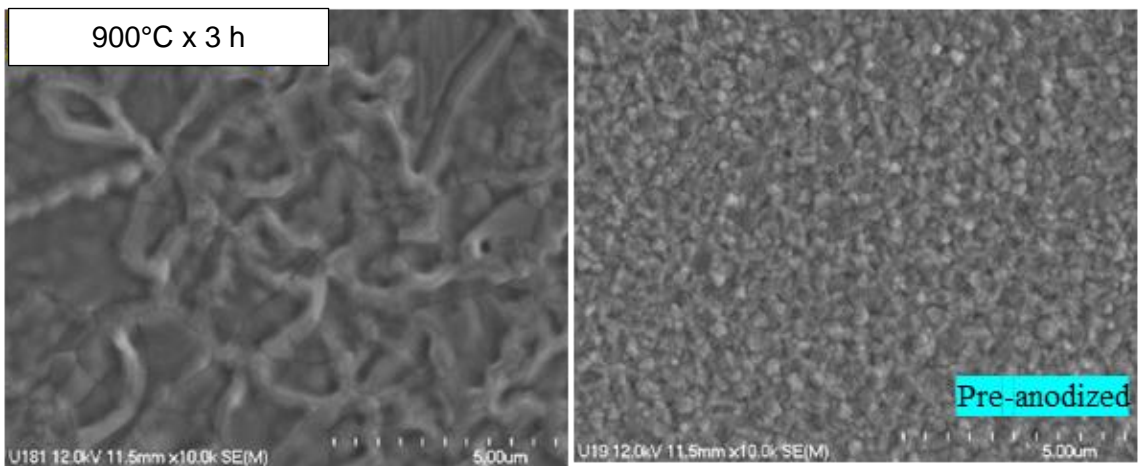


Figure 3.8: SEM images from pre-anodized [right] and regular BCP sample coated at  $900^\circ\text{C}$  for 12 hours [left].

The adjacent SEM and AFM images in Figure 3.9 compare the structure and topography of coatings prepared at  $1000-1100^\circ\text{C}$ . After 12 hours of deposition at  $1000^\circ\text{C}$ , the coating matches the usual appearance of  $\text{Nb}_3\text{Sn}$ . NP samples showed some abnormal grains, potential patchy areas of  $20-40\ \mu\text{m}$  in size and voids, but such structures were absent in the case of pre-anodized and regular BCP samples. Patches showed  $\sim 20$  at. % tin, less than usual  $\text{Nb}_3\text{Sn}$  composition of  $24 \pm 0.5$  at. % Sn from adjacent areas. These patchy regions are discussed in detail later in this chapter. AFM images showed some potential tin residue at the surface. In some cases, patchy areas appeared to have relatively more residue compared to areas with regular grains, but the relevance could not

be confirmed. Similar coatings were obtained with deposition temperature of 1100 °C for only 3 hours, but with relatively small grains. The NP sample still showed some patch-like structures, but less frequently compared to similar samples coated at 1000 °C. A significant increase in grain sizes without any patches was noticed following the extended coating duration of 12 hours at 1100 °C. EDS analysis shows the usual Nb<sub>3</sub>Sn composition. A few near-surface voids were found in some areas.

A short deposition of 5 minutes at 1200 °C resulted in some patchy regions in the NP sample once again. Occurrences of such areas were less frequent in BCP treated pre-anodized and untreated samples. No tin chloride was included in this experiment. The coating produced after 3 hours of deposition at similar conditions resulted in a larger grain size. The grain size further increased with a longer coating of 6 hours.

The AFM images in Figure 3.9 and Figure 3.10 show an apparent variation in roughness. The roughness of coated NP samples from each experiment was compared in terms of the power spectral densities (PSD) from surface height data obtained from 50 μm × 50 μm and 10 μm × 10 μm AFM scans from 4–5 randomly selected areas. The log-log plot of calculated PSD is shown in Figure 3.11. The samples in the legend are on the order of increasing grain size. The average grain size of U183 was the smallest and that of P14 was the greatest. Since the area under the PSD gives the square of root mean square roughness, this analysis shows that surface micro-roughness decreases with an increase in grain size. While roughness at high-frequency regime is only slightly affected, more extended coating at any temperature appears to increase the macro-roughness.

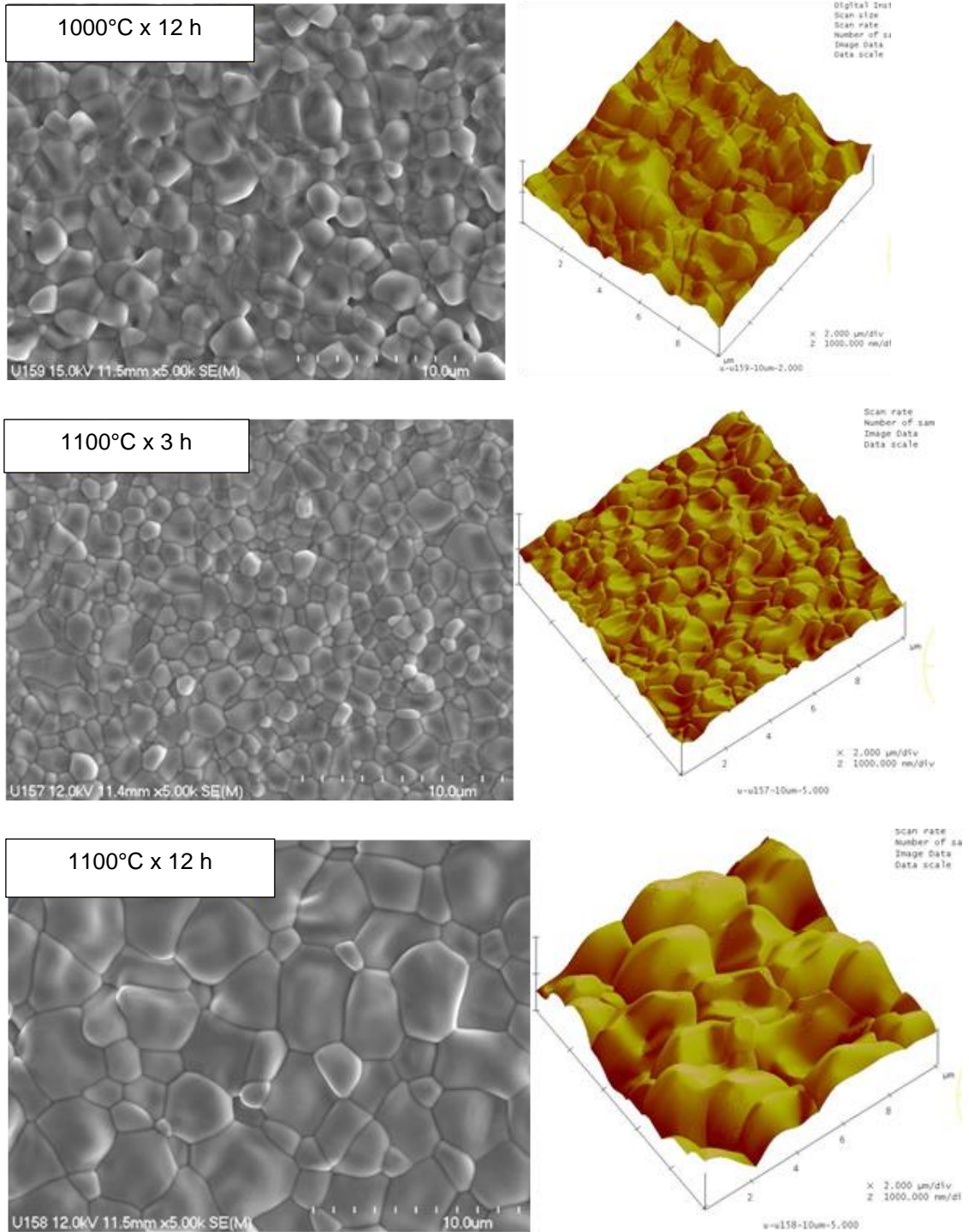


Figure 3.9: Microstructure and topography of  $\text{Nb}_3\text{Sn}$  prepared at 1000–1100 °C for different durations. All the samples received NP before coating. Scale for AFM images is 2  $\mu\text{m}/\text{div}$  along x-direction and 1  $\mu\text{m}/\text{div}$  for z-direction.

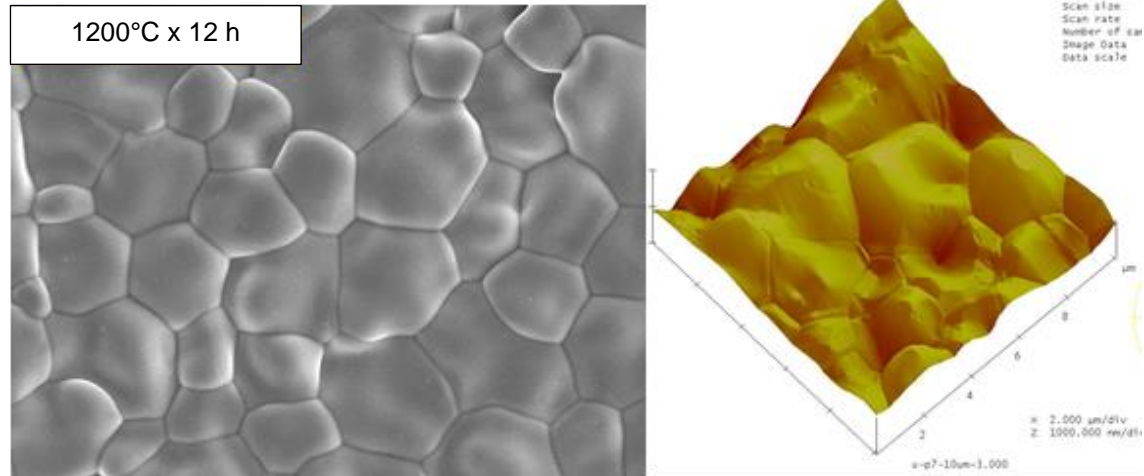
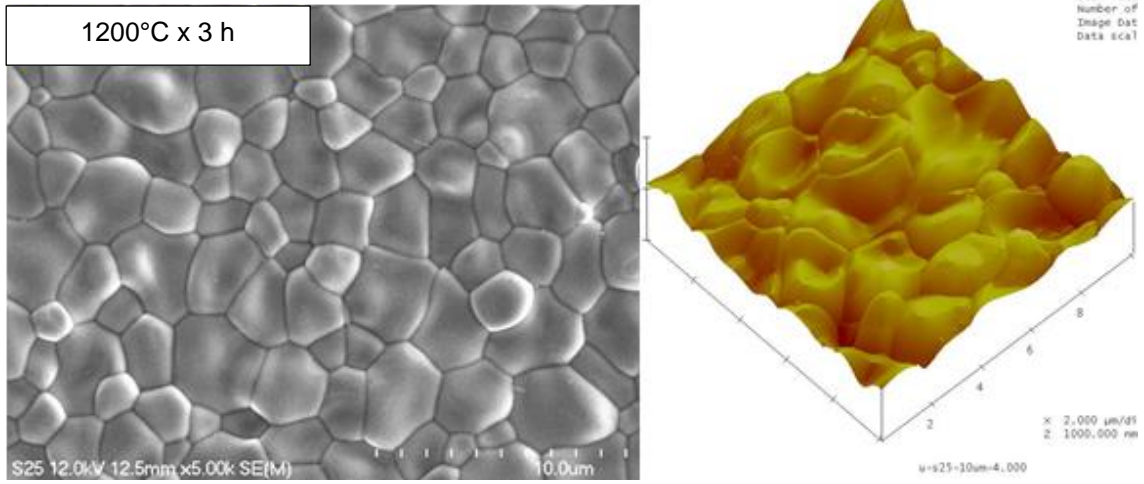
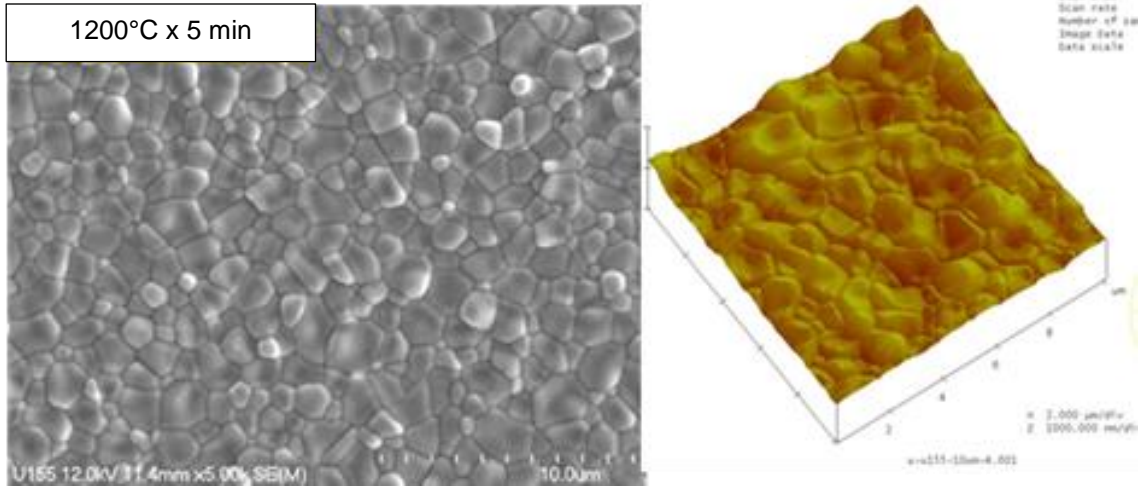


Figure 3.10: SEM and AFM images from NP samples coated at 1200 °C for 5 min, 3 hours, and 12 hours.

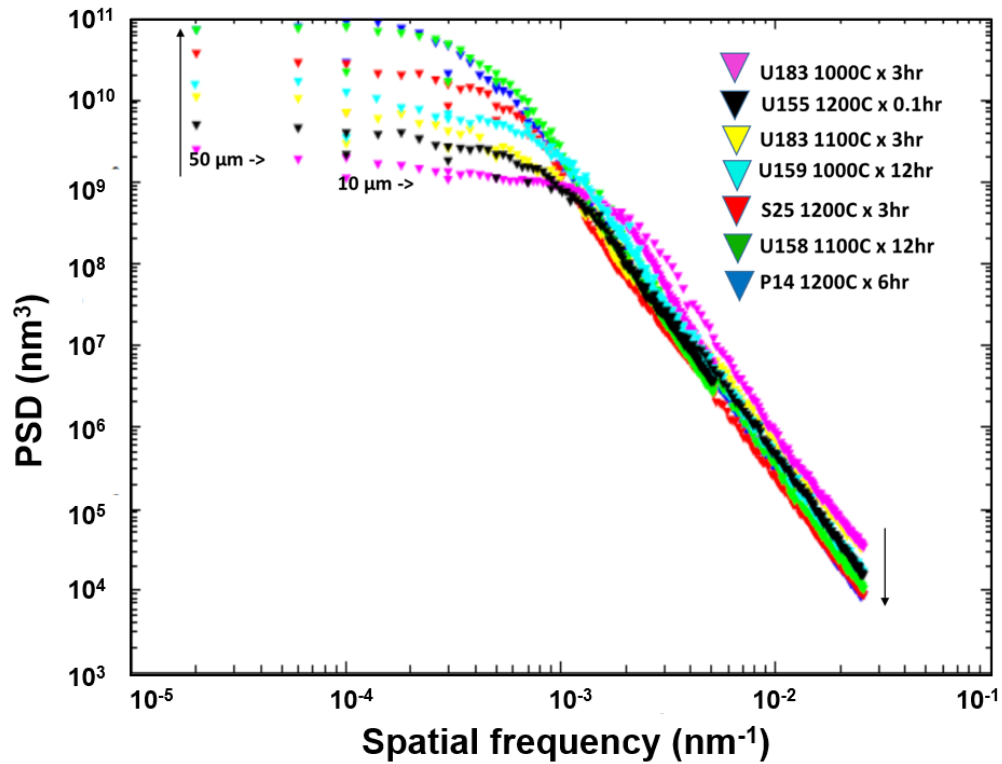


Figure 3.11: PSD comparison of samples coated with different deposition parameters.

XPS depth profile data was collected from pre-anodized and untreated BCP samples coated as discussed above. Those obtained from anodized samples are shown in Figure 3.12. There is a plateau of almost constant tin concentration close to the surface, which is similar for coatings prepared under different conditions and followed by a steady concentration drop before the tin signal vanishes. Such steady drop of Sn concentration could be caused by roughness of the  $\text{Nb}_3\text{Sn-Nb}$  interface. The thickness of the coating, defined as the distance between the surface and the depth at which the Sn signal dropped below 2 percent, varied from a few hundred nm to several  $\mu\text{m}$  depending on the deposition conditions.

The standard coating procedure yielded very similar coatings on Nb surfaces prepared differently (BCP, EP, and NP). Several previously described experiments indicate NP samples have a higher chance of developing patchy regions than BCP

samples. For any given condition, anodized substrates appear to have a lower chance of producing non-uniform coatings, which is consistent with the previous studies [17, 71].

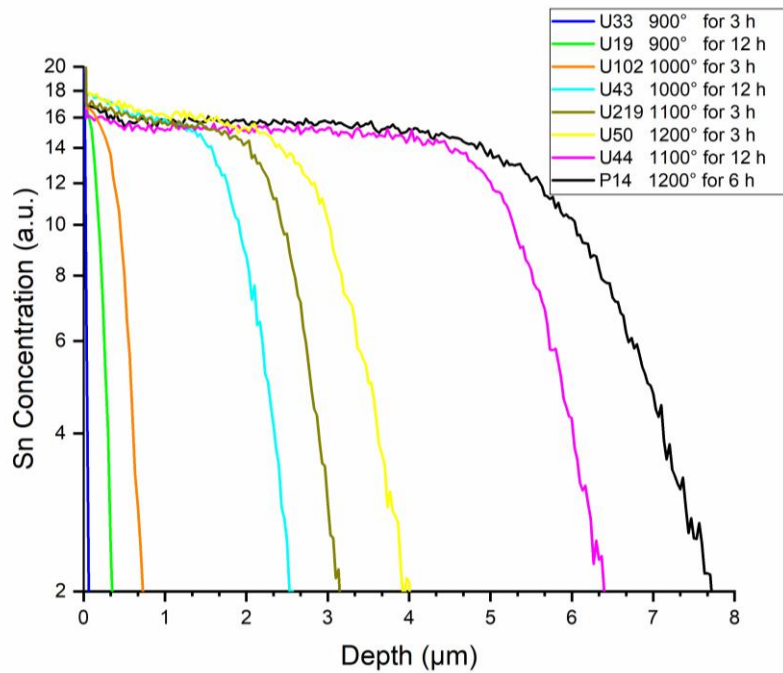


Figure 3.12: XPS depth profile from samples prepared as indicated.

The deposition temperature could affect the coating in several ways. First, it determines the tin evaporation rate, which affects the arrival flux of tin vapor onto the Nb surface. Second, it affects the rate of Sn diffusion. Coating deposited at low temperatures (900 °C for 3 or 12 h and 1000 °C for 3 h) resembled our previous coatings produced with low tin evaporation in the previous section, which indicates the association of low tin availability with the thread like structures during the deposition. Smaller grains and patchy areas appeared on the surface with slightly higher tin availability. XPS depth profile indicates a little to no plateau region of Nb<sub>3</sub>Sn close to the surface for such coatings with a sharp drop of tin content at the Nb<sub>3</sub>Sn-Nb interface. Coatings deposited at higher temperatures seem to avoid patchy region, possibly because of a higher rate of tin arrival at the initial stage of the experiment. Tin vapor at higher temperatures may also have higher kinetic energy required to promote a uniform nucleation site density until well-

connected Nb<sub>3</sub>Sn grain networks are established. It had been recommended in the early days of Nb<sub>3</sub>Sn coating to have a higher temperature for the tin source than for the substrate temperature to improve coating uniformity [17]. The coating time is crucial to determine the thickness of the coating. It is not clear yet quantitatively how the roughness and grain boundaries affect the performance of the cavity, but it appears that the increase of one leads to the decrease of the other or vice versa. More extended coating at any temperature increases the macro-roughness by reducing the grain boundary density with grain growth, as shown in Figure 3.13. The following section presents the research carried out mainly to understand the growth mechanism.

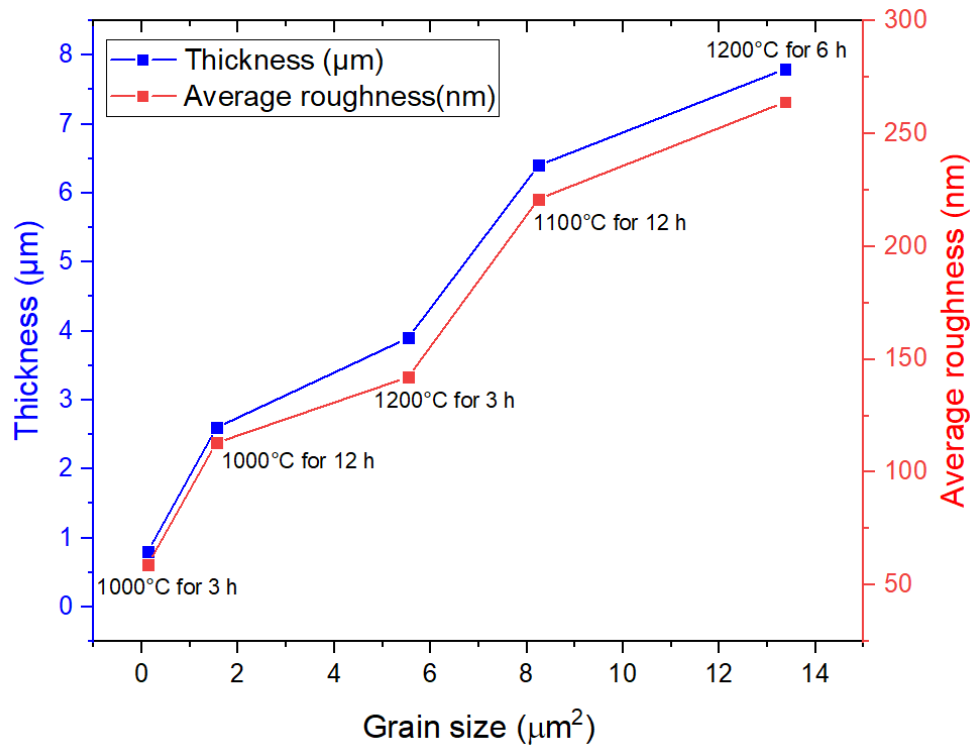


Figure 3.13: Observed relationship between grain size, coating thickness, and surface roughness. Average roughness values (50 μm × 50 μm scan) here were averaged values from five different locations of the sample. Average grain sizes were estimated from 5–6 SEM images of 2000–3500 magnification. Thickness was estimated from XPS depth profiles shown in Figure 3.12.

## 3.2 Growth of Nb<sub>3</sub>Sn in vapor diffusion Process

The quality of coated Nb<sub>3</sub>Sn layers is contingent on understanding the coating formation and growth. Past studies have shown that the coating thickness ( $y$ ) of the Nb<sub>3</sub>Sn layers grown via the widely used vapor diffusion process, does not follow a parabolic relationship with respect to the deposition duration ( $t$ ). The square of layer thickness does not scale linearly with the coating time ( $y^2 \propto t$ ) [84]. Non-parabolic growth indicates that the growth process is not purely diffusion-controlled [18]. Studies have shown a similar growth behavior with other preparation techniques, e.g., bronze processes and Nb(s)-Sn(l) annealing [90–93]. The deviation from the parabolic growth was often explained by the influence of the grain boundaries [90, 91]. At the same time, researchers proposed alternate interpretations, e.g., “*solution-deposition*” mechanism for the non-parabolic growth exponent [92, 93]. Other explanations included the multiphase diffusion during Nb<sub>3</sub>Sn formation, a reduced concentration of tin in the bronze matrix, and Kirkendall void formation [94]. Some studies also indicated a significantly slower growth rate (a lower value of the growth exponent) at 1200 °C, the coating temperature in practice, compared to lower temperatures [93].

Further studies with the contemporary characterization tools are merited to reveal the growth mechanism of Nb<sub>3</sub>Sn in the vapor diffusion process. To gain insight into the mechanism of Nb<sub>3</sub>Sn grain size and thickness growth at the temperatures of interest, we systematically coated samples for a range of durations and repetitions as described below.

### 3.2.1 Overcoat experiments

A set of fine-grain Nb samples treated with BCP was first coated for 1 hour at 1200 °C following a typical Nb<sub>3</sub>Sn coating procedure. After the run, several samples were removed from the coating chamber, and the remaining samples with several new Nb

samples were then coated (“overcoated”) for 1 hour again (without SnCl<sub>2</sub>). The overcoat procedure was repeated for 1, 1, 3, 12, and 60 hour coating durations, respectively, as shown in Table 3.2. There was always residual Sn in the crucible after each coating run.

Table 3.2: Overcoat experiments. Note that each experiment included new uncoated Nb samples along with samples from the previous run.

Experiment	Coating time (h)	Total coating time (h)
Single coat	1	1
1 <sup>st</sup> overcoat	1	2
2 <sup>nd</sup> overcoat	1	3
3 <sup>rd</sup> overcoat	3	6
4 <sup>th</sup> overcoat	12	18
5 <sup>th</sup> overcoat	60	78

### 3.2.2 Results

EDS examination shows ( $24 \pm 0.5$ ) at. % Sn and no notable change in surface composition following each overcoat. Microstructure evolution for sequentially overcoated samples is shown in Figure 3.14. Note that longer coatings resulted in larger grains. The total coating time for these samples varied between 1 and 78 hours. The average surface grain sizes were estimated for both the single-coat and overcoat samples from each coating run of the sequential overcoat series using the linear intercept method [95]. Here, SEM images were captured from 8–10 different locations on each sample, using a magnification where grains were distinctly visible. 4–6 lines were drawn across each image, and the number of intersections between the lines and grain boundaries was

manually counted. The average grain size was determined as the average distance between intersections.

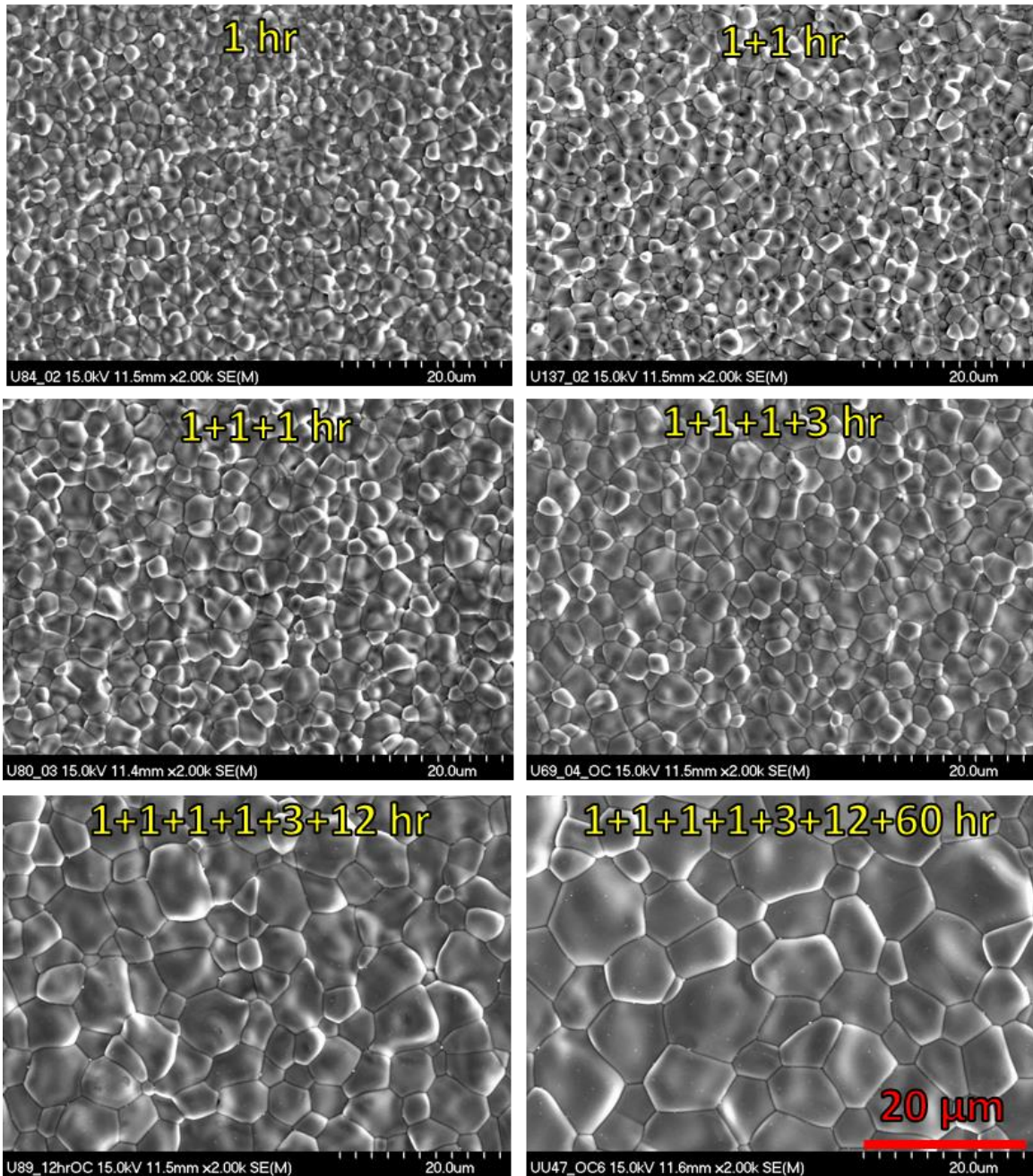


Figure 3.14: SEM images of the sequentially overcoated samples coated at 1200 °C for different durations. Note that all images were captured at the same magnification.

Table 3.3 shows the average grain sizes calculated for different cumulative coating durations. The measurement variation for each sample is expressed as the standard deviation ( $\pm$  SD).

Table 3.3: Average grain sizes for the various total coating times. Note that there are two data sets for 3 hours of the coating. The first data set was obtained from the sample sequentially overcoated in the first three experiments (1+1+1 hour). The second data set was obtained on a new sample coated for 3 hours in the fourth experiment.

Total Coating Time (h)	Average grain size ( $\mu\text{m}$ )
1	$1.60 \pm 0.15$
2	$1.72 \pm 0.18$
3	$2.23 \pm 0.18$
3	$2.20 \pm 0.20$
6	$3.06 \pm 0.23$
12	$3.67 \pm 0.26$
18	$4.41 \pm 0.30$
60	$6.09 \pm 0.46$
78	$6.58 \pm 0.54$

Figure 3.15 shows the grain sizes obtained after different coating times for single-coat and overcoat samples as a function of the coating duration. The error bars are the measurement errors tabulated in Table 3.3. Those errors were used as the weighting factors to obtain fitted lines using nonlinear least square fitting, which is used throughout the chapter to fit nonlinear data. The fitted power law dependence of the grain size on the coating time is given by,

$$z = (1.55 \pm 0.06)t^{0.34 \pm 0.01} \quad (3.1)$$

where  $z$  and  $t$  are the grain size ( $\mu\text{m}$ ) and the coating time (hour) respectively.

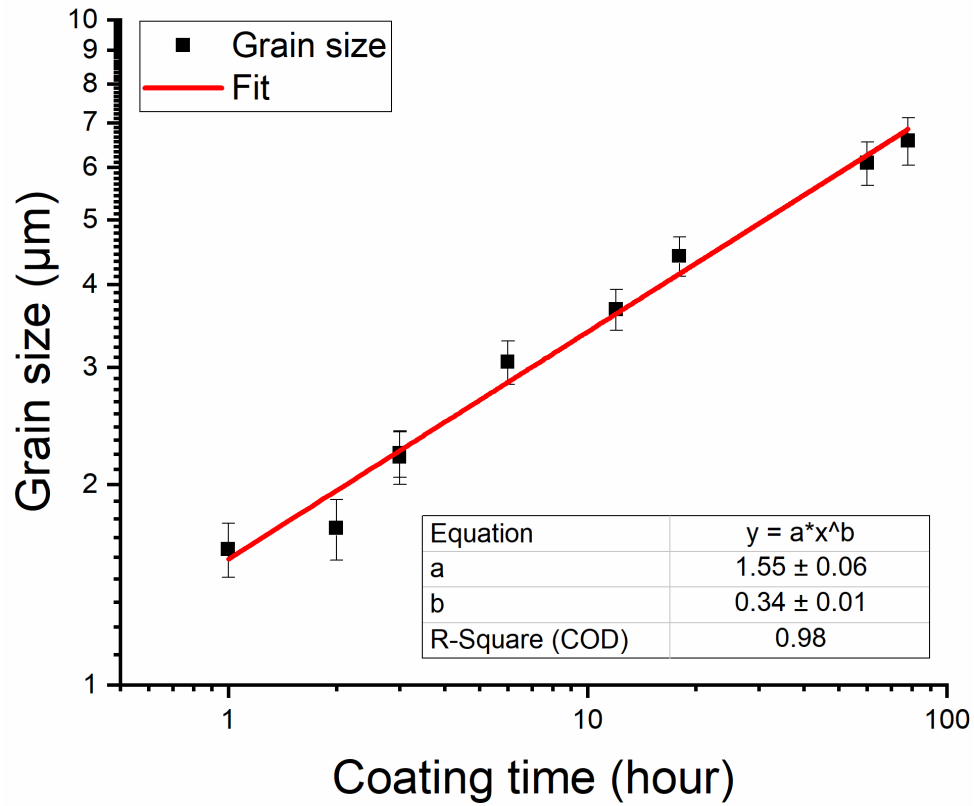


Figure 3.15: Grain size as a function of the coating time at 1200 °C.

Coated samples from each overcoat run were examined with the XPS sputter profile to reveal the composition and thickness of the coating. Tin concentration from the surface to  $\text{Nb}_3\text{Sn-Nb}$  interface, see Figure 3.16, was similar among the overcoat samples, and qualitatively resembles XPS depth profiles from the single-coat samples, as shown in Figure 3.12. A near-constant tin concentration exists from the surface through the thickness of the coating and ends with a steady drop near the  $\text{Nb}_3\text{Sn-Nb}$  interface. The thickness of the coating increased with each overcoat. The depth of the tin concentration plateau from the surface increased with each overcoat. Also, the depth over which tin concentration dropped at  $\text{Nb}_3\text{Sn-Nb}$  interface was found to increase with each overcoat.

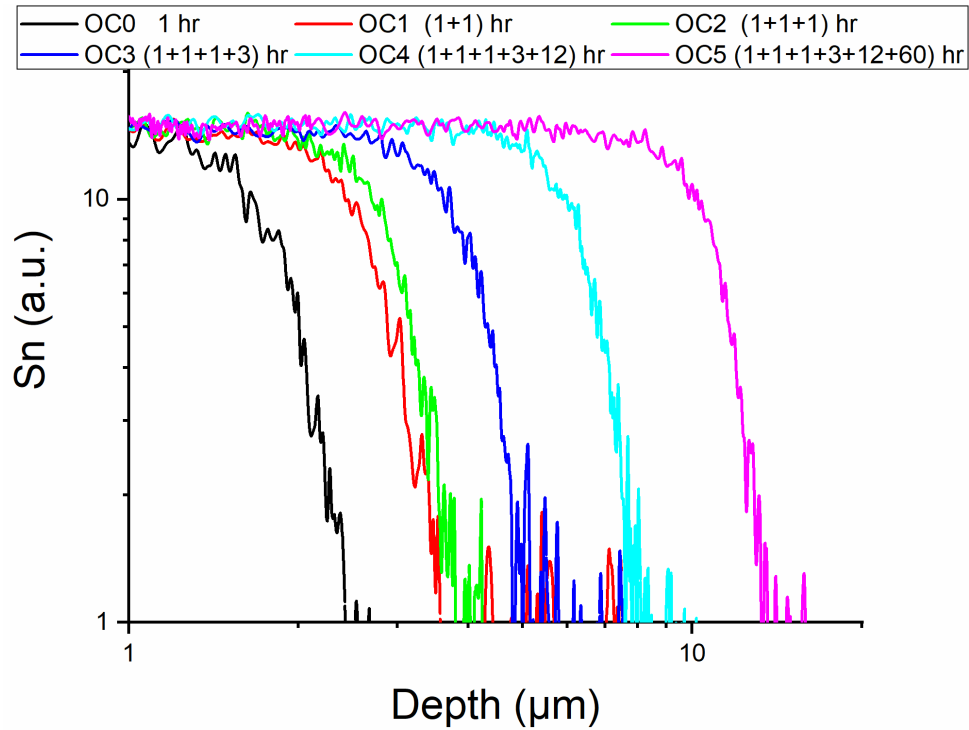


Figure 3.16: XPS depth profiles from the sequentially overcoated samples. OC1 to OC5 represents overcoat samples sequentially coated for 1, 1, 3, 12, and 60 hours, respectively.

Several cross-sectional EBSD images were captured from a sample for each overcoat experiment. EBSD data on samples coated for 1 hour at 1200 °C with  $\text{SnCl}_2$  shows columnar grain structures with deep *cupping*, a depression in the middle of  $\text{Nb}_3\text{Sn}$  grains at  $\text{Nb}_3\text{Sn}$ -Nb interface, see Figure 3.17(a). Grains are elongated next to  $\text{Nb}_3\text{Sn}$  grain boundaries into the Nb substrate in several locations. Following the first overcoat for one hour, see Figure 3.17(b), new grains were seen next to the intersection of  $\text{Nb}_3\text{Sn}$  grain boundaries and  $\text{Nb}_3\text{Sn}$ -Nb interface. Locations where no new grains were formed mostly showed cupping at the  $\text{Nb}_3\text{Sn}$ -Nb interface. Similar observations were made from the sample subjected to another one-hour overcoat, as shown in Figure 3.17(c). The next overcoat for 3 hours resulted in more grains at the interface with cupping in the larger grains, Figure 3.17(d). The black regions within the  $\text{Nb}_3\text{Sn}$  layer are thought to be cracks

produced during the specimen preparation. The EBSD cross-section obtained from a sample with an additional 12 hours of overcoat, Figure 3.17 (e), shows smaller grains at the interface and/or cupping. In some areas, two layers of smaller grains (marked with a black rectangle) were seen. EBSD image from the 60 hours overcoat sample is shown in Figure 3.17 (f). The longest coating resulted in large columnar grains traversing the thickness of the Nb<sub>3</sub>Sn layer. At the Nb<sub>3</sub>Sn-Nb interface, small Nb<sub>3</sub>Sn grains were always observed in between these columnar grains at the end of grain boundaries. Here almost all the grains had depressions at the Nb<sub>3</sub>Sn-Nb interface, that is, a thicker coating close to the grain boundaries.

Nb<sub>3</sub>Sn layer thicknesses were estimated from XPS depth profile data shown in Figure 3.16. Several EBSD and optical images collected on the representative overcoat samples from each experiment were also used to measure the layer thickness. Average layer thicknesses estimated from different characterization techniques are summarized in Table 3. The layer thickness from the XPS depth profile was defined as the distance between the surface and the depth at which the intensity of the Sn signal drops below 2%. The depth resolution of XPS, which by convention corresponds to the distance over which an 84% to 16% change in the maximum signal is measured [96, 97], was used to estimate the accuracy of the thickness value for each sample and is listed as the measurement error in Table 3.4. The discrepancy between the estimated thicknesses obtained from XPS sputter profiles and other measurements is expected because of the surface and interface roughness. Additionally, the preferential sputtering and the roughness induced by sputtering itself can impact the measurement resolution.

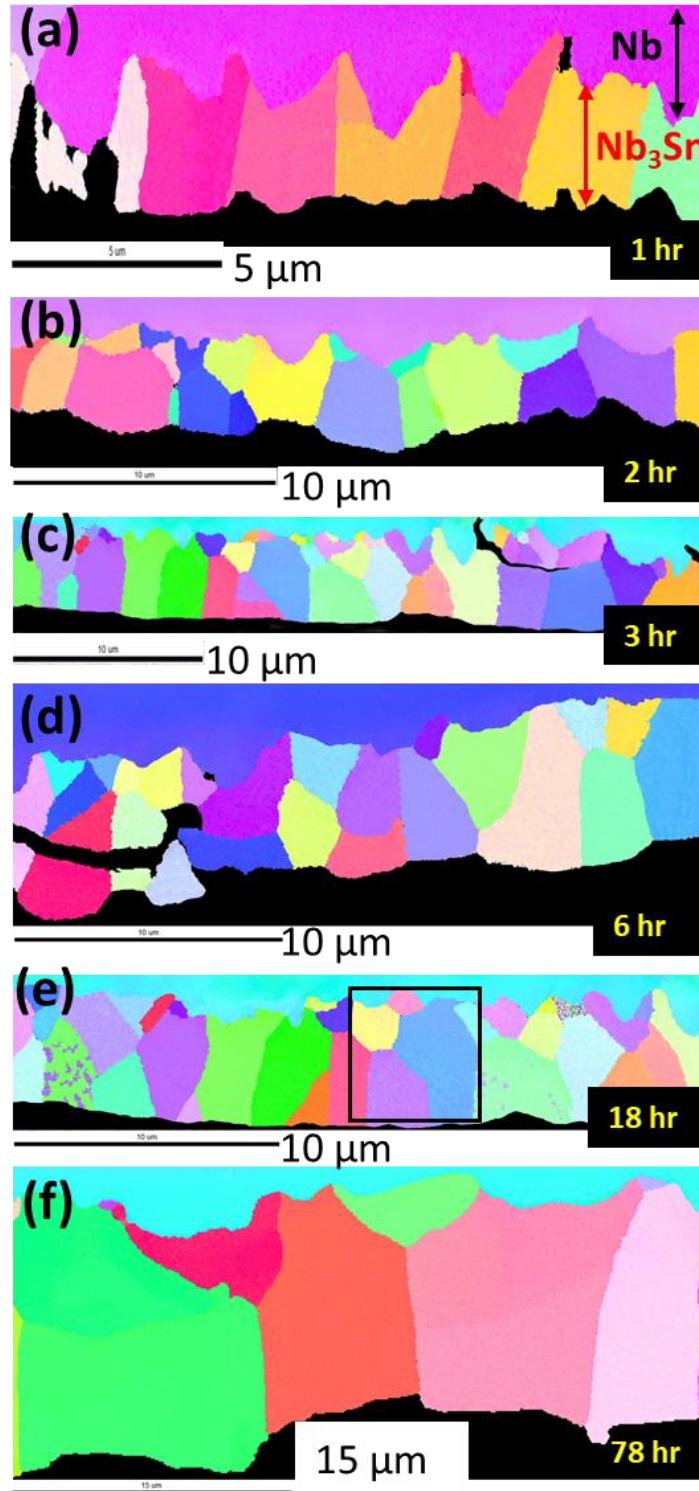


Figure 3.17: Cross-sectional EBSD images from sequential overcoat samples. Note that the different colors here are associated with different crystallographic orientations. Nb<sub>3</sub>Sn grains are significantly smaller than Nb grains, which are represented by a single color at

the top of each image, e.g., (a). The total coating time at 1200 °C is shown at the bottom right corner of each image.

Table 3.4: Estimated average thicknesses for the sequential overcoat samples using different characterization techniques.

Total coating time (h)	Thickness estimated from		
	XPS depth profile (μm)	EBSD images (μm)	Optical images (μm)
1	2.25±0.85	2.03±0.37	2.33±0.28
2	3.41±1.00	3.04±0.33	3.10±0.16
3	3.63±1.05	4.86±0.42	4.74±0.41
6	4.94±1.61	5.44±0.63	5.42±0.31
18	7.69±2.06	7.67±0.55	7.76±0.38
78	12.83±3.40	15.06±1.29	14.26±0.39

Estimated coating thicknesses as a function of the coating time are shown in Figure 3.18. Note that the time dependence of thickness follows a power law with an exponent close to 0.40 for data obtained from different characterization techniques. Compared to XPS and EBSD, thickness estimates from optical images are more accurate as they come from direct examination of cross-sections. Thickness measurements from optical images, as represented by equation (3.2) is considered here for further discussion.

$$y = (2.48 \pm 0.15)t^{0.40 \pm 0.02} \quad (3.2)$$

where  $y$  (μm) and  $t$  (hour) are layer thickness and total coating time respectively.

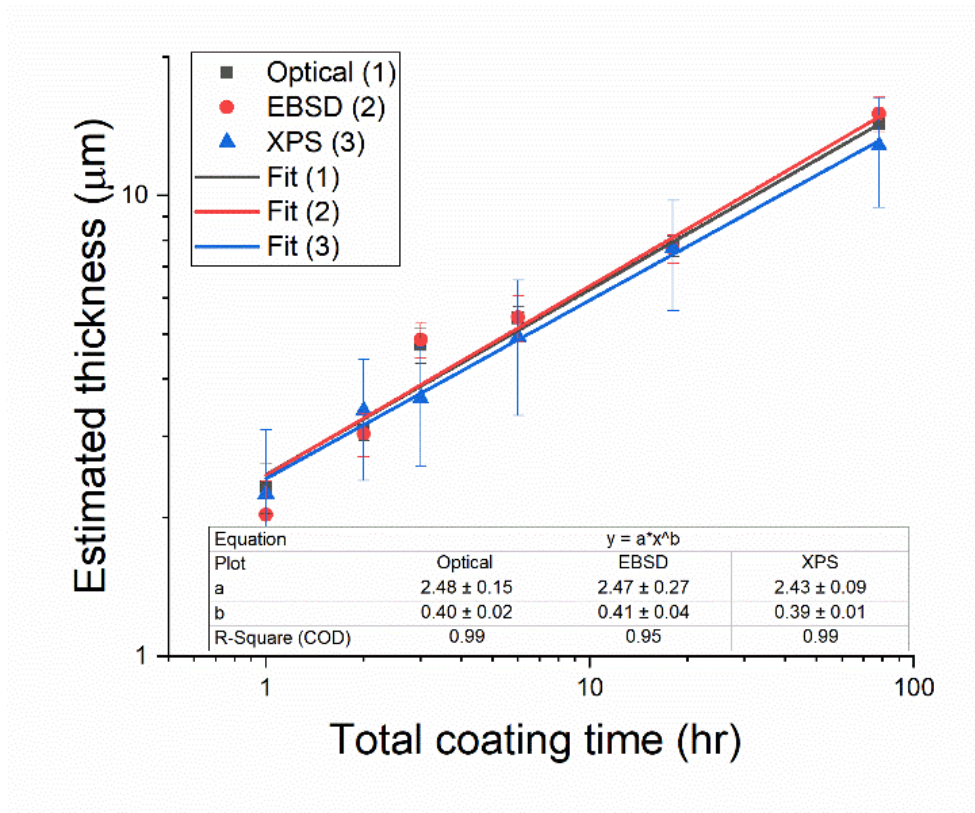


Figure 3.18: Thickness variation with coating time. Note that the error bars are the measurement errors tabulated in Table 3.4. Those errors were used as the weighting factors to fit the data using nonlinear least square fitting.

After 78 hours of the total coating time, the Nb<sub>3</sub>Sn layer appears to be one of the thickest coatings reported so far at the temperature range for the vapor diffusion technique. The thickest coated layer of 14 μm presented an opportunity to compare the Sn concentration obtained from the XPS depth profile to that obtained from EDS cross-sectional line scans. Following EBSD data collection, EDS line scans were performed on the thickest coated layer at three different locations, as shown in Figure 3.19(a) and Figure 3.19(b). The line scans start from the protective layer of platinum over Nb<sub>3</sub>Sn coating and run perpendicular to the surface until reaching into the Nb substrate. EDS line scans in Figure 3.19(c) show that Sn concentration starts to go up as it approaches the coating surface, and the concentration is almost constant throughout the coating thickness before

it starts to decline close to Nb-Nb<sub>3</sub>Sn interface. Compared with XPS data in Figure 3.16, where Sn concentration is constant up to ~9 μm from the surface, EDS scans show near-constant concentration up to ~14 μm for the thickest areas. Note that EDS data appears to show a gradual drop in Sn concentration from the surface to the reaction interface. Since XPS data shows no Sn deficiency on the Nb<sub>3</sub>Sn surface, the actual Sn concentration should be zero in the Pt layer and close to nominal in the Nb<sub>3</sub>Sn surface. The extended rise of Sn concentration at Pt-Nb<sub>3</sub>Sn interface is likely due to the interaction volume: the region of X-ray excitation sampled by the EDS instrument. The depth of X-ray generation is expected to be about a micron (section 2.1.2) for an accelerating voltage of 15 kV. The corresponding lateral spread should be well over a micron. It is seen that the rise of Sn concentration at Pt-Nb<sub>3</sub>Sn interface and its fall at the Nb<sub>3</sub>Sn-Nb interface look very similar. The spatial resolution of EDS is likely the leading cause of the extended Sn drop at Nb<sub>3</sub>Sn-Nb interface, while the actual Sn drop from nominal to zero happens over much shorter distances with a near-constant composition of tin throughout the coating layer.

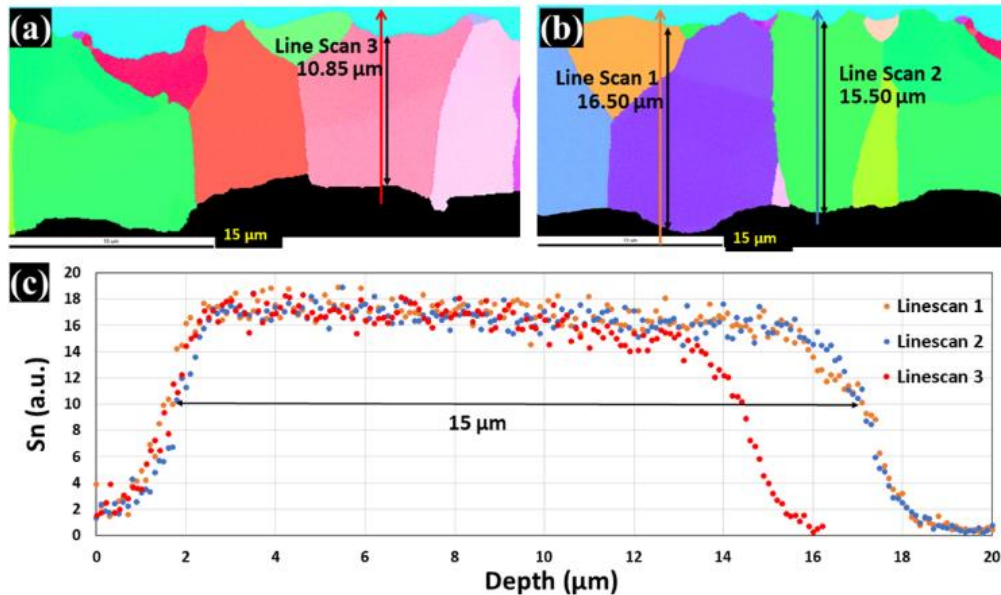


Figure 3.19: Locations of EDS line scans are shown in EBSD images (a) and (b). The measured Sn concentration along the scan line is shown in (c).

### 3.2.3 Growth kinetics

In the first overcoat experiment, single-coat samples were inserted into the coating chamber and coated again under the same conditions. The overcoat did not result in a new Nb<sub>3</sub>Sn layer either below or above the existing one. The existing grains grew transversely and laterally during each overcoat. Smaller grains occasionally observed at the Nb-Nb<sub>3</sub>Sn interface in single-coat samples frequently appeared in the overcoat sample, indicating a new grain formation, as shown in Figure 3.17(b). Note that smaller grains almost always formed at the end of Nb<sub>3</sub>Sn grain boundaries next to the Nb substrate, and they are comparatively smaller than the columnar grains seen in single-coat samples. Similar observations were made repeatedly for sequential overcoat samples. Furthermore, grain growth appeared faster next to Nb<sub>3</sub>Sn grain boundaries, where it intersects the substrate Nb, and less rapidly at the grain center. This can be seen as “*cupping*” at the base of many Nb<sub>3</sub>Sn grains, as shown in Figure 3.17(a). The appearance at the interface seems consistent with the concentration contour suggested in [98], reproduced in Figure 3.20. According to [99], an excess of diffusing atoms may build up in the vicinity of grain boundaries of polycrystalline compound layers adjacent to the other phase, resulting in interface roughening. These observations suggest the grain boundary diffusion as the primary mode for Sn transport to the Nb<sub>3</sub>Sn-Nb interface, where Nb<sub>3</sub>Sn forms.

Single-coat samples in the first overcoat experiment show several grains with V-shaped cupping at the Nb<sub>3</sub>Sn-Nb interface. Five subsequent overcoats for an additional 1, 1, 3, 12, and 60 hours produced similar cross-sections, including small grains at the interface and cupping in the large grains, but at a different scale. Grains grew both laterally and transversely with each overcoat. Note that triangular micron-sized grains appeared at the end of grain boundaries at the Nb<sub>3</sub>Sn-Nb interface after the final overcoat, Figure

3.17(f). These observations again indicate that the grain boundary diffusion primarily controls the growth process.

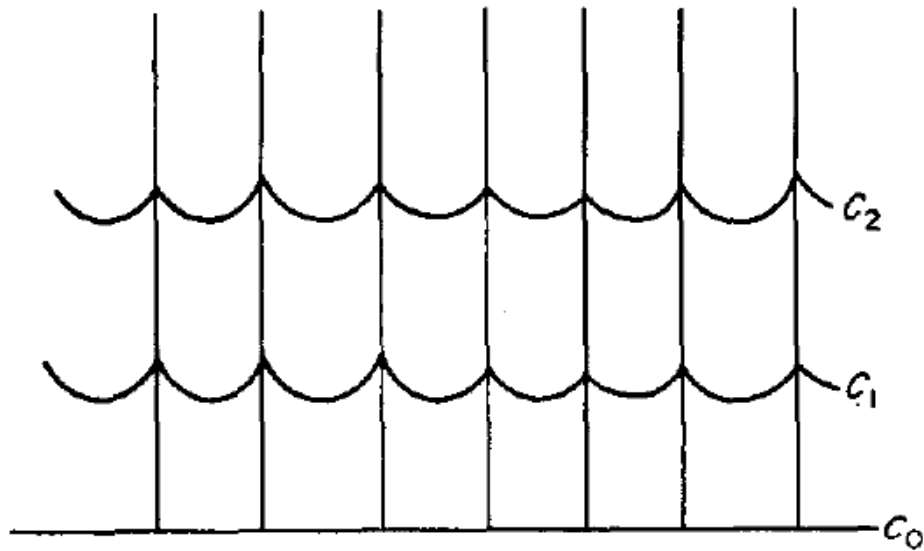


Figure 3.20: The concentration contour produced by grain boundary diffusion in a columnar structure, adapted from [30]. Note that for the vapor diffusion process,  $Nb_3Sn$  formation is simultaneously in progress.

Estimated coating thickness dependence on time is compared with similar measurements reported from Wuppertal University [12] in the log-log plot in Figure 3.21. Note that the coating preparation discussed in our work is very similar to the protocol followed there. Our growth exponent (0.40) was close to the one they reported (0.38), but the prefactor (specific growth rate at  $t=0$ ) was higher in our case. [Note that the actual Wuppertal data from [100] appears to have a growth exponent of 0.36 instead of 0.38].

The semi-log plot, Figure 3.22, shows the prefactor, reported here together with the prefactors reported by other researchers [49]. There is a considerable spread in measured prefactors. Our prefactor appears to be consistent with previously reported values when the data spread is taken into account.

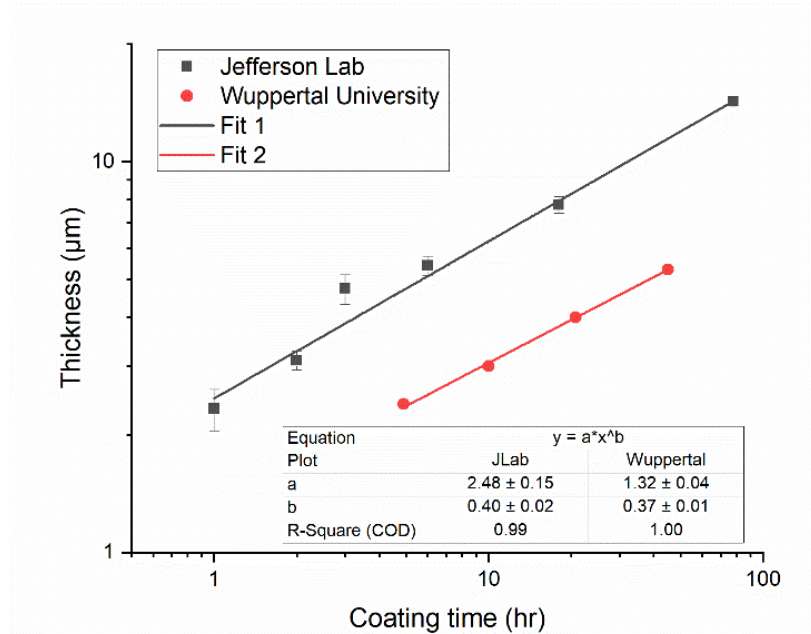


Figure 3.21: Growth kinetics observed in single-coat and overcoat samples compared to the Wuppertal data [12].

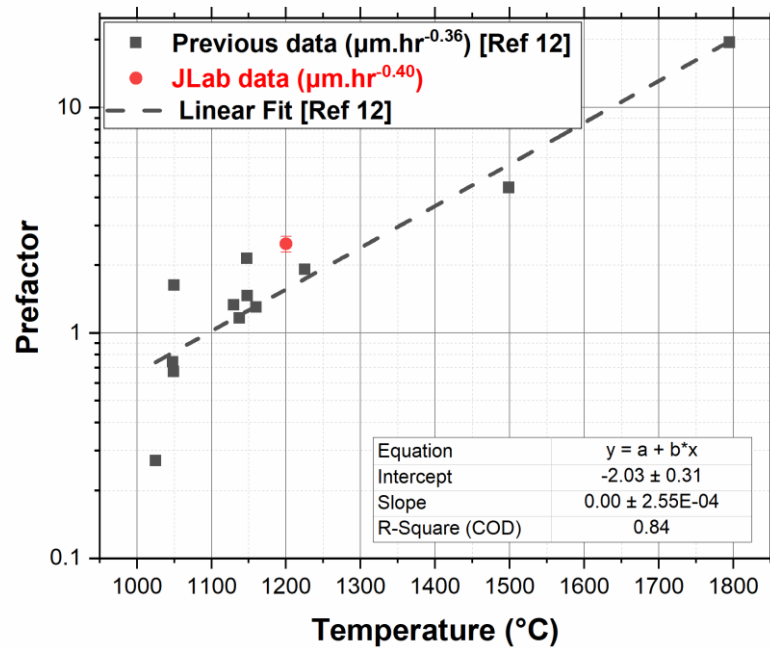


Figure 3.22: The reported values of prefactors at different temperatures. The prefactor value measured in the present study is shown in red. Data from other studies are reproduced from [49].

The higher specific growth rate, prefactor (2.48 vs. 1.377) in the present experiment probably stems from the higher coating temperature (1200 °C vs. Wuppertal's coating temperature of 1160 °C) and higher tin vapor pressure. The vapor pressure variation which primarily depends on the temperature and the surface area of the tin source, may explain the spread in the prefactor values for the similar coating temperature in Figure 9. Note that the vapor pressure of tin at 1200 °C is almost twice that of the vapor pressure at 1150 °C. It is expected that the coating growth rate  $k$  follows an Arrhenius dependence on temperature [101, 102]:

$$\ln k = -\frac{Q}{RT} + C \quad (3.3)$$

where  $Q$  and  $R$  are the activation energy and the ideal gas constant, respectively, and  $C$  is a constant. The dependence of the coating thickness on time may be expressed as,

$$d = k(T) t^n \quad (3.4)$$

where  $d$  is the thickness of the coating. Here the reported value for  $n$  varies between 0 to 1 for  $\text{Nb}_3\text{Sn}$  growth [23]. When  $n$  is equal to 0.5, it is the parabolic growth, which is expected for pure bulk diffusion. Similar growth is also expected for the coating growth via the grain boundary diffusion through a fixed array of grain boundaries [103]. Reported values of grain boundary diffusivity of tin in  $\text{Nb}_3\text{Sn}$  up to 800 °C are several orders of magnitude higher than the bulk diffusivity [94]

Coating thickness values obtained from 1–6 hours of coating (first four data points) are compared with that obtained from 3–78 hours of coating (last four data points) in Figure 3.23. The measured growth exponent,  $(0.49 \pm 0.09)$ , shows a parabolic relationship between the layer thickness and the coating time for a shorter coating up to 6 hours. The growth exponent declined to  $(0.37 \pm 0.02)$  for a relatively longer coating of 3–78 hours. This indicates that the coating growth is initially diffusion-controlled, but it slows down for longer durations. We suggest that with a higher density of grain boundaries (small  $\text{Nb}_3\text{Sn}$

grains) and a thinner coating (short diffusion length) in the beginning, enough tin is supplied to maintain the parabolic growth rate at Nb-Nb<sub>3</sub>Sn interface via bulk and grain boundary diffusion. The growth rate slows down for a longer coating time because of the reduction in grain boundary density (larger grains) and the thicker coated layers (longer diffusion length). It appears that the bulk diffusion in Nb<sub>3</sub>Sn essentially freezes and the grain boundary diffusion dominates for the longer coating times as suggested in [104].

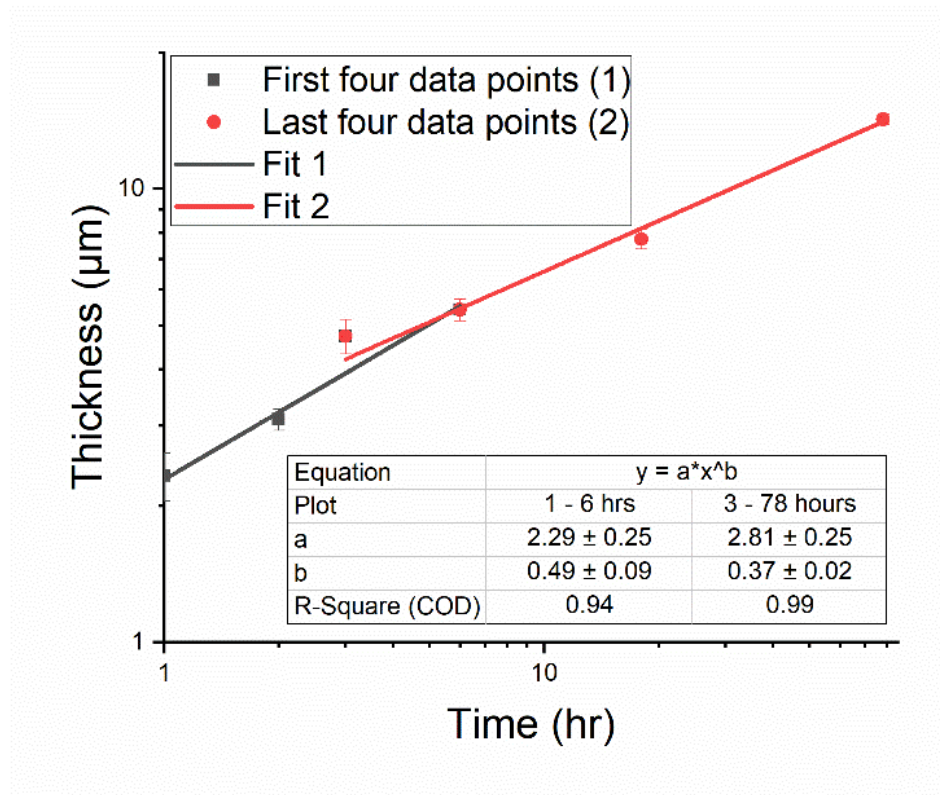


Figure 3.23: Growth kinetics observed in single-coat and overcoat samples. Two straight lines here represent growth kinetics for coating times of 1–6 hours and 6–78 hours.

Several researchers have reported growth exponent  $n$  close to 0.35 for Nb<sub>3</sub>Sn coatings prepared via different processes [90–93, 103]. Such deviation from the parabolic growth was mainly attributed to the grain boundary diffusion in the case of Nb<sub>3</sub>Sn layers prepared by the bronze process. The growth exponent of 0.35 measured by Farrel et al. for multifilamentary Nb<sub>3</sub>Sn was explained theoretically by grain boundary diffusion

combined with a dynamic grain growth [90, 91]. Other explanations for the slower growth rate included the multiphase diffusion during Nb<sub>3</sub>Sn formation, the reduced concentration of tin in the bronze matrix, Kirkendall void formation and the solution-dissolution process [93, 94]. The latter explanations may not necessarily apply to Nb<sub>3</sub>Sn coatings prepared by the tin vapor diffusion since we have never observed any phases other than Nb<sub>3</sub>Sn. A model for the A15 layer growth based on experimental results was also proposed by Reddi [105], who suggested a growth exponent between 0.25 and 0.5, when a significant grain growth is superimposed on the GB diffusion. An identical conclusion was drawn before by Baird [98].

The present data show a similar power law dependence for both the average grain size, Figure 3.15, and the thickness of the coating, Figure 3.18, indicating grain boundary diffusion plays a major role during the growth process. With a substantial increase in the grain size, the number of diffusion paths is reduced, depleting the tin supply at the growth interface. The length of the diffusion path also increases with increasing thickness of the coating. Comparing the average grain size before and after the overcoat experiment (reported before) shows that the grain growth rate varied inversely with pre-overcoated grain size, supporting a faster growth with a higher density of grain boundaries [36].

Within the framework of the grain boundary diffusion model, it is possible to understand the commonly observed patchy regions. Patchy regions, Figure 3.24, are thin regions in the coatings also reported by other researchers [106]. Although patchy regions have been observed commonly, the cause of their formation is not yet established. It is believed that patches form in areas where the nucleation is not as sufficient. The use of a nucleation agent (e.g., SnCl<sub>2</sub>) and/or anodization of the Nb substrate before the coating were found to be advantageous to reduce or eliminate patchy regions [17, 70, 72, 84], which is consistent with our observations. Typically, patches are seen to form in the early

stages of coating and are often associated with low tin fluxes as discussed in the previous section 3.1.

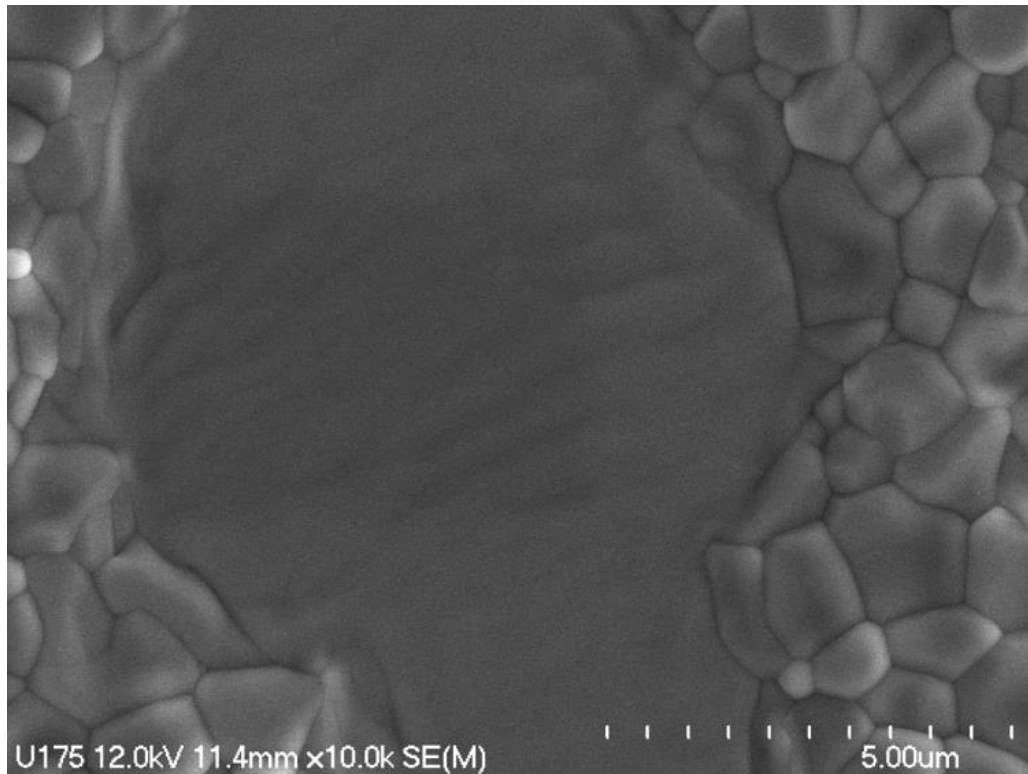


Figure 3.24: SEM image of a patchy area observed in Nb<sub>3</sub>Sn coated sample.

EBSD analysis shows that patchy regions are monocrystalline Nb<sub>3</sub>Sn [63]. An SEM image of a patchy region is shown in Figure 3.25(a). The corresponding EBSD image in Figure 3.25(b) depicts patches as large monocrystalline Nb<sub>3</sub>Sn grains, as indicated by the single-colored regions. Cross-sectional SEM and EBSD images are shown in Figure 3.25(c and d). The patch thickness was measured to be  $194 \pm 59$  nm, roughly an order of magnitude thinner than that of a well-coated area:  $1.6 \pm 0.10$   $\mu$ m. It should be noted that such a thin coating layer could adversely impact RF performance because the RF penetration depth for the Nb<sub>3</sub>Sn material is on the order of 100 nm [107].

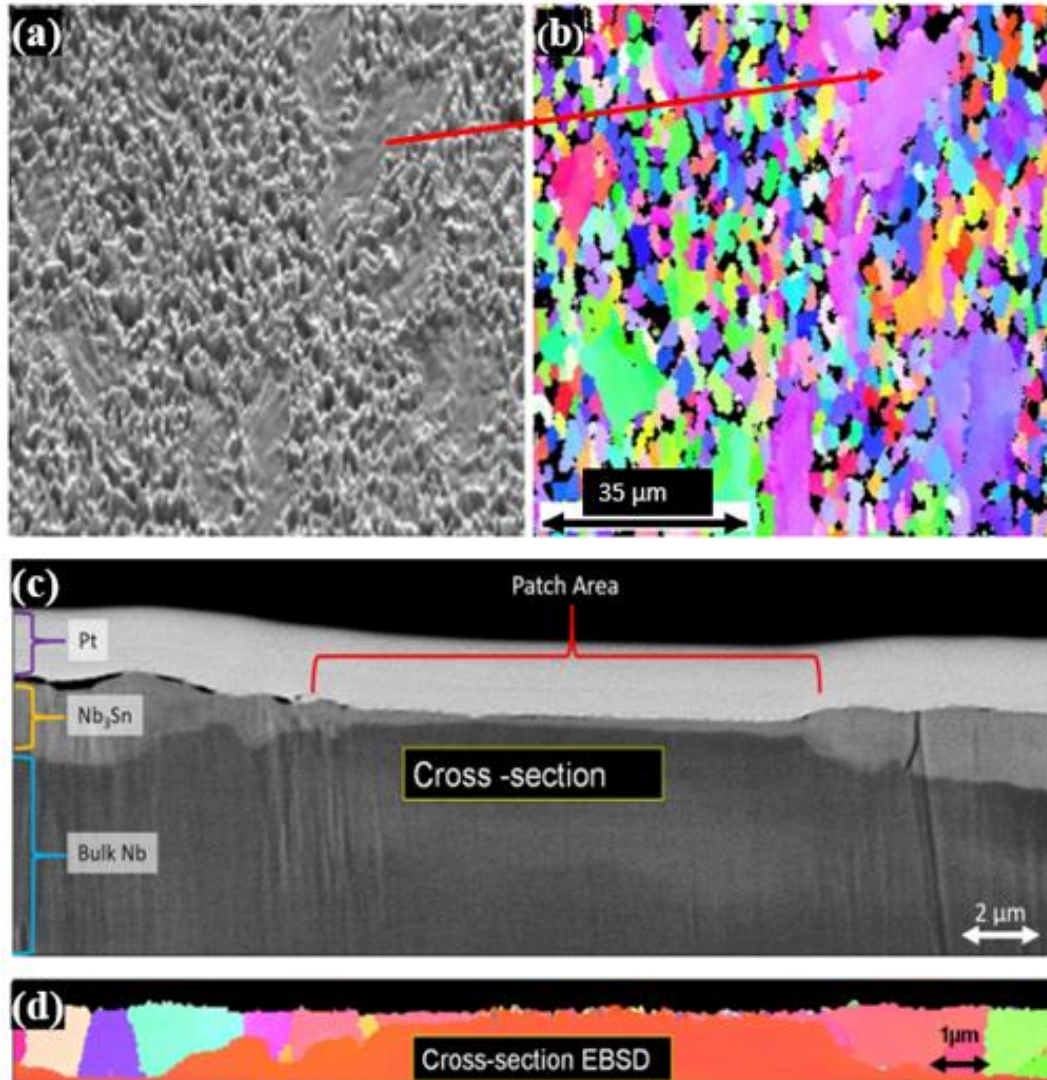


Figure 3.25: (a) SEM image and (b) the corresponding EBSD image of a patchy region. Black areas arise from a combination of grain topography and the low electron beam incident angle (20°). (c) SEM image of FIB cross-section and (d) the corresponding EBSD image of the patchy area.

Note that this substrate was nanopolished prior to coating, that is, the surface roughness before the coating was on the order of a few nanometers. The bulk Nb below the thin Nb<sub>3</sub>Sn coating is thicker than the Nb on either side of the patch where “normal” Nb<sub>3</sub>Sn coating is located, see Figure 3.25(c or d). That is the bulk Nb under the patch was consumed less than elsewhere. Since the starting Nb surface was nanopolished, the

evident roughening indicates that tin diffuses downward into the Nb bulk where it reacts to form a Nb<sub>3</sub>Sn layer at the Nb<sub>3</sub>Sn-Nb interface. Subsequent coating growth progresses downward, consuming Nb as Sn is transported through the Nb<sub>3</sub>Sn layers via grain boundaries to the Nb<sub>3</sub>Sn-Nb interface. Tin is a faster diffusing species in the Nb<sub>3</sub>Sn layer than Nb [102]. Patchy regions are deprived of grain boundaries to facilitate Sn-flux to the growth interface underneath. As discussed above, coating growth is significantly hindered, so the patchy area, once it forms, grows more slowly than grains elsewhere, leading to a thin film compared to the thicker coating in neighboring regions.

### 3.2.4 Grain growth

Nb<sub>3</sub>Sn coating produced by the vapor diffusion process typically displays equiaxed grains (Figure 3.14), which results in a lognormal grain size distribution on the surface [108]. As the coating layer thickness increases with the coating time, Nb<sub>3</sub>Sn grains grow as well. Observed grain structures for each overcoat appear self-similar. Normal grain growth is defined as the uniform increase in the average grain size, due to grain boundary migration. The kinetics of the normal grain growth is generally represented by [109, 110],

$$\langle R \rangle^n - \langle R_0 \rangle^n = \gamma t \quad (3.5)$$

where  $\langle R_0 \rangle$  and  $\langle R \rangle$  are the average grain sizes at time 0 and t respectively; n is grain growth exponent;  $\gamma$  is the kinetic coefficient. It can be expressed as,

$$\gamma = \gamma_0 \cdot \exp\left(\frac{Q}{kT}\right) \quad (3.6)$$

where Q is the activation energy for grain boundary mobility, and  $\gamma_0$  is a constant.

The grain growth exponent (Figure 3.15) measured here was  $n \approx 3$  indicating the normal grain growth. The estimated grain size growth is comparatively slower than the thickness growth, see equation 3.1 and 3.2. The grain growth results in the reduction of grain boundaries. The reduction in the number of grain boundaries due to grain growth

reduces the number of diffusion channels for tin transport to the growth interface and thus imposes the comparable exponent on the layer growth dependence. The prefactors in the time dependence are different between grain growth and layer growth because different diffusion/reaction rates drive them. The layer growth prefactor is defined by the Sn diffusion rate across the grain boundary and the reaction at the Nb<sub>3</sub>Sn-Nb interface. The grain growth prefactor is driven by the Nb/Sn diffusion across the grain boundaries between the grains.

Very few studies have been reported connecting grain growth with layer growth kinetics. According to the dynamic grain size model proposed by Farrel et al. [91], there exists a relation between the layer thickness and the grain growth exponents for substantial growth in grain size:

$$z = \beta(T)t^{0.5(1-m)} \quad (3.7)$$

where  $m$  and  $z$  represent the grain growth and the layer thickness exponents, respectively;  $\beta(T)$  is a temperature-dependent prefactor. For  $m \sim 0.34$ , equation (3.7) gives  $y \propto t^{0.33}$ , which is close to what we obtained experimentally.

Regarding normal grain growth, two main mechanisms of the grain growth are suggested in the literature: GB curvature driven and rotation-coupled grain coalescence (RCGC) [111, 112]. Grain growth takes place via migration of the grain boundaries toward their center of curvature, driven by the decrease in energy associated with the reduction in the length of the grain boundaries. In the RCGC model, grain rotation takes place, resulting in the coalescence of nearby grains, which eliminates the common grain boundary between them. Since both mechanisms can be responsible for grain growth, it is challenging to discern which is dominant for a given material. In the longer coating run of 60 hours, several locations with relatively longer grain boundaries were noticed. Those grain boundaries were pronounced, faded, or almost disappeared between different

locations as shown in Figure 3.26, pointed by arrows. Note that the neighboring grains with a common grain boundary discussed here appear modestly elongated. This observation is consistent with the occurrence of RCGS. Observations made here seem very similar to the grain-coalescence event suggested in [111, 112] as shown in Figure 3.27.

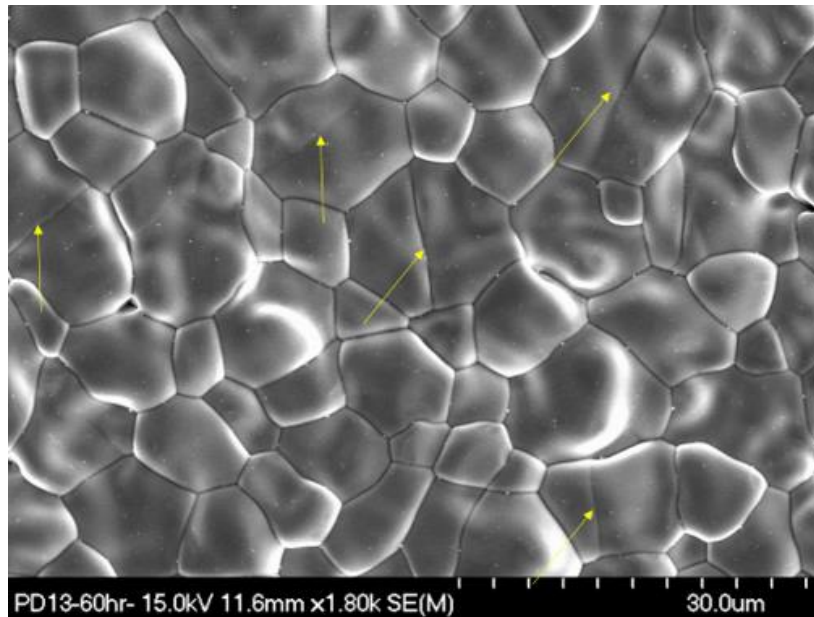


Figure 3.26: SEM image from sample coated for 60 hours at 1200 °C. Note the grain boundaries indicated by yellow arrows.

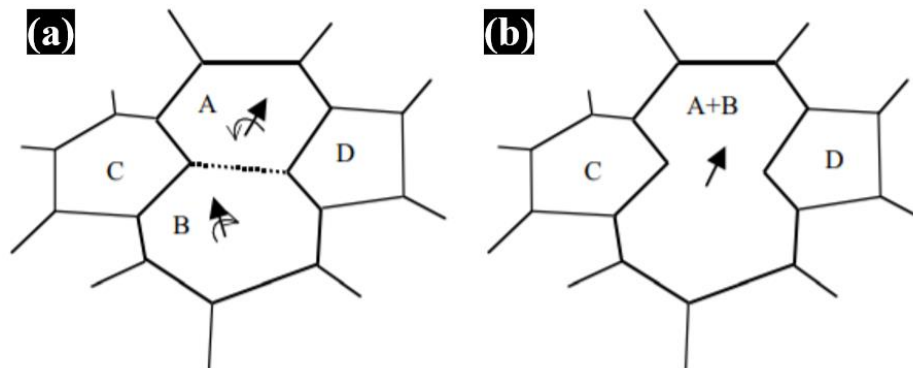


Figure 3.27: Elimination of two triple junctions by a single rotation-coalescence event, adapted from [111]. Topology before (a) and after (b) the coalescence of grains A and B.

### 3.3 Conclusions

Nb<sub>3</sub>Sn coatings prepared by varying several different coating parameters were analysed. It has been found that it is essential to provide sufficient Sn flux (~ 200 atoms nm<sup>-2</sup> min<sup>-1</sup> or higher) to ensure the coating uniformity. Due to lower tin vapor pressure, the coating temperatures of (900–1000) °C are more prone to produce patchy regions with irregular grain structures compared to those at higher temperatures. Besides the coating temperature, coating durations are important parameters that could significantly affect the properties (grain size, thickness, roughness) of Nb<sub>3</sub>Sn coating. Longer deposition time produces thicker coating and larger grain size. Larger grain size correlates with increased surface macro-roughness and thickness of the coating. A similar coating composition was found independent of the deposition temperature within the accuracy of the XPS detector. NP samples showed patches more frequently than other samples which could potentially result from the higher mobility of tin on the smooth surface. Pre-anodization of the substrate reduced the occurrence of non-uniformity significantly for any given coating condition.

Results from the overcoat experiments indicate that tin primarily diffuses towards the Nb<sub>3</sub>Sn-Nb interface through the grain boundaries, resulting in Nb<sub>3</sub>Sn growth into the Nb bulk. The observed non-parabolic growth is consistent with the significant grain growth, which is superimposed on the grain boundary diffusion. The grain size growth can also be fitted with a power law. Fits to the grain growth and thickness growth show that the grain growth rate is slower than the thickness growth rate. Nb<sub>3</sub>Sn layers produced in overcoat experiments seem similar to the continuous layers obtained in the single-coat experiments. Patchy regions in Nb<sub>3</sub>Sn coatings are large single crystalline grains. They are significantly thinner due to fewer grain boundaries available for tin transport.

So far, we discussed the results obtained from sample studies. These studies provided crucial insights into the growth and properties of  $\text{Nb}_3\text{Sn}$ . The larger volume can pose additional challenges to coat and characterize the coating inside a practical SRF cavity. It is essential to study samples that are coated with the cavity to recognize and mitigate those challenges. It can greatly help to understand the limiting factors to the attainable performance of the cavity and could provide pathways to performance enhancement. The study of witness samples and the cutouts from the coated cavity are necessary to correlate material properties with the performance of  $\text{Nb}_3\text{Sn}$ -coated cavities. The following chapter presents studies of witness samples and cutouts from a  $\text{Nb}_3\text{Sn}$ -coated cavity to understand the growth of  $\text{Nb}_3\text{Sn}$  coating inside a cavity, and to correlate material properties with RF performance of  $\text{Nb}_3\text{Sn}$ -coated cavities.

## CHAPTER 4

### **Studies of Samples Coated with SRF Cavity**

Limiting RF fields and the best quality factors of the state-of-the-art Nb<sub>3</sub>Sn cavities are lower than the predicted limits for the ideal Nb<sub>3</sub>Sn [19, 107]. The accelerating gradients are constricted below about 100 mT that corresponds to less than 25% of the theoretical superheating field (~400 mT). RF limits in Nb<sub>3</sub>Sn-coated cavities seem to be caused not by the intrinsic RF properties of Nb<sub>3</sub>Sn superconductor, but by “extrinsic” factors such as localized defects in Nb<sub>3</sub>Sn coatings. Research efforts are presently focused on the characterization of such defects, understanding their formation, and eventually, their reduction or elimination, e.g., see [35, 113, 114]. Large surface area of RF cavities (e.g., ~0.1 m<sup>2</sup> for a 1.5 GHz single-cell cavity) can experience variation in the Nb<sub>3</sub>Sn growth environment, which leads to variation in film structure throughout the surface. Several factors, including the geometry, orientation, distance from the Sn source, contamination inclusion, Sn consumption, residual Sn at the termination of the process, etc. affect coating growth and could result in defect formation. Understanding these technical aspects can guide the improvements in the coating protocol, resulting in better cavity performance. It is important to correlate the coating defects and their formation inside a cavity to RF performance, which will lead to improvements in the coating process and reduction in the number of defects and their severity.

The best approach to correlate the materials properties with RF performance would be to examine samples cut from a coated cavity after RF testing. Although it provides an excellent opportunity to examine the actual cavity coating, it is not always possible to dissect cavities because of the cost, effort, and the time needed to prepare and analyze cavity cutouts. An alternative approach would be to coat witness samples along with each SRF cavity and correlate sample analysis to RF test results. The first part of this chapter will present the analysis of RF losses and materials characterization of cutout samples from a coated cavity. Studies of witness samples linked with the coating process and RF performances of single-cell and multi-cell cavities are discussed afterwards.

## **4.1 RF and material analysis of cutouts from a Nb<sub>3</sub>Sn-coated single-cell cavity**

This study investigated lossy regions from a coated cavity which were identified using JLab thermometry system during the RF testing. The lossy regions of interest were cut out of the cavity after the test and inspected with several characterization techniques.

### **4.1.1 Cavity Coating**

“C3C4” was a 1.5 GHz single-cell cavity made from high purity ( $\approx 300$ ) fine-grain Nb. It was subjected to buffered chemical polishing (BCP) using a solution of 49% HF, 70% HNO<sub>3</sub>, and 85% H<sub>3</sub>PO<sub>4</sub> in the ratio of 1:1:2 for removal of about 20  $\mu\text{m}$  inside and 5  $\mu\text{m}$  outside. It then received high pressure rinsing (HPR) with ultra-pure water, was assembled, and evacuated before the baseline test at 2 K. The cavity was limited by high field Q-slope at  $E_{acc} \approx 27$  MV/m in the baseline test [107]. The low field quality factor was about  $1.6 \times 10^{10}$  at 10 MV/m. After the baseline test, the cavity was removed from the test

stand in the cleanroom, high pressure water rinsed, and allowed to dry in the cleanroom. For the  $\text{Nb}_3\text{Sn}$  coating, Sn and  $\text{SnCl}_2$  were packaged in niobium foil. Three packages contained  $1 \pm 0.1$  g of Sn each and six packages contained  $0.5 \pm 0.05$  g of  $\text{SnCl}_2$  each. These packages were placed inside the cavity onto the niobium foil covering the bottom flange. The top flange of the cavity was covered with Nb foil as well. The cavity was assembled in the cleanroom for coating and double bagged in plastic bags before being transferred to the thin film lab. The cavity was then coated following a typical procedure (500 °C for 1 h for nucleation, then, 3 h of coating at 1200 °C), as described in section 1.2.7. It was the first cavity coated in the newly commissioned furnace that was upgraded later. In Figure 4.1(a) the cavity is shown sitting on the table after removal from the insert. When the Nb cover foils were removed, several features were observed: discoloration was seen on NbTi flanges (b), residues were observed on the bottom Nb cover, and on the Nb foils that contained Sn and  $\text{SnCl}_2$  (c). Further, Sn condensation was seen on the top foil (d).



Figure 4.1: Cavity C3C4 after the coating run. Note discoloration on the NbTi cavity flange (b) and 'tin' droplets on the niobium foil from the cavity top flange (d).

### 4.1.2 Optical Inspection

After the coating, the cavity interior was optically inspected with a KEK-style optical inspection bench [115]. The optical inspection of C3C4 revealed complete coverage of coating on the surface. In one place at the equator area of C3C4, we found several  $\sim 100 \mu\text{m}$ -size features, Figure 4.2 (marked with red ellipses).

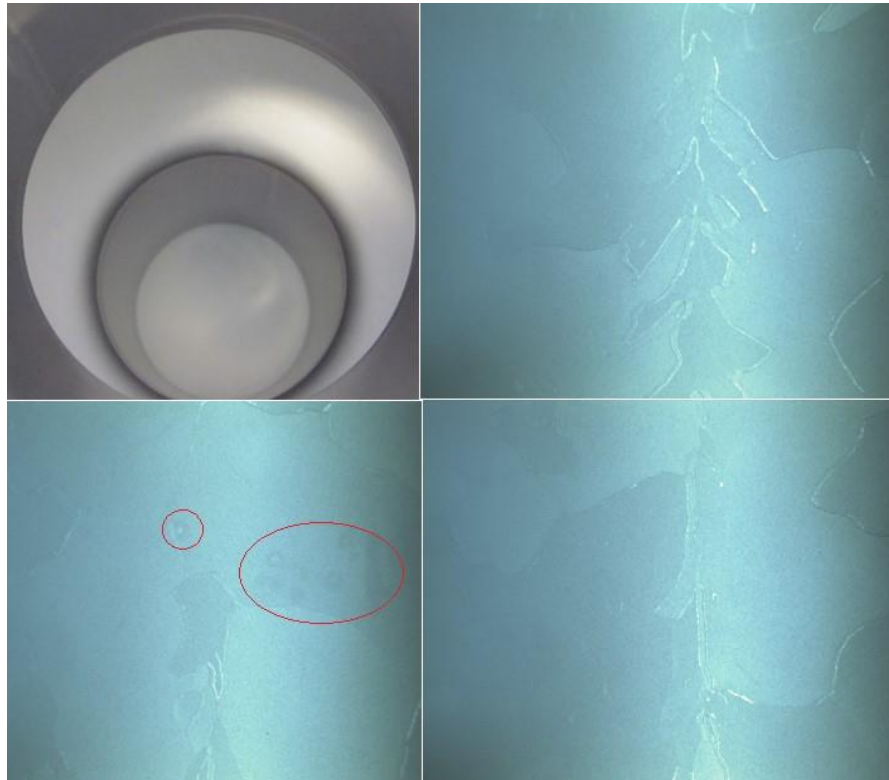


Figure 4.2: Optical inspection pictures of C3C4. (a) shows the coated surface of the cavity viewed via one of the beam tubes. (b) and (d) show characteristic equatorial weld regions of the coated cavity. (c) shows an equatorial region with several observed unusual features marked with red ellipses.

### 4.1.3 RF Test Results

After optical inspections, the cavity was RF tested at 4.3 K and 2.0 K. Typically, four Lakeshore DT-670 diodes were attached to the cavity to monitor the temperature

spread across the cavity during cooldowns: one diode attached to the bottom beam tube, one to the bottom half cell, one to the top half cell, and the last diode was attached to the top beam tube, 90 degrees apart azimuthally each. A network analyzer was used to monitor the resonance frequency and the quality factor (based on 3 dB measurement) of the cavity during cooldowns. The superconducting transition temperature of C3C4 was found to be  $17.9 \pm 0.25$  K. We did not observe any transition at 9 K, which indicates complete  $\text{Nb}_3\text{Sn}$  coverage on the Nb. After coating, the cavity performance was limited by a strong slope in  $Q_0$  at low fields at both 2.0 and 4.3 K helium bath temperature, Figure 4.3. The cavity was then re-tested with a temperature mapping array installed around the cavity. The  $Q_0$  vs.  $E_{acc}$  curve was similar, and the cavity was limited again at low gradients by a strong Q-slope. The low-field  $Q_0$  was better in the re-test, which is attributed to a different cooldown condition. Due to the higher low-field quality factor, a “knee” at about  $E_{acc} = 4$  MV/m is more evident than in the first test.

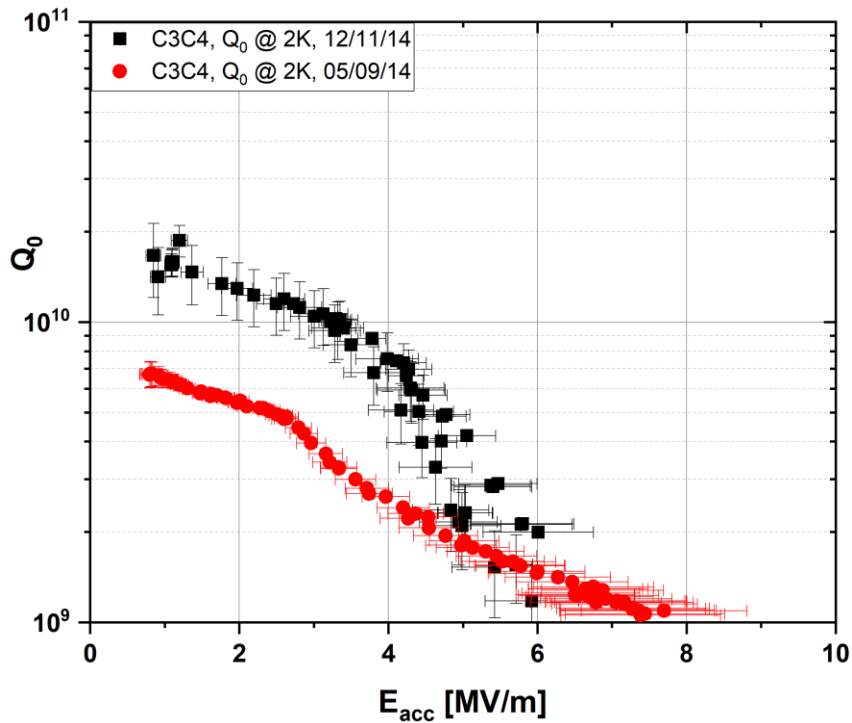


Figure 4.3:  $Q_0$  vs.  $E_{acc}$  for cavity C3C4.

During the latest test, temperature maps of the cavity surface were acquired at different field levels with the JLab temperature mapping system [116]. The system is comprised of 36 boards surrounding the cavity at the equally spaced interval, as seen in Figure 4.4[left]. Each board has 16 temperature sensors mounted on spring-loaded pins that push against the outer surface of the cavity, Figure 4.4 [right]. The temperature difference between the outer cavity surface and the Helium bath at the highest gradient showed three locations of strong heating at (15, 3), (7, 8), and (2, 7). The X-axis and Y-axis here represent board number and sensor number, respectively. For example, (15, 3) represents the location at board 15 and sensor 3. Sensor 1 is at the top iris, sensor 16 at the bottom iris and sensor 8 is at the equator. To assess the heating in other areas, the maximum of the color scale is reduced to 20 mK in Figure 4.5. The three hottest areas mentioned above are now off scale and became white squares. The white square at (26, 5) is an artifact of a malfunctioning sensor. The areas which were cut out are marked with red lines. The number next to the marked areas indicated the number assigned to the extracted sample. This temperature map shows that the heating on the surface is not uniform, with some distributed areas, e.g., at (35, 7), showing more heating than others, e.g., (29, 7). This temperature map was sectioned into areas with different heating behavior to guide the extraction of characteristic samples from different locations.

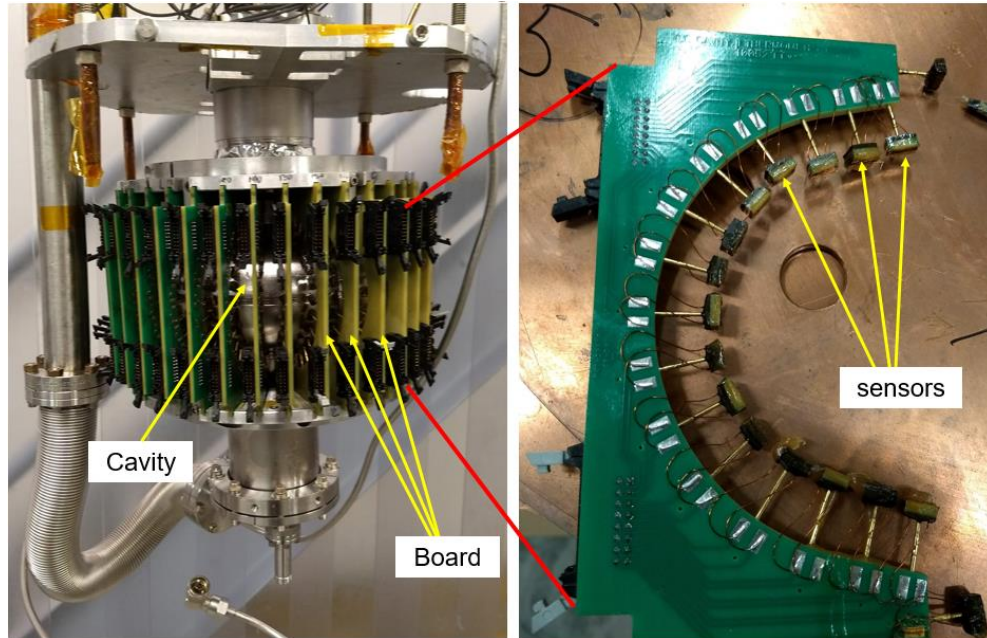


Figure 4.4: Temperature mapping system on a single-cell cavity [left]. The image to the right shows a board with temperature sensors.

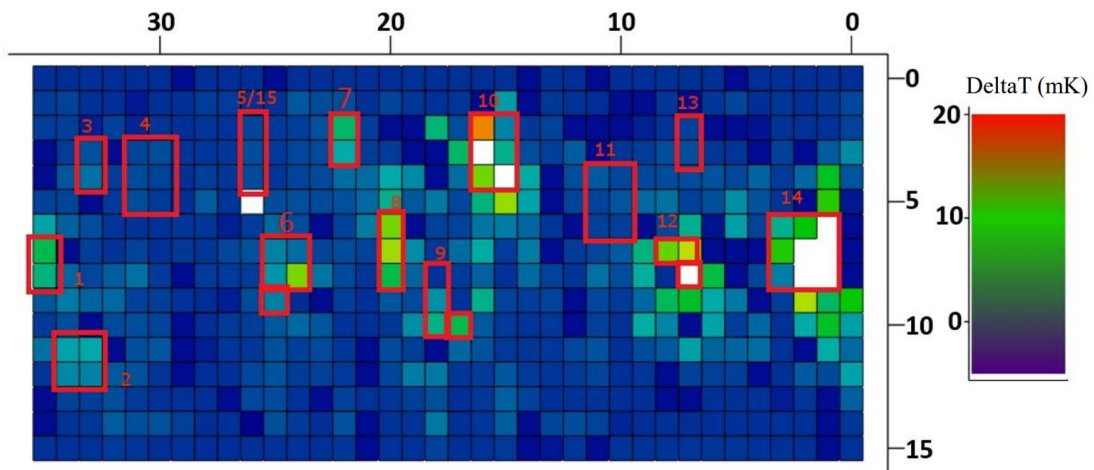


Figure 4.5: Temperature map of C3C4 at  $E_{acc} = 6$  MV/m shows the temperature increase on the outer cavity surface due to RF fields.

#### 4.1.4 Sample Extraction

After the RF test with temperature mapping, the outside surface of the cavity was marked with an engraver according to the temperature map in Figure 4.5. Each area

marked for extraction was encircled with engraver roughly following the contour of the thermometers. Several samples were then milled out with a 3/32 two-flute OSG Exomini TiN-coated end mill running at 3200 rpm as illustrated in Figure 4.6. The cut was cooled with helium gas flowing through 1/4" Tygon tubing. The helium gas nozzle was set approximately 5 cm from the end mill. The temperature of the niobium surface at the cut was checked with an infrared thermometer and never exceeded 40 °C during milling. During the milling, attempts were made not to cut through, but to leave a thin layer of material, to reduce contamination and damage to the internal surface from the milling process. This was not always possible due to cavity curvature, but some material was left when the milling was finished. The samples were then removed with pliers and de-burred.

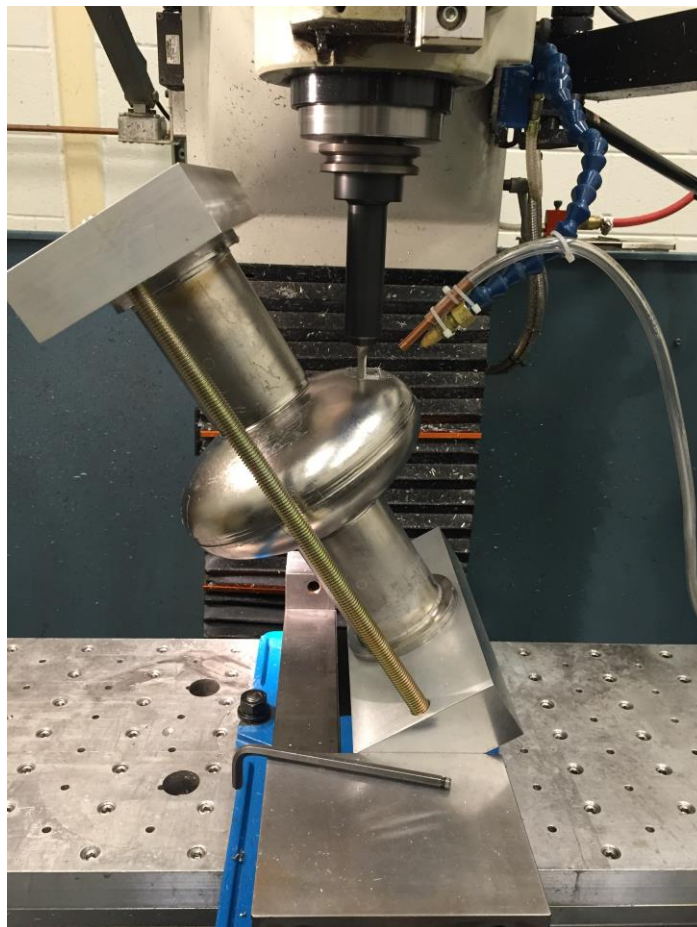


Figure 4.6: Setup used to mill out marked areas from the cavity C3C4 noted in Figure 4.5.

The samples were rinsed with acetone, then with methanol, and dried with ionized nitrogen. The samples were then ultrasonically cleaned in an ultra-pure water bath with 2% of micro-90 followed by ultra-pure water rinse. The samples were rinsed again with acetone, then methanol, and finally dried with ionized nitrogen. Figure 4.7 shows a photo of sample #14 before surface analysis. The edges of the samples were inspected for cutting artifacts with SEM. The artifacts included cracks and contamination largely localized near the edge of each cutout. The appearance of cracks and contaminants was consistent with the inference that these features developed during the cutting process. An example of such artifacts is shown in Figure 4.8. Cracks were found to have a preferential direction and were intergranular, spreading up to several hundreds of micrometers. These cracks are about 100 nm wide extending all the way to the niobium substrate, as shown in Figure 4.9. Contamination was mostly the pure niobium that was probably transferred during the cutting process. Traces of Al and Cu, found occasionally, were confirmed to be derived from the tooling used to prepare cutouts. C and O, which are common handling contaminants, were also observed.

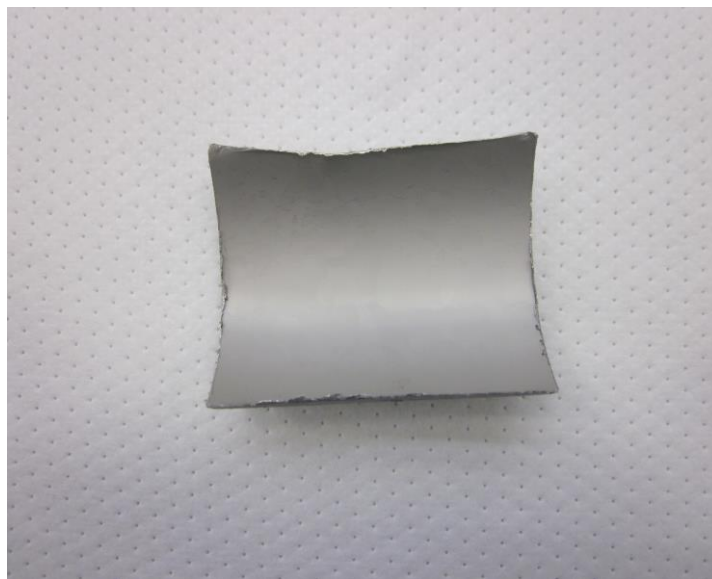


Figure 4.7: Sample #14 (CVT14) following each cleaning step prior to the analysis.

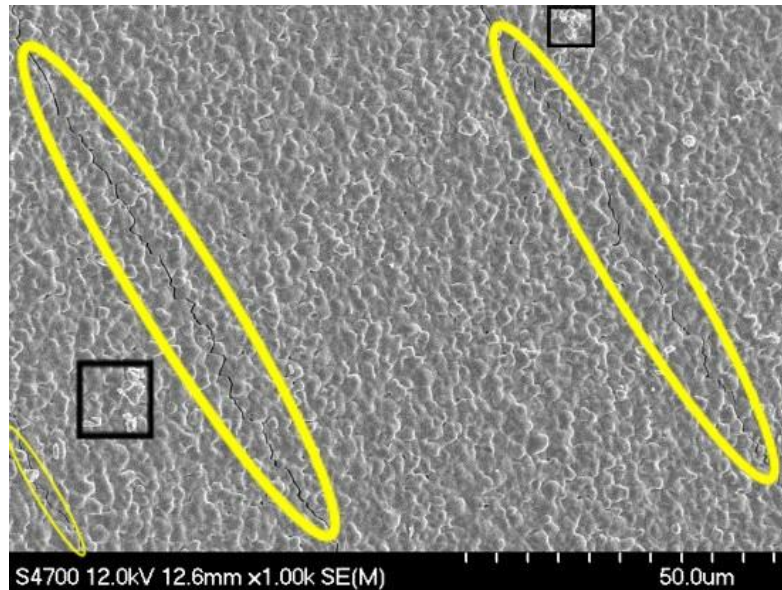


Figure 4.8: Cutting artifacts in CVT8. Note that the cracks are aligned in the same direction. Some traces of contamination can be seen, which was found to be niobium.

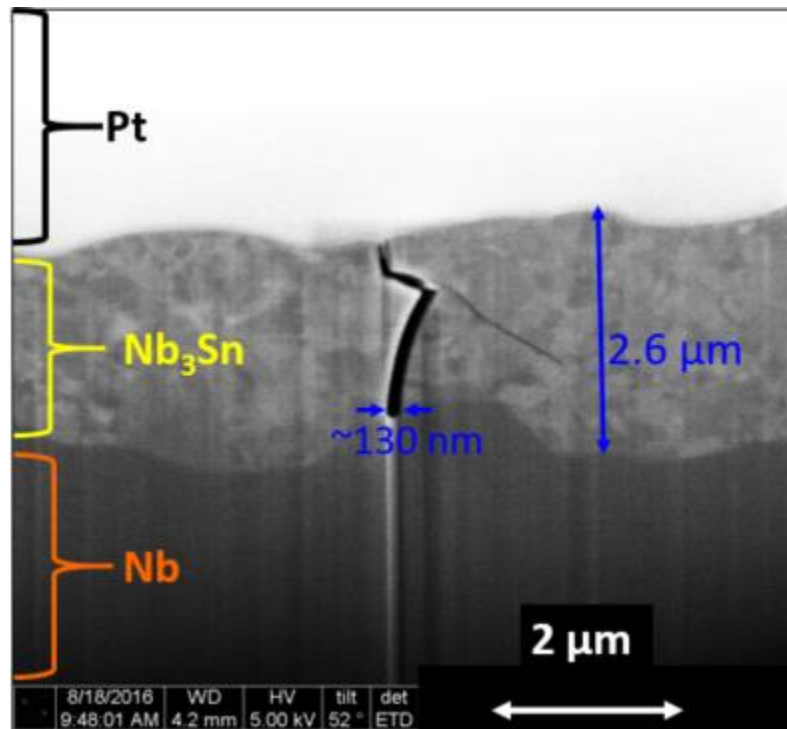


Figure 4.9: Cross-sectional view of a crack observed in CVT14. Note that the crack extends all the way down to the Nb-Nb<sub>3</sub>Sn interface.

### 4.1.5 Temperature Mapping Data Analysis

The typical measurement of the quality factor as a function of field is a measure of the average surface resistance and its field dependence for the cavity as a whole. Temperature mapping during the cryogenic RF test, on the other hand, allows measuring local temperature rise and associate field-dependent loss with specific areas of the cavity. Temperature sensors similar to the ones used here were found to be  $\eta \cong (35 \pm 13)\%$  efficient [115, 117]. That is, the temperature delta indicated by the sensor is  $\eta$  times smaller than the actual surface temperature. The temperature rise of the outside the cavity surface can be related to the RF power dissipated on the inside via the steady-state heat flow equation:

$$\frac{1}{2}R_s H^2 = \frac{1}{R_{Kapitza}(T_s, T_B)}(T_s - T_b) \quad (4.1)$$

where  $R_s$  is the RF surface resistance on the RF side of the cavity,  $H$  is the surface magnetic field amplitude,  $R_{Kapitza}$  is the Kapitza resistance at the helium-cavity exterior interface,  $T_s$  is the temperature of the outside surface of the cavity,  $T_B$  is the helium bath temperature. Since the exterior surface of C3C4 was not coated with  $Nb_3Sn$ , the Kapitza resistance at the helium-niobium (uncoated) interface can be used here. If  $\Delta T$  is the temperature rise measured by the temperature sensors, then  $T_s - T_b = \frac{\Delta T}{\eta}$  and the previous equation can be re-written:

$$R_s = \frac{2}{R_{Kapitza}(T_s, T_B)\eta} \frac{\Delta T}{H^2} \quad (4.2)$$

The surface resistance can be calculated from the equation above, if one knows the Kapitza resistance. It, however, is very dependent on the material and its preparation. Values of Kapitza resistance at 2 K, varying by almost two orders of magnitude have been

reported [118–120]. For chemically polished Nb, the typical value is  $R_{\text{Kapitza}} = 1 \text{ cm}^2 \text{ K/W}$  [119], which will be used in the analysis with an understanding that this value could be a factor of two or three different for the actual C3C4 surface. While there could be a significant variation in the Kapitza resistance between the cavities, the variation between different areas of C3C4 is expected to be small, since the cavity was always treated as a whole. This assumption implies that, while the surface resistance curves may shift up or down, depending on the Kapitza resistance of the actual surface, the relative position of the curves and the field dependence will be the same.

With this caveat, the average RF surface resistance of the cavity can be calculated from the temperature map of the whole cavity surface. Averaging the temperature rise adjusted for the local field amplitude over the entire surface of the cavity, the average surface resistance of the cavity can be calculated from the last equation. The average surface resistance can be calculated this way for each temperature map for each field level. The resulting field dependence of the surface resistance can be converted to the quality factor via  $Q_0 = \frac{G}{\langle R_s \rangle}$ , where  $G = 273$  is the geometry factor for this cavity shape. In Figure 4.10, the intrinsic quality factor derived this way is shown along with the quality factor measured during RF testing using the standard phase-lock loop (PLL) technique. The error bars for the quality factor calculated from the thermometry data are derived from the temperature sensor efficiency spread of 37% and the sensor noise floor, which was assumed to be  $50 \mu\text{K}$ . The typical  $Q_0$  error bars for PLL RF measurements are about 10% (not shown in the plot). Considering different areas of the cavity, a difference in the average surface resistance between the top and the bottom half cells can be evaluated. For example, since the Sn source is located at the bottom flange, a tin vapor pressure gradient may exist along the cavity axis of symmetry possibly resulting in a coating gradient. In Figure 4.10, the average surface resistance of the top half cell vs. the bottom

calculated using thermometry data as a function of field is shown. The analysis shows the top half cell has a higher surface resistance, but the difference is within the error of the analysis. The same analysis applied to the cutouts in Figure 4.5 is shown in Figure 4.12. The temperature rise adjusted for the local field is averaged over the temperature sensors covering the specific cutout area. Figure 4.12 summarizes the data for all the cutouts.

All cutouts were broken down into three groups by the field dependence of their average surface resistance. The first group consists of the samples having weak field dependence; that is, the surface resistance stays constant with the applied field up to the highest field. The second group consists of the cutouts, which have a weak field dependence until  $E_{acc} = 4.5$  MV/m, but have a surface resistance switch and a stronger field dependence above this field. The last group of cutouts comprises the surfaces that have a strongly field-dependent surface resistance from the lowest field. In Figure 4.13, the average surface resistance for the cutouts that have field independent loss is shown. The surface resistance for these samples stays constant with the field. There is an increase in the surface resistance at the accelerating gradients above about 5 MV/m. The increase is within errors, but is evident for all the thermometers in this group, suggesting a systematic effect. In Figure 4.14, the average surface resistance for the cutouts that have a resistance switch at  $E_{acc} = 4.5$  MV/m. This effect is suspected to be caused by a weakly superconducting defect or defects becoming normal conducting at this field level. In Figure 4.15, the average surface resistance for the cutouts that have a strong field-dependent loss increases exponentially with the field at all levels. The temperature at the highest field is an order of magnitude higher than the temperature rise measured at the lowest field.

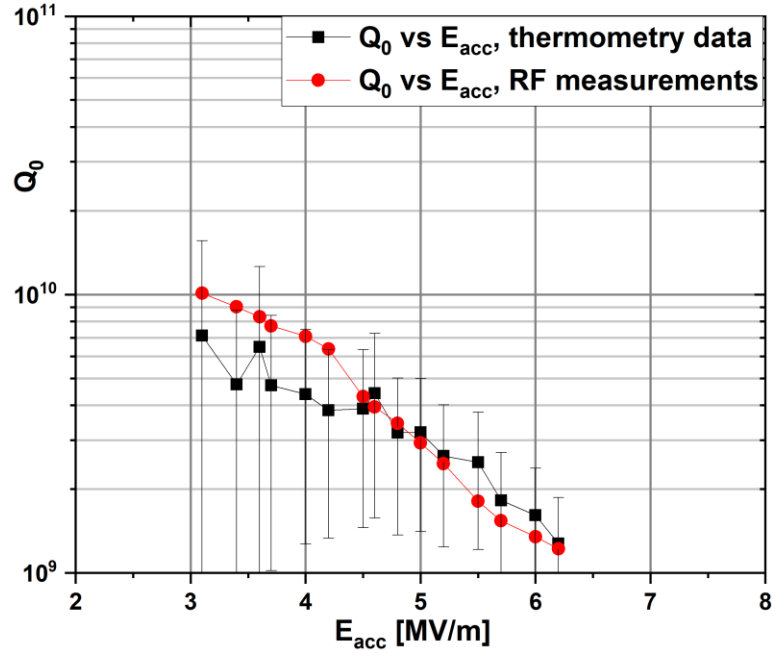


Figure 4.10: The intrinsic quality factor derived from both RF and temperature mapping data.

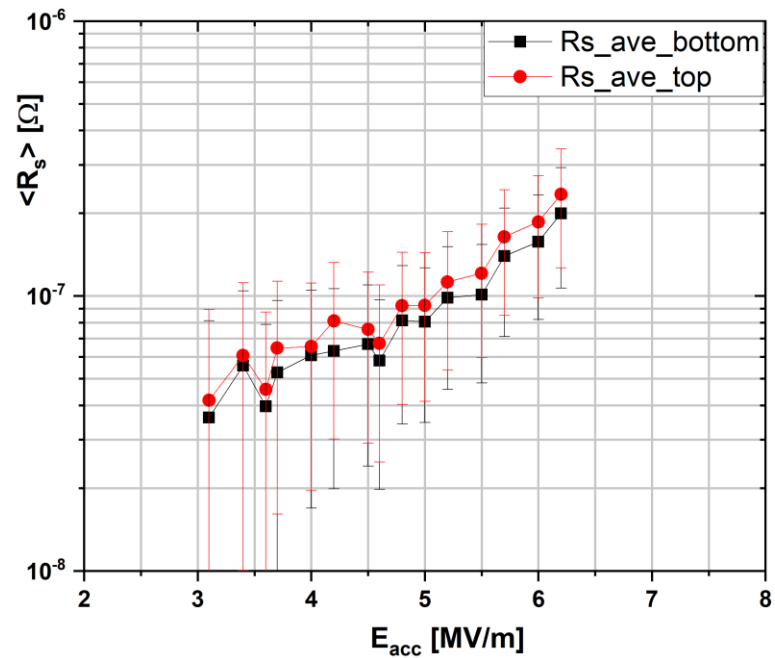


Figure 4.11: The average surface resistance of the top and bottom half cells derived from temperature mapping data.

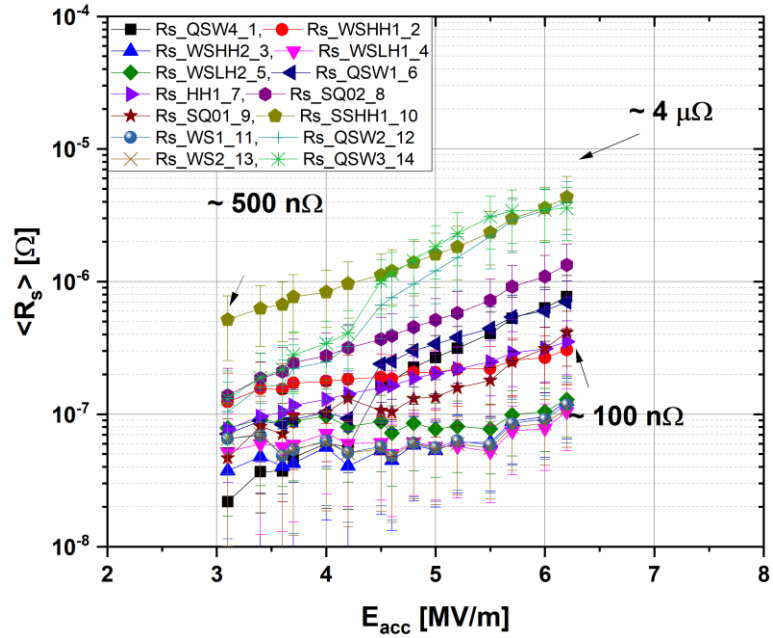


Figure 4.12: The calculated surface resistance dependence with the field for all cutouts.

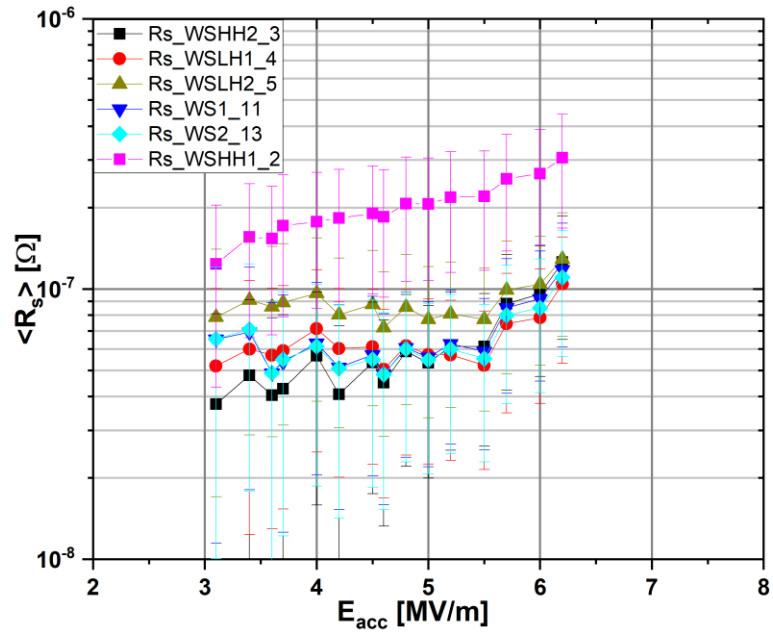


Figure 4.13: The average surface resistance for cutouts that show a nearly field-independent loss.

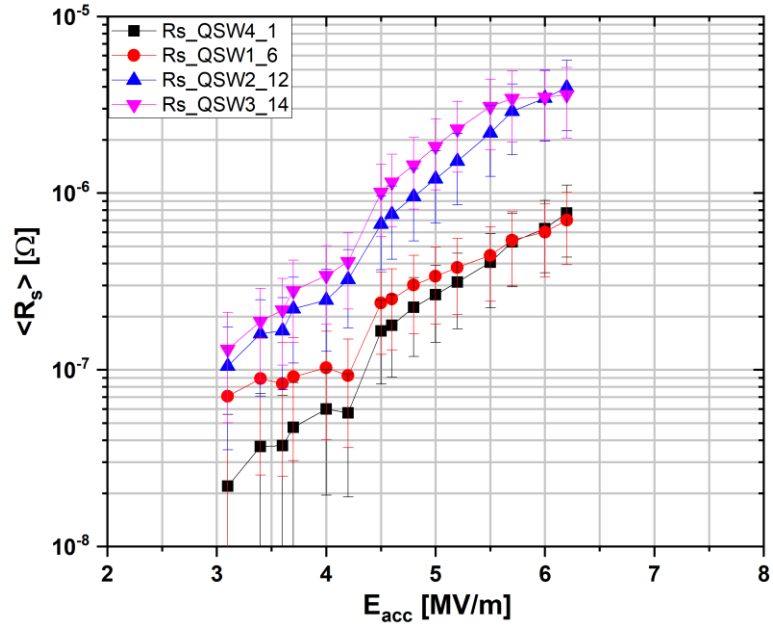


Figure 4.14: The average surface resistance for cutouts that have a resistance switch near  $E_{acc} = 4.5$  MV/m.

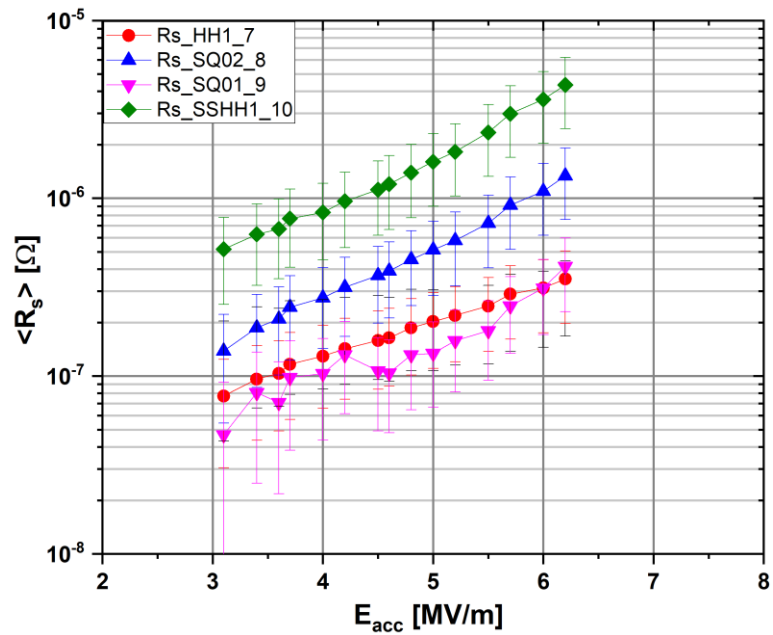


Figure 4.15: The average surface resistance for the cutouts that have a strongly consistent field-dependent loss.

## 4.1.6 Surface Analysis

Six cutouts from the cavity, two samples representing each category of different trend of surface resistances, and two more cutouts representing the top and bottom beam pipes were analyzed with the surface analytical techniques. These were examined with FESEM/ EDS for microstructure and local composition, and AFM was used for surface topography. Focused ion beam (FIB) cross-sections of cutouts were prepared and examined with EBSD and SEM for the crystal structure and the thickness of the coating. Instrument descriptions are available in the previous chapter.

### 4.1.6.1 Microstructure and Local Composition

SEM images captured from multiple locations of each sample showed a mostly uniform coating coverage. Observed microstructures were very similar, as shown in Figure 4.16. Images in the first, second and third columns belong to sets of samples that showed field-independent loss (Figure 4.13), strong field-dependent loss (Figure 4.15), and resistance switch near  $E_{acc} = 4.5$  MV/m (Figure 4.13), respectively. The composition was measured at several locations of each sample. The average compositions of each sample were found to be very similar, as shown in Table 4.1, with slightly lower tin content than the nominal Nb<sub>3</sub>Sn.

On the other hand, cavity samples revealed several voids, including microscopic pits in the coating, as shown in Figure 4.17(a). Note that the term *pit* here refers to the void with well-defined sharp edges at the perimeter. Pit diameters were found to vary between 200 nm to 600 nm. Pits were found typically at vertices, where multiple grain boundaries meet as shown in Figure 4.17(b) and (c). In uncoated Nb, the presence of these voids with sharp edges is understood to be harmful to RF performance of a cavity due to local current and magnetic field enhancement [121, 122]. SEM images with a magnification of 3500–5000 were obtained from 15–20 randomly selected areas of each

cutout. Voids were counted from those images to get an estimate of void density in each cutout. The estimated average number of voids for all the samples was found to be  $(11 \pm 2)$  per thousand square micron area, see in Table 4.1. Approximately one-third of the observed voids were pits, similar to those in Figure 4.17(b) or 17(c).

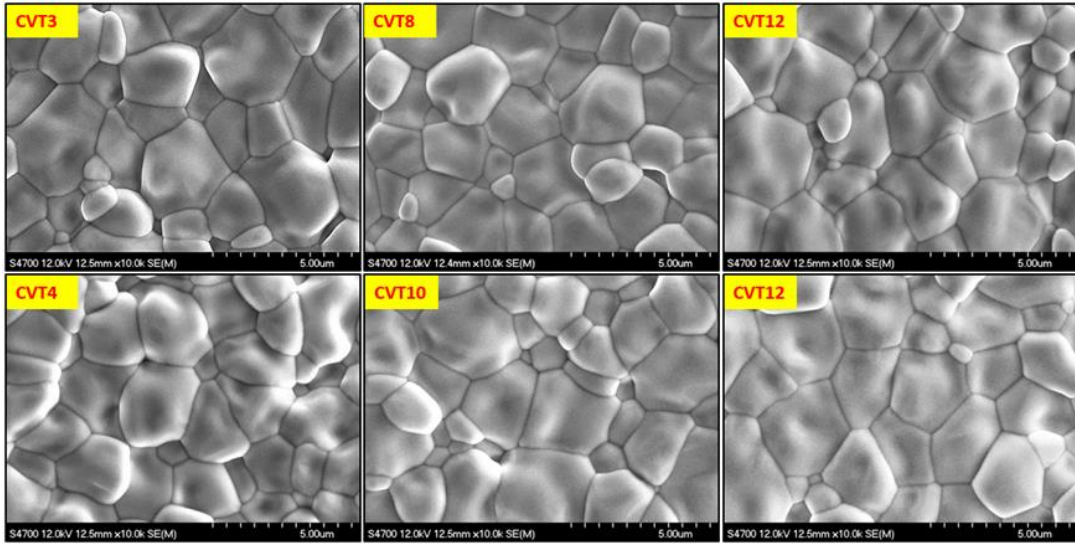


Figure 4.16: SEM images from cutouts representing different field dependence of average surface resistance. Images in the first, second, and third columns belong to sets of samples showing field-independent loss, strong field-dependent loss, and resistance switch near  $E_{acc} = 4.5$  MV/m, respectively.

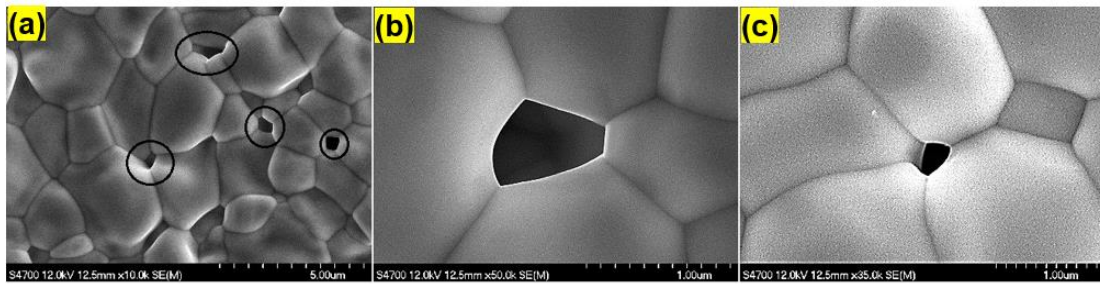


Figure 4.17: Several voids (enclosed by ovals) from sample CVT3 are shown in the SEM image to the left. The other two images show pits found in CVT11 (center) and CVT12 [right]. Bright outlines indicate sharp edges. Note that the diameter of the pit in CVT11 is about 600 nm.

The microstructure of samples extracted from the top and bottom beam pipe appeared different from those obtained from cavity regions, as shown in Figure 4.18. It is evident that the grain size in the beam pipe cutouts is smaller than that of the cutouts from the cell. No voids were observed in beam pipe cutouts. Local composition of coatings from beam pipe cutouts was similar to that of cutouts from cavity regions. Note that the cavity material had higher RRR ( $\approx 300$ ), while beam pipes were made out of reactor-grade niobium (RRR  $\approx 40$ ). The average grain size was determined for cutouts with different surface resistance characteristics by counting the number of grains in several SEM images. The estimated average grain size for cavity cutouts was  $(4.07 \pm 0.40) \mu\text{m}^2$  per grain, which appeared significantly larger than those for beam pipes cutouts, see Table 4.1. Furthermore, the average grain size for the top beam pipe,  $1.35 \mu\text{m}^2$  per grain was smaller than that of the bottom beam pipe,  $2.16 \mu\text{m}^2$  per grain.

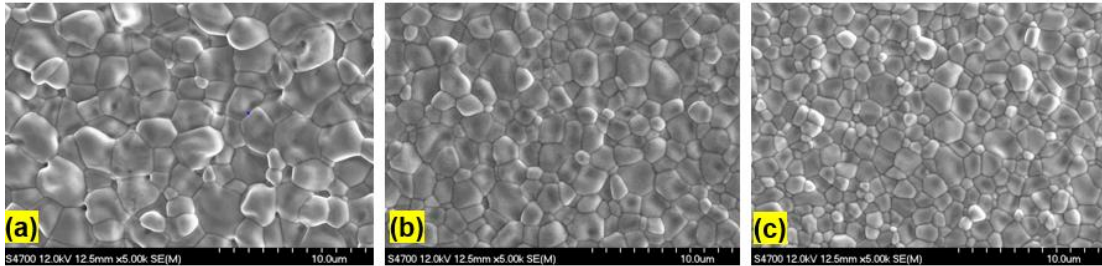


Figure 4.18: SEM images obtained from CVT10 (a), bottom beam pipe (b), and top beam pipe (c).

“Patches” with larger irregular grain structures were found in CVT2, CVT4, CVT8, CVT12, and CVT14 and more rarely in beam pipe cutouts. We already discussed the characteristics of patchy regions in section 3.2.3. These features were not very common. The size of individual patches varied from a few tens to a few hundred square microns. Small patches were seen on the CVT2, CVT4, and beam pipes. Most of those areas had a size equivalent to the area covered by a few regular grains, as shown in Figure 4.19[right]. Larger patches with the size of a few hundred square microns, as shown in

Figure 4.19[left] were encountered in CVT12 and CVT14. Note that these samples showed more coverage of patches than any other cutouts. A few large patches were also observed in CVT8, mostly localized in an unusual area, which will be discussed later. EDS measurement on these smooth areas shows slightly less tin ( $\approx 21$  atomic percent tin) than regular areas ( $\approx 24$  atomic percent tin), possibly because of a thinner coating.

Table 4.1: Summary of estimated materials and RF parameters for different cutouts

Sample #	Distance from equator (cm)	Sn (at %)	Void count (per 1000 $\mu\text{m}^2$ )	Patch coverage (%)	Average grain size ( $\mu\text{m}$ )	Average thickness ( $\mu\text{m}$ )	Max. $R_s$ ( $\mu\Omega$ )	$R_s$ trend
2	4.8	23.35	NA	0.09	NA	2.42 $\pm$ 0.30	0.31	Field independent
4	4.2	23.66	8	0.06	4.10	NA	0.10	
8	0.6	23.69	12	0.34	NA	NA	1.34	Field dependent
10	5.4	23.34	9	-	4.02	2.67 $\pm$ 0.34	4.33	
12	0	23.62	11	0.5	NA	NA	3.95	Field dependent with switch at 4.5 MV/m
14	0.6	23.56	12	0.29	4.08	2.58 $\pm$ 0.44	3.59	
BP Bottom	10	23.54	0	NA	2.16	2.37 $\pm$ 0.19		
BP top	10	24.53	0	NA	1.35	2.03 $\pm$ 0.26		

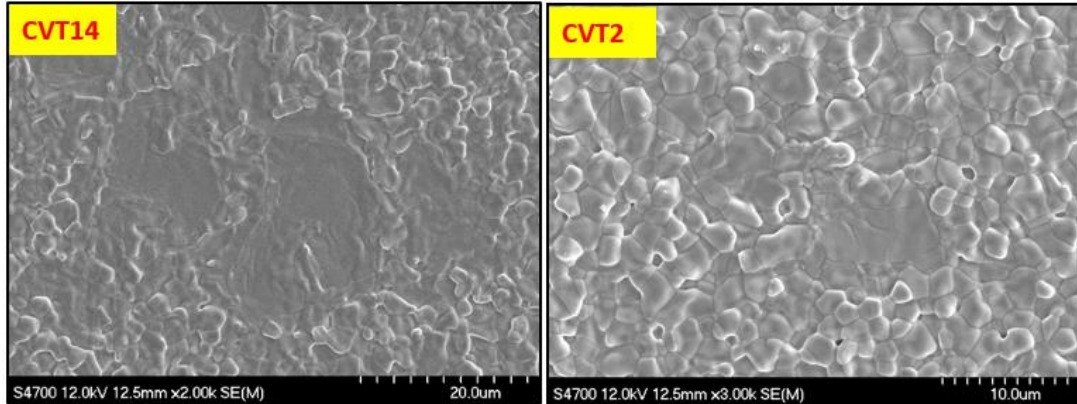


Figure 4.19: SEM image of patchy areas obtained from CVT14 [left] and CVT2 [right].

Patches were frequently observed close to niobium grain boundaries. Such patches are often large or appear to have many small patches close together, as shown in Figure 4.20. In many cases, the occurrences of patches run parallel to a specific niobium grain boundary for several hundred microns (CVT12 and CVT14). SEM images with a magnification of 300–500 were captured from several randomly selected areas of cutouts.

The images were then used to locate and measure the size of patchy regions. Table 4.1 shows the estimated average area covered by patchy regions for each cavity cutout. Patchy regions contribute less than 0.5% surface coverage in any cutout.

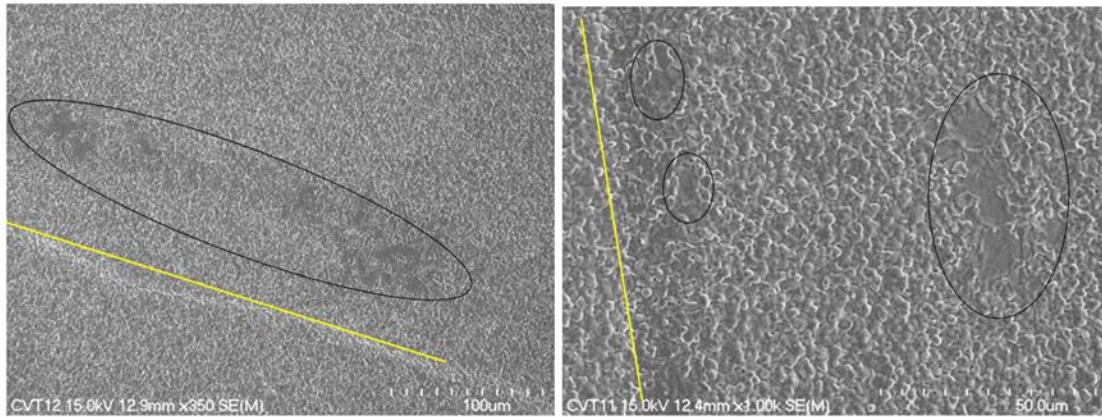


Figure 4.20: Patchy areas near grain boundaries. Yellow lines indicate the grain boundaries. Patchy regions are marked with ellipses.

#### **4.1.6.2 Topography**

AFM was only usable on a few samples due to the curvature of the cutouts. AFM results were consistent with SEM/EDS results to locate pits and irregular grain structures in the coating. A typical illustration of coating topography on the cavity is shown in Figure 4.21. Figure 23 shows the average surface height PSD obtained from different samples. Since the area under a PSD curve corresponds directly to root mean square (RMS) roughness, roughness variation was found not to be very significant. AFM was attempted to obtain the depth profile of a pit. Pits were located in the AFM scans, and depth profile along a line was extracted from different directions as shown in Figure 4.23. It has a very different profile than evident in Figure 4.17. This can also be an artefact caused by the sharper edges of the void compare to the profiling tip. It was found that the depth of these pits varies between 0.5  $\mu\text{m}$  to 1  $\mu\text{m}$ .

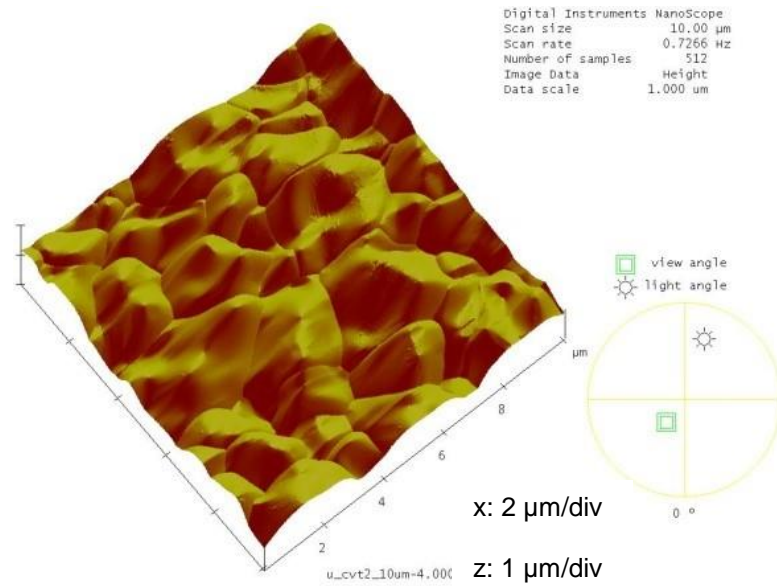


Figure 4.21: AFM image of regular  $\text{Nb}_3\text{Sn}$  coatings on CVT2. Roughness is evident with curved convex facets.

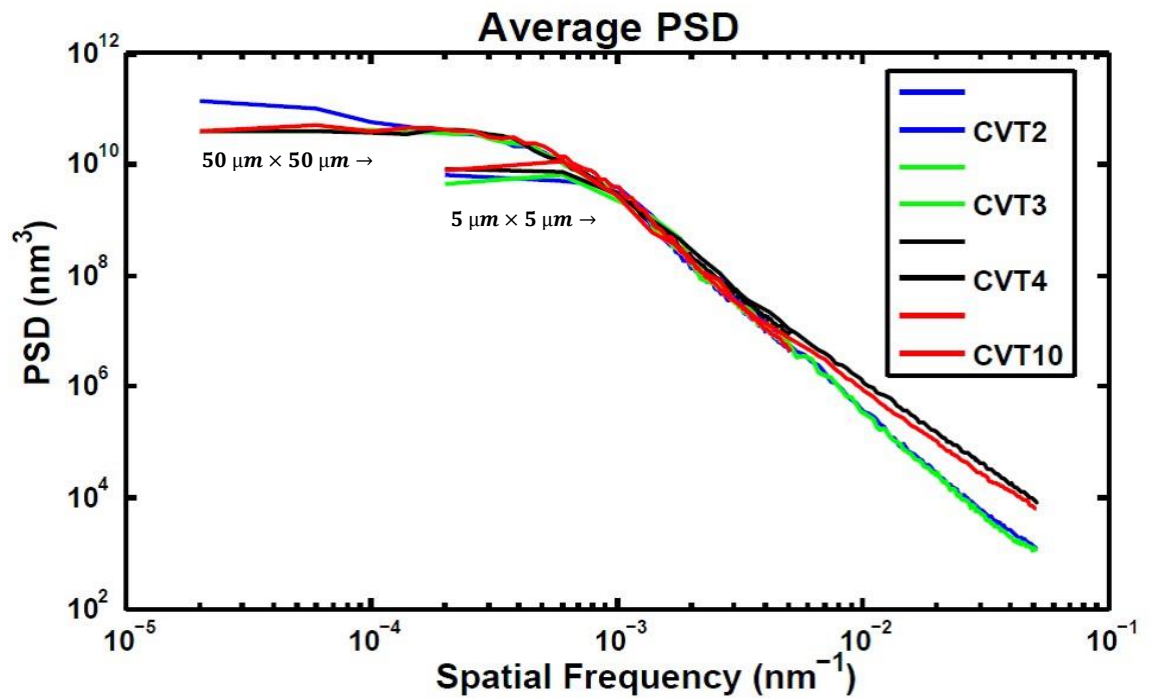


Figure 4.22: Comparison of average PSDs of cutouts calculated using AFM data. CVT4 and CVT10 were rougher in the high-frequency domain (lateral scale  $0.1 \mu\text{m}$  and smaller) than CVT2 and CVT3.

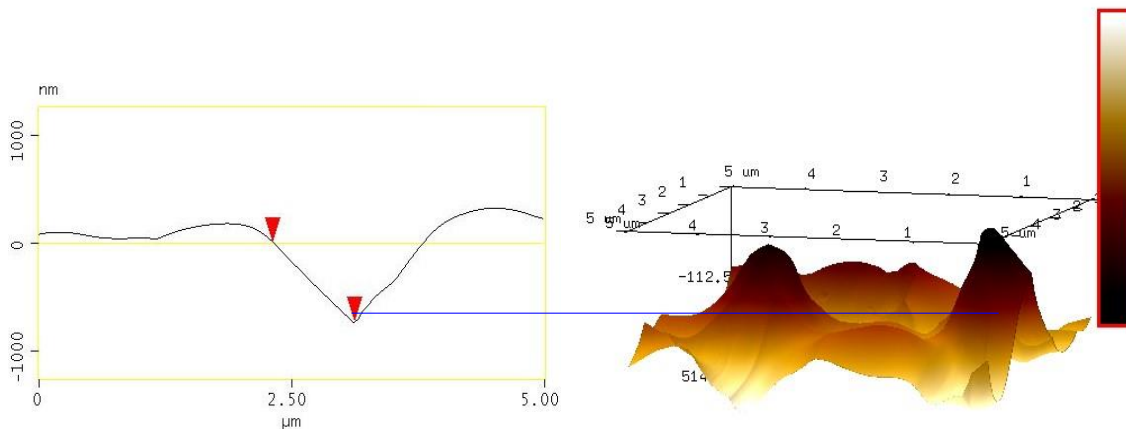


Figure 4.23: Profile of a pit observed in CVT2. Pit appears to be  $\approx 750$  nm deep.

#### 4.1.6.3 Cross-section Analysis

Cross-sections from samples were prepared using a focused ion beam (FIB), as discussed in section 3.1. SEM images of cross-sections were then captured to measure the coating thickness, as shown in Figure 4.24[left]. Coating thickness was measured at several locations of the cutout samples obtained from the cavity region and beam pipes. The coating thickness was found to be greater in cavity regions compared to beam pipes. The coating appeared to be thicker in the bottom beam pipe compared to that in the top beam pipe. The thickness of the coating was found to be as little as 400 nm in patchy areas; see Figure 4.25[right].

EBSID images were captured from cutout cross-sections to examine the structure of the coating further. Representative orientation image maps (OIM) obtained are shown in Figure 4.25. As presented in the previous chapters, columnar grains were normally observed, going from the surface at the top to the  $\text{Nb}_3\text{Sn-Nb}$  interface at the bottom. We also observed the formation of non-columnar small grains at the  $\text{Nb}_3\text{Sn-Nb}$  interface.

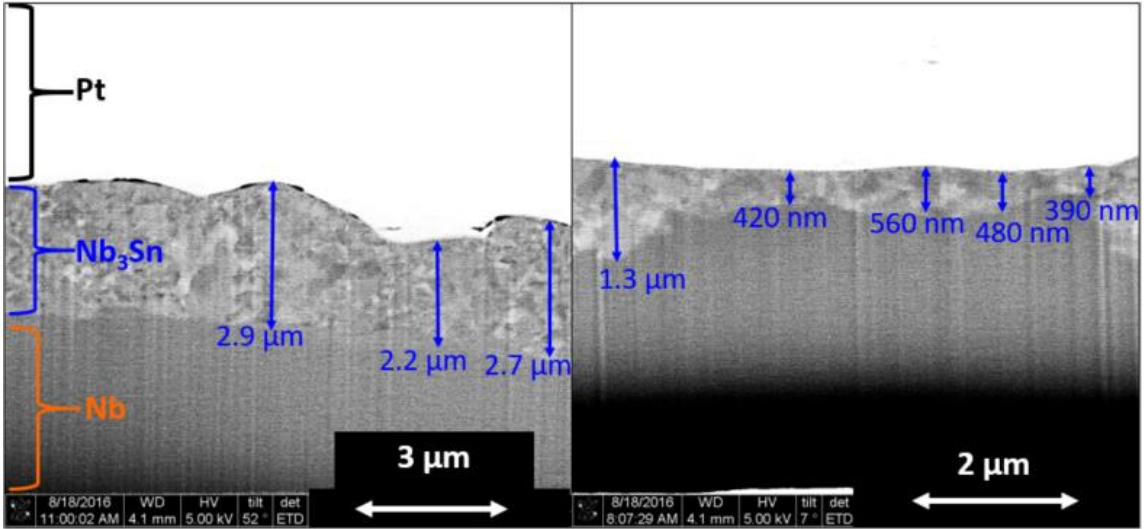


Figure 4.24: SEM image of a FIB cross-section obtained from CVT 10 on the left. Thickness varied from 2.34–2.96  $\mu\text{m}$ . FIB cross-section of a patchy area similar to Figure 4.19 on the right. The coating is significantly thin (400–600 nm) compared to the neighbouring area ( $> 1.3 \mu\text{m}$ ).

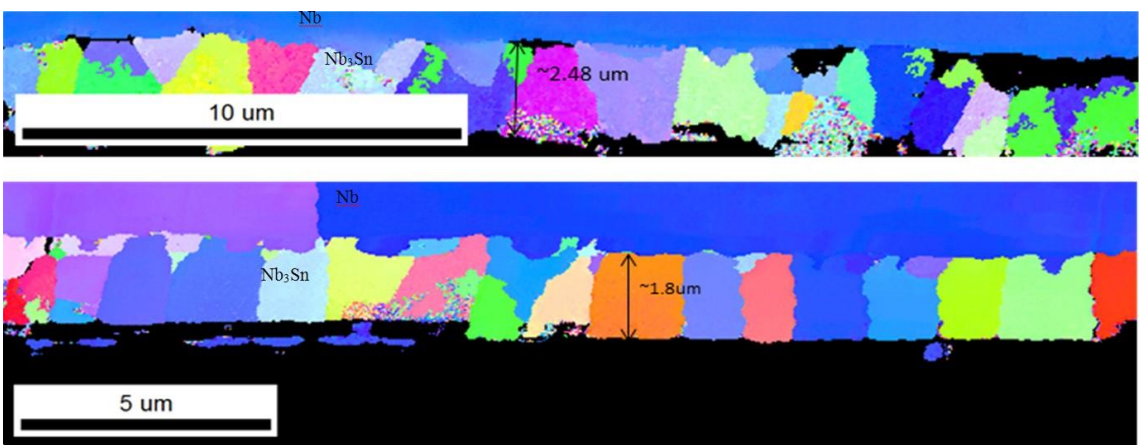


Figure 4.25: EBSD image from sample CVT 10 at the top, which is cut from the cavity region. Image at the bottom is from beam pipe cutout. Beam pipe has a thinner coating with more columnar grains than CVT10. Some instrumental artefacts (dark area in between Nb-Nb<sub>3</sub>Sn grains) are present.

#### 4.1.6.4 Other Defects

Besides patches and pits, other defects were found in some samples. One such defect is bright spots observed by SEM on coated surfaces (Figure 4.26). The contrast difference might have arisen due to the difference in topography. These features were found sometimes on CVT2 and CVT4, but frequently seen in CVT10. These spots were found to have different shapes with carbon-enriched boundaries, as shown in Figure 4.27. Note that the ratio of Nb to Sn was not altered within these bright spots when examined with EDS, suggesting that the SEM signature is due to very thin surface contamination. Unlike other cutouts, CVT10 had a large area with a different appearance than usual coating as shown in Figure 4.28. It comprises the usual  $\text{Nb}_3\text{Sn}$  grains, but dark spots appear in each of those grains. Similar dark areas were also noticed in intergranular spots. EDS found an excess of carbon and oxygen from dark spots. An AFM image collected from CVT10, see Figure 4.29, also shows the presence of residues on the surface.

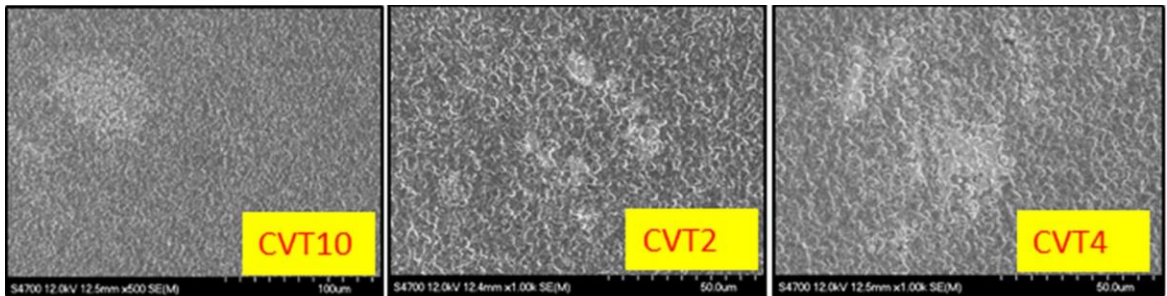


Figure 4.26: Bright spots observed in different cutouts.

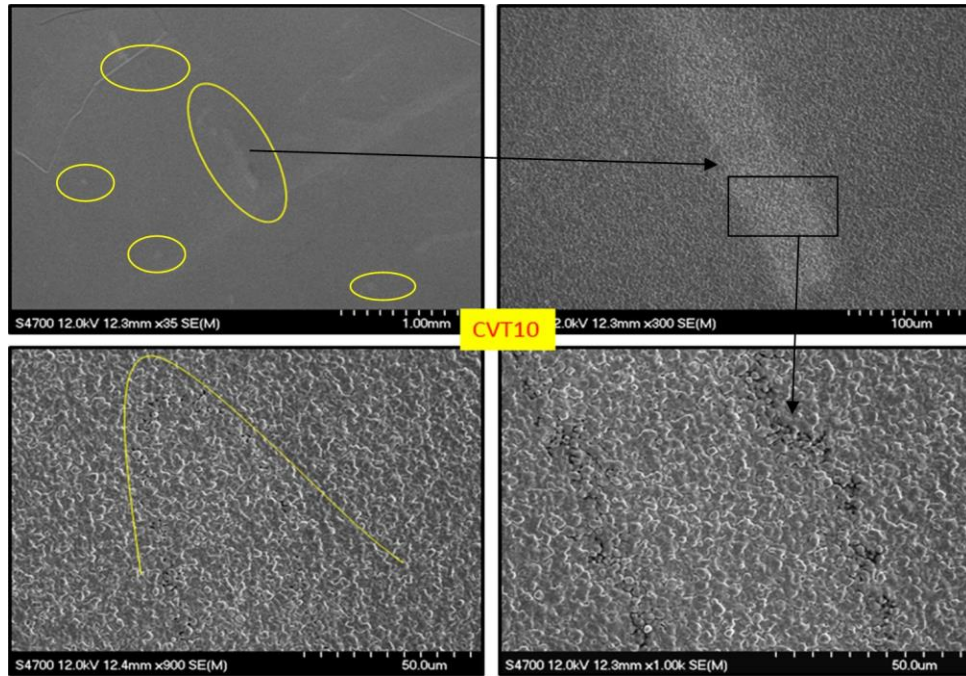


Figure 4.27: Bright spots observed in CVT10. Note EDS examination of dark boundaries of these features shows a clear presence of carbon.

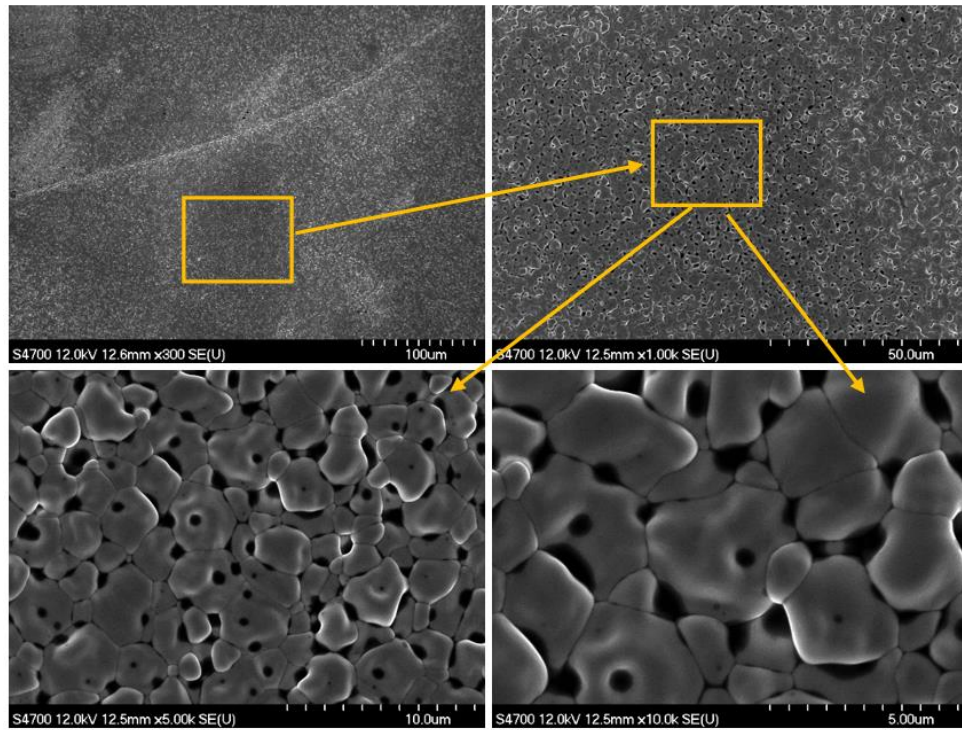


Figure 4.28: An unusual appearance of coating in CVT10.

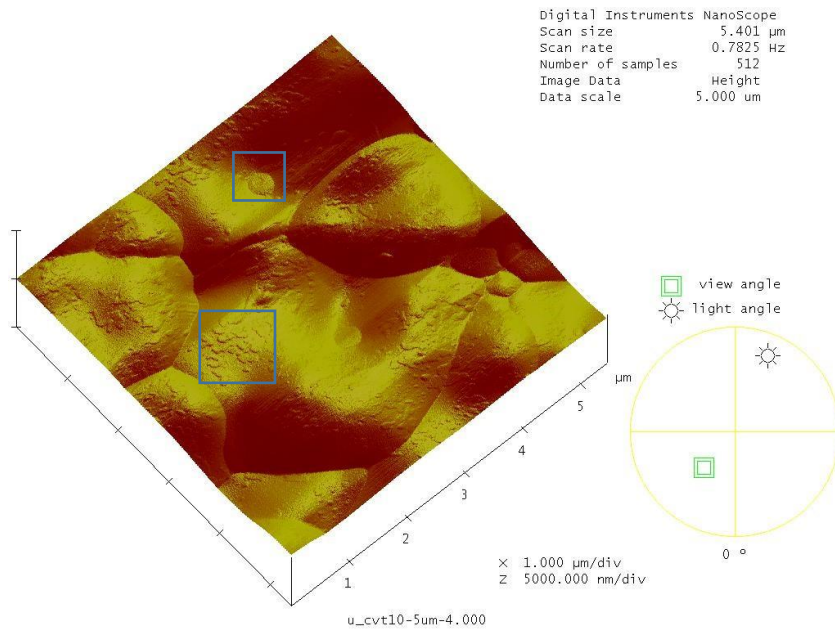


Figure 4.29: AFM image from CVT 10. Note the residue covering the surface.

A circular feature of 100μm diameter was present in CVT14, as shown in Figure 4.30. The circular area was found recessed compared to its adjacent areas, considering the contrast in the SEM image. The edge of this feature showed a significant presence of carbon and oxygen. The composition and grain structure were found similar inside and outside of this feature. Another noticeable area was discovered in CVT8. The area, which appeared relatively dark in SEM images is shown in Figure 4.31(a). Note that the area covered by this constituent was more than 40000  $\mu\text{m}^2$ ; that is, the diameter was  $\approx 700 \mu\text{m}$ . SEM images show well-defined boundaries, Figure 4.31(b, c, and e), that distinguish this area from areas with usual looking coating. Large patches were also seen at the boundary, as shown in Figure 4.31(f). Figure 4.31(d) and (e) respectively show grains from the unusual area under discussion, and nearby area with usual appearances. Corresponding EDS spectra show significant amounts of carbon from dark areas compared to regular areas. This unusual area of CVT8 has similar characteristics of the unusual area found in CVT10, Figure 4.28.

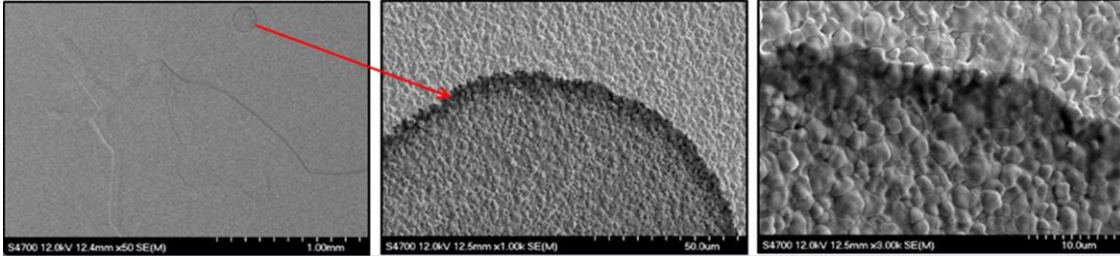


Figure 4.30: Defect found in CVT14.

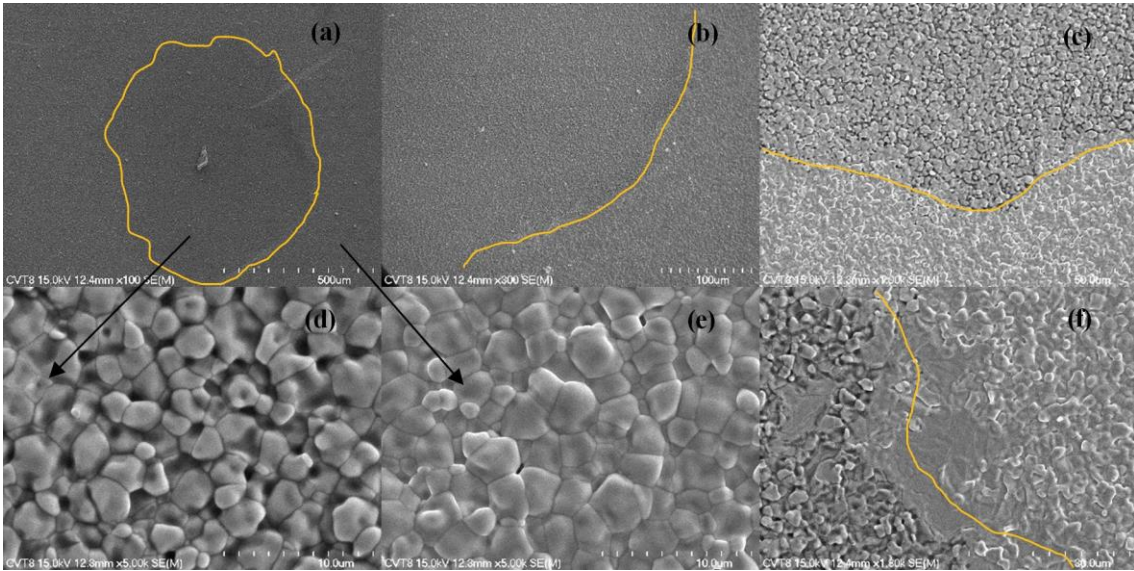


Figure 4.31: Detailed structure within the defect found in CVT8. (a) shows the unusual area marked with yellow lines. (b), (c) and (e) shows the transition from unusual area to regular area. (d) and (f) show close-up views of grains from unusual and regular areas, respectively. Note the patchy region found close to the transition.

### 4.1.7 Discussion

SEM examination of cutout samples obtained from different areas of the cavity showed that the coating was mostly uniform. The measured value of superconducting transition temperature ( $\sim 18$  K), close to the value expected for the nominal composition of  $\text{Nb}_3\text{Sn}$  (18.3 K) also indicated a good coverage of  $\text{Nb}_3\text{Sn}$ . Patchy areas containing irregular grains were present in several cutouts. Cross-section measurements revealed

that such irregular Nb<sub>3</sub>Sn grains are significantly thinner than those elsewhere, Figure 4.24. Since RF field penetration in Nb<sub>3</sub>Sn is in the order of a few hundred nanometers, the thickness of such patchy areas is not large enough to fully shield the underlying Nb<sub>3</sub>Sn-Nb interface and underlying niobium from the RF field. Underlying niobium has higher surface resistance and will cause additional RF losses compared to the regular Nb<sub>3</sub>Sn grains. A correlation between the relative abundance of the irregular grains and stronger RF field dependence is seen in the thermometry data. Thermometry data for the CVT8, CVT12, CVT14 cutouts indicates average surface resistance above 1  $\mu\Omega$  at  $E_{acc}=6$  MV/m and a field dependence exponent above 3, and patchy areas in these samples exceed 0.2%. Inefficient RF shielding patchy regions contribute to the additional RF loss in these samples. One observation is that all three cutouts CVT8, CVT12, and CVT14 are from the equator region of the cavity, which seems to be more likely to develop such features, Figure 4.32.

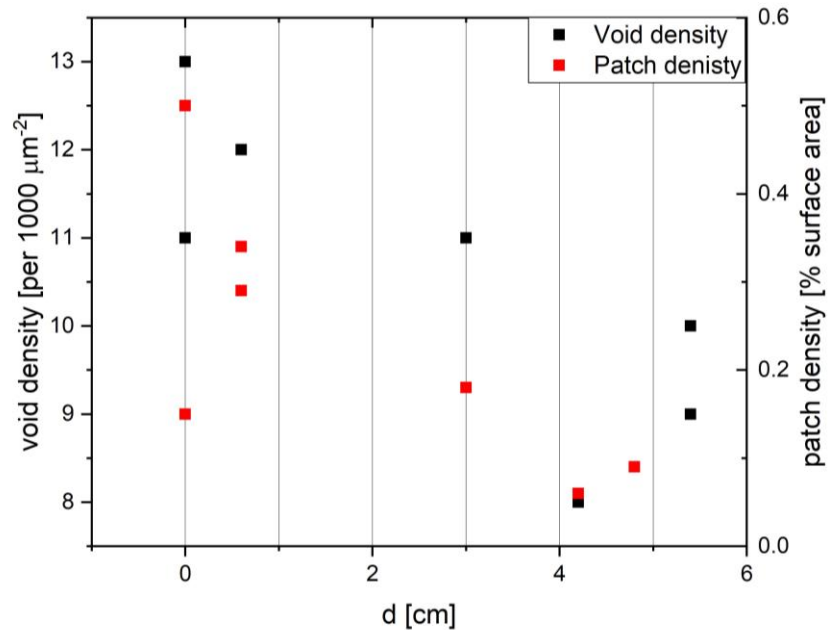


Figure 4.32: Defect density as a function of distance from the equator. Note the negative correlation; defects are more likely to occur in the regions close to the equator.

Electron beam welding areas feature larger grains that form during the solidification process of the weld seam. The cavity equator region is also the region, furthest out-of-sight from the tin evaporation source. Since tin flux to such regions is supplied via scattering and surface diffusion, the equator regions may see less tin flux than the in-sight areas, and the formation of thin regions may be linked to low tin flux. With less tin supplied to these regions, one expects overall less tin content and hence a thinner Nb<sub>3</sub>Sn layer thickness. Thickness measurements of the Nb<sub>3</sub>Sn films in different cutouts did not show significant variation with the cutout position on the cavity surface, and the films both on in-sight and out-of-sight surfaces have similar thicknesses (Table 4.1). This suggests that the amount of tin available for grain boundary diffusion and Nb<sub>3</sub>Sn formation during the coating growth is similar or exceeds the diffusion rate for both in-sight and out-of-sight cavity regions during the film coating process. The amount of available tin in the out-of-sight areas will depend on the sticking coefficient and surface ad-atom mobility. Nb<sub>3</sub>Sn growth is done typically at temperatures above 1000 °C in the vapor diffusion process, where the sticking coefficient can be lower, and the surface ad-atom mobility is higher than those at the nucleation temperature [123, 124], helping coating uniformity. The nucleation process is done at about 500 °C, where the sticking coefficient is higher, and surface ad-atom mobility is lower, impeding uniformity of tin coating. During the nucleation stage, some out-of-sight areas may remain poorly covered with tin. Once the process progresses to the growth stage, such areas will present large bare niobium areas to arriving tin atoms with higher mobility at this stage. Due to the absence of pre-nucleated centers and high tin mobility, such areas will promote the growth of large single-crystal grains, which will subsequently grow slower due to the absence of grain boundaries. This model indicates that film nucleation is critical to growing film without thin regions, and the film grown on cavity C3C4 may have suffered from low tin flux during the nucleation phase.

In the past, researchers also linked such thin areas to the substrate grain orientation [125]. They reported that single crystal substrate with (111) and (531) planes resulted in more patchy areas than the substrates with (110) and (100) orientation. Beam welding areas are likely to have large grains, on the order of 100  $\mu\text{m}$ , resembling single crystal substrates, which may include similar crystal orientations favorable for non-uniformity. It has been reported recently that the accumulation of tin particles during the nucleation stage can vary for different grains of niobium [59]. A finding of patchy areas in a large grain sample was reported before [86]. As we discussed in the previous chapter, substrate pre-anodization was found to reduce these areas. The pre-anodization technique was recently utilized at Cornell University to overcome these patchy regions [72]. The average coverage of patchy regions in our dissected cavity (< 0.25%), which was not pre-anodized, is very similar to the result obtained with pre-anodizing by researchers at Cornell University. It is possible that the larger amount of  $\text{SnCl}_2$  used in JLab may provide higher Sn vapor pressure to uniformly nucleate the large surface area of a cavity. Also, the coating temperature of  $\text{Nb}_3\text{Sn}$  at Jefferson Lab, 1200  $^\circ\text{C}$ , is higher than that used at Cornell, 1100  $^\circ\text{C}$ , providing higher flux of tin during the coating. As per our discussion in section 3.2.3, patches have thinner coating because of fewer grain boundaries and longer grain boundary diffusion paths to supply fresh Sn to mid-grain at the Nb- $\text{Nb}_3\text{Sn}$  interface.

The average RMS roughness was found close to 100 nm in the cutout samples for 5  $\mu\text{m}$   $\times$  5  $\mu\text{m}$  scans, slightly higher than 70 nm in samples coated before [31]. The difference is expected because of relatively larger grains and thicker coating in cavity cutouts, see section. The variation of roughness between examined samples was not very significant when average PSDs from the data obtained with AFM were compared.

Microscopic pits were observed in all the cutouts except those from beam pipes. Average number of pits between different cutouts were very similar. Grain growth competition and rapid coalescence of small grains during the deposition step are speculated to create such structures. These defects, reported first here, may affect the RF performance as the magnetic field can enhance locally at sharp edges of these structures.

Coating thickness and grain size were found to vary between the cavity region and beam pipes. One obvious difference between them was the RRR value of the fabrication material. There has been limited research to understand the relationship between RRR of substrate niobium and the Nb<sub>3</sub>Sn growth process. Peiniger et al. reported that the density of Nb<sub>3</sub>Sn nucleation centers was strongly reduced if one uses medium RRR niobium (RRR = 120) compared to low RRR niobium (RRR ≈ 40) [32]. The phenomenon causing the differences has not yet been established. Considering the potential for more nucleation sites in beam pipe (low RRR niobium) compared to cavity cell areas (high RRR), the observed difference in the number of grains or the average grain size may be understood. Grain size variation between cavity cutouts was not significant, but the difference in grain size between the top beam pipe and bottom beam pipe was significant. One possible reason for such a difference could be the distance from the tin source during the coating. The top beam pipe, which is farther from the tin source, may have received a lower flux of tin during the coating process compared to the bottom. Since we did not see such an asymmetry between cavity cutouts, another potential reason for smaller grains in the top beam pipe could be the proximity to the top heat shield and pump line. The temperature of the top beam pipe during the coating may have been lower than the beam pipe, if the heat shield was not perfect. Note that we have seen condensed tin on the niobium foil covering the top beam pipe during the coating.

Other carbon-enriched defects, similar to those depicted in Figure 4.28 and Figure 4.29 may indicate that some contaminant may already present at these spots on the starting substrate niobium. If that is the case, it appears that impurity segregation to the surface can happen without a dramatic influence on Nb<sub>3</sub>Sn growth. Unusual and big carbon enriched areas present in CVT8 and CVT10 are strong candidates for localized heating. The circular defect found in CVT14, Figure 4.30, could be another similar case where the niobium might have a circular depression, susceptible to retaining carbonaceous impurities prior to the coating. Residue, observed in CVT10 with AFM, Figure 4.29, may not appear in SEM image because of the limited sensitivity of SEM/EDS, but it could be something that can also impair the RF performance. The higher density of patchy regions in CVT12 and CVT 14 appear to be well correlated with the observed surface resistance switch at ~ 4.5 MV/m. The carbon-rich features seem to correlate with strong field-dependent resistance. The absence of such features results in a material with relatively field-independent surface resistance.

Since intermetallic A15 compounds are extremely brittle, Nb<sub>3</sub>Sn is vulnerable to fracture. It is known that brittle fractures can propagate faster along the direction perpendicular to the applied stress. Cracks observed in cutouts typically started from the edge and propagated in the same direction away from the edge, indicating that they were formed due to the applied mechanical stress during dissection.

The following section presents witness sample analysis with RF performances of several single-cell and five-cell cavities. It will provide more insight into the coating properties relative to the coating process and RF performance.

## **4.2 Witness Sample analysis linked with coating process and cavity performances**

During the cavity coatings, witness samples were included to provide a proxy for the cavity interior surface. Their analysis revealed interesting features of the Nb<sub>3</sub>Sn coating process. Together with whole cavity RF test results, these analyses guided continuing improvements in the coating process. This section presents analyses of several witness samples coated with single-cell and five-cell cavities. Results from the analysis relevant to cavity performance prompted changes in the coating process, which we will discuss along with cavity results.

### **4.2.1 Witness sample studies and single-cell cavity coatings**

As we discussed in section 1.2.6, the coated cavities at JLab initially had low-field quality factors ( $Q_0$ ) as high as  $> 1 \times 10^{10}$  at 4 K but suffered strong Q-slope, limiting the attainable maximum gradient. This Q-slope, very similar to the one seen in early cavities coated at Wuppertal University, was consistently observed in several cavities [20, 47]. From the cutout studies presented in the previous section, the coating inside the cavity could have lossy regions because of the localized defects. One important question to ask here is, are these defects solely responsible for the signature Q-slopes seen in several Nb<sub>3</sub>Sn cavities? Our samples showed a significantly higher level of Ti in the Nb<sub>3</sub>Sn layer compared to the witness sample obtained from Cornell, where Q-slope free cavities were produced at the time (section 3.1.3), it hinted at the possible Ti migration from NbTi flanges of cavities during cavity coating. We often observed (yellowish or purplish) discoloration of the niobium cover next to NbTi flanges after the cavity coating, as in the C3C4 coating discussed above (Figure 4.1). The notable discoloration was also seen in alumina hardware used during the coating, see Figure 4.33. EDS examination of such discolored

alumina hardware shows a significant amount of Ti confirming Ti loss from the NbTi flanges. Ti from NbTi flanges was found to affect the field dependence of  $Q_0$  in Nb cavities [89, 126]. At Wuppertal, the potential source of Ti could be Ti foils, which were used as getter material on the outside of coated cavities to maintain the purity of niobium during the Nb<sub>3</sub>Sn coating. So, Ti was considered as a potential culprit for the observed Q-slope.

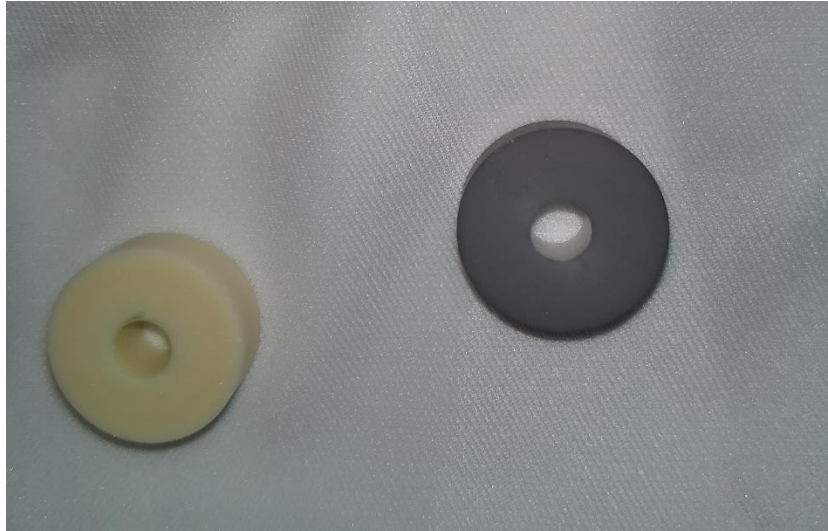


Figure 4.33: Alumina hardware before [left] and after [right] the coating of a cavity with NbTi flanges. EDS examination shows a significant amount of Ti (Al : Ti = 2 : 3) following the coating.

Following the coating system upgrade in 2017, Ti-free hygiene was adopted for Nb<sub>3</sub>Sn coating by avoiding cavities with Nb-Ti flanges. Witness sample analysis had confirmed the reduction of the Ti-level. Almost a Q-slope free Nb<sub>3</sub>Sn cavity was then produced for the first time, but Q was below  $1 \times 10^{10}$  at 2 K [26]. Since then several cavities were coated and tested, and still encountered Q-slopes.

Witness samples were typically analyzed to understand the causes and their remedies. We will mainly focus on two experimental single-cell cavities, RDT10 and RDT7, which were coated several times with witness samples. Unlike C3C4 cavity, which had NbTi flanges, RDT10 and RDT7 were fabricated entirely of niobium. The performance of

each (uncoated Nb) cavity was limited to  $\sim 30$  MV/m by a high field Q slope during the baseline test at 2 K. Each cavity was coated individually according to a typical Nb<sub>3</sub>Sn coating process as discussed for C3C4 in section 4.1.1. Unlike the C3C4 coating, Sn was loaded in an open-top Nb crucible that is expected to enhance the evaporation rate by increasing the active surface area of Sn. Both ends of the cavity were closed with Nb plates before installation into the furnace. A witness sample was typically hung inside the cavity by attaching it to the top cover using a Nb wire. The temperature profile included a nucleation step at  $\sim 500$  °C for an hour and a coating step of three hours at  $\sim 1200$  °C. The temperature was monitored with sheathed type C thermocouples attached to the cavity at different locations. There was a temperature gradient of  $\sim 20$  °C between the top and bottom of the cavity.

Figure 4.34[right] shows post-coating pictures from RDT7 and RDT10. Post-coating inspection indicated uniform coatings inside both of cavities. Samples obtained from each cavity coating were examined with SEM/EDS. These images, Figure 4.34[left] showed uniform coating in both samples. EDS analysis of both samples revealed  $(24.5 \pm 0.5)$  at. % Sn, close to the nominal composition of Nb<sub>3</sub>Sn. However, high-resolution SEM images from each sample revealed residues on the surface. Note that the C3C4 cavity had no such residues. These residues were a few tens of nanometers in diameter, as shown in Figure 4.35. Precise probing of those features was not always possible with EDS resolution, but some of the larger residues showed  $\sim 30$  at. % Sn compared to  $\sim 24\%$  in neighboring areas. This indicated them to be Sn-rich particles. Sn is known to be a superconducting material with a transition temperature ( $T_c$ ) of only  $\sim 3.7$  K [127]. Since the intrinsic surface resistance, i.e., the BCS resistance varies as  $R_{BCS} \sim \exp(-1.76T_c/T)$ , Sn has higher surface resistance than Nb<sub>3</sub>Sn at 2 K and it is already normal conducting at

4 K. Because of higher surface resistance, it will exhibit higher dissipation and will lead to a stronger thermal feedback effect, degrading the cavity performance.

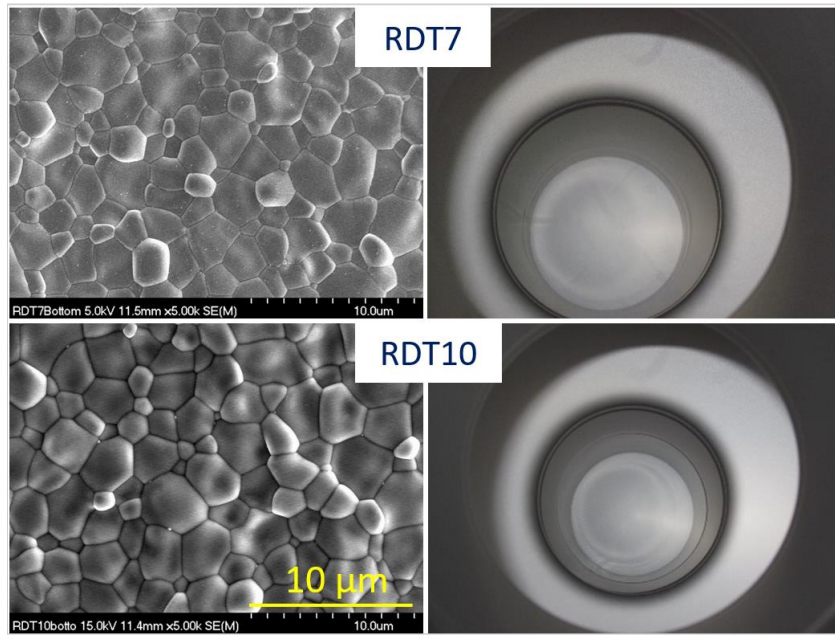


Figure 4.34: Top left and bottom left images are SEM images captured from witness samples coated with RDT7 and RDT10, respectively. Images to the right show the interior appearance of the cavities after coating.

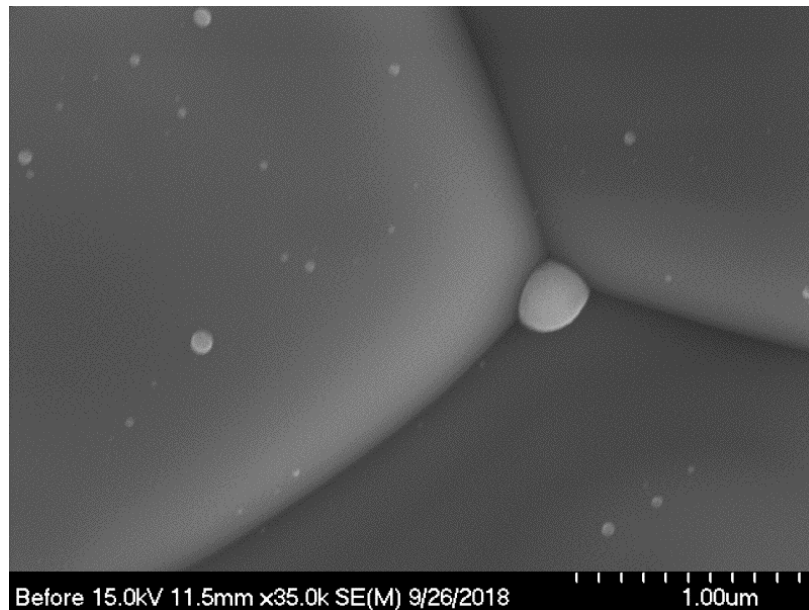


Figure 4.35: Sn residue on Nb<sub>3</sub>Sn coating.

RF testing at both 4 K and 2 K showed precipitous Q-slope in each cavity. Low field  $Q_0$  at 4 K was  $\geq 1 \times 10^{10}$ , but dropped sharply before quenching at  $\sim 11$  MV/m. The coating experiments were repeated twice more on RDT10 with some variation in coating temperature, and all consistently produced a similar performance. Since Sn-residues appeared on the witness sample from each coating, they were considered as a potential causative of observed Q-slope. The witness samples were subjected to acid treatments and annealing to remove residues from the surface. We will be discussing these in the next chapter. Despite SEM images showing improved surface following some post-treatments, cavity performance was not improved.

#### **4.2.1.1 Two-cavity setup**

Another approach pursued was to avoid residue formation on the cavity surface during the coating. We speculated that the Sn-rich residues were the result of Sn condensation from residual Sn vapor, which is present inside the cavity at the end of the coating. In an attempt to reduce Sn condensation in the cavity of interest, another single-cell cavity was added on top, and maintained temperature gradient between two cavities to re-distribute residual Sn-condensation

Cavity to be coated (RDT7 or RDT10) was connected to another single-cell cavity, RDT2, which had microscopic pits and was planned to be colder during coating and to act as a getter for residual Sn vapor, as shown in Figure 4.36. About  $\sim 3.4$  g of tin and 3 g of  $\text{SnCl}_2$  were placed at the bottom similar to the first set of experiments. Since coating volume was increased, the coating setup also included a secondary tin crucible, which was loaded with 1.4 g of Sn. It was attached to the top cover with a Nb rod and hung inside the bottom beam pipe of RDT2. A witness sample was suspended from the secondary Sn crucible with Nb wire. The heat profile was similar to the previous experiments in a single-cavity setup, except there was a temperature gradient of  $\sim 85$  °C between the top and

bottom of the whole setup, as shown in Figure 4.37. This was made possible by adjusting the temperature of the separate heat zones of the furnace. The bottom tin container was mostly covered with a diffuser, which was a thick molybdenum disk with holes.

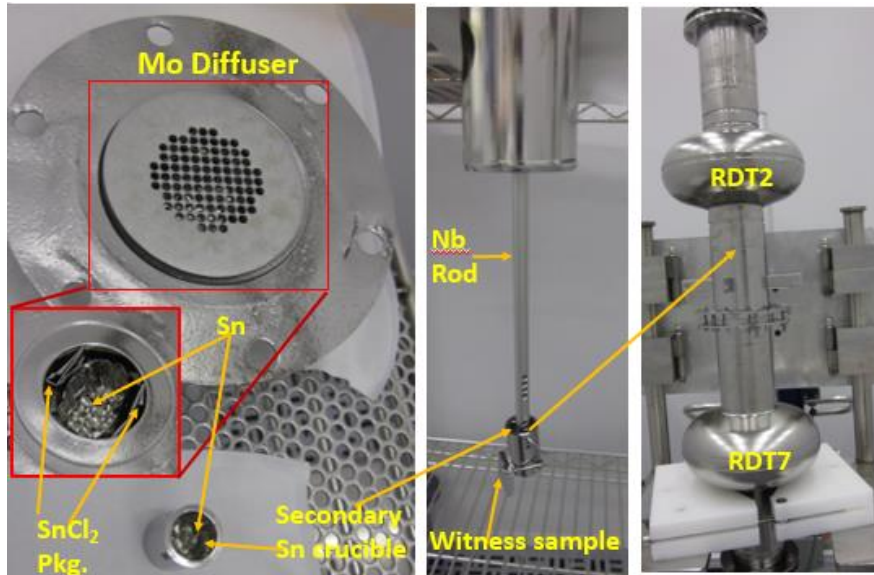


Figure 4.36: Two-cavity setup for RDT7 coating.

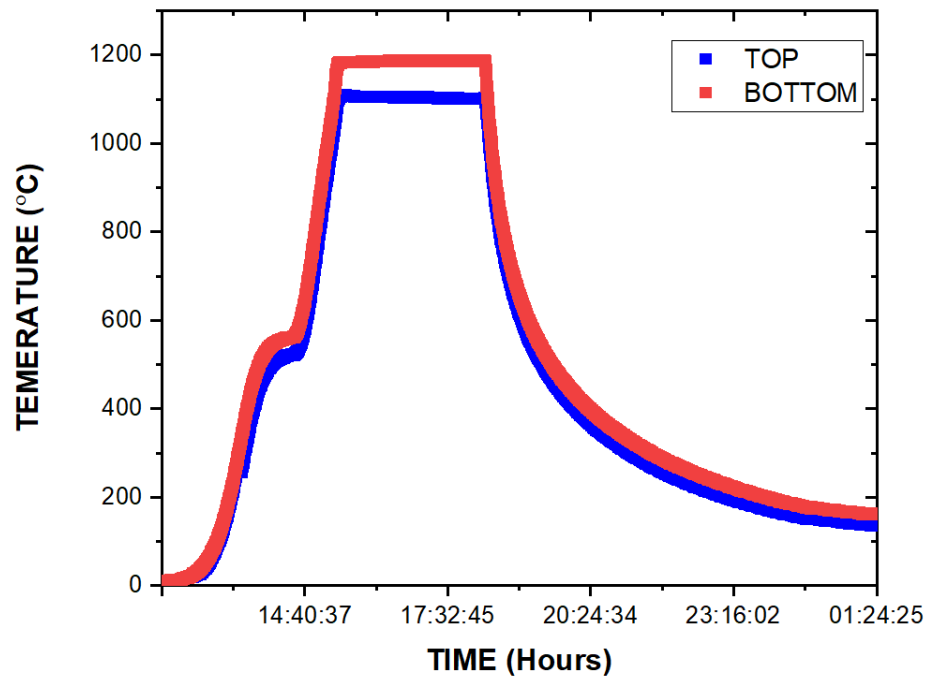


Figure 4.37: Temperature profile used to coat cavities in a two-cavity setup.

RDT7 and RDT2 were paired first and coated. The interior surface of RDT7 appeared uniformly coated during visual inspection. SEM examination of the witness sample exhibited Sn-residues again. Note that the witness sample here was inside RDT2. Since it was suspended from the secondary Sn-crucible, which was attached to the Nb rod hung from the top cover, it could have a lower temperature than the cavity, and would thus be more likely to have Sn-residues. RF test results obtained from the RDT7 are shown in Figure 4.38. The measured value of low field  $Q_0$  was  $3 \times 10^{10}$  at 4 K and  $1 \times 10^{11}$  at 2 K without any significant Q-slope. The cavity maintained a  $Q_0$  of  $\sim 2 \times 10^{10}$  at 4 K and  $> 4 \times 10^{10}$  at 2 K before quench at  $> 15$  MV/m. The cavity performance of RDT7 showed noteworthy improvement in the typical Q-slope, compared to data previously reported from Wuppertal and Jefferson Lab.

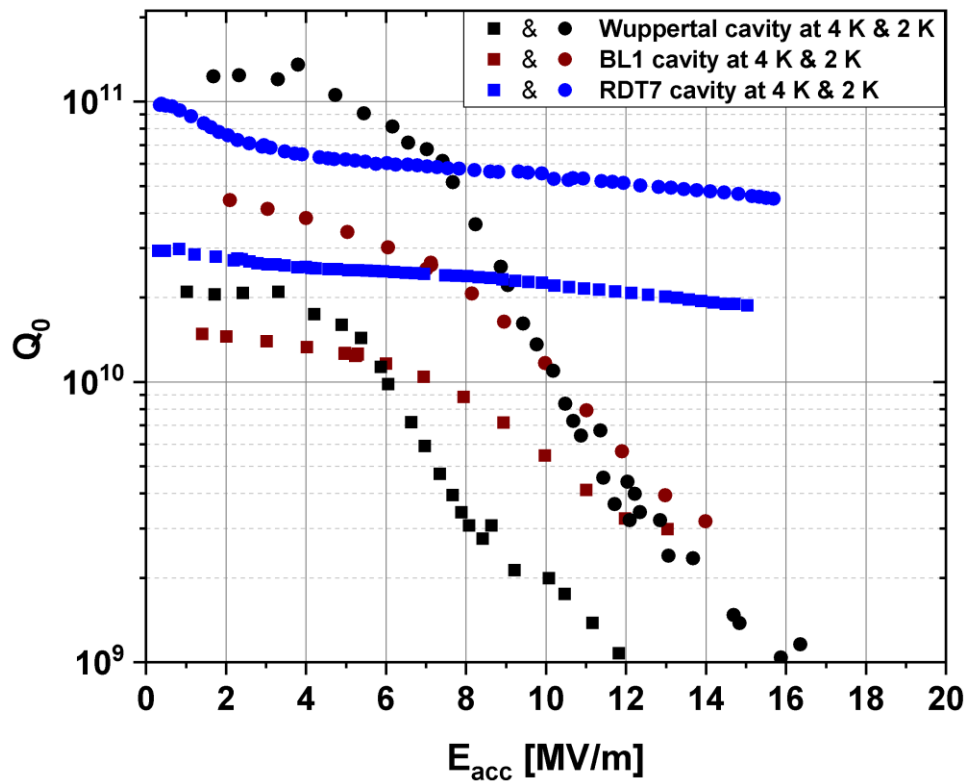


Figure 4.38: Comparison of RF results from RDT7 with previous data with Q-slopes

Next, RDT10 was coated together with RDT2 with a similar setup and parameters used for RDT7. Another witness sample was installed next to RDT10, which more likely represents the cavity coating. Some non-uniformity was visible in the cavity, see Figure 4.39[right]. SEM images from the witness sample, next to RDT10, revealed some patchy regions, as shown in Figure 4.34 [left]. The RF test result of this cavity (not shown here) was very similar to the previous test result of RDT10 exhibiting a Q-slope. Despite having a similar temperature profile compared to the prior coating of RDT7, it is found that the consumed amount of tin was almost half (1.7 g vs. 3.3 g) during RDT10 coating compared to the tin consumed during the previous RDT7 coating. This is consistent with the previous study presented in section 3.1.2 that low flux of tin appeared to result in patchy Nb<sub>3</sub>Sn coating. The reasons behind the lower tin evaporation are not understood completely. We speculate that the reduction in the active surface area of the molten tin pool reduced the evaporation rate. Note that the Mo diffuser used in RDT7 coating broke and was replaced with a new one, which had smaller holes. Also, it was also suspected that the new diffuser has shifted from its original position during the installation into the furnace. Another attempt was made to coat RDT10 again without the diffuser to allow maximum tin evaporation. The cavity was coated uniformly this time, but it was found that Sn was splattered and carried over to the cavity. SEM/EDS analysis of the witness sample confirmed the splattering of tin. The cavity was not tested. The diffuser made from Nb foil, which almost replicated molybdenum diffuser used in RDT7 coating was used in the third attempt to coat RDT10. Supplied tin was reduced based on the RDT7-RDT2 coating experiment, to limit tin vapor at the end of the coating process. Note that each cavity receives ~15 μm removal EP removal between the two coatings to renormalize the substrate surface.

Post-coating inspection showed uniform coating inside the cavity. The Sn consumption was very similar to RDT7 coating. Examination of witness samples, one from

the bottom and another next to the bottom beam pipe of RDT2 showed uniform coating without any tin residue or patches, shown in Figure 4.40. EDS examination showed the usual  $Nb_3Sn$  composition. RF test results from RDT10 now appeared similar to RDT7 except for the quench field, which was lower in RDT10. The latest test results from RDT10 and RDT7 are compared to the ones after their first coating in Figure 4.41.

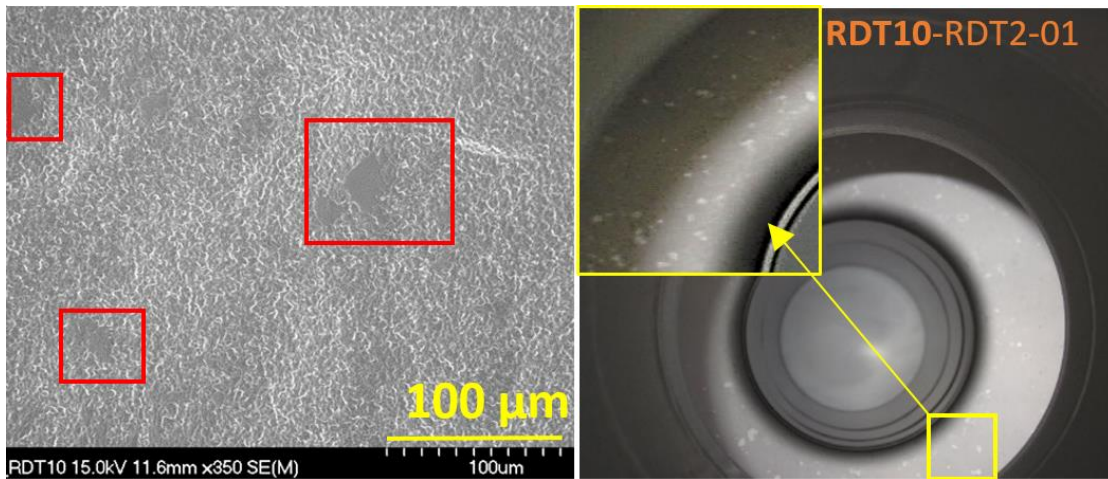


Figure 4.39: RDT10-RDT2 coating. SEM image [left] shows patchy regions observed in the witness sample. Non-uniformity in the coating can be seen in the right picture. Note that the top half cell had less non-uniformity than the bottom.

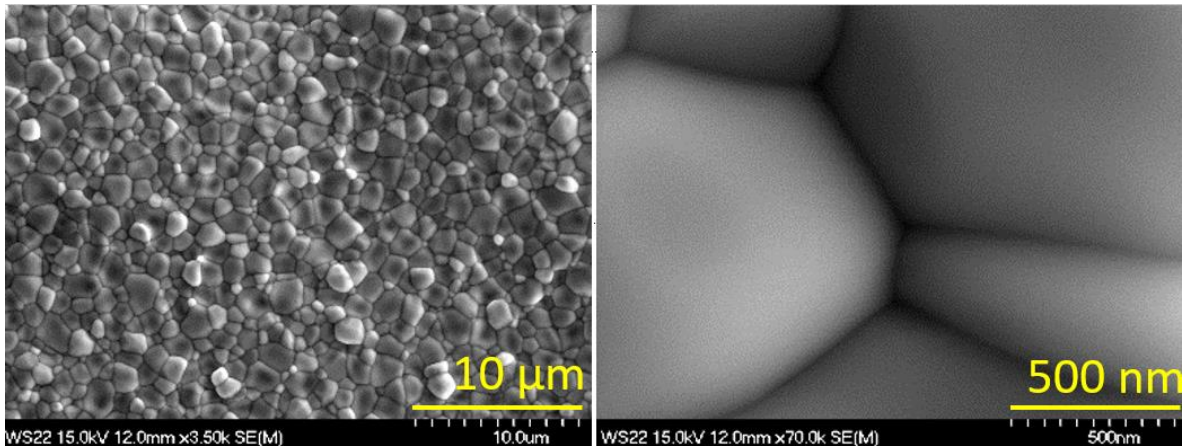


Figure 4.40: SEM images from RDT10-RDT2 coating. Note that there is no Sn residue on the surface [right].

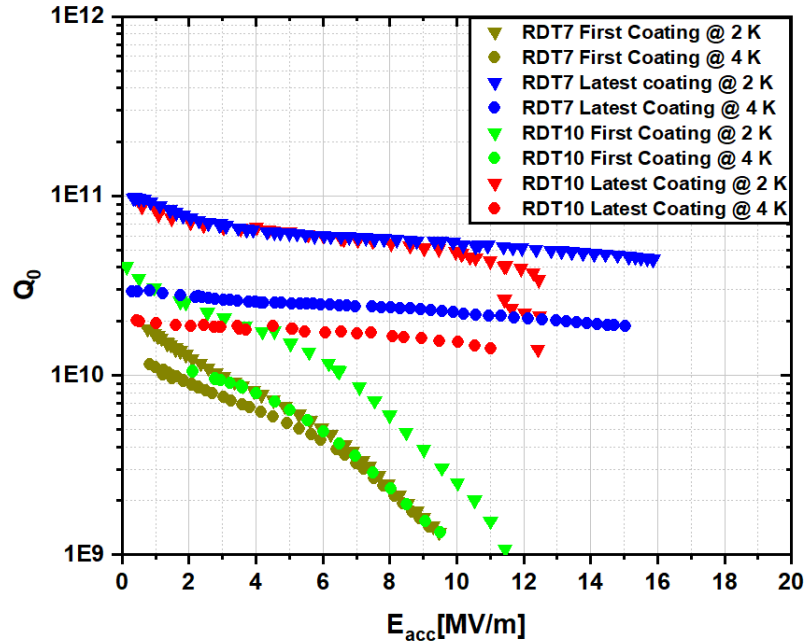


Figure 4.41: Comparison of the latest RF test results from RDT10 and RDT7 with those after their first coating. RDT10 is expected to have higher  $Q_0$  at 4 K than presented here as we expect losses on the flanges because of shorter beam pipes.

#### 4.2.2 Witness sample studies and five cell cavity coatings

Besides the progress made in single-cell cavity coating, an important goal is translating single-cell results into five-cell CEBAF cavities.  $Nb_3Sn$ -coated five-cell CEBAF cavities are suitable to test them at JLab upgraded injector test facility (UITF), which will use one quarter cryomodule to deliver 10 MV energy gain to electron beam.  $Nb_3Sn$  cavities are yet to be tested under an actual accelerator environment. Significantly larger volumes of multi-cell cavities makes it challenging to obtain uniform coatings. Initial attempts to coat five-cell cavities using a protocol similar to that used to coat single-cell cavities revealed an up-down asymmetry in the cavity coating. Cells at the top of the cavity, which were away from the Sn and  $SnCl_2$  source during the process had developed a non-uniform coating, as shown in Figure 4.42. Non-uniformity was mainly seen in the out-of-sight regions of top-cells, farther from the tin source at the bottom. Cells at the bottom were

uniformly coated. For further insight, a witness Nb rod was coated with a five-cell cavity. The rod was located along the cavity axis inside the cavity. Visual inspection of the witness rod was consistent with the non-uniformity inside the cavity surface with a shiny appearance next to top cells of the cavity. The rod was cut into pieces and samples next to each cell were examined with SEM. The coating was uniform up to the center cell of the cavity as shown in Figure 4.43. The density of patches increased progressively from the center to the top.

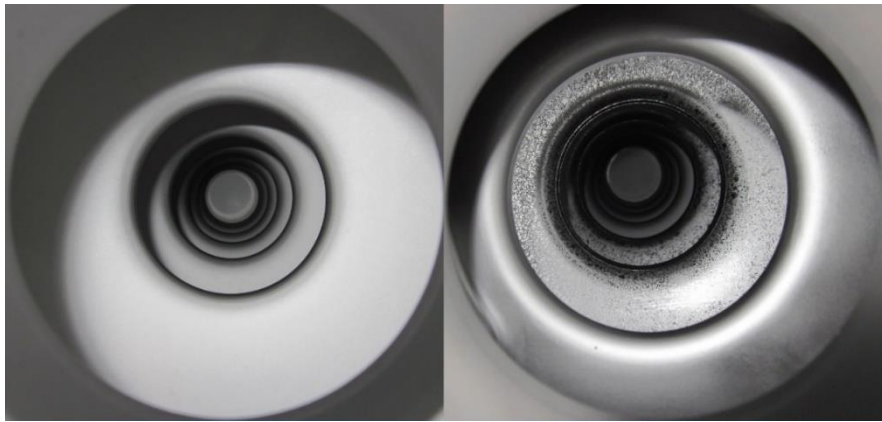


Figure 4.42: Post-coating appearance of IA110. The view from the bottom (next to the Sn source) is on the left. The picture at the left is the view from the top. Up-down asymmetry is evident.

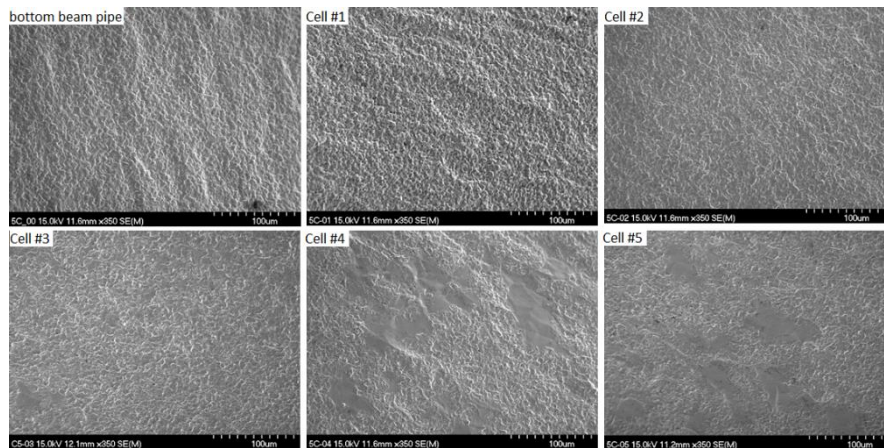


Figure 4.43: SEM images from the witness rod coated with a five-cell cavity. Note the absence of patchy regions in the first few cells.

The visual appearance of the non-uniformity had features similar to those observed in some of the samples produced in previous studies. Such non-uniformity was seen in the “sitting edges” of the sample, where it was supported inside the sample chamber, as shown in Figure 4.44. The examination of witness samples often revealed that the non-uniformity is often correlated with large patchy regions. This observation is consistent with our discussion in section 3.1.2. It indicated that a single source of Sn/SnCl<sub>2</sub> is not sufficient to maintain uniform tin flux inside the cavity.

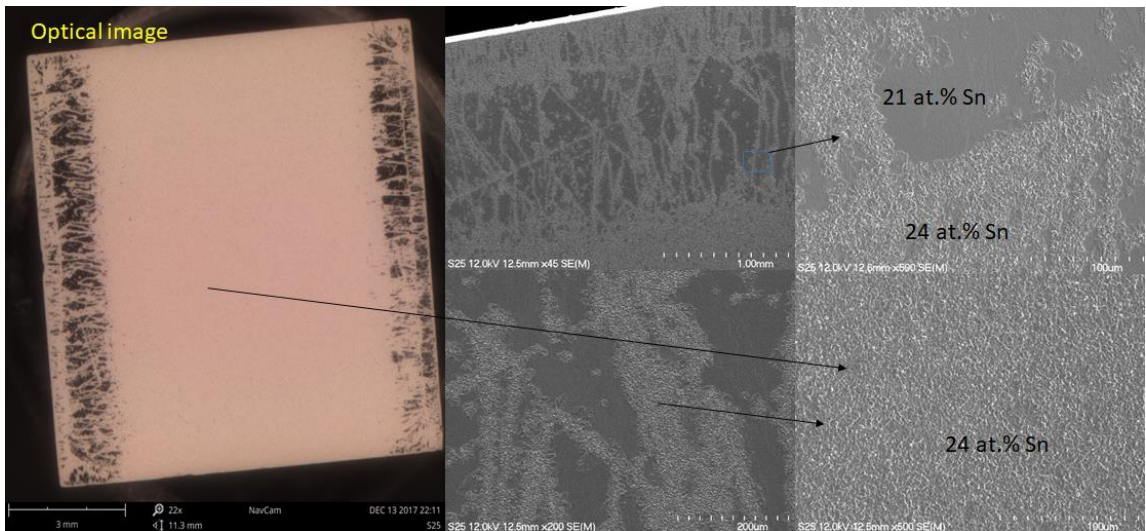


Figure 4.44: Optical and SEM images from a coupon sample. The non-uniform appearance was seen in the sitting edge of the sample. The optical appearance and SEM images are consistent with the non-uniformity seen in the five-cell cavity coatings.

#### **4.2.2.1 Setups with supplementary Sn sources**

The problem of non-uniformity was mitigated by the addition of a secondary Sn source, which hung at about the middle of the cavity by a Nb rod attached to the top cover. It was found that the cavity with up-down asymmetry had a lower  $Q_0$  compared to that of a uniformly coated cavity (Figure 4.45). Quality factors above  $3 \times 10^{10}$  at 4 K and in excess of  $10^{11}$  at 2 K were measured in a nearly evenly coated cavity. Accelerating gradients were limited to 2–5 MV/m. Secondary Sn source reduced the non-uniformity, but also resulted

in Sn nano-residues in witness samples (Figure 4.46). However, the gradient limitations were linked to the pre-existing macroscopic defects in the multi-cell cavities initially used for these studies.

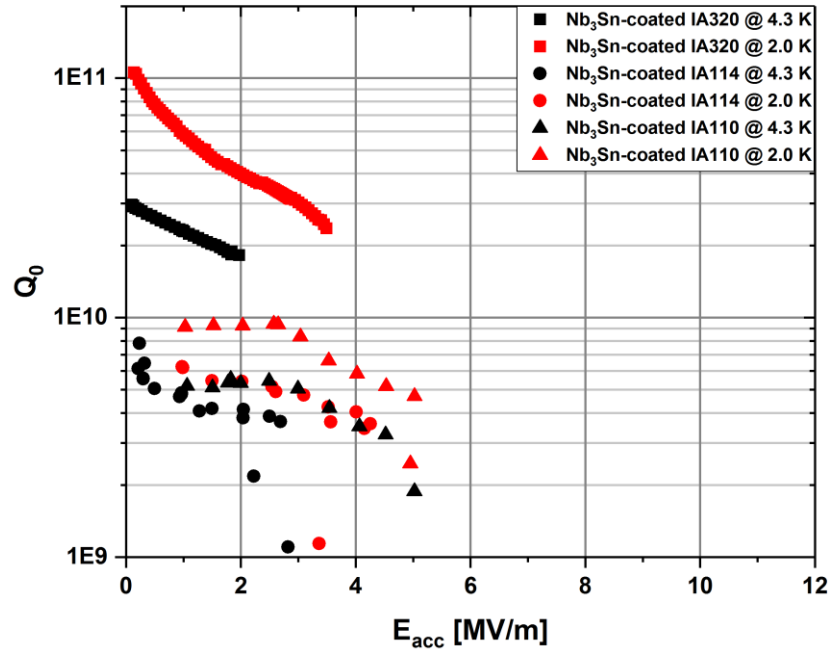


Figure 4.45: Results from the first few five-cell cavities coated at JLab. IA320 was coated uniformly, whereas IA110 and IA114 had up-down asymmetry.

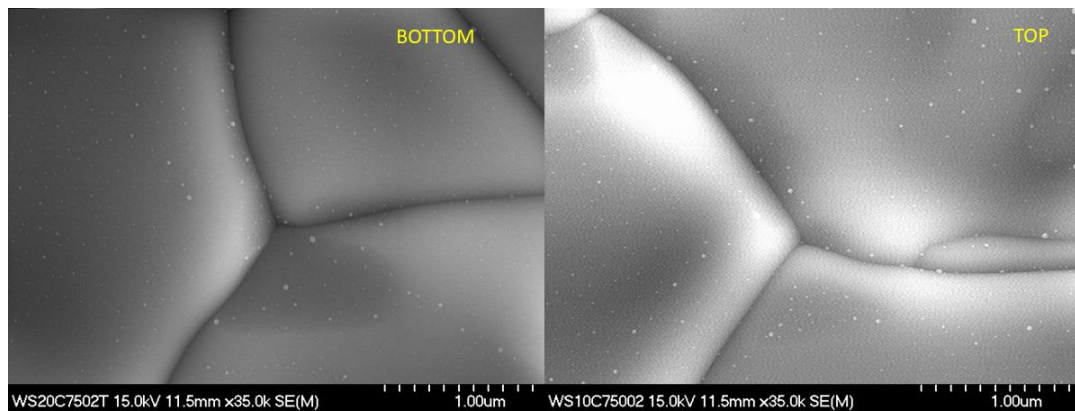


Figure 4.46: Sn residue seen on the surface following the coating with two Sn sources.

Two (C-75 CEBAF) five-cell cavities [128], 5C75-RI-NbSn1 and 5C75-RI-NbSn2, were recently purchased from RI Research Instruments GmbH with a purpose to have a good quality, defect-free Nb substrate. As-received cavities were first subjected to optical

inspection and followed by 120  $\mu\text{m}$  EP and 800  $^{\circ}\text{C}$  baking for 2 h. They further received 25  $\mu\text{m}$  EP before the final HPR. Cavities attained maximum gradients of about 23 MV/m (5C75-RI-NbSn1) and 28 MV/m (5C75-RI-NbSn2), both maintaining  $Q_0 > 10^{10}$  up to 23 MV/m.,cf., previously coated 5-cell cavities had reached  $\sim 10$  MV/m with  $Q_0 < 10^{10}$  in baseline tests.

5C75-RI-NbSn1 was coated first. A few modifications were introduced in the coating process. The supplied amount of tin for the coating was reduced based on our previous experiments to reduce excess tin that would be left at the end of the coating process, which we had concluded was the source of Sn nano-residues on the surface. The coating time was reduced to 6 h instead of 24 h. It was expected to produce a relatively smoother coating with shorter coating time, as discussed in section 3.1.4. Another reason for this change was linked to another study presented in chapter 6, in which Sn-loss from  $\text{Nb}_3\text{Sn}$  coating was discovered following the annealing of coated samples without Sn. Simialr treatment given to a coated cavity also degraded the cavity performance. A temperature gradient of about  $\sim 85$   $^{\circ}\text{C}$  was maintained by adjusting the heating zones, similar to two-cavity coating. The pictures from the interior surface of the cavity are shown in Figure 4.47. Note that the fundamental power coupler side of the cavity resides at the bottom during the coating. The cavity appeared to have a visible non-uniformity in the view from the top. SEM images from a witness sample that was close to the top cell showed patchy regions, as expected for such appearances. Sn residues were still found on the surface, but their density appeared less than those observed in previous five-cell cavity coatings.

A new tin source was added to avoid non-uniformity in the next coating of C75-RI-NbSn2. There were three tin sources inside the cavity: first at the bottom, second around the center, and the third close to the top. The amount of supplied tin was further adjusted.

The coating process otherwise was similar to the previous coating of the C75-RI-NbSn1 cavity. The cavity was coated uniformly this time, as seen in Figure 4.48. SEM examination of witness samples showed no Sn-residues at the surface, Figure 4.49[right]. A witness sample that was close to the top cell showed only a few patchy regions occasionally with otherwise uniform Nb<sub>3</sub>Sn coating, as shown in Figure 4.49[left].



Figure 4.47: Pictures C75-RI-NbSn1 taken from the bottom [left] and the top [right]. The coating looks non-uniform from the top.



Figure 4.48: Pictures from C75-RI-NbSn2 taken from the bottom [left] and the top [right]. The coating looks mostly uniform from each side.

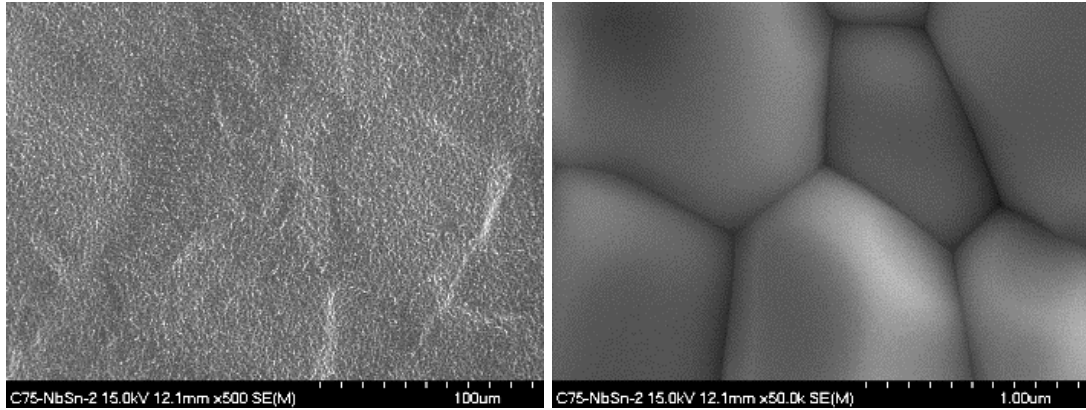


Figure 4.49: SEM images from the witness sample coated with C75-RI-NbSn2. Note the absence of patchy regions [left] and tin Sn-residues [right].

Both cavities were tested at about 4 K and 2 K following a typical cold RF procedure, described in [129]. Test results from both cavities are presented in Figure 4.50. The low field  $Q_0$  is about  $7 \times 10^9$  at 4 K and  $2 \times 10^{10}$  at 2 K for 5C75-RI-NbSn1. 5C75-RI-NbSn2 has a low field  $Q_0$  of about  $1 \times 10^{10}$  at 4 K, and  $2.5 \times 10^{10}$  at 2 K. 5C75-RI-NbSn1 and 5C75-RI-NbSn2 were limited to 9 MV/m and 13 MV/m respectively, both exhibiting a mild Q-slope. The lower quality factor of 5C75-RI-NbSn1 is linked to the presence of patchy regions and Sn-residues. The performance of these cavities shows significant improvements compared to previous results obtained with coated older cavities, Figure 4.45. Both cavities reached accelerating gradients useful to accelerator applications.

### 4.2.3 Discussion

Despite the potential for promising quality factor and accelerating gradient,  $Nb_3Sn$  cavities are vulnerable to precipitous Q-slope. Reported first by Wuppertal University in the 1980s, the cause of such slope, also known as “*Wuppertal slope*,” has not yet been established completely. Jlab followed Siemens configuration with a single heater and active pumping during the coating, which is different from Wuppertal or Cornell setup, but still initially resulted in Q-slopes similar to Wuppertal’s at the beginning. Early studies of

control samples, as well as cutouts from the coated cavity with Q-slope, indicated mostly uniform coatings with a composition close to nominal Nb<sub>3</sub>Sn and it seemed that localized defects were responsible for the slope. The Ti-contamination from Nb-Ti flanges was another potential candidate responsible for the Q-slope. Several (all niobium) cavities coated later resulted in Q-slope, but as discussed above, they were linked with the presence of Sn-residue, patchy regions associated with non-uniformity, and also with macroscopic defects in the starting Nb substrate. Most of those recognized factors were reduced by modifying the coating process optimizing the evaporation, consumption, and distribution of Sn during the coating process.

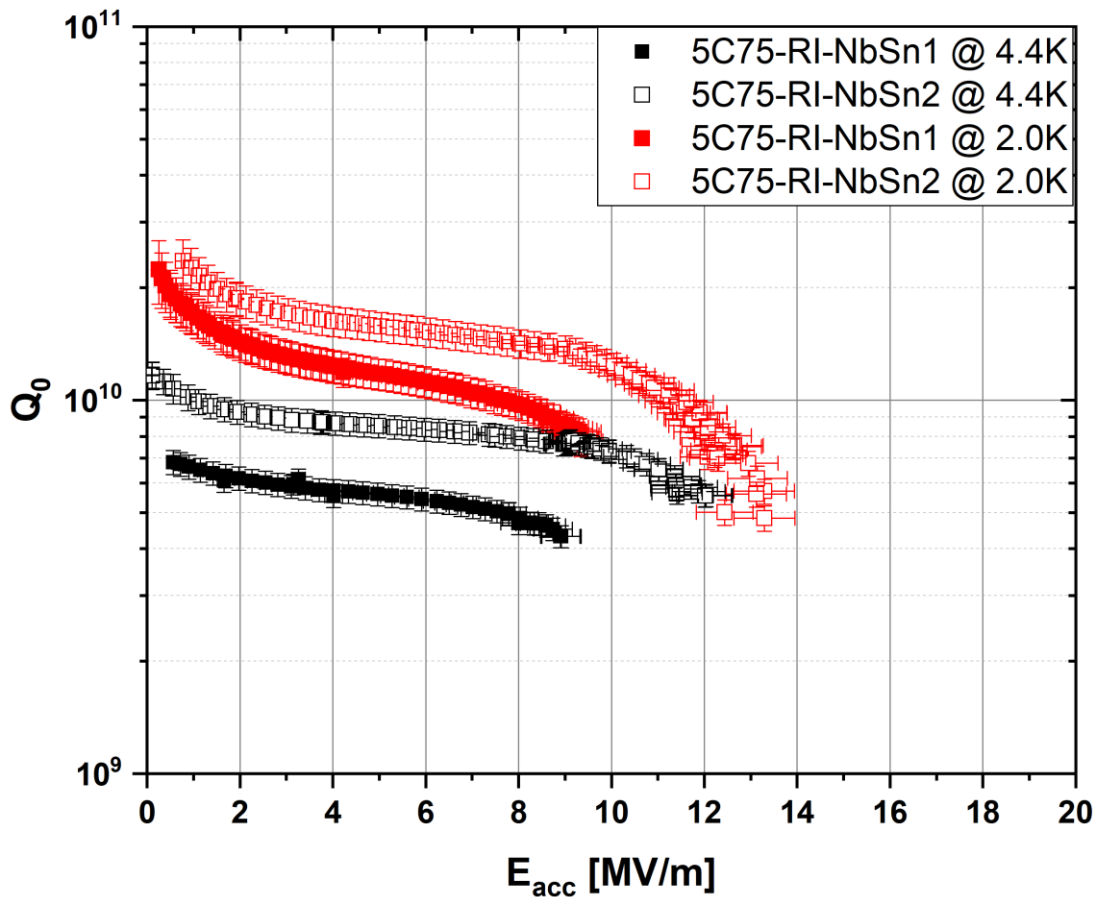


Figure 4.50: Test results from C75-RI-NbSn1 and C75-RI-NbSn2 at 4 K and 2 K.

### 4.3 Conclusions

Several areas with different RF loss characteristics were located with thermometry mapping measurements during the RF test of a Nb<sub>3</sub>Sn-coated cavity. Samples from these areas were extracted and analyzed with materials characterization techniques. RF analysis of the cutout regions showed three systematic trends in surface resistance with increasing accelerating field: weak field-dependent, strong field-dependent, and field-dependent switch (at 4.5 MV/m). Each cutout had similar microstructures, thickness, and composition of Nb<sub>3</sub>Sn. Voids were commonly seen in each cutout extracted from the cavity region but not in the samples from the beam pipes, which also had relatively smaller grain sizes. This indicates that the purity of the niobium substrate influences the growth and microstructural properties of Nb<sub>3</sub>Sn. Several cutouts possess patchy regions with a thinner coating. A higher density of patchy regions was observed in the equator region and seems to result in a surface resistance switch at 4.5 MV/m and strong field dependency. The presence of large regions with carbon contamination also appears to contribute to strong field-dependent surface resistance.

Analysis of witness samples coated with single-cell cavities revealed Sn-rich residues on the surface. In an attempt to reduce Sn residues formation during the coating process, changes were made in to single-cell cavity coating process, which resulted in nearly Q-slope free cavities. The best-coated cavity had a  $Q_0 \geq 2 \times 10^{10}$  at 4 K and  $> 3 \times 10^{10}$  at 2 K before quenching at  $E_{acc} \geq 15$  MV/m. Q-slope free results were reproduced in both experimental cavities, which had Q-slope before. Besides the issues discussed for single-cell cavities, five-cell cavities suffer non-uniformity with the single Sn-source because of larger volume. The addition of extra Sn-source improved the coating uniformity, but also increases the chance to deposit Sn-residue on the surface. With the addition of supplementary Sn sources, quality substrate, and optimum Sn supply, it was

possible to produce a five-cell cavity reaching  $E_{acc}$  above 10 MV/m without a significant Q-slope.

$Nb_3Sn$  cavities are vulnerable to precipitous Q-slope, which appeared to be caused by several factors, including possible Ti-contamination, non-uniformity, and accumulation of Sn-residues on the surface. The coating uniformity and residual accumulation at the surface were reduced by modifying the coating process, which improved the performance of both single-cell and multi-cell cavity. Evaporation, consumption, and distribution of Sn during the coating delicately affect the resulting coating, which can significantly impact the RF performance of the cavity. The significant performance difference between the old five-cell cavities (with pre-existing defects) and the new five-cell cavities (without obvious defects) points out to have quality substrates for better RF performance.

We discussed the characteristics of the coating process and produced coatings so far. As it was exposed, it is challenging to engineer near-perfect coating surfaces, favorable for an excellent RF performance, without some kind of post-coating treatments that could improve the surface quality. We will explore several post-processing techniques developed for Nb cavities in the next chapter to improve surface properties, mainly to produce clean and smooth surfaces.

## CHAPTER 5

### **Post-coating Treatments of Nb<sub>3</sub>Sn-coated Nb**

It has been pointed out that the peak surface magnetic field in an RF cavity can locally exceed the critical field due to field enhancement at microstructures on the RF surface [121, 130, 131]. Sharp changes in topography such as those at step edges, terraces, grain boundaries, and peaks and valleys, are sources of the field enhancement. The continuous distribution of nano-defects can suppress the superheating field everywhere [122]. The cleanliness is equally important as the smoothness of the RF surfaces [130, 131]. State-of-the-art cavity fabrication and processing of Nb cavities emphasizes obtaining a very smooth as well as clean surfaces. Several post-processing techniques (EP, BCP, baking, impurity doping, etc.) have been developed for Nb cavities to enhance cavity performance [132–135]. Some provide control over cleanliness and topography of the final RF surface, and others help to have chemically favorable conditions near-surface for better performance.

The vapor diffusion process used here produces somewhat rough surfaces of Nb<sub>3</sub>Sn because of the microstructure. The typical appearance of grains is faceted, and grooved grain boundaries are present throughout the surface. In previous chapters, we described several topographic characteristics of coated surfaces resulting from different processing conditions. The characteristic roughness appears to have no dependence on the initial substrate treatments. We found that reduction of grain boundaries (larger grain

size) correlates with an increase in average surface roughness. The AFM image in Figure 5.1 highlights the topography of a Nb<sub>3</sub>Sn-coated surface. The presence of pits with sharp edges seen here is most likely detrimental to RF performance.

Another problem we encountered was the accumulation of Sn-residues on RF surface during the coating of single-cell and multi-cell cavities. Analysis of C3C4 cutouts (Section 3.2) revealed that contamination present on the substrate surfaces could transfer to the coated surface. The controlled removal of the top few layers of a coated surface may also reduce surface defects and contamination by exposing a good quality Nb<sub>3</sub>Sn underneath. The development of post-coating treatments that can help to manage the topography of Nb<sub>3</sub>Sn coated surfaces, leading to smoother, cleaner, or both, is highly desirable. Such treatments are expected to improve the quality of as-coated surfaces resulting in better RF performance.

Oxypolishing was explored both at Siemens and Wuppertal [47, 51, 53]. Siemens researchers had often seen remarkable improvement of  $Q_0$  at 1.5 K, in the regime of residual resistivity compared to that at 4.2 K [53]. One of the explanations was that the treatment was able to remove the contaminated layer of Nb<sub>3</sub>Sn (from sealed-off quartz ampulla) which resulted in better performances. In other studies, they observed pitting within the grains and grain boundaries following oxypolishing treatments with a total anodization voltage of about 200 V [69]. Performance degradation of about 50% for  $Q_0$  and the onset  $E_p$  was reported from Wuppertal after 20 V oxypolishing [47]. Several cycles of HF immersion followed by water rinsing and mechanical polishing (CBP) at Cornell resulted in a substantial increase in Q-slope, limiting both the  $Q_0$  and  $E_{acc}$  [86]. Sample studies were started recently at JLab and Cornell to understand the effect of different post-coating treatments, including EP, BCP, and oxypolishing [136–139].

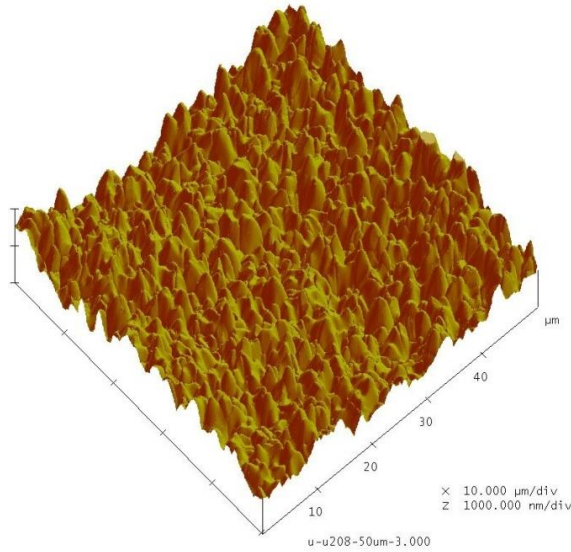


Figure 5.1: Typical topography of a Nb<sub>3</sub>Sn coating.

The thin film coating poses unique challenges in applying any material removal or surface processing techniques. Many established techniques developed typically for pure bulk metals may not produce the same action because of the compound nature of Nb<sub>3</sub>Sn. The limited thickness of the coating layer is another significant challenge as it allows only a few microns thick materials to process.

We have explored several techniques on as-coated Nb<sub>3</sub>Sn coating, aiming at smooth and clean surfaces. We primarily analysed the effect of several techniques (BCP, EP, and oxypolishing) used on Nb cavities. We also investigated the effect of annealing and acid treatments (HF, HNO<sub>3</sub>, and HCl) on coated surfaces. Nb<sub>3</sub>Sn samples to be discussed in this chapter were produced in several different coating experiments, discussed in previous chapters.

## 5.1 BCP

Standard BCP solution, a mixture of 49% HF, 70% HNO<sub>3</sub>, and 85% H<sub>3</sub>PO<sub>4</sub> by volume ratio of 1:1:1 or 1:1:2 was applied to Nb<sub>3</sub>Sn coated samples. The treatments were done for 5 seconds at 17 °C, which corresponds to the Nb removal rate of ~ 8 or 3 μm/min

for 1:1:1 or 1:1:2 BCP solution respectively [140]. BCP (1:1:1) was done for 16, 32, or 50 s on Nb<sub>3</sub>Sn coated samples to observe stripping of the coating substrate for re-use in next coating.

The surfaces resulting from 5 s flash BCP experiments are shown in Figure 5.2. It is evident that the BCP solution rapidly attacked the Nb<sub>3</sub>Sn surfaces. The surfaces are rougher because of non-uniformly etching. The distinct appearance of the surface obtained after 5 s of 1:1:1 BCP compared to that with 1:1:2 BCP solution may stem from the higher etching rate with 1:1:1 BCP solution. Note that, the sample U128 was given extra HF rinse for 30 minutes after 1:1:2 BCP as it appeared dark brownish after the initial treatment. HF rinse did not change that visual appearance. Some grains in U128 showed features consistent with HF rinsed samples, discussed later. EDS measurement shows a similar composition prior to the treatment indicating residual Nb<sub>3</sub>Sn layers on the surface. XPS ratios of Nb to Sn were found to be 3.08 and 3.52 for U128 and U162, shown in Figure 5.2.

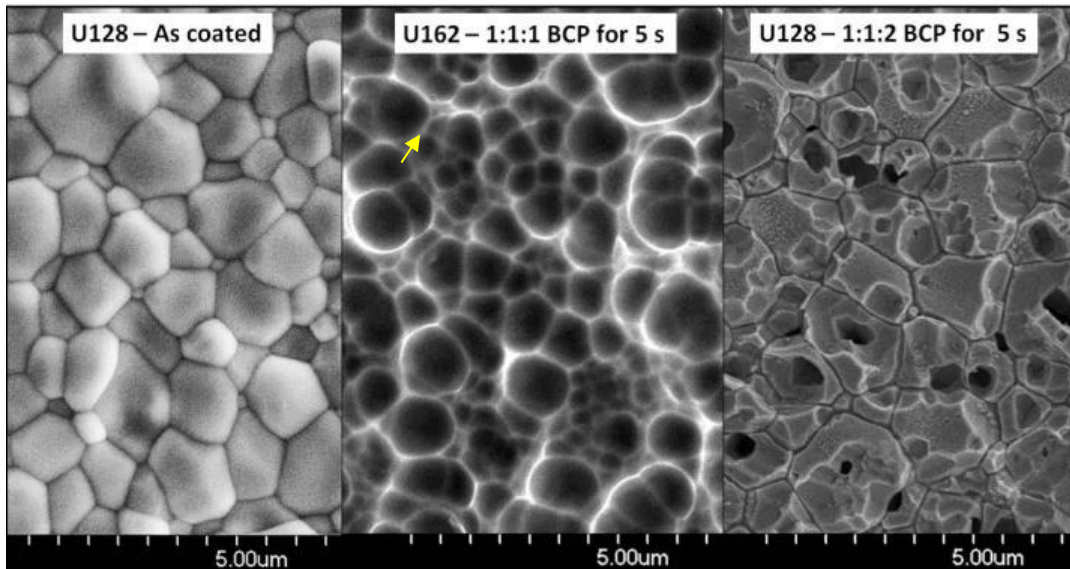


Figure 5.2: SEM images of Nb<sub>3</sub>Sn coated samples before and after flash BCP for 5 seconds. Note that darker areas represent the concave structures in sample U162, which were confirmed with AFM. Bright curves are sharp edges.

Evolution of surfaces following longer 1:1:1 BCP (for 16, 32, or 50 s) is shown in Figure 5.3. The structure seen after 5 s of 1:1:1 BCP appeared to evolve into a honeycomb structure after 16 s. Sub grain faceting was observed after 32 s, and these structures get bigger after longer BCP for 50 s. EDS shows complete removal of the coating layer following 32 s 1:1:1 BCP. It indicates that a minimum of 10  $\mu\text{m}$  BCP may be needed to renormalize the substrate Nb.

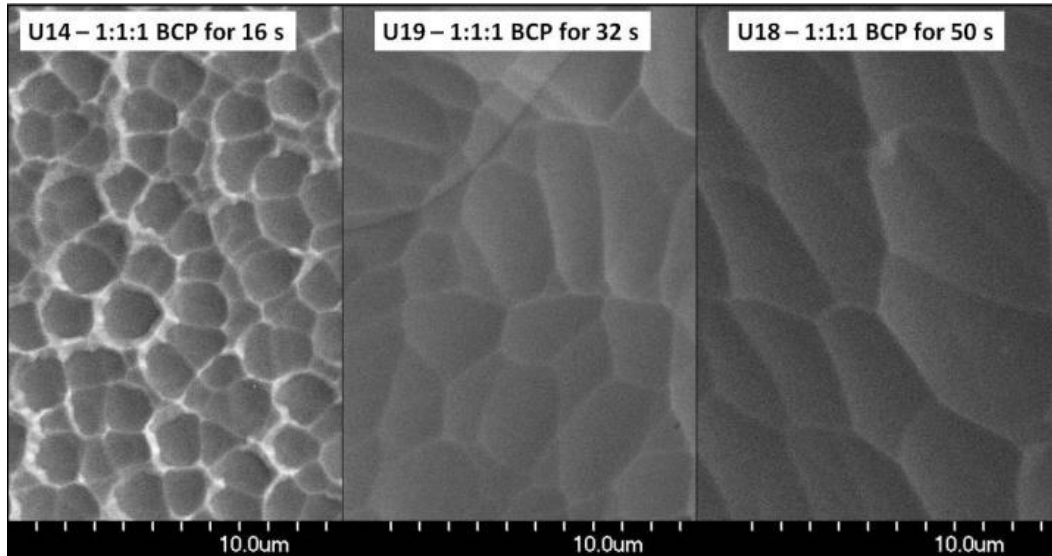


Figure 5.3: Evolution of  $\text{Nb}_3\text{Sn}$  coated Nb following BCP.

## 5.2 Electro-chemical Treatment

Electropolishing (EP) is another successful technique used on Nb cavities for material removal and for smoothing of the surface [141–143]. Typical EP for Nb consists of 1:9 or 1:10 volume ratio of the mixture of 49% HF and 95–98%  $\text{H}_2\text{SO}_4$  with current density 30–100  $\text{mA}/\text{cm}^2$  [140, 143]. A typical I-V curve for electropolishing treatment, shown in Figure 5.4, consists of three major regions that depend on the applied cell voltage [144]. The first region from  $V_a$ – $V_b$  results in etching. The plateau between  $V_b$  and  $V_c$  is the region where the polishing effect is achieved. Higher voltages beyond  $V_c$  involve the evolution of gaseous oxygen. The area around  $V_b$  often has an oscillating current.

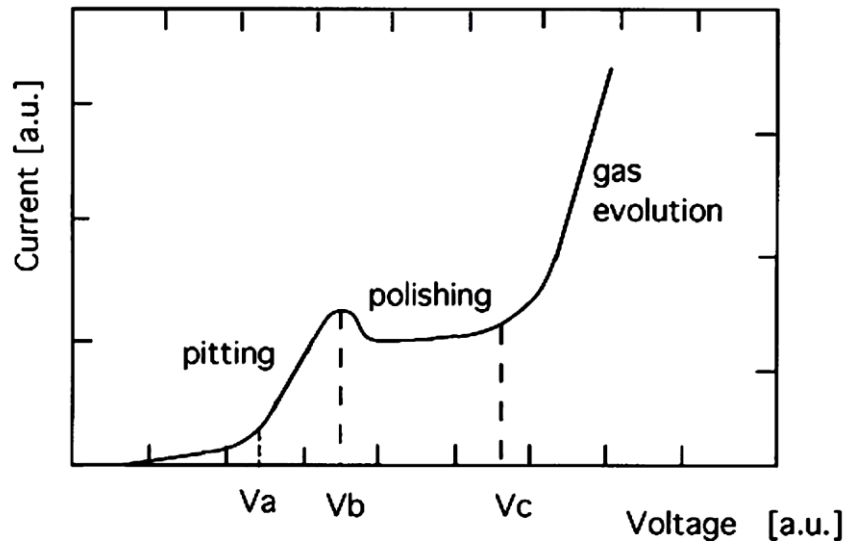


Figure 5.4: Typical I-V characteristics for electropolishing [144].

$Nb_3Sn$  coated samples were treated first in a standard 1:10 EP solution at room temperature for 15 and 30 minutes without applied voltage. Subsequent SEM/EDS examination of the samples revealed no apparent change in composition or microstructure of the surface, indicating the stability of  $Nb_3Sn$  in the electropolishing solution. An exploratory electrochemical treatment was given to a sample in a standard EP solution with a cell voltage of 8.5 V at 6 °C for one minute, similar to the one that is used to polish Nb samples. The surface appeared smoother compared to untreated sample in SEM images (not shown here). Non-uniform etching pits that were obtained with flash BCP were absent from this surface. EDS examination did not find any difference in composition following the treatment. XPS measurement shows Nb to Sn ratio of about 2.95, which was similar in another sample dipped in EP solution without applied voltage. These initial observations motivated for further experimental investigations described below.

The experimental setup for electrochemical treatments consisted of an electrolyte solution in a polytetrafluoroethylene (PTFE) container, an aluminum or graphite cathode, and the  $Nb_3Sn$ -coated sample as an anode. A schematic of the experimental setup is

shown in Figure 5.5. Similar to typical electropolishing of Nb, a 1:10 volume ratio of the mixture of 49% HF and 98% H<sub>2</sub>SO<sub>4</sub> was used as an electrolytic solution. Since the first goal of this work was to determine the possibility of electropolishing Nb<sub>3</sub>Sn coatings, current-voltage (I-V) characteristics of the process were measured using Gamry Instruments Reference 3000 potentiostat controlled with a commercial software package.

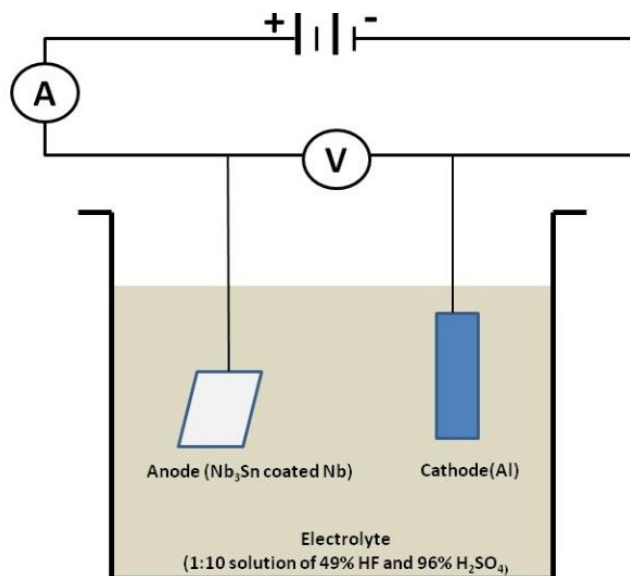


Figure 5.5: Experimental setup used for electro-chemical treatment.

A cylindrical Nb sample and an identical Nb<sub>3</sub>Sn-coated sample coated at 1200 °C for 6 hours were used to measure the I-V characteristics at 21 °C. The comparison of current densities for applied voltages from 0 to 8 volts is presented in Figure 5.6. This measurement was limited to 8 volts to avoid complete removal of Nb<sub>3</sub>Sn. Data acquisition time was 80 seconds for this measurement. SEM/EDS examination of the sample following the measurement of the I-V characteristics confirmed that the Nb<sub>3</sub>Sn layer was not stripped completely. As shown in Figure 5.6, both the Nb and Nb<sub>3</sub>Sn-coated sample have similar I-V characteristics. The constant current density plateau suggests a possible polishing region beyond 3.5 V. This measurement was found to be reproducible. The extended I-V characteristics measurement up to 20 V appeared like that of Nb.

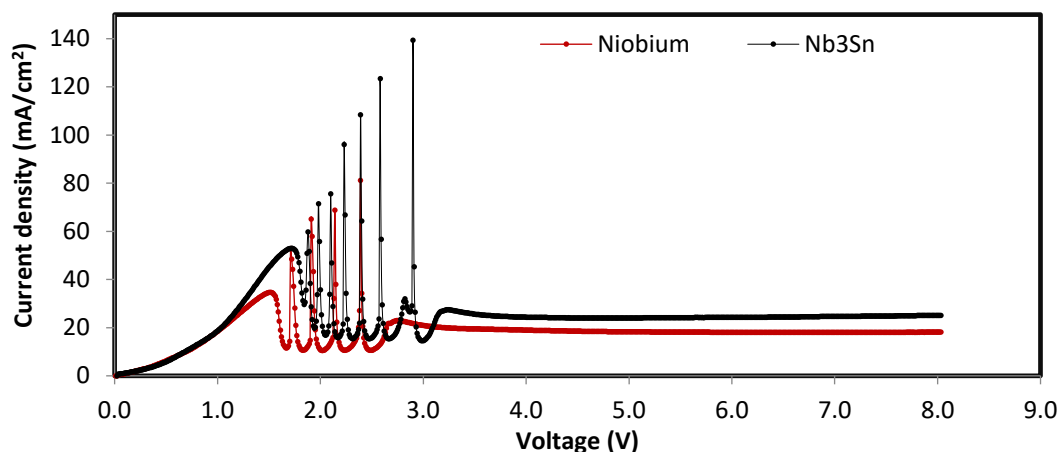


Figure 5.6: I-V characteristics for Nb and Nb<sub>3</sub>Sn-coated Nb samples.

Following the I-V measurement, Nb<sub>3</sub>Sn-coated samples U187, U199, and U202 (BCP Nb coated for 6 hours at 1200 °C) were electropolished at 6.5 V for 1 minute, 2 minutes and 3 minutes, respectively. The surfaces obtained for each sample following the treatments, along with as-coated reference sample U208, are shown in Figure 5.7 and Figure 5.8: Nb<sub>3</sub>Sn-coated samples after 2 min (U199–first row) and 3 min of electrochemical treatment (U202–second row) at 21°C. The first rows of images represent 50 μm × 50 μm scan areas whereas second rows images represent 10 μm × 10 μm scan areas. Note that the reference sample U208 had tin residues on the surface. Topographic modification from each treatment was evident, with a smoother appearance of treated surfaces compared to untreated surfaces, when examined with SEM. Grain boundaries were less prominent, and grain facets were less steep after each treatment. AFM measurements of roughness are tabulated in Table 5.1. A roughness reduction is evident after the treatment. The measured R<sub>q</sub> from a 50 μm × 50 μm scan area decreased from 300–500 nm for the as-coated sample to 225–350 nm after one minute of treatment, 180–220 nm after 2 minutes of treatment and 130–290 after 3 minutes of treatment. A similar trend also emerged in 10 μm × 10 μm scans, indicating a roughness reduction. Measured current density during these experiments was ~ 30 mA/cm<sup>2</sup>. Note that the estimated rate

of removal for Nb<sub>3</sub>Sn (14.5 nm/minute per mA/cm<sup>2</sup>) was slightly higher than Nb (13.5 nm/minute per mA/cm<sup>2</sup>). The estimation assumes the nominal composition of Nb<sub>3</sub>Sn, and it does not change the stoichiometry following a treatment.

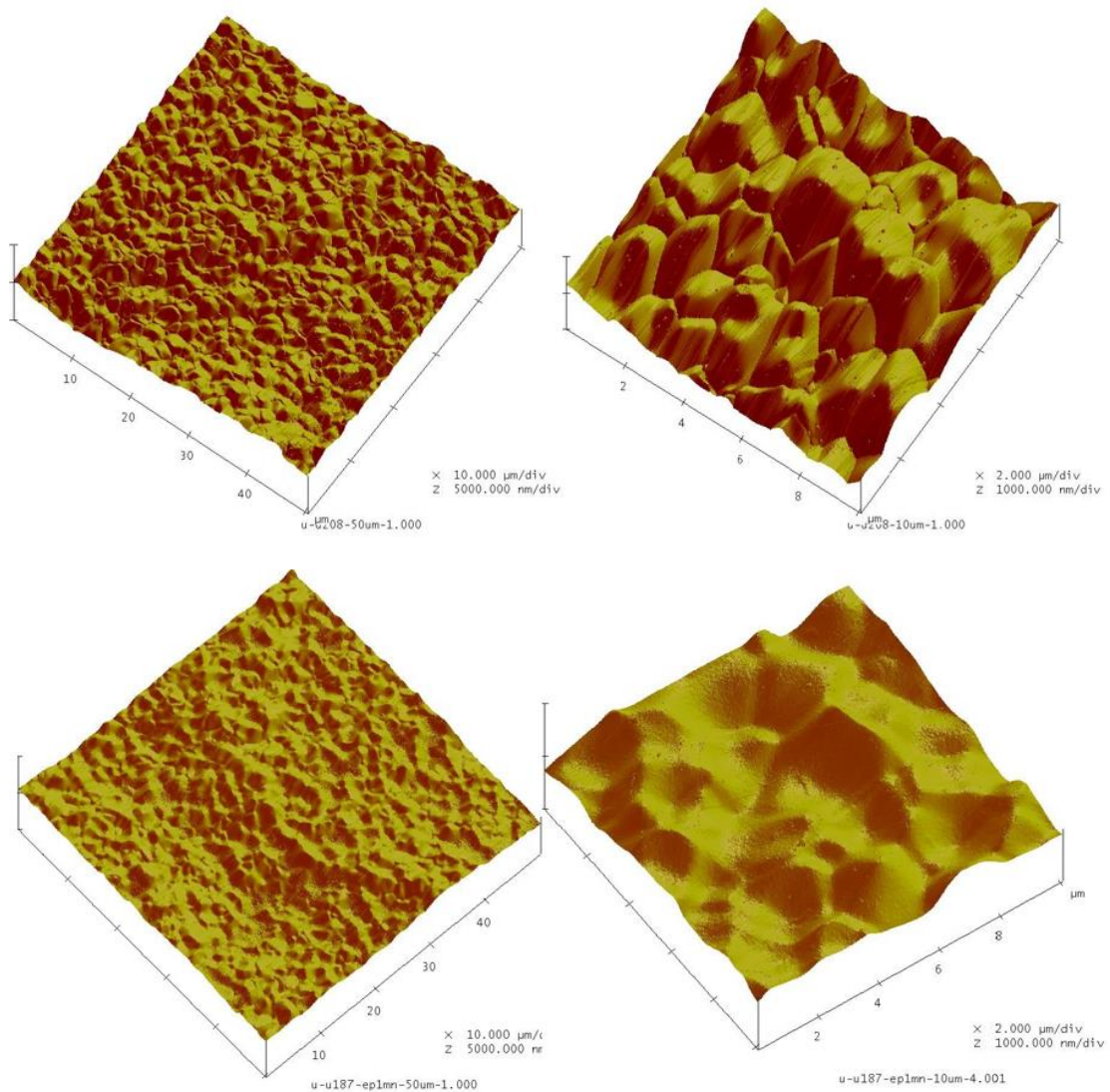


Figure 5.7: Nb<sub>3</sub>Sn-coated samples before (U208–first row) and after 1 min of electrochemical treatment (U187–second row) at 21 °C.

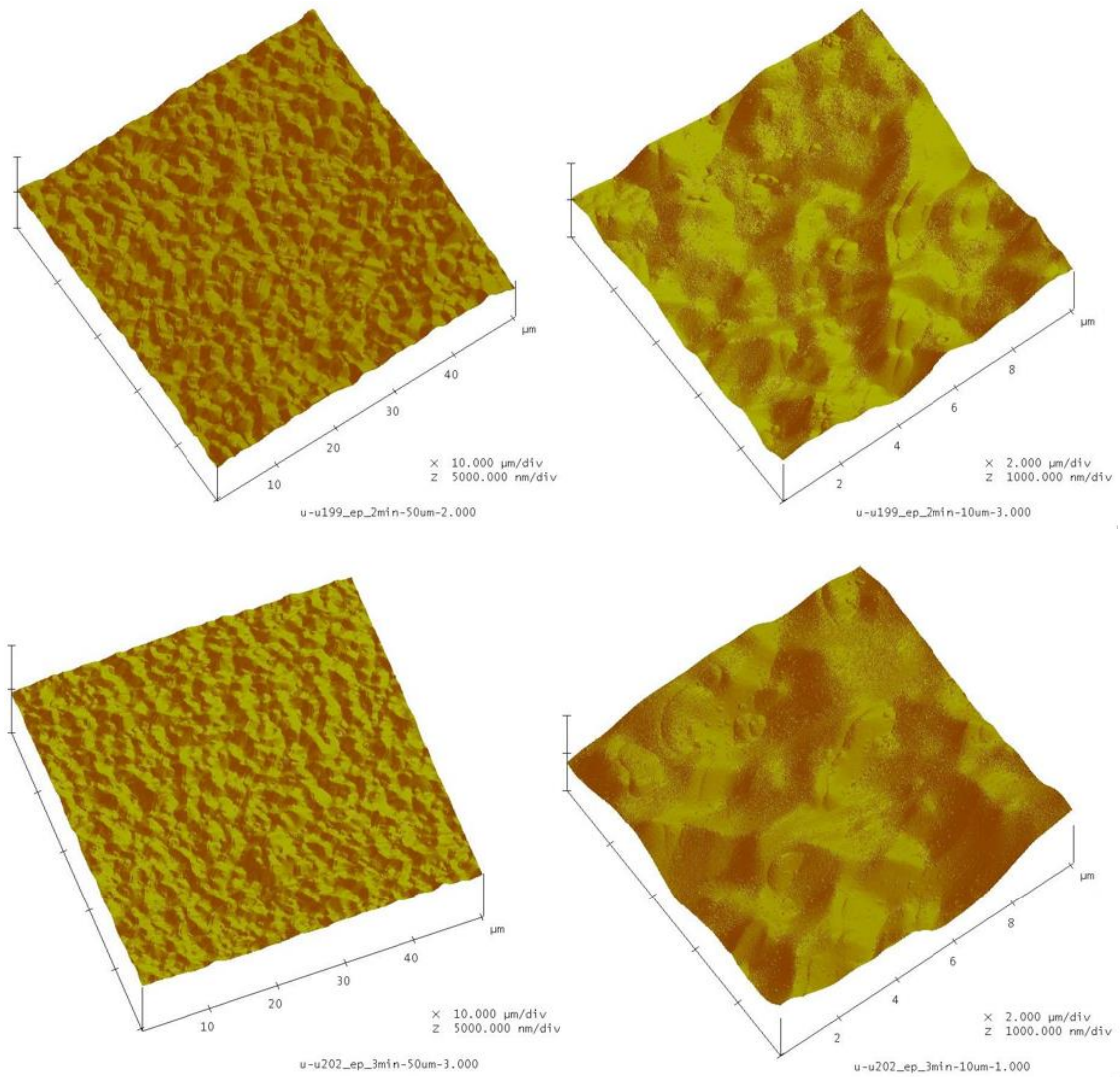


Figure 5.8: Nb<sub>3</sub>Sn-coated samples after 2 min (U199–first row) and 3 min of electrochemical treatment (U202–second row) at 21°C. The first rows of images represent 50 μm × 50 μm scan areas whereas second rows images represent 10 μm × 10 μm scan areas.

Table 5.1: Roughness of samples before and after electrochemical treatment at 21 °C.

	U208 As coated	U187 1 min EP	U199 2 min EP	U202 3 min EP
$R_q$ nm (50 $\mu$ m x 50 $\mu$ m)	296	225	179	286
	340	310	199	183
	285	261	159	129
	474	346	220	150
$R_q$ nm (10 $\mu$ m x 10 $\mu$ m)	162	112	80	144
	224	142	133	156
	168	175	88	103
	177	117	108	81

In the second set of experiments, the electrolytic solution was cooled down to 1 °C in an ice bath in order to lower the current density. The current density varied between 15–20 mA/cm<sup>2</sup> during the second set of experiments. That gives the removal rate of 220–290 nm per minute. Samples U107, U152, U208, and U214 were electropolished with an applied voltage of 6.5 V for 1, 1.5, 2 and 2.5 minutes at 1 °C, 3 °C, 4 °C and 5 °C, respectively. Note that samples U208 and U214 were coated in the same experimental run as U187, U199, and U202. U107 and U152 were nanopolished and coated with the usual protocol (1 h of nucleation at 500 °C and 3 h of coating at 1200 °C). In contrast to the samples that received BCP treatment prior to the coating, there appears to be no significant roughness variation location to location in coated nanopolished samples. Figure 5.9 shows the AFM images of as-coated and treated samples. Treated surfaces appeared smoother than as-coated surfaces like the first set of experiments. As shown in Table 2, the roughness measurements from the two scan sizes are similar. Comparing nanopolished samples, the range of measured values for  $R_q$  of a 50  $\mu$ m x 50  $\mu$ m scan

decreases from 175–198 nm for the as-coated sample to 109–131 nm after 1.5 minutes of electropolishing. Significant roughness reduction was also observed in U208 and U214 following the treatment.

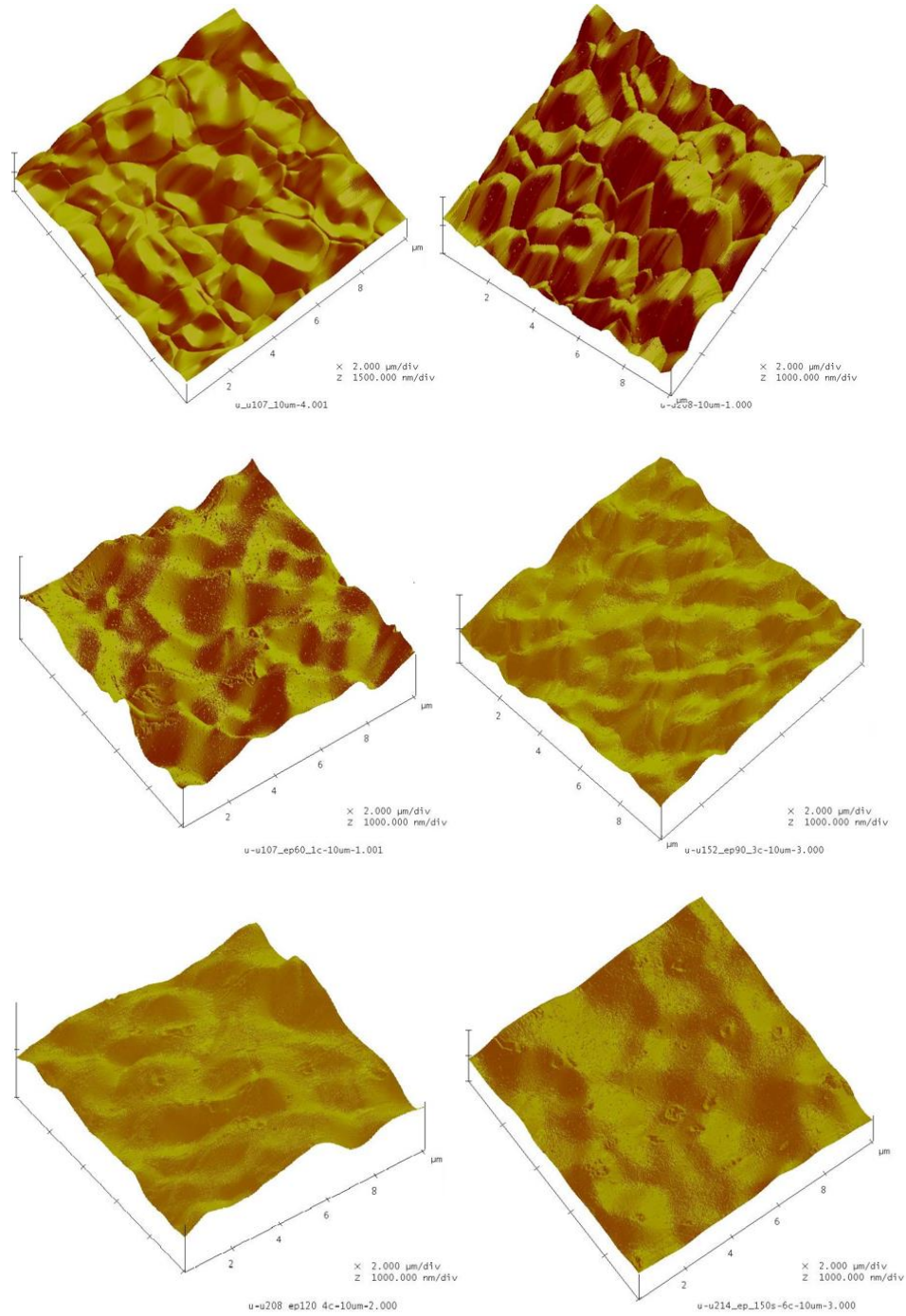


Figure 5.9: Nb<sub>3</sub>Sn-coated samples before and after electrochemical treatment at < 6 °C. Images obtained from as-coated samples U107 and U208 are shown in the first row.

Samples in the first and second columns respectively received NP and BCP before the coating. Samples U107, U152, U208, and U214 received 1, 1.5 and 2 and 2.5 minutes of treatments, respectively.

PSD was calculated for 3 of each 50  $\mu\text{m} \times 50 \mu\text{m}$  scans from samples prepared in identical conditions following the treatment. The obtained log-log plot is shown in Figure 5.10. Note that the area under the PSD curve corresponds directly to root-mean-square (RMS) roughness. The reduction of roughness usually is evident for each spatial frequency, but some scans had some deviation (e.g. U208 in high-frequency regime, Figure 5.10). Each sample was examined using EDS following the experiment. Following electrochemical treatment,  $24 \pm 1$  atomic percent tin was still found in each sample, indicating no significant change in composition. Note that the lateral and depth resolution of EDS are on the order of a micron, so minor variations in composition at the surface may not be discernible. Some residue-like surface features were seen on some samples following treatment.

Table 5.2: Roughness of samples before and after electrochemical treatment < 6 °C.

	U107 No EP	U107 1 min EP at 1 °C	U152 1 min EP at 3 °C	U208 2 min EP at 4 °C	U214 2.5 min EP at 5 °C
$R_q$ nm (50 $\mu\text{m} \times 50 \mu\text{m}$ )	196	148	109	242	182
	192	87	109	273	157
	175	142	111	306	162
	198		131	237	
$R_q$ nm (10 $\mu\text{m} \times 10 \mu\text{m}$ )	194	130	109	131	102
	197	57	111	128	94
	164	123	97	104	75
	181		110	148	

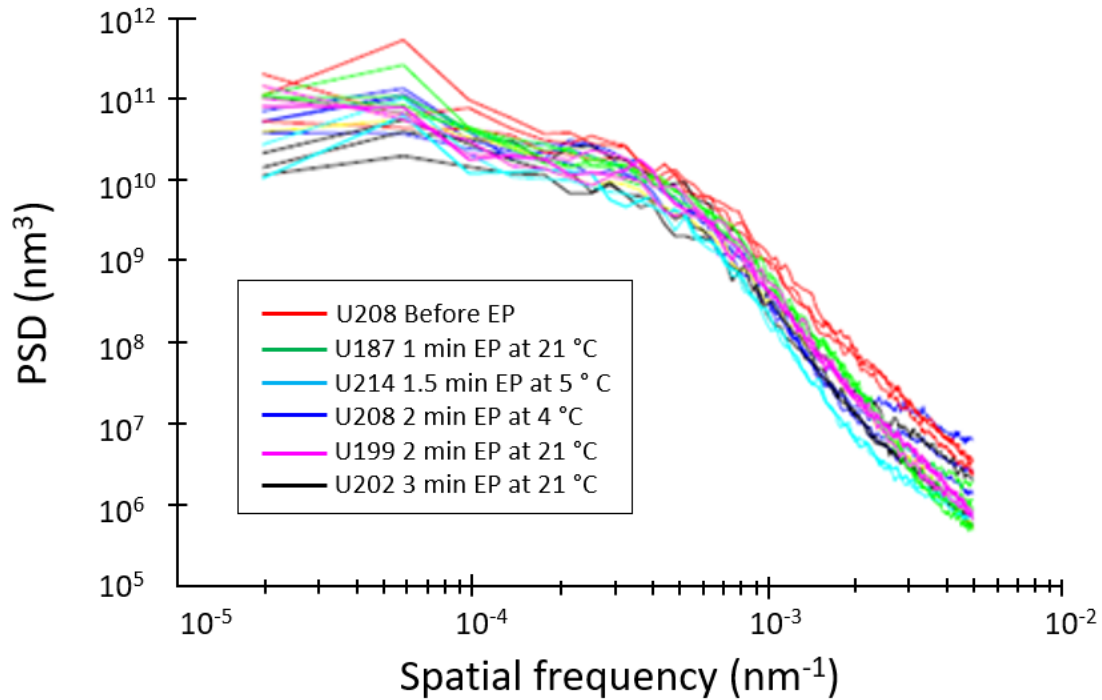


Figure 5.10: Comparison of PSDs from Nb<sub>3</sub>Sn coated samples before and after EP. Note that all the samples were coated in the same run.

Next, the volume ratio of 49% HF and 98% H<sub>2</sub>SO<sub>4</sub> in the electrolytic solution was varied as 1:49, 2:48, 3:47, or 4:46. Since, decreasing of HF volume ratio results in lower anodic current density, it was expected to lower the removal rate, making it suitable to process a thin layer of coating. The expected removal rate for each electrolytic solution was estimated from the anodic current density data reported elsewhere for Nb electropolishing with different ratios of acid solution [141]. The anodic plateau current density falls approximately linearly with the reduction of the HF/H<sub>2</sub>SO<sub>4</sub> volume ratio. Nb<sub>3</sub>Sn coated samples were electropolished in each solution for the approximately targeted removal of 50–500 nm. Expected removal rates were ~70, 130, 200 or 240 nm/min with 1:49, 2:48, 3:47 and 4:46 volume ratio of 49% HF and 96% H<sub>2</sub>SO<sub>4</sub> respectively. A fixed voltage of 6.5 V was used for each treatment. The temperature of

electrolyte was within 22–25 °C at the beginning, which occasionally changed by 1–2 °C by the end of the experiment.

The first set of samples prepared in the same coating run was subjected to electropolishing in 1:49, 2:48, 3:47 EP solution for ~ 50 nm and 200 nm removal. A comparison of roughness before and after treatments is presented in Table 5.3. It appears that the roughness slightly increased or stayed the same following each treatment. Surfaces after the EP treatment in 1:49 solutions are shown in Figure 5.11, see (b) and (c). Grains appeared to develop some new features following the procedure, which may have increased the roughness. Similar removal was attempted in another set of coated samples, prepared in the same coating run with a 4:46 EP solution. XPS examination revealed Nb to Sn ratio of 3.54 and 3.55 following 200 nm and 500 nm removal. The roughness reduction here after each treatment as evident in 50  $\mu\text{m} \times 50 \mu\text{m}$  scans is shown in Table 5.3. It indicated a modest surface smoothing. AFM images from these treatments are shown in Figure 5.11, see (e), (f), and (g). Note that the suspected tin residue disappeared after 50 nm EP in this case. A similar set of coated samples was also electropolished for ~ 500 nm material removal in each mixture of acid solution. The roughness presented in Table 5.3 shows a roughness reduction in each case. Minimum roughness was achieved with a 4:46 EP solution.

Table 5.3: Averaged root mean square roughness ( $R_q$ ) of samples after ~ 50nm, 200 nm, and 500 nm EP removal. Note that the  $R_q$  value of similar untreated sample was  $(251 \pm 39)$  nm and  $(328 \pm 10)$  nm for  $10 \mu\text{m} \times 10 \mu\text{m}$  and  $50 \mu\text{m} \times 50 \mu\text{m}$ , respectively.

	50 nm removal		200 nm removal		500 nm removal	
	$R_q$ nm ( $10 \times 10 \mu\text{m}^2$ )	$R_q$ nm ( $50 \times 50 \mu\text{m}^2$ )	$R_q$ nm ( $10 \times 10 \mu\text{m}^2$ )	$R_q$ nm ( $50 \times 50 \mu\text{m}^2$ )	$R_q$ nm ( $10 \times 10 \mu\text{m}^2$ )	$R_q$ nm ( $50 \times 50 \mu\text{m}^2$ )
HF:H <sub>2</sub> SO <sub>4</sub>						
1:49	285 ± 64	326 ± 7	222 ± 25	303 ± 29	239 ± 42	292 ± 9
2:48	213 ± 37	312 ± 21	245 ± 23	324 ± 13	265 ± 32	293 ± 7
3:47	203 ± 17	296 ± 16	235 ± 27	323 ± 10	239 ± 42	285 ± 10
4:46	197 ± 12	281 ± 10	224 ± 20	272 ± 9	209 ± 15	263 ± 26

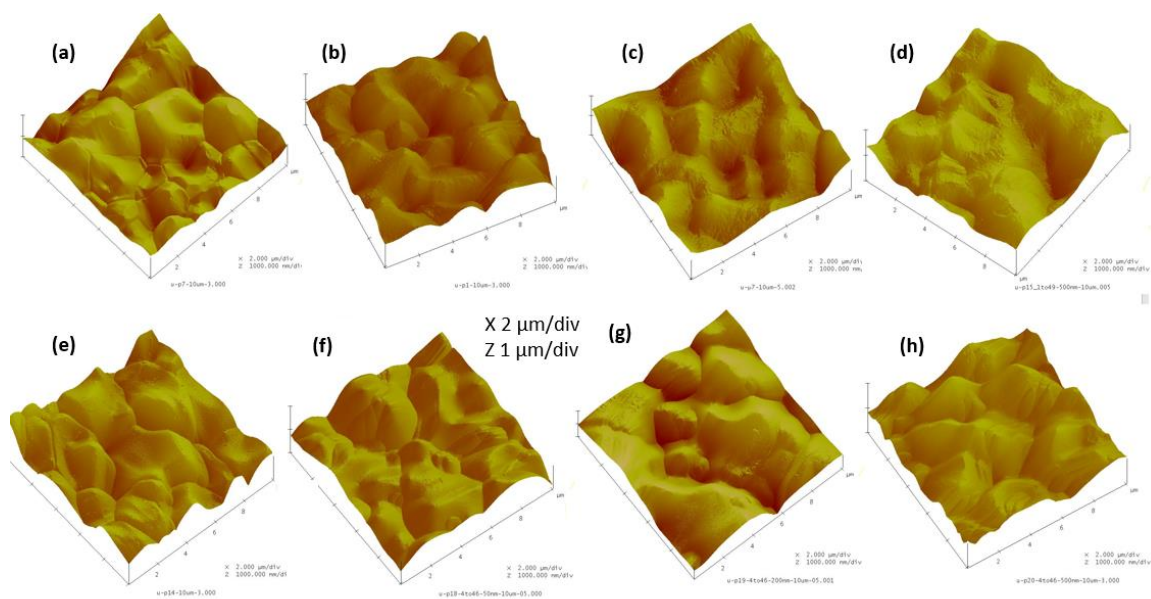


Figure 5.11: Topography of surfaces after electropolishing. (a) and (e) are as coated reference Nb<sub>3</sub>Sn surfaces. (a), (b) and (c) were coated together, showed no tin residues. Others were from another coating run showing potential tin residues as seen in (e). (b), (c) and (d) respectively received ~ 50 nm, 200nm, and 500 nm EP removal in 1:49 volume ratio mixture of 96% HF and 48% H<sub>2</sub>SO<sub>4</sub>. (f), (g) and (h) subjected to EP for similar removal of ~ 50nm, 200 nm, and 500nm in 4:46 volume ratio of 96% HF and 48% H<sub>2</sub>SO<sub>4</sub>.

### 5.3 Oxypolishing

For oxypolishing, an oxide layer is grown on the Nb<sub>3</sub>Sn coated surface via electrochemical anodization and subsequently removed by rinsing with HF. Multiple cycles of anodization and HF rinsing may be needed to achieve the desired amount of material removal. The thickness of the oxide layer can be controlled by applying a fixed voltage. A fixed cell voltage of 10, 20, 30, 40, or 50 V was applied to grow anodic oxide layers on Nb<sub>3</sub>Sn coated samples. A setup similar to that shown in Figure 5.5 was used with a 15% NH<sub>4</sub>OH solution electrolyte. The corresponding oxide layer thicknesses were then

determined by XPS sputter profiles, and calibrated by FIB cross-section combined with SEM [145]. It was found that  $\sim 2.4$  nm/V of an oxide layer was grown on the surface, see Figure 5.12. This thickness-voltage relation is close to Stimmell's observation, 2.8 nm/V, who used 3%  $\text{H}_2\text{SO}_4$  solution electrolyte [48].

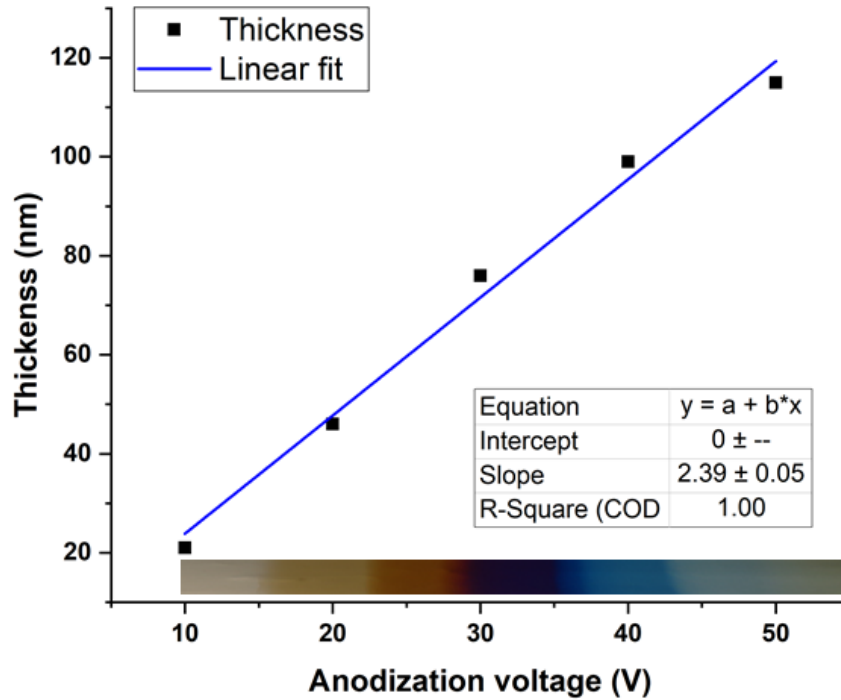


Figure 5.12: Thickness-voltage relation for the oxide layer grown in  $\text{Nb}_3\text{Sn}$ . The image next to the x-axis, obtained by sequentially anodizing a  $\text{Nb}_3\text{Sn}$ -coated Nb foil, shows the colors of the oxide layer for different voltages.

Each anodized sample was then given an HF rinse for 10 minutes. After a few seconds of exposure to HF, the color of each sample changed to grey, the typical appearance of  $\text{Nb}_3\text{Sn}$  coating. SEM examination showed some new features on the surface. Similar observation was made when 30 V anodized samples were rinsed for 5 and 10 minutes, as shown in Figure 5.13. Those features were absent when the sample was exposed shortly for 1–2 minutes. Note that similar but smaller features were also

developed on the surface after one hour of HF rinse, discussed later. Residue formation on an oxypolished  $\text{Nb}_3\text{Sn}$  surface had also been reported before [48].

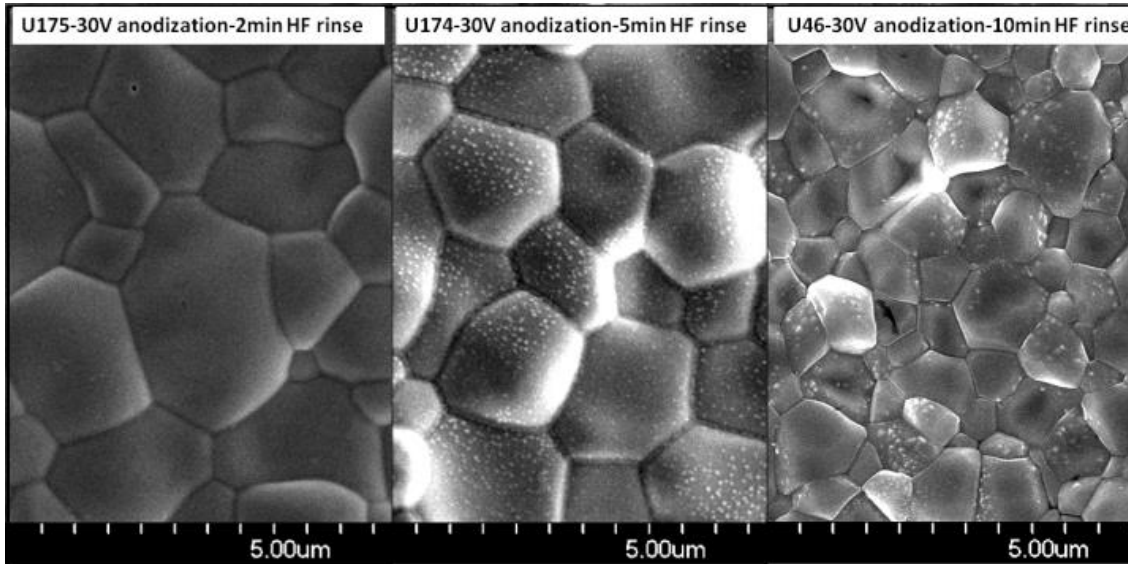


Figure 5.13: Surfaces obtained by HF rinsing of 30 V anodized samples for different intervals. Note that new features, indicated by bright grainy appearance in SEM image were developed on the surface after 5 minutes.

In another set of experiments, four samples coated with  $\text{Nb}_3\text{Sn}$  were subjected to 1, 2, 3 and 4 cycles of 50 V anodization followed by 90 s HF rinsing. EDS analysis of oxypolished samples shows the usual composition (~ 24 at. % Sn), whereas XPS analysis showed Nb to Sn ratios to of 3.22, 3.70, 3.30, and 3.56 for oxypolished samples for 1 to 4 cycles respectively. The obtained surface following 4 cycles of oxypolishing is shown in Figure 5.14. It qualitatively resembles the electropolished  $\text{Nb}_3\text{Sn}$  surfaces, presented in Figure 5.8.

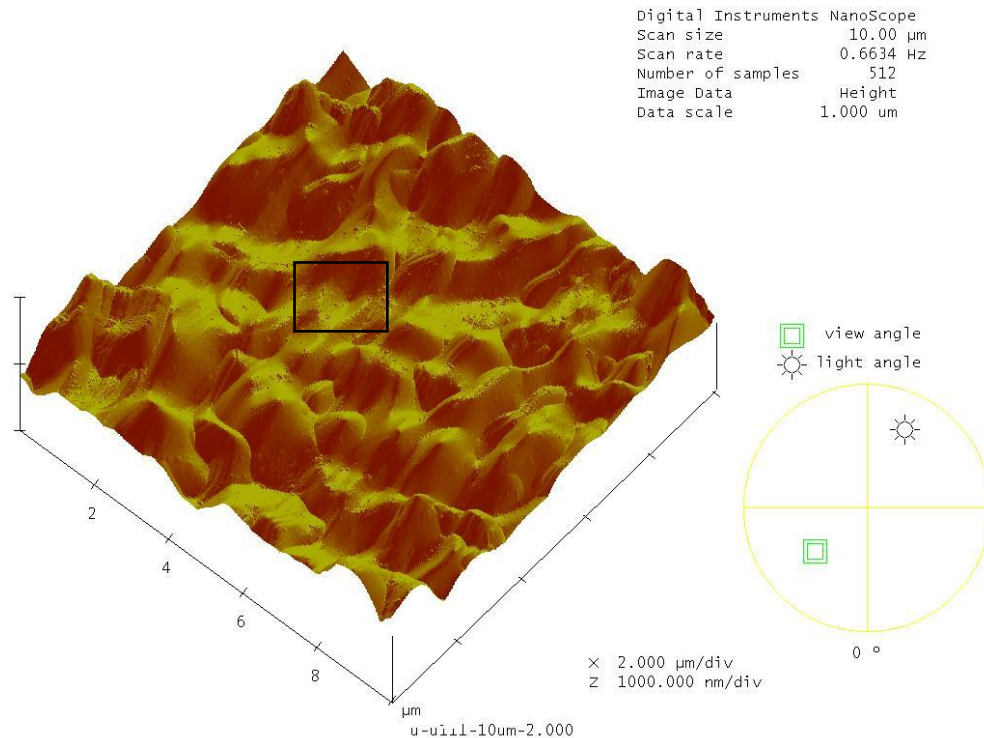


Figure 5.14: AFM image from sample U111, which received 4 cycles of 50V anodization followed by 90 s HF rinse. Small features (like in the black rectangle) appear on the surface.

A final set of samples was subjected to 2, 8, and 12 cycles of oxypolishing (30 V anodization and 30 s HF rinse each time) in successive experiments for an approximate expected removal of 50 nm followed by an additional 200 nm, and then 300 nm removal. AFM images in Figure 5.15 show surfaces following each treatment. Surface roughness was found to be a little less or similar following each treatment compared to the reference as-coated sample. Table 5.4 summarizes AFM roughness measurements. As reported before by Siemens researchers [69], pitting on the surface was not observed here, but irregularly etched spots or features that look like residue were noticed, within grains after ~ 500 nm EP or oxypolishing removal, as shown in Figure 5.16. XPS surface analysis showed Nb to Sn ratios of 3.51 and 3.54, respectively, following 8 and 12 cycles of oxypolishing.

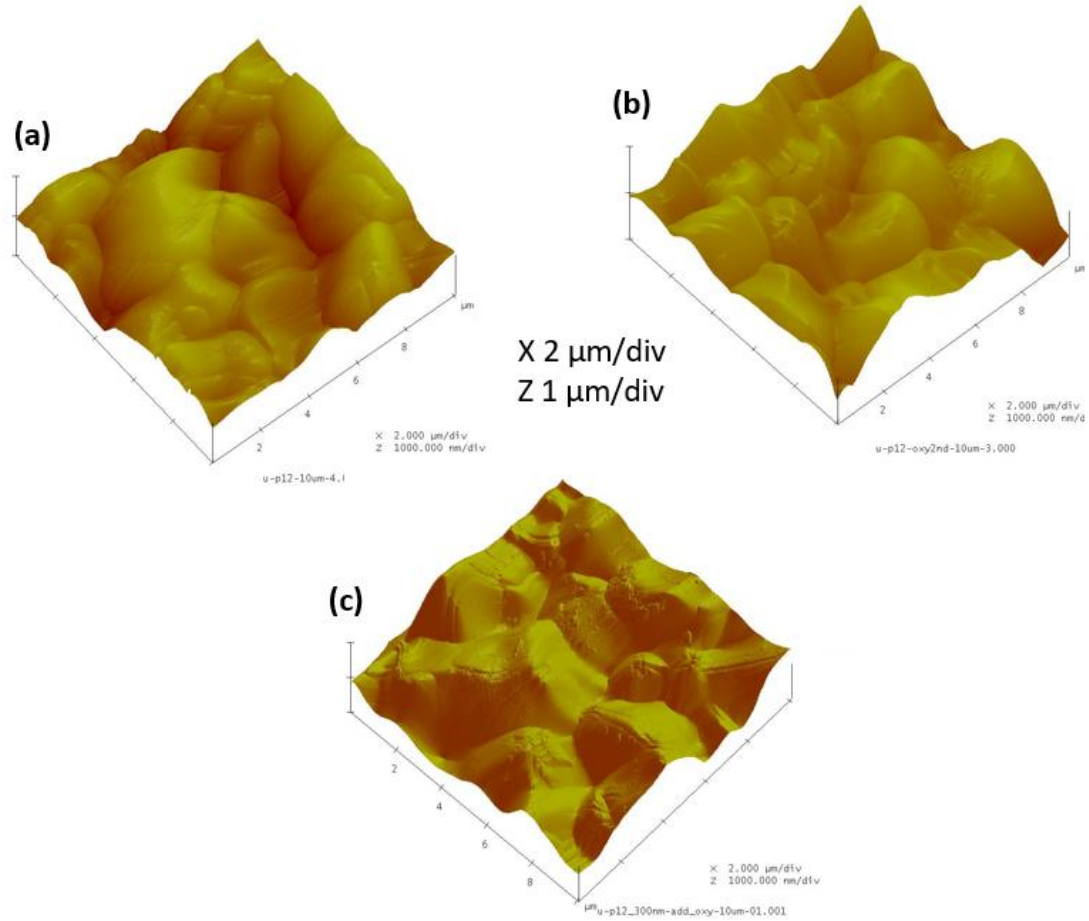


Figure 5.15: (a), (b) and (c) received 2, 8 and 12 cycle of 30 V oxypolishing for ~50 nm, 200 nm and 550 nm removal successively.

Table 5.4: Estimated roughness for sequentially oxypolished samples.

Oxypolishing	Expected removal (nm)	R <sub>q</sub> nm (10 μm × 10 μm)	R <sub>q</sub> nm (50 μm × 50 μm)
0 V	0	251 ± 39	328 ± 10
30 V × 2	50	213 ± 12	291 ± 7
30 V × 8	+ 200	244 ± 47	302 ± 12
30 V × 12	+ 300	196 ± 17	311 ± 11

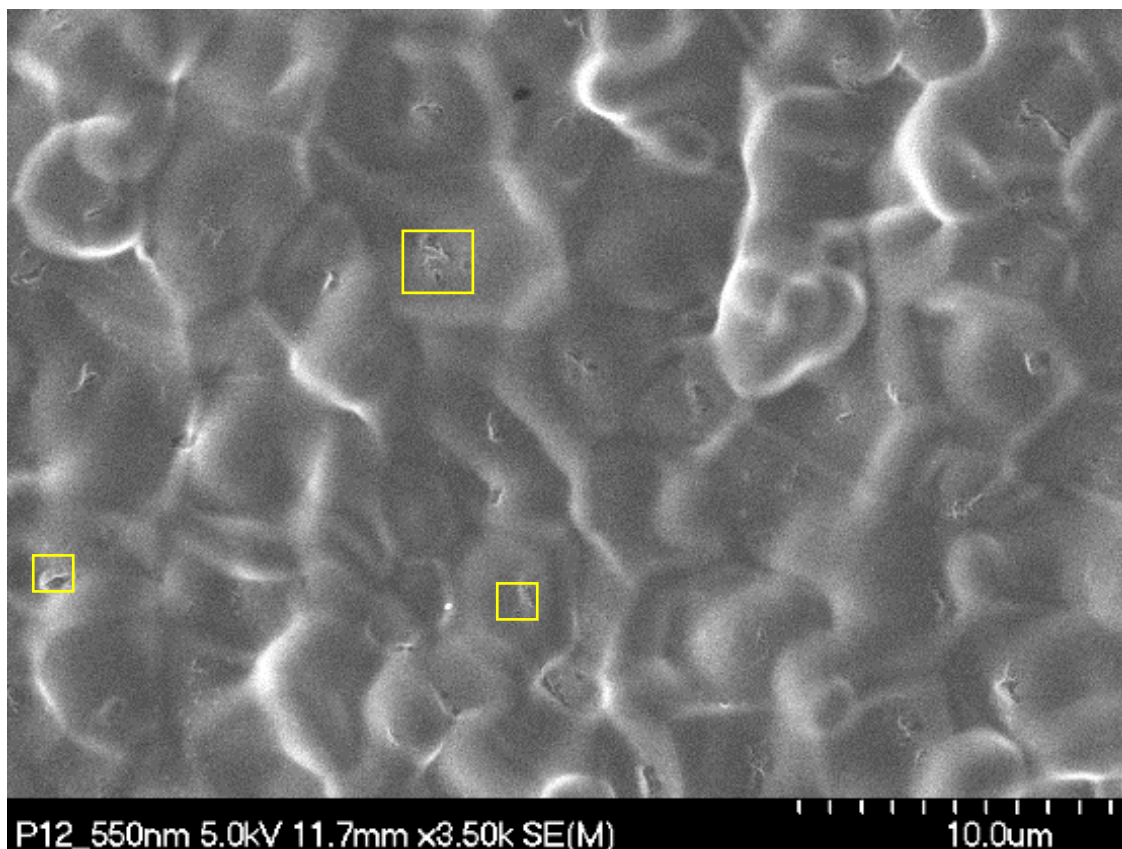


Figure 5.16: SEM image SEM image from sample after 22 successive oxypolishing (~ 550 nm removal). Note new features, as in inside yellow boxes.

## 5.4 Acid Immersion

### 5.4.1 HF Immersion

XPS analysis of  $\text{Nb}_3\text{Sn}$  coated samples shows that the surface is largely covered with  $\text{Nb}_2\text{O}_5$  and  $\text{SnO}_2$  [52, 146]. HF is well-known to dissolve  $\text{Nb}_2\text{O}_5$  and expected to remove  $\text{SnO}_2$ . Four coated samples were dipped in bottle-strength, 49% HF solution for 1, 5, 30, and 60 minutes at room temperature. Samples were then rinsed with de-ionized water before SEM/EDS analysis. SEM examination of samples rinsed for 1 and 5 minutes did not show any notable changes on the surface. However, new features emerged after prolonged HF immersion for 30 or 60 minutes. A comparison of AFM images before and

after 30 minutes in HF are shown in Figure 5.17. Grain facets appeared sharper after 60 minutes of HF rinsing indicating a gradual etching of the coated surface. SEM images shown in Figure 5.18 shows sharp grain boundaries, which was also confirmed with AFM.

EDS did not show any significant differences in the composition following HF dipping for any duration. Note that the depth resolution of EDS measurement ( $\sim 1 \mu\text{m}$ ) may not be sensitive enough to evaluate the change in composition at the surface. XPS surface analysis showed Nb to Sn ratios of 3.46, 2.98, 3.59, and 3.60 for 1, 5, 30, and 60 minute rinsed samples, respectively. Note that XPS measurements for as-coated  $\text{Nb}_3\text{Sn}$  coated samples show Nb to Sn ratios close to 3, typically a bit lower than what we observed in oxypolished, electropolished, or HF rinsed samples.

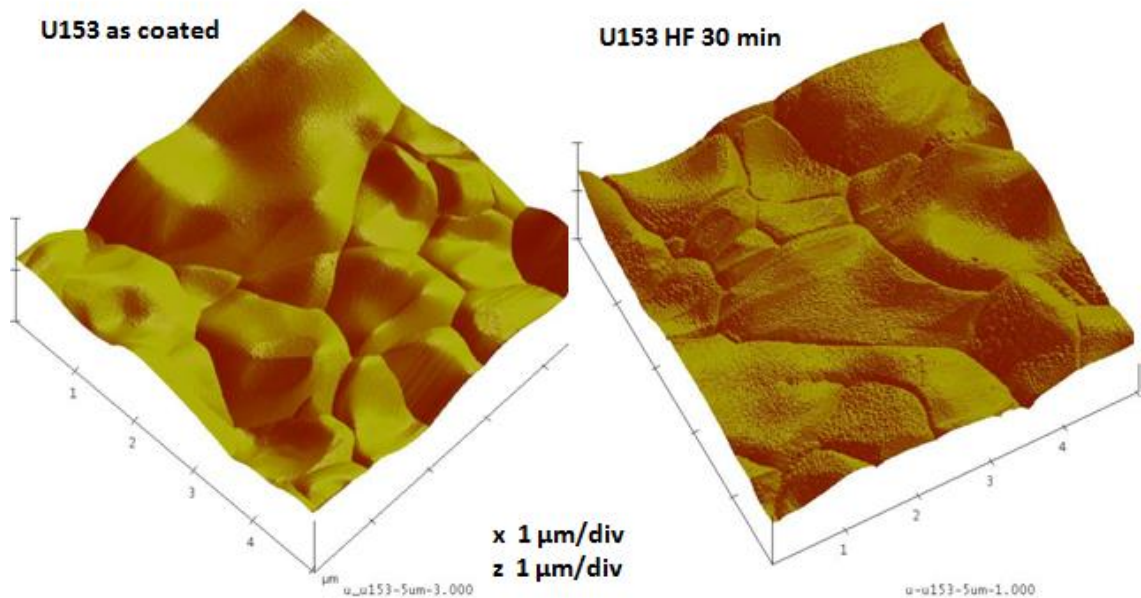


Figure 5.17: AFM images of  $\text{Nb}_3\text{Sn}$  coated sample U153 before [left] and after [right] 30 min HF immersion. Note the rough appearance of each grain that after the treatment.

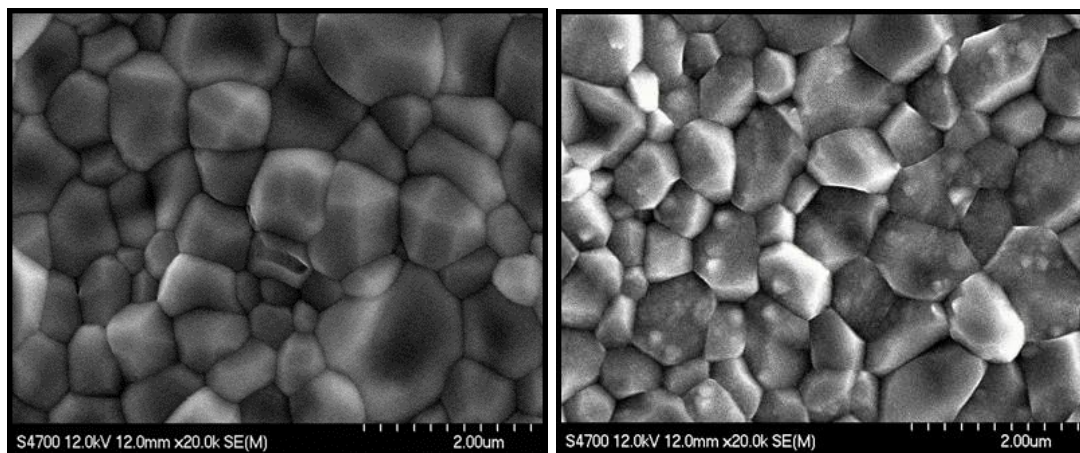


Figure 5.18: SEM images from samples after 5 min and 1 h dipping in HF. Note small features developed in the grains following 1 h treatment.

### 5.4.2 HNO<sub>3</sub> Immersion

Sn-residues can potentially deposit on Nb<sub>3</sub>Sn-coated surfaces at the end of the coating process. Reported before by early researchers [48], these residues are one of the recurrent issues discovered in our coating experiments, as discussed in Chapter 4. Several Nb<sub>3</sub>Sn-coated samples with Sn-residues on the surfaces were immersed in magnetically stirred HNO<sub>3</sub> solution at conditions described below. The desired outcome was to remove these residues from the surface. Each sample was examined with SEM/EDS following the treatment. Results from various HNO<sub>3</sub> immersion conditions are summarized in Table 5.5. The best outcome for the removal of Sn-residues was obtained with 22% HNO<sub>3</sub> at ~110 °C, as shown in Figure 5.19.

### 5.4.3 HCl Immersion

We dipped several Nb<sub>3</sub>Sn-coated samples with Sn-residues in 38% or 5% HCl for durations described below aiming to remove the Sn-residues. The first set of samples were soaked for 5 min to 6 h in 38% HCl at room temperature. SEM examination showed

no notable changes on the surface following these treatments. Another set of similar samples was then dipped in dilute 5% HCl at room temperature for 15 min to 3 h. The Sn-residues in each sample were reduced significantly. Almost complete removal of Sn-residues was observed following a one-hour soak in 5% HCl at room temperature (Figure 5.20).

Table 5.5: SEM result from coated samples immersed in HNO<sub>3</sub> solution at different conditions

HNO <sub>3</sub> Concentration (%)	Immersion Time (min)	Immersion Temperature (°C)	Results
70	5–15	Room Temp	No effect in Sn-residues or the coating
70	≥ 5	~ 100 °C	Notably reduced Sn-residues
22	5	~ 110 °C	Completely removed Sn-residues
5	5–5	Room Temp	Notably reduced Sn-residues

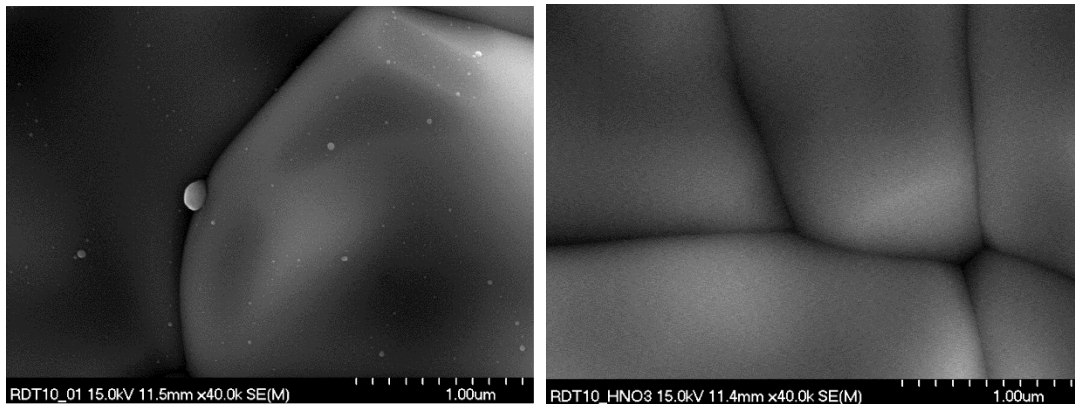


Figure 5.19: SEM images of witness sample coated with RDT10 before [left] and after [right] 22% HNO<sub>3</sub> soak at ~110 °C. Bright features are Sn-rich residues.

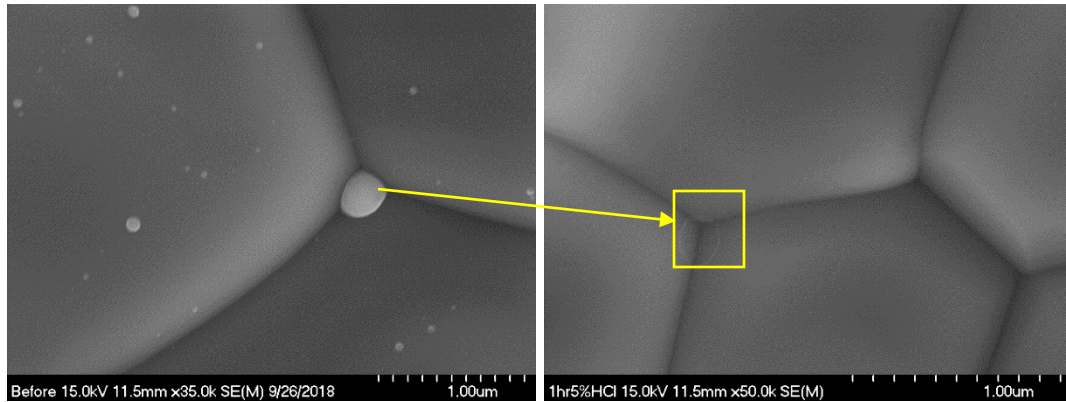


Figure 5.20: SEM images of witness sample coated with RDT7 before [left] and after [right] 5% HCl soak for one hour

## 5.5 Annealing

Annealing of  $\text{Nb}_3\text{Sn}$ -coated cavities has been previously investigated. Siemens researchers annealed coated cavities for some hours at 1050 °C without Sn to “clean” the grain boundaries. Since grain boundaries play a vital role in transporting tin into Nb during the growth of the coating, they were considered as potential “weak links” between the grains [69]. While yet to be confirmed, grain boundaries were speculated to have different stoichiometry than  $\text{Nb}_3\text{Sn}$ . The annealing was expected to improve the off-stoichiometric nature of grain boundaries. Cornell researchers pursued annealing of the cavities (at ~ 1100 °C for 0.5–6.5 h with the tin heater turned off) to increase the grain size of the material [86]. Both studies showed no dramatic improvement in the RF performance following the annealing. The results were even a little worse than those before annealing. The primary goal of annealing in our studies was to evaporate potential Sn-residues from the coated cavity surface for potential improvement in cavity performance.

First, we annealed a coated cavities, which had Q-slope, for 2 hours at 1100 °C. Both ends of the coated cavity were closed with Nb covers which were freshly etched with BCP. Witness samples, one previously coated and the other a new (not coated) Nb were

also placed inside the cavity before annealing. Post-annealing inspection showed some discoloration in Nb covers exposed inside the cavity, possible indication of a thin coating layer deposited during the process. RF test at both at 2 K and 4.2 K showed degradation of  $Q_0$  following the annealing. Figure 5.21 compares cavity performance at 4 K before and after annealing. Almost constant  $Q_0$  was measured up to  $\sim 4$  MV/m unlike the as-coated cavity but followed by a sharp Q-slope.

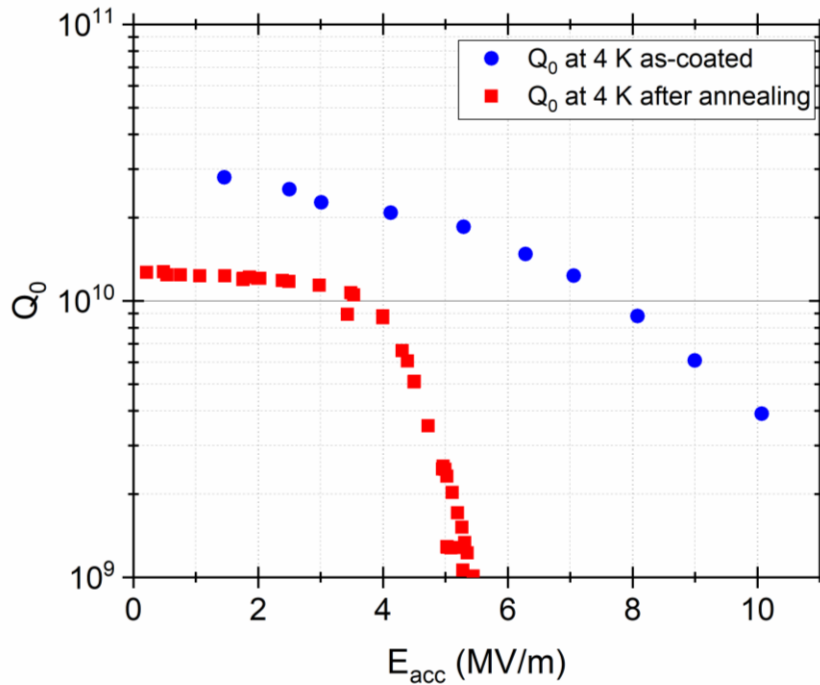


Figure 5.21: RF performance of the cavity before and after annealing. The test was limited by input RF power.

SEM/EDS examination showed no tin residues on the previously coated witness samples, indicating the disappearance of Sn residues. The Sn content appeared  $\sim 1$  at. % less than before, which is within the instrumental error. However, the other Nb sample, not coated before, appeared coated in SEM image, Figure 5.22. EDS analysis showed  $\sim 10$  at. % Sn, which indicates that the Sn was transferred from the  $Nb_3Sn$  coating inside the cavity during the annealing. The loss of Sn from the coating may explain the degradation of the cavity performance. The depletion of Sn upon annealing at 950–

1000 °C was reported before [38, 147]. They estimate an evaporation rate of ~ 0.50 monolayers of Sn per second at 950 °C [38]. We have also seen Sn loss from Nb<sub>3</sub>Sn films grown by multilayer sequential magnetron sputtering during the annealing process [148].

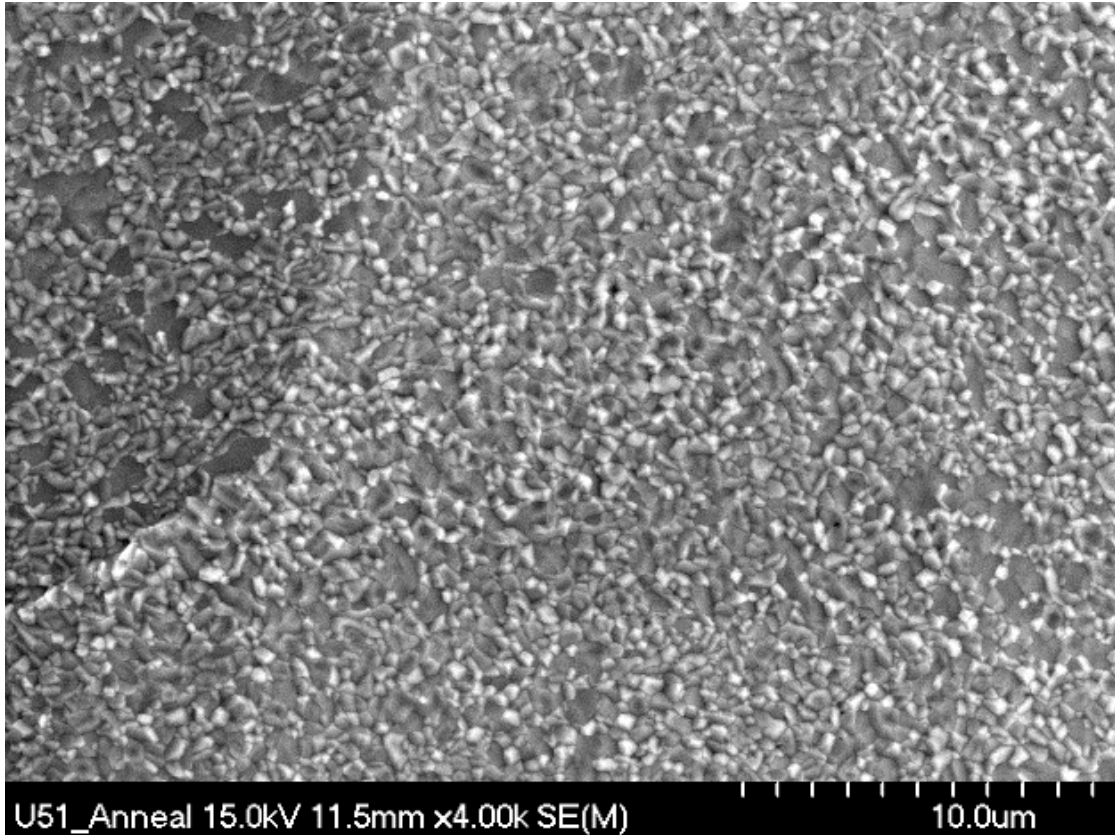


Figure 5.22: SEM image from Nb sample after annealing at 1100 °C for 2 hours with a coated cavity.

Since the loss of Sn from the coating was somewhat unexpected, we annealed three Nb<sub>3</sub>Sn coated samples for 12 h at 1200 °C. They were prepared at 1200 °C with a coating times of 1 h, 12, and 60 h, as discussed in Chapter 3. SEM images captured from these samples showed unusual grain structures (Figure 5.23). In some cases crack-like structures developed after the annealing. EDS examination of each sample showed only 1–2 at. % Sn remaining, confirming the evaporation of Sn from Nb<sub>3</sub>Sn layers.

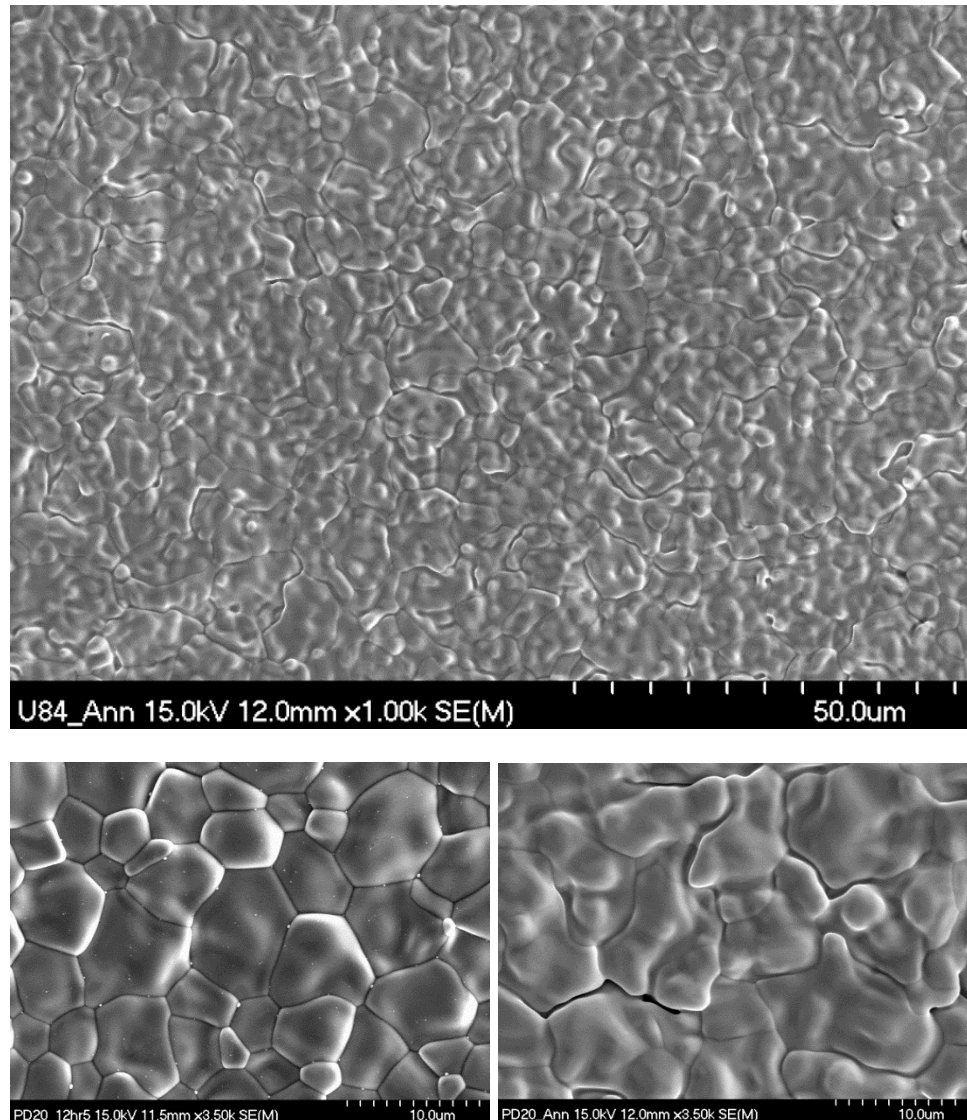


Figure 5.23: SEM image at the top was from the sample that was coated for 1 h, and annealed for 12 h at 1200 °C. Other images are from another sample coated for 12 h, before (bottom-left) and after (top-right) annealing at the same conditions.

## 5.6 Conclusions

Chemical, electro-chemical, and thermal treatments were applied to  $\text{Nb}_3\text{Sn}$  surfaces aiming to clean and smooth them. BCP treatment appears to attack rapidly producing a very rough surface, forming depressions with sharp edges. In electropolishing, the measurement of the I-V characteristics indicated the polishing of

Nb<sub>3</sub>Sn surface may be possible. The topography of coated coupon samples before and after electropolishing shows smoothening. In contrast to BCP treatment, material removal in electropolishing is more controllable and uniform. The actual mechanism of polishing is not yet understood, but observed current-voltage characteristics suggest a diffusion-limited process similar to Nb. HF contents in the standard EP electrolyte were reduced in different ratios to allow longer treatment time for a given thickness removal. Data suggested that the standard EP electrolyte had a better smoothening effect than HF-reduced electrolytes, which has not yet been understood. Although oxypolished surfaces were similar to electropolishing-produced surfaces, only a light smoothening was evident. In general, electropolishing or oxypolishing did not increase the roughness or damaged the surface notably. XPS measurement typically showed Nb to Sn ratio slightly higher than 3 after each treatment. It is possible that the as-coated sample may contain a tin-rich layer on the surface, resulting in lower Nb/Sn ratios, but this requires further examinations. Irregularly etched spots or residues-like features were observed in several samples following HF rinsing, oxypolishing, or electropolishing. The genesis of these features is not yet understood. It could be a result of different etching rates for Nb and Sn or the precipitation of reaction products. Under certain conditions, HNO<sub>3</sub> or HCl removes Sn-residues from the coated surface. We annealed a coated cavity with a witness Nb sample in another attempt to evaporate Sn residue from the surface. The niobium witness sample was covered with Nb-Sn coating following the annealing. Since the only source of tin was the Nb<sub>3</sub>Sn layer on the cavity in this setup, Sn transfer to the witness samples indicates tin evaporation from Nb<sub>3</sub>Sn films, leading to Sn loss from the coating layer. RF testing of the cavity also showed significant degradation of performance following the annealing potentially from the Sn loss. The dedicated experiment with coated coupon samples confirmed the Sn loss following annealing.

## CHAPTER 6

### Summary and Outlook

$\text{Nb}_3\text{Sn}$  is a prospective material for future SRF accelerator cavities. Tin vapor diffusion is a promising and successful technique to fabricate them in which the interior surface of Nb cavities is reacted with Sn vapor to grow a few-micron-thick surface layers. This dissertation has presented results from numerous experiments that provide important insight into different aspects of growth and properties of  $\text{Nb}_3\text{Sn}$  coatings. Important conclusions drawn from each study are already presented at the end of each chapter. In this chapter, we will summarize them together before presenting an outlook.

#### 6.1 Summary

We discussed results from samples prepared under many different nucleation conditions in Chapter 2. The nucleation step was found to give two forms of tin on the Nb surface: the two-dimensional phase of extra tin deposits on the surface between three-dimensional tin particles, resembling the Stranski-Krastanov growth mode. Omitting the nucleation step in the coating process increases the chances of forming patchy regions. Varying nucleation parameters resulted in various surface structures, but that alone had no significant impact on the subsequent final coating, at least as seen in SEM/EDS examination. Chapter 3 presented experimental outcomes of the growth of the coating at elevated temperatures. Coating temperatures of (900–1000) °C resulted in more patchy

regions than those at higher temperatures. A similar observation was made for the coating grown with lower flux ( $< 100 \text{ atom}\cdot\text{nm}^{-2}\cdot\text{min}^{-1}$ ) of tin, indicating the need for sufficient Sn flux ( $\sim 200 \text{ atom}\cdot\text{nm}^{-2}\cdot\text{min}^{-1}$  or higher) at the initial stage of the coating to ensure uniformity. Besides the coating temperature, coating durations can significantly affect the coating properties (grain size, thickness, roughness). Extending the coating time was found to produce thicker and rougher coatings with larger grain sizes. The average coating thickness and grain size varied  $\sim (2\text{--}15) \mu\text{m}$  and  $\sim (2\text{--}7) \mu\text{m}$ , respectively, for the total coating time ranging from 1 h to 78 h. Increased grain size correlates well with increased surface macro-roughness and thickness of the coating. Pre-anodization (30 V, 15%  $\text{NH}_4\text{OH}$  solution) of the substrate reduced the occurrence of non-uniformity at any given coating condition. Material analysis hinted at possible Ti-contamination from Nb-Ti flanges and was considered as a major culprit to recurrent Q-slopes in  $\text{Nb}_3\text{Sn}$  cavities at JLab.

We also introduced overcoat experiments (sequential growth of multiple coating layers) in Chapter 3 to investigate the growth and kinetics of  $\text{Nb}_3\text{Sn}$  during the process. The results indicated that the coating grows primarily by tin diffusion to the film-substrate interface via  $\text{Nb}_3\text{Sn}$  grain boundaries, where it reacts with Nb to form  $\text{Nb}_3\text{Sn}$ . That explains why the patchy regions are significantly thinner. Since patchy areas are large single crystalline grains, the coating growth is hindered due to fewer grain boundaries available for tin transport. The observed non-parabolic growth is consistent with the significant grain growth resulting in the reduction of grain boundary diffusion. Accordingly, the grain size growth can also be fitted with a power law. Overcoat experiments resulted in equiaxed and columnar grains, which scaled with coating time. The microstructure and composition appeared similar to those obtained from single-coat experiments.

Chapter 4 presented results from the studies of witness samples and cutouts from preparing a  $\text{Nb}_3\text{Sn}$ -coated cavity. These studies provided firsthand information to understand the growth of  $\text{Nb}_3\text{Sn}$  coating inside a practical SRF cavity, and to correlate

materials findings with RF properties of coated cavities. Thermometry mapping measurements identified several locations with different RF loss characteristics during a testing of a Nb<sub>3</sub>Sn-coated cavity. These were excised. Each cutout fitted one of the three systematic surface resistance trends: weak field-dependent, strong field-dependent, and field-dependent switch (at 4.5 MV/m). No notable differences in thickness and composition were found between the cutouts that had different trends of surface resistance. We discovered voids, which were not reported before, in each cutout extracted from the cell region. No voids were present in the samples from the beam pipes, which also had relatively smaller grain sizes indicating the possible influence of Nb purity on the microstructure of Nb<sub>3</sub>Sn. A higher density of patchy regions near the equator seems to be associated with surface resistance switch at 4.5 MV/m and strong field dependency. The presence of unusual large regions with carbon contamination appears to be associated with regions showing strong field-dependent surface resistance. This highlights the need for assured cleanliness of substrate cavities.

Chapter 4 also reported the results from the examination of several witness samples coated with single-cell and multi-cell cavities that led to modifying the coating protocols. Analysis of witness samples coated with single-cell cavities revealed a distribution of Sn-rich residue on the surface. The two-cavity setup with a temperature gradient ~ 85 °C was adopted to avoid Sn residue on the surface (of the cavity to be coated) by promoting the condensation of residual tin on the colder (dummy) cavity. These changes made in the coating process reduced the Q-slope significantly. The best-coated cavity had a Q<sub>0</sub> of ~ 2 × 10<sup>10</sup> at 4 K and ~ 5 × 10<sup>10</sup> at 2 K before quenching at ≥ 15 MV/m. Analysis of witness samples coated with the first five-cell cavities that resulted in up-down asymmetry showed large patchy regions. The non-uniformity was once again attributed to the lower flux of tin to the upper cells, in “out of sight” areas. The addition of secondary Sn-source improved the coating uniformity but deposited Sn-residue on the surface as in

single-cell cavity coatings. The uniformity was correlated with a higher value of quality factor, but the limited accelerating gradient is attributed to macro defects present in the substrate prior to the coating. With the addition of supplementary Sn sources, quality substrates, and adjusted Sn supply, it was possible to produce a five-cell cavity reaching  $E_{acc} > 10$  MV/m without significant Q-slope.

Several mechanisms were linked to a strong quality factor degradation in Nb<sub>3</sub>Sn cavities. Those include possible Ti-contamination, non-uniformity, and accumulation of Sn-residues on the surface. The coating uniformity and residual accumulation at the surface were reduced by modifying the coating process, which improved the performance of both single-cell and multi-cell cavities. Evaporation, consumption, and distribution of Sn during the coating play important roles defining the quality of the resulting coating, which significantly impacts the RF performance of the cavity. Results from C3C4 and several five-cell cavities affirm the need to have a quality substrate to achieve best RF performance.

We explored several electrochemical, chemical, and thermal treatments to improve the smoothness and cleanliness of coated surfaces in Chapter 5. While BCP harshly attacked Nb<sub>3</sub>Sn surfaces, electropolishing appears to be a potential technique for surface smoothening. Oxypolishing is another technique to be considered. We applied several acid treatments to the Nb<sub>3</sub>Sn coated surfaces. HCl or HNO<sub>3</sub> immersion at certain conditions appears to remove Sn-residues from the surface.

## **6.2 Outlook and Future Work**

In this dissertation, we mainly investigated two major stages of the coating process: nucleation and growth. The intermediate stage between the two still needs an in-depth investigation. It is particularly important as the first layers of the coating form here.

Since further growth of Nb<sub>3</sub>Sn happens at the coating-Nb interface, the defects that could form on the coating at the early stage could carry over to the RF surface.

In several instances, we have reported the formation of patchy regions associated with a low-flux of tin. Below a certain threshold the coating seemed to vary depending on the distance from the Sn source. It is essential to have a sufficient flux of Sn, delivered uniformly all over the surface. The addition of well-engineered “smart” Sn-sources, equipped with independent temperature control, would help to produce uniform coating without any residues throughout the cavity surface. Another potential option would be to inject a small amount of inert gas to enhance vapor-phase scattering. The latter option may especially benefit larger (bigger diameter) and multi-cell cavity coating, where even the addition of Sn-sources may not adequately distribute Sn in out-of-sight areas.

It is not yet clear how the Nb<sub>3</sub>Sn grain boundaries affect the RF performance of the cavity. It is essential to study the composition and possible grain boundary segregation. As we presented, one way to reduce grain boundary density is to increase the coating time, and worth trying in actual cavity coatings. Since these coatings are thicker, they could be suitable for electropolishing in further studies.

In this dissertation, we have explored several coating conditions resulting in coatings with different properties (grain size, roughness, thickness, etc.). We used typical coating parameters (1 or 5 h nucleation at 500 °C and 3–6 h coating at 1200 °C) to coat the majority of cavities. The main focus has been to grow uniform coatings optimized for these conditions. Since we better understand now how to deposit coating uniformly, it worth applying different sets of coating parameters resulting in different surface properties (e.g., smaller grain, thin coating, and lower roughness vs. larger grain, thick coating, and higher roughness). The study of different surface properties linked with RF performance can lead to coating conditions or surface properties, which may push the current performance limit of Nb<sub>3</sub>Sn cavities further.

Our initial investigation of EP and oxypolishing of coated samples indicates smoothening on Nb<sub>3</sub>Sn surfaces. The surface composition and post-treatment surface residues need further investigation. Understanding the electropolishing mechanism could help to optimize the EP process for suitable topographic modifications. Post-processing studies with thicker coating could be beneficial to understand and apply them for RF cavities.

In closing, Nb<sub>3</sub>Sn is currently the leading alternative material that could potentially replace Nb in SRF cavities. Several labs have demonstrated useful cavity performances in R&D single-cell cavities. Accelerator five-cell Nb<sub>3</sub>Sn cavities have already achieved accelerating gradients that are useful for accelerator application. The logical next step is Nb<sub>3</sub>Sn cryomodule test in an accelerator environment. Nb<sub>3</sub>Sn material is drawing attention from small compact accelerator applications, aiming to employ cryo-coolers for cavity cooling. The future of Nb<sub>3</sub>Sn relies upon further material studies in conjunction with process optimization and RF performance. Looking at the trend of recent progress, broadened applications, and growing attention, Nb<sub>3</sub>Sn could be the SRF material for the future.

## Appendix A

The goal of this section is to present fundamental concepts regarding the superconducting radio frequency (SRF) technology, broadly used for particle accelerators. A brief introduction of RF superconductivity is presented first summarizing some of the most important theories. The concept of surface resistance under the RF field is explained next, which is then followed by an introduction to SRF accelerator cavities. The chapter progresses describing the basic working principle and important figures of merits of SRF cavities. Following this, the dominance and limitations of niobium as almost the only one SRF cavity material are explained, which in turn justify the pursuit of alternate superconducting materials to niobium. The basic features that an ideal alternate superconducting material preferred to possess are outlined next, and finally, the potential SRF cavity materials are introduced.

Readers seeking an in-depth understanding of the contents presented in this chapter are referred to [149–153].

### A.1 Superconductivity

The superconductivity was discovered in 1911 by Kamerlingh Onnes when he observed a sudden drop in the resistance of mercury to zero at 4.2 K [154], as shown in Figure A.1.1. Superconductivity is the property of materials to conduct DC electric current with apparently zero resistance. All superconductors exhibit this property at a particular temperature known as critical or transition temperature,  $T_c$ . It implies that if a current is passed through the superconducting material, the current should flow forever without any

dissipation. Meissner and Ochsenfeld discovered another characteristic property of superconductors in 1933, while measuring the magnetic field distribution outside superconducting tin and lead samples [155]. Known as the Meissner effect, the property of superconductors is to expel magnetic field, Figure A.1.1 [right].

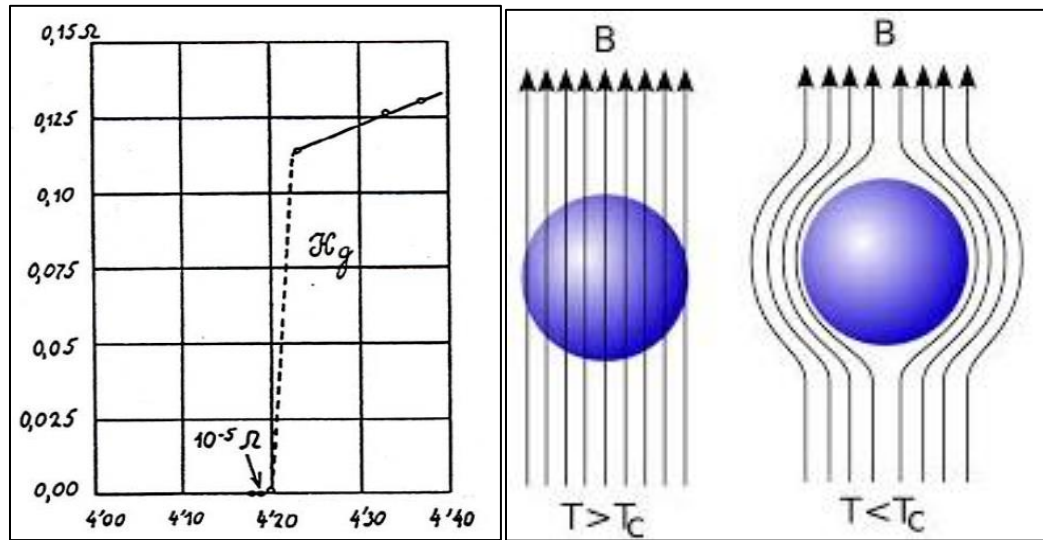


Figure A.1.1: Historic plot of resistance ( $\Omega$ ) versus temperature (K) by Kamerlingh Onnes showing drop in resistivity of mercury at 4.2 K, signifying the superconducting transition [left] [154]. Graphic representation of the Meissner effect [right].

There are two types of superconductors: type I and type II. The zero resistance property is similar in both cases, but they behave differently in the presence of a magnetic field. Type I superconductors remain in a perfect Meissner state, i.e., expel the magnetic field until a critical applied field  $H_c$  reached. Type I superconductors become normal conductors above the critical field  $H_c$ . Most of the superconducting elemental metals with relatively low critical temperature  $T_c$  fall into this class. Type II superconductors completely expel a magnetic field below the lower critical field  $H_{c1}$ . Above the lower critical field, they are favorable to enter into a third state known as mixed or vortex state Figure A.1.2 [left]; whereby normal conducting cores form in the superconductor. Each of these cores carries a quantum of magnetic flux and is circled by a vortex of superconducting current, see

Figure A.1.2 [right]; thus these cores are often known as Abrikosov vortices, fluxoids, or fluxons. Above the upper critical field  $H_{c2}$ , type II superconductors become normal conductors. Superconducting materials used in SRF applications, such as Nb and Nb<sub>3</sub>Sn, are type II superconductors.

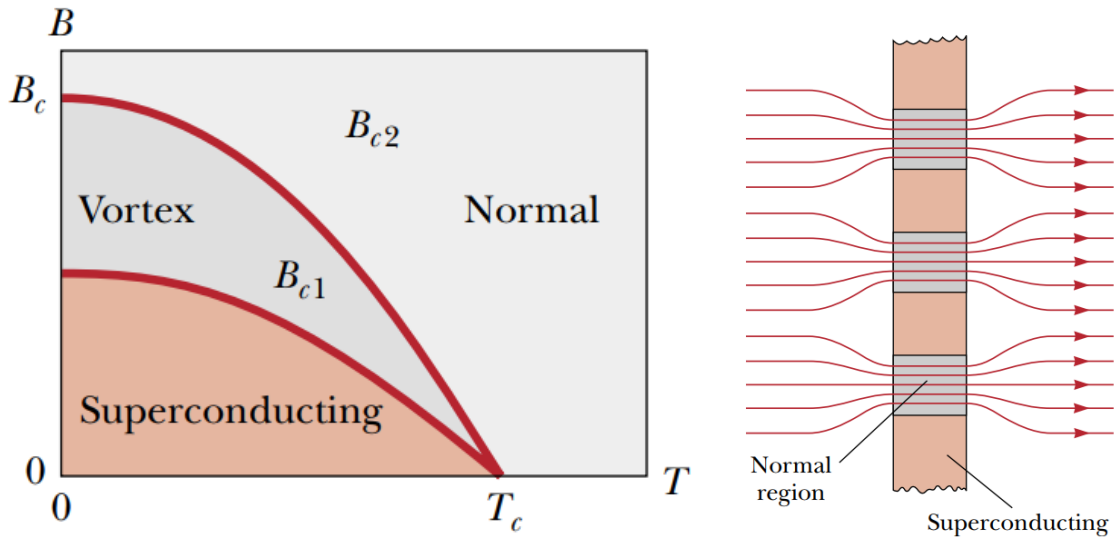


Figure A.1.2: Critical magnetic fields as a function of temperature for a type II superconductor is shown in Figure to the left. A schematic diagram of a type II superconductor in the vortex state is shown in the image to the right. The sample contains normal conducting cores, unshaded regions through which magnetic flux lines can penetrate. Figure adapted from [156].

Since the discovery of superconductivity, many theories were proposed to explain the mechanism that could match and predict the characteristics of these materials. Some of the important theories, still in the application are London theory, the Ginzburg-Landau theory, and the BCS theory. Derivations of these theories are beyond the scope of this dissertation, but a brief discussion on the fundamental aspect of each of them are presented here.

Fritz and Heinz London brothers proposed an equation, which provided a phenomenological description of magnetic field expulsion in a superconductor in 1935 [157]. The equation related the supercurrent density  $\vec{J}_s$  to the magnetic field given by,

$$\vec{\nabla} \times \vec{J}_s = -\frac{n_s e^2}{m_e} \vec{B} \quad \text{a.1}$$

where  $n_s$  is the density of the super-electrons. In combination with the Maxwell equation,  $\vec{\nabla} \times \vec{B} = \mu_0 \vec{J}_s$ , we get the following equation for the magnetic field in a superconductor

$$\nabla^2 \vec{B} - \frac{\mu_0 n_s e^2}{m_e} \vec{B} = 0 \quad \text{a.2}$$

For a simple geometry where the boundary between a superconducting surface and vacuum is normal to the x-axis, and magnetic field is parallel to the surface along the y-axis, Eq. (2) becomes

$$\frac{d^2 B_y}{dx^2} - \frac{1}{\lambda_L^2} B_y = 0 \quad \text{a.3}$$

where  $\lambda_L = \sqrt{\frac{m_e}{\mu_0 n_s e^2}}$  is a very important length parameter in superconductivity known as the *London penetration depth*. The solution of the differential equation is,

$$B_y(x) = B_0 e^{-\frac{x}{\lambda_L}} \quad \text{a.4}$$

This implies that the magnetic field does not drop to zero abruptly at the superconducting surface, but penetrates into the material with exponential attenuation. London penetration depth,  $\lambda_L$  gives the distance over which there is an interaction of the superconductor with an applied magnetic field. Despite the theory was successful to explain the Meissner effect, the theory was only correct for weak fields.

A theory that rectified the pitfall of London theory was proposed by Vitaly Lazarevic Ginzburg and Lev Davidovich Landau in 1950 [158]. The Ginzburg-Landau theory was a phenomenological theory based on Landau theory of second order phase transitions. It

allowed the calculation of macroscopic quantities of the material in the superconducting state if one assumed the phase transition to be of second order. The estimated results from Ginzburg-Landau theory were able to accurately match the experimental results of the time. The theory predicted another important length parameter,  $\xi$ , known as coherence length in addition to the London penetration depth  $\lambda$ . Another important dimensionless parameter known as the Ginzburg-Landau parameter,  $\kappa$  was proposed.  $\kappa$  defined as the ratio of  $\lambda$  and  $\xi$ , which predicts the magnetic behavior of superconductors categorizing them. Type I superconductors are those with  $0 < \kappa < 1/\sqrt{2}$ , and Type II superconductors those with  $\kappa > 1/\sqrt{2}$ . While useful and accurate for macroscopic quantities close to the superconducting transition temperature, GL theory did not provide the microscopic understanding of the superconductivity.

Here we should introduce two important parameters: the thermodynamic critical field and the superheating field. As discussed at the beginning, when we cool down a superconductor below  $T_c$  the material enters into the superconducting state from the normal conducting state. This phase transition is comparable to the transition from water to ice below the freezing temperature and can be analyzed from a thermodynamic point of view. The relevant thermodynamic energy here is the so-called Gibbs free energy ( $G$ ). According to the Meissner effect, the magnetic energy is expelled out from the material when it goes to the superconducting state, which raises the free energy in the superconducting state. The energy balance can be expressed as,

$$G_s(T, H) = G_s(T, 0) + \frac{1}{2}\mu_0 H^2 \quad \text{a.5}$$

where  $G_s$  is the free energy density. The second term is the energy density due to a magnetic field. The material is in superconducting state only if the free energy in the superconducting state,  $G_s(H)$ , is less than that in the normal state,  $G_n(H)$ . At the critical

field, the free energies in the superconducting and normal state should be equal. So thermodynamic critical field  $H_c$  is given by,

$$H_c = \sqrt{\frac{2}{\mu_0}(G_n(T, 0) - G_s(T, 0))} \quad \text{a.6}$$

For type II superconductor,  $H_{c1} < H_c < H_{c2}$ . Theoretically, the critical RF magnetic field is considered to be the so-called superheating field  $H_{sh}$ , Similar to the superheating phenomenon in which a liquid is heated to a temperature higher than its boiling point without boiling, the maximum field can persist beyond  $H_c$  (Type I superconductor) or  $H_{c1}$  (type II superconductor) in the metastable state up to  $H_{sh}$ . The superheating field is estimated within Ginzburg-Landau theory, depends on Ginzburg-Landau parameter  $\kappa$  in the various limits, and is given by,

$$\begin{aligned} H_{sh} &= \frac{0.89}{\kappa} H_c \\ H_{sh} &= 1.20 H_c \\ H_{sh} &= 0.75 H_c \end{aligned} \quad \text{a.7}$$

for  $\kappa \ll 1$ ,  $\kappa \approx 1$ , and  $\kappa \gg 1$  respectively.

It wasn't until 1957, when John Bardeen, Leon N Cooper and John R. Schrieffer (BCS) proposed a successful theory that explained the microscopic origins of superconductivity that could quantitatively predict the properties of superconductors [159]. Superconductivity was explained by a bound state formed between two electrons, known as Cooper pair, which can move without dissipation, and provide the zero resistance of superconductor. The electrons in a Cooper pair are entangled over the coherence length  $\kappa$ . Below the critical temperature of the superconductor, the phonon-mediated attraction between electrons condenses them to into Cooper pairs, bosonic (integer spin) quasiparticles. In a superconductor, the DC current is conducted by these Cooper pairs, rather than individual electrons. The pairing process brings the electrons into a

significantly lower energy state, such that there exists an energy gap,  $\Delta$  between the superconducting and normal conducting states. At  $T = 0\text{ K}$ , almost all electrons condense into pairs, but they break up at higher temperature. The fraction of unpaired electron will increase exponentially with increasing temperature as  $\exp(-\Delta/kT)$ . In order to break a Cooper pair, an energy of  $2\Delta$ , the energy gap of a superconductor is required. BCS theory relates the energy gap to the  $T_c$  of the material by

$$1.76K_B T_c = \Delta(T = 0) \quad \text{a.8}$$

Above the critical temperature, all the electrons are unpaired and superconducting state disappears. Under the DC field, the pairs carry all the current shielding field from unpaired electrons offering a zero-resistance, the hallmark of superconductors. Although cooper pairs move without friction, they possess finite inertia. When AC or RF field is applied, they are unable to screen unpaired electron completely, resulting in non-zero resistivity below the critical temperature. Such resistance, significantly smaller compared to the normal conducting state, at temperature  $T$  below  $T_c/2$  and frequency  $f \ll kT_c/h$  is given by [153],

$$R_s = \left( \frac{A f^2}{T} \right) e^{-\frac{\Delta}{k_B T}} + R_{res} \quad \text{a.9}$$

where  $A$  is the factor, which depends on material purity,  $h$  and  $k_B$  are the Plank and Boltzmann constants respectively. The temperature-dependent first term on the right-hand side is known as BCS resistance. When a superconductor is cooled below  $T_c$ , BCS resistance gets exponentially small, and the surface resistance  $R_s$  approaches to residual resistance  $R_{res}$ . Several factors can contribute to  $R_{res}$  which include:

- Trapped magnetic field
- Normal conducting residue near the surface
- Grain boundaries
- Metal-oxide interface

- Surface defects

The temperature dependence of the low-field surface resistance of bulk niobium at 1.3 GHz is shown in Figure A.1.2. The data shows a deviation of  $R_s$  from exponential dependence as the temperature decreases close to 0 K to  $R_{res}$ . For niobium, the BCS surface resistance at 1.3 GHz amounts to about 800 n $\Omega$  at 4.2 K and drops to 15 n $\Omega$  at 2 K. The exponential temperature dependence is the reason that operation at  $\sim 2$  K is essential for achieving high accelerating gradients in combination with very high quality factors. We will introduce accelerating gradient and quality factor of a cavity next.

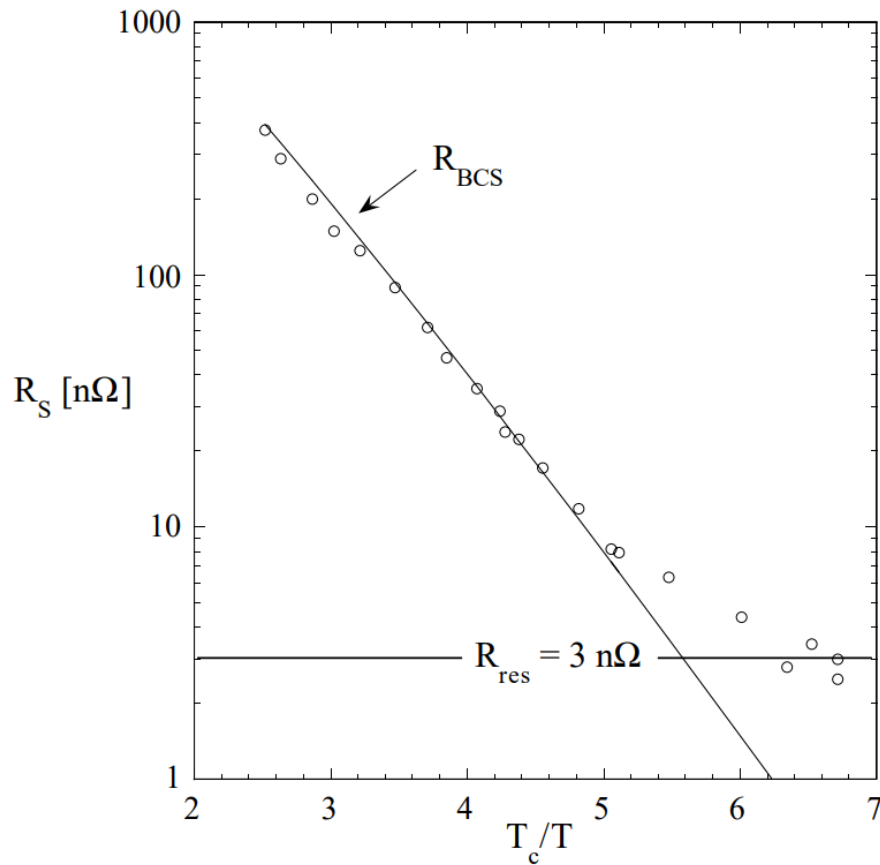


Figure A.1.2: Variation of low-field surface resistance of bulk niobium (1.3 GHz 9-cell TESLA cavity) with the temperature, shows saturation to a temperature-independent value of  $R_s$ ,  $R_{res}$  at low temperatures [160].

## A.2 SRF cavity

Radiofrequency cavities (RF) are resonators capable of storing electromagnetic energy. They are used to accelerate charged particle beams in accelerators. RF cavities are made from normal conducting materials (typically water-cooled copper operating near room temperature) or from the superconducting materials (most commonly niobium operating at cryogenic temperatures cooled by liquid helium). As discussed in the previous section, superconducting materials have the advantage of having much smaller surface resistance  $R_s$ , reducing the RF dissipation in the cavity walls by 5–6 order of magnitude compared to that normal conducting cavities. This allows SRF cavities to operate at high fields in continuous wave mode, that is, the RF power is continuously applied with 100% duty factor. Copper cavities would overheat and melt if operated in CW at these fields. It should be noted that the copper cavities offer higher accelerating fields ( $\geq 100$  MV/m) for short pulse (microsecond) and very low duty factor (0.1%).

Operating mode of acceleration is normally chosen with the lowest frequency, i.e.,  $TM_{010}$  mode with a longitudinal electric field. The electromagnetic field is distributed inside a cavity in such a way that the electric field is maximum along the beam axis (iris), where the magnetic field is minimum. Similarly, the equatorial region has the maximum magnetic field and the minimum electric field. SRF cavity is designed as a single resonator, single-cell, or coupled resonators, multi-cell. SRF cavities are installed in a section of particle accelerators called cryomodule, which is cooled down to very low operating temperatures (around 2 K or 4 K). These temperatures are essential to attain minimal surface resistance see Figure A.1.3. A simple schematic diagram of a multi-cell cavity in a cryomodule is shown in Figure A.2.1.

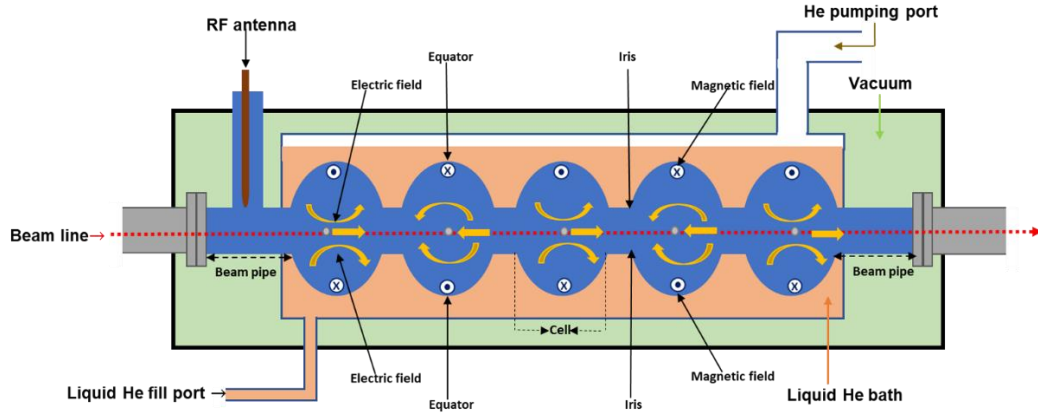


Figure A.2.1: Schematic diagram of the cross-section of a multi-cell SRF cavity excited in TM010 mode inside a cryomodule. The electric field oscillates back and forth along the beam axis. Correct timing of the beam arrival will result in acceleration. The cryomodule is equipped with an antenna that couples external RF power from an external RF source.

There are two main parameters to characterize the performance of a resonant cavity namely the accelerating gradient and the quality factor. The performance of a superconducting RF cavity is typically presented by a plot of the quality factor ( $Q_0$ ) as a function of the accelerating field ( $E_{acc}$ ). The accelerating gradient  $E_{acc}$  represents the energy gain of the beam per unit length of the cavity. It determines the length of an accelerator required to achieve particular energy, that is, increasing  $E_{acc}$  reduces the length of the accelerator. If  $V_c$  is the accelerating voltage per unit particle's charge across a cavity cell of length  $l_c$ ,

$$E_{acc} = \frac{V_c}{l_c} \quad \text{a.10}$$

$l_c$  is determined in such a way that the charged particle beam gain maximum energy for its velocity.

The quality factor  $Q_0$  represents the efficiency with which the RF energy is stored in the cavity. The higher value of  $Q_0$  results in reduction of required power for the operation

of particle accelerator. It is quantified by the ratio of electromagnetic energy stored to the dissipation in the cavity wall per RF cycle.

$$Q_0 = \frac{\omega U}{P_c} = \frac{\omega \mu_0 \int_V |\vec{H}|^2 dv}{\int_S R_s |\vec{H}|^2 ds} \quad \text{a. 11}$$

where  $U = \frac{1}{2} \mu_0 \int_V |\vec{H}|^2 dv$  and  $P_c = \frac{1}{2} \int_S R_s |\vec{H}|^2 ds$  are stored energy and dissipated power respectively. Here the RF magnetic field  $H(\vec{r}, \omega)$  for the excited mode with angular frequency  $\omega = 2\pi f$  is integrated over the cavity volume  $V$  and surface  $S$ . Since  $R_s$  is the only material-dependent factor, the equation can further condense into

$$Q_0 = \frac{G}{\langle R_s \rangle} \quad \text{a. 12}$$

Where the geometry factor  $G$  is given by

$$G = \frac{\omega \mu_0 \int_V |\vec{H}|^2 dv}{\int_S |\vec{H}|^2 ds} \quad \text{a. 13}$$

Geometry factor is determined by the shape of a cavity. Here it will be useful to compare the values of  $R_s$  for the normal conductor and superconductor. The value of  $R_s$  at about 1 GHz for cavity grade superconducting niobium at 2 K is approximately  $10 \text{ n}\Omega$  compared to that of copper close to  $7 \text{ m}\Omega$  [161]. It indicates that application of niobium achieves five orders of magnitude gain in  $Q_0$ .

The ratio of peak surface fields to the accelerating field,  $\frac{E_{pk}}{E_{acc}}$  and  $\frac{H_{pk}}{E_{acc}}$  are two other important factors useful to optimize the cavity shapes depending on accelerator application. The high surface electric field could lead to performance degradation by electron field emission. The surface magnetic field defines the ultimate limit of accelerating gradient.

### A.3 Niobium for SRF cavities

There are several superconductors that may be considered for SRF accelerator cavities. Bulk niobium ( $T_c \sim 9.2$  K,  $H_{sh} \sim 200$  mT and  $\Delta \sim 1.45$  meV) is dominant because of the best superconducting properties among all the pure elements. The material is more appealing for the fabrication of complicated shaped cavities because of its mechanical properties. Other than Nb, only lead has been rarely used in SRF accelerators. However, since it is mechanically soft it must be coated on a substrate such as copper or stainless steel to give the cavity sufficient mechanical strength. Over the past five decade, continual research and development efforts had been invested to advance the Nb SRF cavity technology. Many extrinsic mechanisms limiting the cavity performance were discovered, and adequate processes were developed to avoid them. Following these advances, the state-of-the-art niobium cavities are now approaching the performances set by the intrinsic material properties [2], [3]. One of such examples, A.2.1 shows the performance of an R&D cavity reaching close to the maximum theoretical gradient. This naturally quests for exploration beyond the bulk niobium.

Recent developments with impurity doping/infusion shows some room available to enhance the quality factor [89, 162], but magnetic field limitation indicates only a limited margin is available to push accelerating fields further. It should also be noted that niobium cavities often require to operate at  $\sim 2$  K for optimal performance, which demands complicated cryogenic facilities, and it is one of the major cost drivers for SRF-based accelerators. Those limitations urge for new innovations, which may require the pursuit of other forms of niobium or other superconductors.

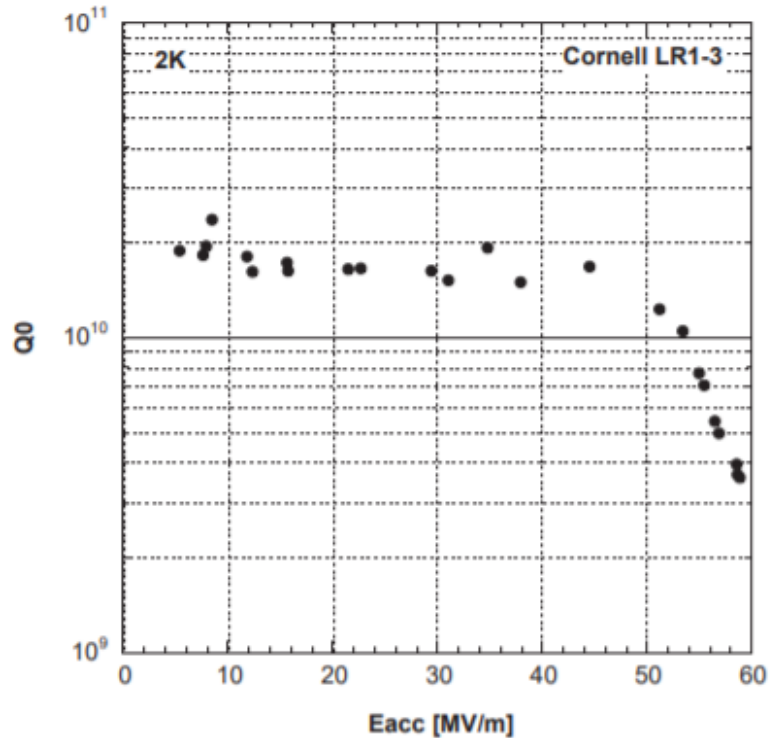


Figure A.2.2: RF performance of 1.3 GHz single-cell cavity. The attained maximum gradient here close to the fundamental limit to the accelerating gradient (57 MV/m) predicted for the Nb [107].

#### A.4 Alternate SRF cavity materials to bulk niobium

Two major factors merit consideration: potential to surpass the state-of-art niobium cavity performance and/or the major cost reduction for potential alternate materials to bulk niobium. That presents three options, in progress currently: a thin film of niobium, superconductors other than niobium and superconducting multilayer structures. If one can obtain the similar RF performance to that of bulk Nb from a thin Nb layer of few hundreds on nm (penetration depth of Nb  $\sim$  40 nm) on fabrication-friendly, less expensive metal with higher thermal conductivity, e.g. Cu, it promises cost savings in materials and possibly provide conveniently better cooling option, e.g. channel cooling instead of bath cooling. The concept of superconducting multilayer structures, proposed by A. Gurevich requires

the deposition of alternating superconductor and insulator layers (S-I-S layers) of thickness smaller than the penetration depth  $\lambda$  inside a cavity, which allows retaining the Meissner state higher than the bulk  $H_{c1}$  resulting in a significant enhancement in the achievable accelerating gradient [163].

An application of alternate superconductors is an appealing option to move passed niobium in SRF cavity application. It should be noted that a good material candidate for SRF application should possess superior superconducting properties, and also satisfy the technical aspects of fabrication and operation of SRF cavity defined by non-superconducting properties. Some of the important features to qualify a new superconductor as a potential SRF material are:

- High  $T_c$ ; High  $\Delta$ ; low surface resistance, also a low residual resistance at  $T \rightarrow 0$  for the high quality factor
- A high superheating magnetic field which determines the theoretical limit of the SRF breakdown
- S-wave superconductor:
- High thermal conductivity to transfer the RF dissipated power through the cavity wall
- Good mechanical properties and malleability favorable to cavity fabrication (forging, deep drawing, etc.)
- Preclude non-superconducting or poor-superconducting phases

Since all the possible candidates beyond Nb are compound, it is technically challenging to create them, which is the reason why they were given less attention in the past. There does not exist an ideal superconductor that would meet all the criteria listed above, but there are several potential materials with the potential to surpass niobium in

SRF cavities are shown in Table 1. A recent review, [163], provides an overview of the development of different materials.

Table A.1: Potential alternate SRF cavity materials with superconducting parameters [164].

Material	T <sub>c</sub> (K)	$\rho_n$ ( $\mu\Omega\text{cm}$ )	H <sub>c</sub> (0) (T)	H <sub>c1</sub> (0) (T)	H <sub>c2</sub> (0) (T)	$\lambda$ (nm)	$\Delta$ (meV)	$\zeta$ (nm)
Nb	9.2	2	0.20	0.18	0.28	40	1.5	35
NbN	16.2	70	0.23	0.02	15	200350	2.6	3-5
NbTiN	17.3	35		0.03	15	150-200	2.8	5
Nb <sub>3</sub> Sn	18	8-20	0.54	0.05	28	80-100	3.1	4
V <sub>3</sub> Si	17	4	0.72	0.07	24.50	179	2.5	3.5
Nb <sub>3</sub> Al	18.7	54			33	210	3	
Mo <sub>3</sub> Re	15	10-300	0.43	0.03	3.50	140		
MgB <sub>2</sub>	40	0.1-1	0.43	0.03	3.5-60	140	2.3/7.2	5

## References

- [1] R. D. Kephart et al., "SRF, Compact Accelerators for Industry & Society", in Proc. 17th Int. Conf. RF Superconductivity (SRF'15), Whistler, Canada, Sep. 2015, paper FRBA03, pp. 1467-1473.
- [2] F. Furuta et al., "Experimental Comparison at KEK of High Gradient Performance of Different Single Cell Superconducting Cavity Designs", in Proc. 10th European Particle Accelerator Conf. (EPAC'06), Edinburgh, UK, Jun. 2006, paper MOPLS084.
- [3] R. L. Geng, G. V. Ereemeev, H. Padamsee, and V. D. Shemelin, "High Gradient Studies for ILC with Single Cell Re-entrant Shape and Elliptical Shape Cavities made of Fine-grain and Large-grain Niobium", in Proc. 22nd Particle Accelerator Conf. (PAC'07), Albuquerque, NM, USA, Jun. 2007, paper WEPMS006, pp. 2337-2339.
- [4] B. T. Matthias et al, "Superconductivity of Nb<sub>3</sub>Sn", Physical Review, vol. 95, (6), pp. 1435, 1954.
- [5] G. F. Hardy and J. K. Hulm, "Superconducting silicides and germanides," Physical Review, vol. 89, (4), pp. 884, 1953.
- [6] J. Hulm, "Superconductivity research in the good old days," IEEE Trans. Magn., vol. 19, (3), pp. 161-166, 1983.
- [7] J. P. Charlesworth, I. Macphail and P. E. Madsen, "Experimental work on the Nb-tin constitution diagram and related studies," J. Mater. Sci., vol. 5, (7), pp. 580-603, 1970.
- [8] C. Toffolon et al, "Reassessment of the Nb-Sn system," Journal of Phase Equilibria, vol. 23, (2), pp. 134, 2002.
- [9] C. Toffolon, C. Servant and B. Sundman, "Thermodynamic assessment of the Nb-Sn system," Journal of Phase Equilibria, vol. 19, (5), pp. 479, 1998.
- [10] H. Okamoto, "Nb-Sn (Nb-Tin)," Journal of Phase Equilibria, vol. 24, (4), pp. 380, 2003.
- [11] A. Godeke, "A review of the properties of Nb<sub>3</sub>Sn and their variation with A15 composition, morphology and strain state," Superconductor Science and Technology, vol. 19, (8), pp. R68, 2006.

- [12] C. Sanabria, "A new understanding of the heat treatment of Nb-Sn superconducting wires". Diss. The Florida State University, 2017.
- [13] G. D. Cody and R. W. Cohen, "Thermal conductivity of Nb<sub>3</sub>Sn," *Reviews of Modern Physics*, vol. 36, (1), pp. 121, 1964.
- [14] F. Koechlin and B. Bonin, "Parametrization of the niobium thermal conductivity in the superconducting state," *Superconductor Science and Technology*, vol. 9, (6), pp. 453, 1996.
- [15] G. Ciovati et al. "High-current conduction cooled superconducting radio-frequency cryomodule." U.S. Patent Application No. 15/882,211. 2019.
- [16] R. C. Dhuley et al, "Thermal link design for conduction cooling of SRF cavities using cryocoolers," *IEEE Trans. Appl. Supercond.*, vol. 29, (5), pp. 1-5, 2019.
- [17] B. Hillenbrand et al, "Superconducting Nb<sub>3</sub>Sn cavities with high microwave qualities," *IEEE Trans. Magn.*, vol. 13, (1), pp. 491-495, 1977.
- [18] G. Müller et al, "Status and prospects of Nb<sub>3</sub>Sn cavities for superconducting linacs," in *Proceedings of the Workshop on Thin Film Coating Methods for Superconducting Accelerating Cavities*, 2000.
- [19] A. Godeke, "Performance boundaries in Nb<sub>3</sub>Sn superconductors PhD Thesis Univ. of Twente," Enschede, the Netherlands ISBN, pp. 90-365, 2005.
- [20] P. Boccard, P. Kneisel, G. Müller, J. Pouryamout, and H. Piel, "Results From Some Temperature Mapping Experiments on Nb<sub>3</sub>Sn RF Cavities", in *Proc. 8th Int. Conf. RF Superconductivity (SRF'97)*, Padova, Italy, Oct. 1997, paper SRF97D32, pp. 1094-1102.
- [21] M. Peiniger and H. Piel, "A superconducting Nb<sub>3</sub>Sn coated multicell accelerating cavity," *IEEE Trans. Nucl. Sci.*, vol. 32, (5), pp. 3610-3612, 1985.
- [22] S. M. Deambrosis et al, "A15 superconductors: An alternative to niobium for RF cavities," *Physica C: Superconductivity*, vol. 441, (1-2), pp. 108-113, 2006.
- [23] S. Posen and M. Liepe, "RF Test Results of the first Nb<sub>3</sub>Sn Cavities Coated at Cornell", in *Proc. 16th Int. Conf. RF Superconductivity (SRF'13)*, Paris, France, Sep. 2013, paper TUP087, pp. 666-669.
- [24] S. Posen et al., "Development of Nb<sub>3</sub>Sn Coatings for Superconducting RF Cavities at Fermilab", in *Proc. 9th Int. Particle Accelerator Conf. (IPAC'18)*, Vancouver, Canada, Apr.-May 2018, WEPML016, pp. 2718-2720.
- [25] G. V. Ereemeev, W. A. Clemens, K. Macha, H. Park, and R. S. Williams, "Commissioning Results of Nb<sub>3</sub>Sn Cavity Vapor Diffusion Deposition System at JLab", in *Proc. 6th Int. Particle Accelerator Conf. (IPAC'15)*, Richmond, VA, USA, May 2015, WEPWI011, pp. 3512-3514.

- [26] U. Pudasaini et al., "Nb<sub>3</sub>Sn Multicell Cavity Coating at JLab", in Proc. 9th Int. Particle Accelerator Conf. (IPAC'18), Vancouver, Canada, Apr.-May 2018, pp. 1798-1803. doi:10.18429/JACoW-IPAC2018-WEYGBF3.
- [27] R. D. Porter et al., "Next Generation Nb<sub>3</sub>Sn SRF Cavities for Linear Accelerators", in Proc. 29th Linear Accelerator Conf. (LINAC'18), Beijing, China, Sep. 2018, pp. 462-465. doi:10.18429/JACoW-LINAC2018-TUPO055.
- [28] G. J. Rosaz et al., "Development of Nb<sub>3</sub>Sn Coatings by Magnetron Sputtering for SRF Cavities", in Proc. 17th Int. Conf. RF Superconductivity (SRF'15), Whistler, Canada, Sep. 2015, paper TUPB051, pp. 691-694.
- [29] M.N. Sayeed, H. Elsayed-Ali, G. V. Ereemeev, M. J. Kelley, C. E. Reece, and U. Pudasaini, "Magnetron Sputtering of Nb<sub>3</sub>Sn for SRF Cavities", in Proc. 9th Int. Particle Accelerator Conf. (IPAC'18), Vancouver, Canada, Apr.-May 2018, pp. 3946-3949. doi:10.18429/JACoW-IPAC2018-THPAL129.
- [30] E. Barzi et al, "Synthesis of superconducting Nb<sub>3</sub>Sn coatings on Nb substrates," Superconductor Science and Technology, vol. 29, (1), pp. 015009, 2015.
- [31] Z. Q. Yang, Y. He, and F. Pan, "Several Experimental Phenomena of Sn Nucleation on Nb Surface Observed at IMP", in Proc. 29th Linear Accelerator Conf. (LINAC'18), Beijing, China, Sep. 2018, pp. 412-416. doi:10.18429/JACoW-LINAC2018-TUPO038.
- [32] E. A. Ilyina et al, "Development of sputtered Nb<sub>3</sub>Sn films on copper substrates for superconducting radiofrequency applications," Superconductor Science and Technology, vol. 32, (3), pp. 035002, 2019.
- [33] P. Kneisel, "History of Nb<sub>3</sub>Sn developments for superconducting RF cavities - A review," JLAB Technical Note, JLAB-TN-13-04, 2012.
- [34] Ereemeev Grigory, "A review of Nb<sub>3</sub>Sn vapor diffusion process development for SRF cavities," 2012.
- [35] S. Posen and D. L. Hall, "Nb<sub>3</sub>Sn superconducting radiofrequency cavities: fabrication, results, properties, and prospects," Superconductor Science and Technology, vol. 30, (3), pp. 033004, 2017.
- [36] S. Posen et al., "Nb<sub>3</sub>Sn at Fermilab: Exploring Performance", presented at the 19th Int. Conf. RF Superconductivity (SRF'19), Dresden, Germany, Jun.-Jul. 2019, paper THFUB1.
- [37] R. D. Porter, M. Liepe, and J. T. Maniscalco, "High Frequency Nb<sub>3</sub>Sn Cavities", presented at the 19th Int. Conf. RF Superconductivity (SRF'19), Dresden, Germany, Jun.-Jul. 2019, paper MOP011.
- [38] J. M. Dickey, M. Strongin and O. F. Kammerer, "Studies of thin films of Nb<sub>3</sub>Sn on Nb," J. Appl. Phys., vol. 42, (13), pp. 5808-5820, 1971.

- [39] A. A. Rossi et al., "Nb<sub>3</sub>Sn Films by Multilayer Sputtering", in Proc. 14th Int. Conf. RF Superconductivity (SRF'09), Berlin, Germany, Sep. 2009, paper TUOBAU06, pp. 149-154.
- [40] S. M. Deambrosis, "6 GHz cavities: a method to test A15 intermetallic compounds Rfproperties," PhD dissertation, University of Padova, 2008.
- [41] S. Mitsunobu, "Status of KEK studies on MgB<sub>2</sub>." In Proc. 4th Int. Workshop on Thin Films and New Ideas for Pushing the Limits of RF Superconductivity (Padua). 2010.
- [42] M. Krishnan, C James and B Bures, "Energetic Condensation Growth of Nb<sub>3</sub>Sn, MoRe and MgB<sub>2</sub> films for SRF Accelerators", 5th International Workshop Int. Workshop on Thin Films and New Ideas for Pushing the Limits of RF Superconductivity ", 2012.
- [43] C. A. Neugebauer, "Thin Films of Niobium Tin by Codeposition," J. Appl. Phys., vol. 35, (12), pp. 3599-3603, 1964.
- [44] E. Saur and J. Wurm, "Preparation and superconducting properties of niobium wire samples with Nb 3 Sn coating." Natural Sciences 49.6 (1962): 127-128.
- [45] G. Arnolds and D. Proch, "Measurement on a Nb 3 Sn structure for linear accelerator application," IEEE Trans. Magn., vol. 13, (1), pp. 500-503, 1977.
- [46] P. Kneisel, O. Stoltz and J. Halbritter, "Measurements of superconducting Nb 3 Sn cavities in the GHz range," IEEE Trans. Magn., vol. 15, (1), pp. 21-24, 1979.
- [47] P. Kneisel et al, "Nb<sub>3</sub>Sn Layers on High-Purity Nb Cavities with Very High Quality Factors and Accelerating Gradients", in Proc. 5th European Particle Accelerator Conf. (EPAC'96), Sitges, Spain, Jun. 1996, paper WEP002L.
- [48] J. B. Stimmell, "Microwave superconductivity of Nb<sub>3</sub>Sn," PhD dissertation, Cornell University, 1978.
- [49] M. Peiniger, M. Hein, N. Klein, G. Müller, H. Piel, and P. Thüns, "Work on Nb<sub>3</sub>Sn Cavities at Wuppertal", in Proc. 3rd Int. Conf. RF Superconductivity (SRF'87), Lemont, IL, USA, Sep. 1987, paper SRF87E04.
- [50] M. Liepe and S. Posen, "Nb<sub>3</sub>Sn for SRF Application", in Proc. 16th Int. Conf. RF Superconductivity (SRF'13), Paris, France, Sep. 2013, paper WEIOA04, pp. 773-776.
- [51] S. Posen, M. Merio, A. Romanenko, and Y. Trenikhina, "Fermilab Nb<sub>3</sub>Sn R&D Program", in Proc. 17th Int. Conf. RF Superconductivity (SRF'15), Whistler, Canada, Sep. 2015, paper TUPB048, pp. 678-680.
- [52] G. V. Ereemeev, M. J. Kelley, C. E. Reece, U. Pudasaini, and J. Tuggle, "Progress With Multi-Cell Nb<sub>3</sub>Sn Cavity Development Linked With Sample Materials Characterization", in Proc. 17th Int. Conf. RF Superconductivity (SRF'15), Whistler, Canada, Sep. 2015, paper TUBA05, pp. 505-511.

- [53] B. Hillenbrand and H. Martens, "Superconducting Nb<sub>3</sub>Sn cavities with high quality factors and high critical flux densities," J. Appl. Phys., vol. 47, (9), pp. 4151-4155, 1976.
- [54] U. Pudasaini, G. Ciovati, G. V. Eremeev, M. J. Kelley, I. P. Parajuli, and C. E. Reece, "Recent Results from Nb<sub>3</sub>Sn-Coated Single-cell Cavities Combined with Sample Studies at Jefferson Lab", in Proc. 10th Int. Particle Accelerator Conf. (IPAC'19), Melbourne, Australia, May 2019, paper WEPRB110, pp. 3066-3069.
- [55] P. Kneisel, "Surface Preparation of Niobium", in Proc. 1st Int. Conf. RF Superconductivity (SRF'80), Karlsruhe, Germany, Jul. 1980, paper SRF80-2.
- [56] M. Wilhelm, S. Frohmader and G. Ziegler, "Production of High Current V3Ga and Nb<sub>3</sub>Sn Multifilament Conductors Using Chemical Transport Reactions," Mater. Res. Bull., vol. 11, (5), pp. 491-495, 1976.
- [57] Band 46 Sn [B] Gmelins Handbuch der Anorganischen Chemie (Weinheim: Verlag Chemie) pp. 176.
- [58] Landolt-Boernstein Auflage 6, Band II, Teil2, Bandteil:a Zahlenwerte und Funktionen aus Physik, Chemie, Astronomie, Geophysik und Technik
- [59] U. Pudasaini et al, "Initial growth of tin on niobium for vapor diffusion coating of Nb<sub>3</sub>Sn," Supercond. Sci. Technol. 32 045008, 2019.
- [60] Kanaya, K. A., and S. Okayama. "Penetration and energy-loss theory of electrons in solid targets." Journal of Physics D: Applied Physics 5.1 (1972): 43.
- [61] R. Castaing, "Electron probe microanalysis." In Advances in electronics and electron physics, vol. 13, pp. 317-386. Academic Press, 1960. [57] J. C. Vickerman and I. S. Gilmore, Surface Analysis: The Principal Techniques. John Wiley & Sons, 2011.
- [62] C.A. Anderson, M.F. Hasler, in X-ray Optics and Microanalysis, Fourth International Congress on X-ray Optics and Microanalysis, Orsay, 1965, eds. by R. Castaing, P. Deschamps, K. Philibert (Herman, Paris, 1966), p. 310.
- [63] J. Tuggle et al, "Electron backscatter diffraction of Nb<sub>3</sub>Sn coated niobium: Revealing structure as a function of depth," Journal of Vacuum Science & Technology B, Nanotechnology and Microelectronics: Materials, Processing, Measurement, and Phenomena, vol. 37, (5), pp. 052901, 2019.
- [64] J. C. Vickerman and I. S. Gilmore, Surface Analysis: The Principal Techniques. John Wiley & Sons, 2011.
- [65] R. Hesse, P. Streubel and R. Szargan, "Improved accuracy of quantitative XPS analysis using predetermined spectrometer transmission functions with UNIFIT 2004," Surf. Interface Anal., vol. 37, (7), pp. 589-607, 2005.
- [66] C. J. Powell and A. Jablonski, "No title," NIST Electron Inelastic-Mean-Free-Path Database 71, Version 1.1, 2000.

- [67] Z. Wu and J. M. Dickey, "Growth mode of tin on a niobium substrate," *Thin Solid Films*, vol. 371, (1-2), pp. 161-166, 2000.
- [68] C. Eisenmenger-Sittner et al, "Stranski–Krastanov growth of Sn on a polycrystalline Al film surface initiated by the wetting of Al by Sn," *Surf. Sci.*, vol. 489, (1-3), pp. 161-168, 2001.
- [69] B. Hillenbrand, "The Preparation of Superconducting Nb<sub>3</sub>Sn Surfaces for RF Applications", in Proc. 1st Int. Conf. RF Superconductivity (SRF'80), Karlsruhe, Germany, Jul. 1980, paper SRF80-3.
- [70] U. Pudasaini et al, "Surface studies of Nb<sub>3</sub>Sn coated samples prepared under different coating conditions," in 18th Int. Conf. on RF Superconductivity (SRF'17), Lanzhou, China, July 17-21, 2017, 2018, pp. 894-899, pp. THPB069
- [71] D. L. Hall et al., "High Performance Nb<sub>3</sub>Sn Cavities", in Proc. 18th Int. Conf. RF Superconductivity (SRF'17), Lanzhou, China, Jul. 2017, pp. 667-673. doi:10.18429/JACoW-SRF2017-WEXA01.
- [72] D. L. Hall, "New Insights into the Limitations on the Efficiency and Achievable Gradients in Nb<sub>3</sub>Sn SRF Cavities." PhD. Diss., Cornell University, 2017.
- [73] H. Tian et al, "Surface studies of niobium chemically polished under conditions for superconducting radio frequency (SRF) cavity production," *Appl. Surf. Sci.*, vol. 253, (3), pp. 1236-1242, 2006.
- [74] B. R. King et al, "Kinetic measurements of oxygen dissolution into niobium substrates: In situ X-ray photoelectron spectroscopy studies," *Thin Solid Films*, vol. 192, (2), pp. 351-369, 1990.
- [75] Q. Ma and R. A. Rosenberg, "Angle-resolved X-ray photoelectron spectroscopy study of the oxides on Nb surfaces for superconducting rf cavity applications," *Appl. Surf. Sci.*, vol. 206, (1-4), pp. 209-217, 2003.
- [76] H. Yorucu and F. R. Sale, "The production of Nb-Sn powder by vapor deposition method," *Journal of Electronic Materials*, vol. 21, (1), pp. 625-631, 1992.
- [77] J. M. Brear and F. R. Sale, "The vapour phase stannising of copper," *Journal of the Less-Common Metals*, vol. 38, (2), pp. 221-232, 1974.
- [78] I. Gaballah and M. Djona, "Processing of spent hydrotreating catalysts by selective chlorination," *Metallurgical and Materials Transactions B*, vol. 25, (4), pp. 481-490, 1994.
- [79] J. D. Gilchrist, "Extraction Metallurgy." Pergamon Press plc, 1989, (1989): 431.
- [80] J. Gonzalez et al, "Chlorination of niobium and tantalum ore," *Thermochimica Acta*, vol. 311, (1-2), pp. 61-69, 1998.

- [81] M. Delheusy, "X-ray investigation of Nb/O interfaces," PhD diss., Université Paris, 2008.
- [82] H. Wadley et al, "Mechanisms, models and methods of vapor deposition," *Progress in Materials Science*, vol. 46, (3-4), pp. 329-377, 2001.
- [83] M. R. Fellingner, H. Park and J. W. Wilkins, "Force-matched embedded-atom method potential for Nb," *Physical Review B*, vol. 81, (14), pp. 144119, 2010
- [84] M. Peiniger et al, "Work on Nb<sub>3</sub>Sn Cavities at Wuppertal", in Proc. 3rd Int. Conf. RF Superconductivity (SRF'87), Lemont, IL, USA, Sep. 1987, paper SRF87E04.
- [85] P. Kneisel et al. "Properties of Superconducting Nb<sub>3</sub>Sn Layers Used in RF Cavities." *Advances in Cryogenic Engineering*. Springer, Boston, MA, 1978. 442-448.
- [86] S. Posen, "Understanding and Overcoming Limitation Mechanisms in Nb<sub>3</sub>Sn Superconducting RF Cavities", PhD Diss., Cornell University, 2015.
- [87] H. Tian et al, "A novel approach to characterizing the surface topography of niobium superconducting radio frequency (SRF) accelerator cavities," *Appl. Surf. Sci.*, vol. 257, (11), pp. 4781-4786, 2011.
- [88] C. Xu et al, "Enhanced characterization of niobium surface topography," *Physical Review Special Topics-Accelerators and Beams*, vol. 14, (12), pp. 123501, 2011.
- [89] P. Dhakal et al, "Effect of high temperature heat treatments on the quality factor of a large-grain superconducting radio-frequency niobium cavity," *Physical Review Special Topics-Accelerators and Beams*, vol. 16, (4), pp. 042001, 2013.
- [90] H. H. Farrell, G. H. Gilmer and M. Suenaga, "Diffusion mechanisms for the growth of Nb<sub>3</sub>Sn intermetallic layers," *Thin Solid Films*, vol. 25, (1), pp. 253-264, 1975.
- [91] H. H. Farrell, G. H. Gilmer and M. Suenaga, "Grain boundary diffusion and growth of intermetallic layers: Nb<sub>3</sub>Sn," *J. Appl. Phys.*, vol. 45, (9), pp. 4025-4035, 1974.
- [92] G. N. Ronami et al, "Investigation of diffusion in the Nb-Sn system," *Izvestiya Akademii Nauk SSSR, Neorganicheskie Materialy*, vol. 7, (9), pp. 1490-1493, 1971.
- [93] C. F. Old and I. Macphall, "The mechanism and kinetics of growth of the superconducting compound Nb<sub>3</sub>Sn," *J. Mater. Sci.*, vol. 4, (3), pp. 202-207, 1969.
- [94] H. Müller and T. Schneider, "Heat treatment of Nb<sub>3</sub>Sn conductors," *Cryogenics*, vol. 48, (7-8), pp. 323-330, 2008.
- [95] ASTM E112–13 (2016) Standard Test Methods for Determining Average Grain Size, ASTM International, West Conshohocken, PA. [Www.Astm.Org](http://www.Astm.Org).
- [96] ASTM E-42, Standard Terminology Relating to Surface Analysis E 673-91c, ASTM, Philadelphia, 1992.

- [97] S. Hofmann, "Sputter depth profile analysis of interfaces," Reports on Progress in Physics, vol. 61, (7), pp. 827, 1998.
- [98] J. D. Baird, "The formation of intermediate alloy layers in the inter-diffusion of metals," Journal of Nuclear Energy.Part A.Reactor Science, vol. 11, (2-4), pp. 81-88, 1960.
- [99] V. I. Dybkov, Reaction Diffusion and Solid State Chemical Kinetics: Handbook. 2010.
- [100] Jun Ding, "Preparation and Investigation of Superconducting Nb<sub>3</sub>Sn Layers in Multicellular 3 GHz Accelerator Resonators.", Wuppertal University, 1986.
- [101] R. H. Parker, An Introduction to Chemical Metallurgy: International Series on Materials Science and Technology. 201626.
- [102] A. K. Kumar and A. Paul, "Interdiffusion and growth of the superconductor Nb<sub>3</sub>Sn in Nb/Cu (Sn) diffusion couples," J Electron Mater, vol. 38, (5), pp. 700-705, 2009.
- [103] S. Foner and B. B. Schwartz, Superconductor materials science: metallurgy, fabrication, and applications. Vol. 68. Springer Science & Business Media, 2012.
- [104] X. Xu, "A review and prospects for Nb<sub>3</sub>Sn superconductor development," Superconductor Science and Technology, vol. 30, (9), pp. 093001, 2017.
- [105] B. V. Reddi et al, "Models for growth kinetics of A-15 compounds by solid state diffusion," Philos. Mag. A, vol. 38, (5), pp. 559-568, 1978.
- [106] Y. Trenikhina et al, "Performance-defining properties of Nb<sub>3</sub>Sn coating in SRF cavities," Superconductor Science and Technology, vol. 31, (1), pp. 015004, 2017.
- [107] H. Padamsee, J. Knobloch and T. Hays, "RF Superconductivity for Accelerators John Wiley & Sons," Inc., New York, pp. 199, 1998.
- [108] C. Becker et al, "Analysis of Nb<sub>3</sub>Sn surface layers for superconducting radio frequency cavity applications," Appl. Phys. Lett., vol. 106, (8), pp. 082602, 2015.
- [109] C. V. Thompson, "Grain growth in thin films," Annual Review of Materials Science, vol. 20, (1), pp. 245-268, 1990.
- [110] B. Kim, K. Hiraga and K. Morita, "Kinetics of normal grain growth depending on the size distribution of small grains," Materials Transactions, vol. 44, (11), pp. 2239-2244, 2003.
- [111] D. Moldovan et al, "Role of grain rotation during grain growth in a columnar microstructure by mesoscale simulation," Acta Materialia, vol. 50, (13), pp. 3397-3414, 2002.
- [112] A. J. Haslam et al, "Mechanisms of grain growth in nanocrystalline fcc metals by molecular-dynamics simulation," Materials Science and Engineering: A, vol. 318, (1-2), pp. 293-312, 2001.

- [113] J. Lee et al, "Atomic-scale analyses of Nb<sub>3</sub>Sn on Nb prepared by vapor diffusion for superconducting radiofrequency cavity applications: a correlative study," Superconductor Science and Technology, vol. 32, (2), pp. 024001, 2018.
- [114] U. Pudasaini, M. J. Kelley, G. V. Eremeev, C. E. Reece, and J. Tuggle, "Examination of Cutouts Inner Surfaces from Nb<sub>3</sub>Sn Coated Cavity", in Proc. 28th Linear Accelerator Conf. (LINAC'16), East Lansing, MI, USA, Sep. 2016, pp. 189-192, Paper MOPLR023.
- [115] Y. Iwashita, Y. Tajima and H. Hayano, "Development of high resolution camera for observations of superconducting cavities," Physical Review Special Topics-Accelerators and Beams, vol. 11, (9), pp. 093501, 2008.
- [116] G. Ciovati et. al, "A 2-cell temperature mapping system for ILC cavities." Jefferson Lab Technical Note, TN-08-012 (2008).
- [117] Knobloch Jens, "Advanced Thermometry Studies of Superconducting RF Cavities", PhD. Diss., Cornell University, 1997.
- [118] M. Fouaidy et. Al., "Kapitza conductance and thermal conductivity of materials used for SRF cavities fabrication," in 9th Int. Conf. RF Superconductivity (SRF'99), Nov. 1999, pp. 263-266.
- [119] J. Amrit and M. X. Francois, "Heat flow at the niobium-superfluid helium interface: Kapitza resistance and superconducting cavities," J. Low Temp. Phys., vol. 119, (1-2), pp. 27-40, 2000.
- [120] A. Aizaz et al, "Measurements of thermal conductivity and Kapitza conductance of niobium for SRF cavities for various treatments," IEEE Trans. Appl. Supercond., vol. 17, (2), pp. 1310-1313, 2007.
- [121] T. Kubo, "Magnetic field enhancement at a pit on the surface of a superconducting accelerating cavity," Progress of Theoretical and Experimental Physics, vol. 2015, (7), 2015.
- [122] T. Kubo, "Field limit and nano-scale surface topography of superconducting radio-frequency cavity made of extreme type II superconductor," Progress of Theoretical and Experimental Physics, vol. 2015, (6), 2015.
- [123] K. S. SreeHarsha, Principles of Physical Vapor Deposition of Thin Films. 2006. Elsevier, 2006.
- [124] W. Yuming and W. Alfred, An Introduction to Physics and Technology of Thin Films. 1994.
- [125] P. Kneisel et al, "On properties of superconducting Nb<sub>3</sub>Sn used as coatings in RF cavities," IEEE Trans. Magn., vol. 13, (1), pp. 496-499, 1977.
- [126] M. Peiniger, PhD Diss., Wuppertal University, 1989.

- [127] D. K. Finnemore and D. E. Mapother, "Superconducting properties of tin, indium, and mercury below 1 K," *Physical Review*, vol. 140, (2A), pp. A507, 1965.
- [128] F. Marhauser et. al., "C75 cavity specifications and commissioning of the prototype cavity pair" Jefferson Lab Technical Note, JLAB-TN-17-055, 2017.
- [129] G. V. Eremeev and U. Pudasaini, "Development of Nb<sub>3</sub>Sn Multicell Cavity Coatings", in Proc. 10th Int. Particle Accelerator Conf. (IPAC'19), Melbourne, Australia, May 2019, pp. 3070-3073. Paper WEPRB111.
- [130] J. Knobloch, R. L. Geng, H. Padamsee, and M. Liepe, "High-Field Q Slope in Superconducting Cavities due to Magnetic Field Enhancement at Grain Boundaries", in Proc. 9th Int. Conf. RF Superconductivity (SRF'99), Santa Fe, NM, USA, Nov. 1999, paper TUA004, pp. 77-91.
- [131] A. Dzyuba, A. Romanenko and L. D. Cooley, "Model for initiation of quality factor degradation at high accelerating fields in superconducting radio-frequency cavities," *Superconductor Science and Technology*, vol. 23, (12), pp. 125011, 2010.
- [132] A. Grassellino et al, "Unprecedented quality factors at accelerating gradients up to 45 MVm<sup>-1</sup> in niobium superconducting resonators via low temperature nitrogen infusion," *Superconductor Science and Technology*, vol. 30, (9), pp. 094004, 2017.
- [133] A. Grassellino et al, "Accelerating fields up to 49 MV/m in TESLA-shape superconducting RF niobium cavities via 75C vacuum bake," arXiv Preprint arXiv:1806.09824, 2018.
- [134] C. Z. Antoine, "How to achieve the best SRF performance:(Practical) Limitations and possible solutions," arXiv Preprint arXiv:1501.03343, 2015.
- [135] P. Dhakal et al, "Enhancement in quality factor of SRF niobium cavities by material diffusion," *IEEE Trans. Appl. Supercond.*, vol. 25, (3), pp. 1-4, 2014.
- [136] U. Pudasaini, M. J. Kelley, G. V. Eremeev, C. E. Reece, and J. Tuggle, "Studies of Electropolishing and Oxypolishing Treated Diffusion Coated Nb<sub>3</sub>Sn Surfaces", in Proc. 9th Int. Particle Accelerator Conf. (IPAC'18), Vancouver, Canada, Apr.-May 2018, pp. 3954-3957, Paper THPAL131.
- [137] U. Pudasaini, M. J. Kelley, G. V. Eremeev, C. E. Reece, and H. Tian, "Electrochemical Finishing Treatment of Nb<sub>3</sub>Sn Diffusion-coated Niobium", in Proc. 18th Int. Conf. RF Superconductivity (SRF'17), Lanzhou, China, Jul. 2017, pp. 900-905. Paper THPB070.
- [138] U. Pudasaini, M. J. Kelley, G. V. Eremeev, C. E. Reece, and J. Tuggle, "Post-Processing of Nb<sub>3</sub>Sn Coated Nb", in Proc. 8th Int. Particle Accelerator Conf. (IPAC'17), Copenhagen, Denmark, May 2017, pp. 1190-1193. Paper MOPVA144..
- [139] R. D. Porter, F. Furuta, D. L. Hall, M. Liepe, and J. T. Maniscalco, "Effectiveness of Chemical Treatments for Reducing the Surface Roughness of Nb<sub>3</sub>Sn", in Proc. 8th Int.

Particle Accelerator Conf. (IPAC'17), Copenhagen, Denmark, May 2017, Paper MOPVA124.

[140] G. Ciovati, "RF superconductivity: Physics, technology and applications; surface preparation," U.S. Particle Accelerator School, 2015.

[141] H. Tian et al, "The mechanism of electropolishing of niobium in hydrofluoric–sulfuric acid electrolyte," J. Electrochem. Soc., vol. 155, (9), pp. D563-D568, 2008.

[142] N. W. Khun, M. Sumption and G. S. Frankel, "Smoothing of niobium by electropolishing," J. Appl. Electrochem., vol. 43, (8), pp. 829-838, 2013.

[143] M. P. Kelly and T. Reid, "Surface processing for bulk niobium superconducting radio frequency cavities," Superconductor Science and Technology, vol. 30, (4), pp. 043001, 2017.

[144] PA Jaquet, Trans. Electrochem, Soc. 69 (1936) 629.

[145] J. Tuggle, M. J. Kelley, G. V. Ereemeev, C. E. Reece, and H. Xu, "Structure and Composition of Nb<sub>3</sub>Sn Diffusion Coated Films on Nb", in Proc. 17th Int. Conf. RF Superconductivity (SRF'15), Whistler, Canada, Sep. 2015, paper TUPB046, pp. 669-672.

[146] J. Halbritter and A. Darlinski, "Angle resolved XPS studies of oxides at Nb-, NbN-, NbC- and Nb<sub>3</sub>Sn-surfaces," IEEE Trans. Magn., vol. 23, (2), pp. 1381-1384, 1987.

[147] J. A. Strozier et al, "Alloys of Sn and Ge on Nb surfaces," J. Appl. Phys., vol. 47, (4), pp. 1611-1615, 1976.

[148] M. N. Sayeed et al, "Structural and superconducting properties of Nb<sub>3</sub>Sn films grown by multilayer sequential magnetron sputtering," J. Alloys Compounds, 2019. Volume 800, 5, 2019, Pp. 272-278.

[149] H. Padamsee, J. Knobloch and T. Hays, RF Superconductivity for Accelerators. Vol. 2011. New York: Wiley-vch, 2008.

[150] M. Tinkham, Introduction to superconductivity. Courier Corporation, 2004.

[151] C. E. Reece and G. Ciovati, "Superconducting radio-frequency technology R&D for future accelerator applications," in Reviews of Accelerator Science and Technology: Volume 5: Applications of Superconducting Technology to Accelerators Anonymous 2012.

[152] P. Schmüser, "Basic principles of RF superconductivity and superconducting cavities," 2006.

[153] A. Gurevich, "Theory of RF superconductivity for resonant cavities," Superconductor Science and Technology, vol. 30, (3), pp. 034004, 2017.

[154] H. Kamerlingh Onnes, "The resistance of pure mercury at helium temperatures," Commun.Phys.Lab.Univ.Leiden, B, vol. 120, 1911.

- [155] W. Meissner and R. Ochsenfeld, "A new effect on the entry of superconductivity." *Natural Science* 21.44 (1933): 787-788.
- [156] R. A. Serway, J. M. Clemens, and A. M. Curt. *Modern physics*. Cengage Learning, 2004 (Chapter 12 — [web resources](#)).
- [157] F. London and H. London, "The electromagnetic equations of the supraconductor," *Proceedings of the Royal Society of London. Series A-Mathematical and Physical Sciences*, vol. 149, (866), pp. 71-88, 1935.
- [158] V. L. Ginzburg and L. D. Landau, "On the theory of superconductivity," *On Superconductivity and Superfluidity*. Springer, Berlin, Heidelberg, 2009. 113-137.
- [159] J. Bardeen, L. N. Cooper and J. R. Schrieffer, "Microscopic theory of superconductivity," *Physical Review*, vol. 106, (1), pp. 162, 1957.
- [160] B. Aune et al, "Superconducting TESLA cavities," *Physical Review Special Topics-Accelerators and Beams*, vol. 3, (9), pp. 092001, 2000.
- [161] G. Ciovati, "AC/RF Superconductivity," *arXiv Preprint arXiv:1501.07398*, 2015.
- [162] A. Grassellino et al, "Nitrogen and argon doping of niobium for superconducting radio frequency cavities: a pathway to highly efficient accelerating structures," *Superconductor Science and Technology*, vol. 26, (10), pp. 102001, 2013.
- [163] A. Gurevich, "Enhancement of rf breakdown field of superconductors by multilayer coating," *Appl. Phys. Lett.*, vol. 88, (1), pp. 012511, 2006.
- [164] A. Valente-Feliciano, "Superconducting RF materials other than bulk niobium: a review," *Superconductor Science and Technology*, vol. 29, (11), pp. 113002, 2016.